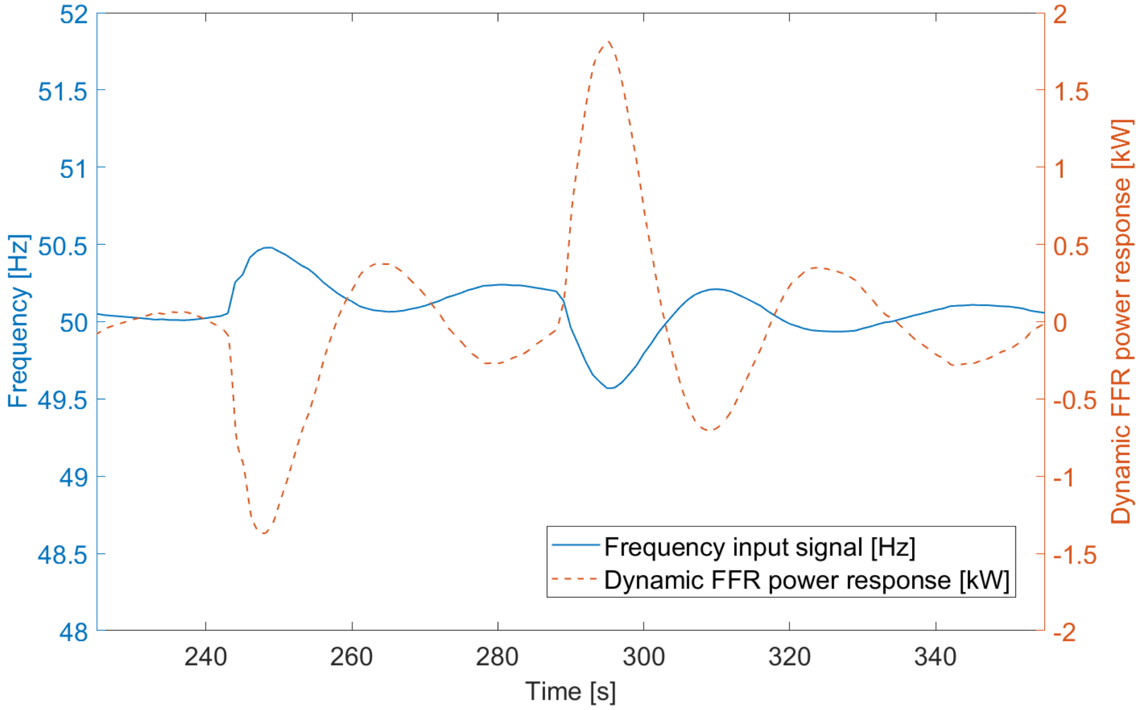

Dynamic FFR from wind power

- from simulation to reality

Master's thesis in Sustainable energy systems

LISA DACKLIN

DEPARTMENT OF ELECTRICAL ENGINEERING

CHALMERS UNIVERSITY OF TECHNOLOGY
Gothenburg, Sweden 2024
www.chalmers.se

MASTER'S THESIS 2024

Dynamic FFR from wind power

- from simulation to reality

LISA DACKLIN

Department of Electrical Engineering
CHALMERS UNIVERSITY OF TECHNOLOGY
Gothenburg, Sweden 2024

Dynamic FFR from wind power
- from simulation to reality
LISA DACKLIN

Supervisors: Sophia Appelstål, Svenska kraftnät, Henrik Ekestam, Svenska kraftnät, Magnus Ellsén, department of Electrical Engineering, Chalmers, Linn Saarinen, Svenska kraftnät.
Examiner: Ola Carlson, department of Electrical Engineering, Chalmers.

Degree project report 2024
Department of Electrical Engineering
Chalmers University of Technology
SE-412 96 Gothenburg
Sweden
Telephone +46 31 772 1000

Cover: Example of dynamic FFR power response to a recorded frequency input signal.

Typeset in LaTeX
Gothenburg, Sweden 2024

Dynamic FFR from wind power
- from simulation to reality
LISA DACKLIN
Department of Electrical Engineering
Chalmers University of Technology

Abstract

As future forecasts of less inertia in the power system require new types of reserves, dynamic Fast Frequency Reserve (FFR) is a new suggested ancillary service that is investigated in this project to be provided by wind power. Two different prototypes were developed to test dynamic FFR from wind power, through simulations and practical tests with Chalmers wind turbine at Björkö. Both prototypes work by adding an additional torque contribution from a dynamic FFR controller, which follows a frequency input signal dynamically, to the electrical reference torque estimated by the National Renewable Energy Laboratory (NREL) controller. To mitigate that the NREL controller counteracts dynamic FFR, the prototypes offer different solutions in adjusting the rotational speed entering the NREL controller. Prototype A works by slowing down the effects of the NREL controller, while prototype B tries to estimate an unaffected rotational speed as input to the NREL controller. The overall results indicate that dynamic FFR from wind power looks promising, as the dynamic response allows for intended energy recovery. Step tests with both prototypes show clearly that the power increases or decreases as intended, and that the rotational speed consequently decreases or increases, but also that the endurance could be a potential problem. Furthermore, simulations show that efficiency decrease due to dynamic FFR could be an issue. Different wind conditions are also a potential challenge, but dynamic FFR could still be enabled during low wind velocity conditions by adjusting the torque-rotational speed curve. Closed loop simulations with the power system show that both prototypes improves the frequency minimum, nadir, and following maximum, zenith, during a large disturbance. Bode plots show that prototype A, given the settings that were used for the prototype, almost fulfils requirements set for Power Oscillation Damping - active power (POD-P), and that the frequency stability of the power system can be improved by dynamic FFR provided by prototype A in situations with inertia down to 100 GWs. Specifics on design and technical requirements must be further investigated, and practical tests must be carried out on conventional wind turbines, since they might not face the same issues with endurance due to greater moment of inertia.

Keywords: emulated inertia, synthetic inertia, fast frequency control, virtual synchronous generator (VSG), wind power, rotational energy, kinetic energy

Acknowledgements

I would like to thank several people for supporting and guiding me through this project. At Chalmers, I would like to thank my examiner Ola Carlson and supervisor Magnus Ellsén. Ola, for his endless enthusiasm and knowledge in wind power, and engagement along the way. Magnus, for guiding and discussing with me during the many hours we spent together doing measurements on the wind turbine at Björkö, and also for his expertise, as it made the testing very fun and instructive. I really appreciate how you both have been very available and interested in this project.

At Svenska kraftnät, I would like to thank my supervisors Sophia Appelstål, Henrik Ekestam and Linn Saarinen for giving me the opportunity to do this thesis. Thank you for helping me develop in this area and sharing your knowledge with me. You are all very proficient and supportive. It has been a true pleasure having you all as my supervisors.

Finally, I would like to thank all colleagues at Svenska kraftnät I have gotten to know during this spring. You have all been very kind and helpful, which made me feel at home from start.

Lisa Dacklin, Gothenburg, June 2024

List of Acronyms

Acronyms that have been used throughout this thesis are listed below.

AEM	Alert State Energy Management
FFR	Fast Frequency Reserve
FCR-N	Frequency Containment Reserve - Normal
FCR-D	Frequency Containment Reserve - Disturbance
FRR	Frequency Restoration Reserve
LER	Limited Energy Reservoir
MPPT	Maximum Power Point Tracker
NEM	Normal State Energy Management
NREL	National Renewabe Energy Laboratory
POD-P	Power Oscillation Damping - active power
PV	Photovoltaic
RES	Renewable Energy Sources
ROCOF	Rate of Change of Frequency
SOC	State of Charge
TSO	Transmission System Operator
VRE	Variable Renewable Energy

Nomenclature

A nomenclature summarising all parameters that have been used throughout this project is presented below.

Parameters

A	Area swept by turbine blades $[m^2]$
A_{in}	Input signal amplitude $[-]$
A_{out}	Output signal amplitude $[-]$
b	Damping constant $[-]$
β	Pitch angle $[°]$
β_{opt}	Optimal pitch angle $[°]$
C	Capacitance $[F]$
C_p	Power coefficient $[-]$
E	Energy $[J]$
E_k	Rotational energy in power system $[Ws]$
E_{rot}	Rotational energy stored in turbine $[J]$
E_{FFR}	Rotational energy change in turbine due to dynamic FFR $[J]$
E'_{FFR}	High-pass filtered rotational energy change in turbine due to dynamic FFR $[J]$
f	Frequency $[Hz]$
f_c	Cut-off frequency $[Hz]$
$f_{c,HP}$	High-pass filter cut-off frequency $[Hz]$
$f_{c,LP}$	Low-pass filter cut-off frequency $[Hz]$
$f_{c,NEM}$	High-pass filter cut-off frequency $[Hz]$
$f_{c,NREL}$	Low-pass filter cut-off frequency $[Hz]$
η	Generator efficiency $[-]$
J	Moment of inertia $[kgm^2]$

λ	Tip speed ratio $[-]$
λ_{opt}	Optimal tip speed ratio $[-]$
M	Magnitude $[-]$
P	Power $[W]$
$P_{delivery}$	Delivery of dynamic FFR $[W]$
P_{el}	Electric power $[W]$
P_{FFR}	Power response due to dynamic FFR $[W]$
P_{in}	Power input signal $[W]$
P_{kin}	Power from stored rotational energy $[W]$
P_{mech}	Mechanical power captured by the wind $[W]$
P_{nom}	Rated generator power $[W]$
P_{out}	Power output signal $[W]$
P_{ref}	Reference value, normal active power $[W]$
ρ	Air density $[\frac{kg}{m^3}]$
r	Turbine radius $[m]$
R	Resistance $[\Omega]$
T	Period $[s]$
τ	Torque $[Nm]$
τ_{el}	Electric torque $[Nm]$
τ_{FFR}	Torque reponse due to dynamic FFR $[Nm]$
τ_{mech}	Mechanical torque of wind turbine $[Nm]$
τ_{NREL}	Optimal torque estimated by the NREL controller $[Nm]$
τ_{tot}	Sum of τ_{NREL} and τ_{FFR} $[Nm]$
τ_c	Time constant $[s]$
$\tau_{c,HP}$	High-pass filter time constant $[s]$
$\tau_{c,LP}$	Low-pass filter time constant $[s]$
$\tau_{c,NEM}$	High-pass filter time constant $[s]$
$\tau_{c,NREL}$	Low-pass filter time constant $[s]$
v	Wind velocity $[\frac{m}{s}]$
v_{est}	Estimated wind velocity $[\frac{m}{s}]$
v_{tip}	Tip speed of turbine blade $[\frac{m}{s}]$
ϕ	Phase change $[^\circ]$
ϕ_{in}	Phase of input signal $[^\circ]$
ϕ_{out}	Phase of output signal $[^\circ]$

ω	Rotational speed $[\frac{rad}{s}]$
ω'_0	Estimated rotational speed $[\frac{rad}{s}]$
ω_c	Cut-off frequency $[\frac{rad}{s}]$
ω_g	Generator rotational speed $[\frac{rad}{s}]$
ω_{nom}	Rated rotational speed $[\frac{rad}{s}]$
ω_{min}	Cut-in rotational speed $[\frac{rad}{s}]$
ω_{max}	Cut-out rotational speed $[\frac{rad}{s}]$
ω'_{FFR}	Rotational speed change due to dynamic FFR $[\frac{rad}{s}]$
ω_t	Turbine rotational speed $[\frac{rad}{s}]$

Contents

List of Figures

List of Tables

1

Introduction

This chapter describes the reason for studying the topic, as well as the purpose with the project. Limitations within the scope are also described. Specific questions to answer during the project are determined, and social, ethical and environmental aspects are discussed.

1.1 Background

As part of the energy transition, the share of Renewable Energy Sources (RES) in power production has increased a lot the past decade, and is estimated to continue doing so [1]. The Swedish power system was designed with big amounts of inertia in the system, mainly provided by hydro and nuclear power, whose big turbines and generators are synchronously connected to the grid [1], contributing to slow down disturbances in the system. In contrast, new Variable Renewable Energy (VRE) technologies like wind power and solar Photovoltaic (PV), do not contribute with inertia to the power system, as they instead connect with the grid through power converters [2]. However, it is possible to provide synthetic inertia from for example wind power if certain adjustments are done in the entity's control system [2]. With the increase of VRE technologies, the amount of inertia in the system decreases, and the current ancillary services, Frequency Containment Reserves (FCR) are, among several things, for example not fast enough to compensate for the quicker Rate of Change of Frequency (ROCOF). Consequently, a remedial action was implemented as the static Fast Frequency Reserve (FFR) [3], to compensate for the decrease of inertia in the system and mitigate the initial frequency dip during large disturbances. However, with continued development of increased shares of VRE, the static FFR will not be sufficient to compensate for the lack of inertia. Therefore, a new remedial action is researched as dynamic FFR, which is expected to further compensate for the lack of rotational energy in the system, until the slower ancillary services are activated, and if possible, also dampen oscillations while stabilising the frequency after a disturbance. Since it is possible to quickly extract additional active power from a wind turbine by utilising the kinetic energy stored in the wind turbine [4], wind power is an interesting candidate to provide dynamic FFR.

1.2 Purpose

The aim of the project is to determine technical possibilities to provide dynamic FFR from wind power, and how the power system can benefit from it. More specifically, which strengths and weaknesses this reserve would have, and how it should be designed to utilise the abilities of wind power, and cooperate with the power system, existing ancillary services and static FFR.

1.3 Limitations

The project will not consider the ancillary services Frequency Restoration Reserves (FRR) during simulations as the interaction between FFR and FRR is assumed negligible. Due to time constraints, the project will not treat legal and economic considerations, but rather be purely technical. Furthermore, potential mechanical wear due to dynamic FFR will be excluded from the scope of this report. Lastly, the project will take off with already implemented simulation models, and focus will not lie in validating these existing models.

1.4 Precision of the problem

- How should dynamic FFR from wind power be designed to most efficiently minimise frequency deviation and stabilise the frequency, while being compatible with both wind power and the existing power system?
- What technical strengths and weaknesses exist when providing dynamic FFR from wind power?
- What tests should be carried out to capture wanted and unwanted behavior?
- How should parameters be optimised to achieve good stability and performance?

1.5 Social, ethical and environmental aspects

Since the project will focus on literature studies, simulations and practical tests to determine feasibility of a new remedial action in the power system, most social, ethical and environmental aspects are considered negligible within the scope of the project. However, since the project investigates a topic indicating a future with less technologies providing rotational energy to the power system and larger shares of VRE like wind power, social, ethical and environmental aspects can be considered futuristically. Building of wind power parks require land, which could be in conflict with other interests of using the land for other purposes. Development of sea-based wind power could perhaps mitigate these problems. Nevertheless, implementation of wind power affects the local environment, which can affect local ecosystems negatively. Materials needed to build wind power also requires energy, and production of these generally contributes to pollution. Furthermore, critical materials are needed to produce wind turbines [5]. However, all power production technologies come with different risks, environmental impacts and other drawbacks.

2

Theory

Relevant theory applied during the project will be described in this chapter. The mentioned subjects are described based on either literature studies or gained experience from experiments and education of a real wind turbine studied during the project, with guidance from supervisors and examiner. The main areas studied are wind power, frequency stability, and design of dynamic FFR.

2.1 Wind power

Relevant theory and equations related to wind power is described in this section, and the model used for simulations is described. Lastly, different behaviours of the wind turbine, depending on operation conditions, are described.

2.1.1 Wind power theory

The mechanical power that a turbine can obtain from the wind [6] is given as

$$P_{mech} = \frac{1}{2}\rho A Cp(\lambda, \beta) v^3 \quad [W], \tag{2.1}$$

where ρ is the density of air $[\frac{kg}{m^3}]$, A is the area swept by the wind turbine blades $[m^2]$, Cp is the power coefficient $[-]$, and v is the wind velocity $[m/s]$.

The Betz limit defines a theoretical maximum on how much power a turbine can extract as a power coefficient Cp of $\dfrac{16}{27} \approx 0.59$ [7]. How big Cp can be varies depending on the studied turbine, and is determined from a relationship between the tip speed ratio λ and pitch angle β, as illustrated in Figure 2.1 for the studied turbine in this report.

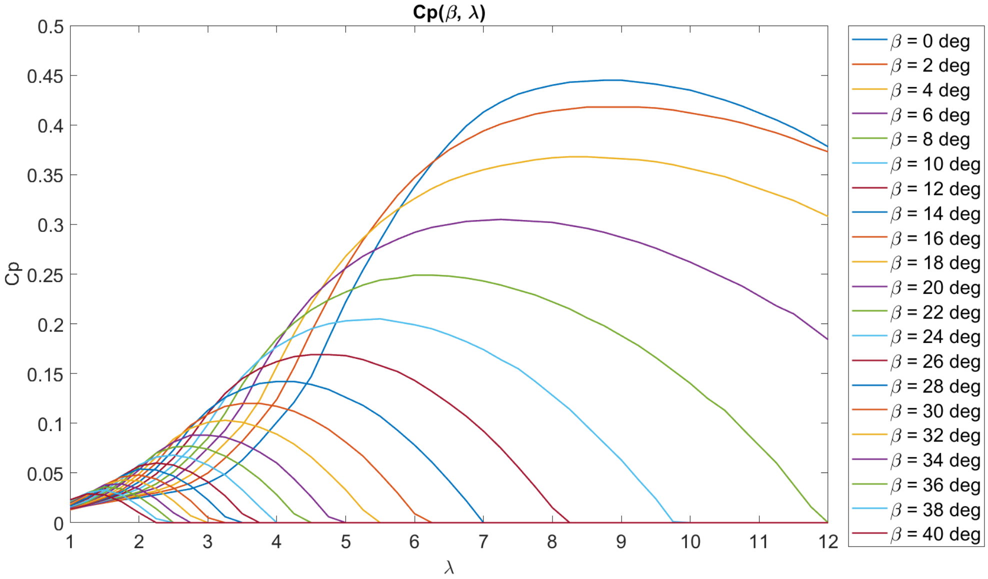

Figure 2.1: Plot showing the relationship between the power coefficient Cp, pitch angle β and tip speed ratio λ. The plot illustrates how β must decrease to maximize Cp of the turbine, to remain in optimal operation, with increasing λ due to increased rotational speed.

The parameter β can be varied to adjust the performance of the wind turbine. Generally for optimal performance during steady state operation below rated rotational speed and cut-out wind velocity, this means that it is set as low as possible, as illustrated in Figure 2.1, typically $\beta_{opt} = 0°$ or $\beta_{opt} = 2°$. The advantage of using 2° instead of 0° is that the the larger angle will adjust faster to slow down the rotational speed in case it reaches cut-out speed. The tip speed ratio λ which also affects the performance of the turbine is given as

$$\lambda = \frac{v_{tip}}{v} = \frac{\omega_t r}{v} \quad [-], \tag{2.2}$$

where ω_t is the rotational speed of the wind turbine $[\frac{rad}{s}]$, and r is the radius of the wind turbine $[m]$.

There exists an optimal value for λ, which means that there exists different optimal tip speeds and thus optimal rotational speeds depending on the wind velocity, and the wind turbine control system strives for this value by adjusting the electrical torque. The relationship between power and torque is defined as

$$P_{el} = \tau_{el}\omega_t \quad [W], \tag{2.3}$$

where τ_{el} is the electrical torque $[Nm]$.

The relationship between τ_{mech} and τ_{el} is defined in the swing equation [8] as

$$\frac{d\omega}{dt} = \frac{\tau_{mech} - \tau_{el}}{J} \quad [\frac{rad}{s^2}], \tag{2.4}$$

where τ_{mech} is the mechanical torque $[Nm]$, τ_{el} is the electrical torque $[Nm]$, and J is moment of inertia $[kgm^2]$.

An ordinary differential equation is obtained by taking damping of the rotational speed into account to resemble reality better as

$$\frac{d\omega}{dt} = \frac{\tau_{mech} - \tau_{el} - b\omega}{J} \quad [\frac{rad}{s^2}], \tag{2.5}$$

where ω is the rotational speed $[\frac{rad}{s}]$, and b is a damping constant $[\frac{Nm}{rad/s}]$.

The electrical power obtained from the wind turbine can be determined either from equation 2.3 or as

$$P_{el} = P_{mech}\eta_{el} \quad [W], \tag{2.6}$$

where η is the efficiency of the generator $[-]$.

The rotational energy stored in the wind turbine can be calculated as [9]

$$E_{rot} = \frac{J\omega_t^2}{2} \quad [J], \tag{2.7}$$

and can also be described as the integral of the kinetic power of the turbine as

$$E_{rot} = \int_{t_0}^{T} P_{kin} dt \quad [J]. \tag{2.8}$$

2.1.2 Wind turbine model

A simulation model representing the wind turbine was provided by Chalmers for the project. The model is based on a reference wind turbine described by the National Renewabe Energy Laboratory (NREL) [10], and a more detailed description of the used simulation model is available in a report from Chalmers [11]. The most relevant parts of the model will be described in this section. Figure 2.2 shows an overview of the model, which consists of several blocks, an NREL controller representing a Maximum Power Point Tracker (MPPT), DC generator, dynamics, estimate wind velocity, and estimate power.

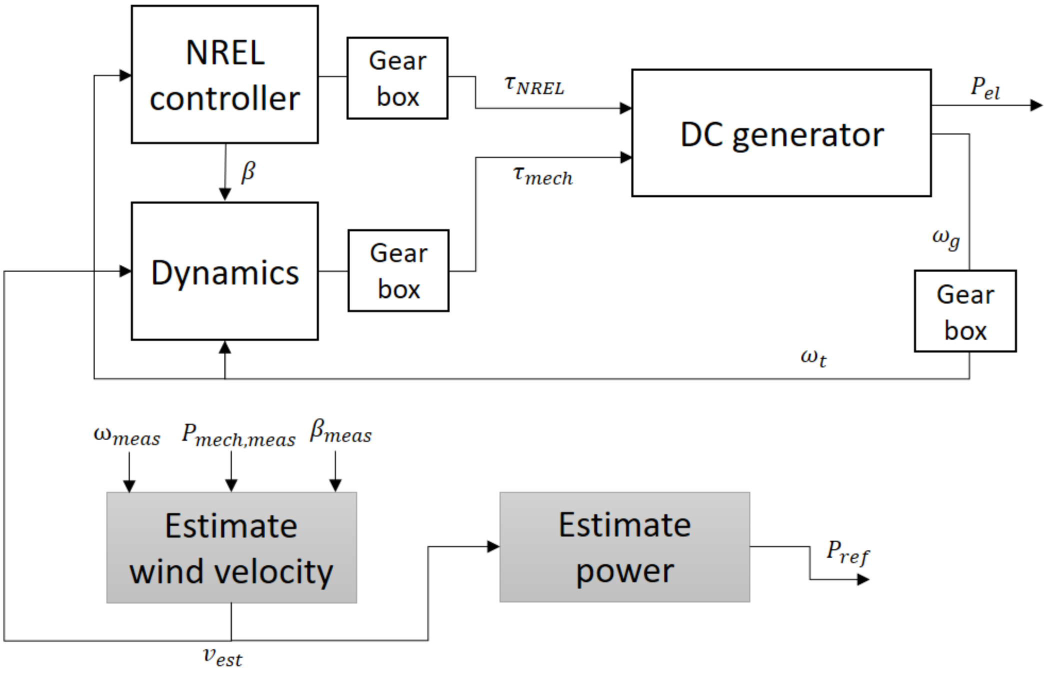

Figure 2.2: Scheme of wind turbine model used for simulations.

NREL controller (MPPT) is the controller of the wind turbine system, which consists of a look-up table to find the optimal electrical torque τ_{NREL}, and pitch angle β. This means that the controller represents a MPPT, which strives for the wind turbine to stay in optimal operation. The MPPT follows a torque-rotational speed curve that is described in [11], where also the logic determining the pitch angle is described.

DC generator The generator uses a PI-controller to minimise the error of the electric torque estimated by the MPPT, and then determines the rotational speed through equation 2.5. The electric power output is then calculated from equation 2.3. A gear box is included in contrast to the real wind turbine, with a gear box ratio of 20.

Dynamics is the part where the mechanical torque τ_{mech} that the turbine experiences due to the wind is calculated through equation 2.1.

Estimate wind velocity is a block that estimates the wind velocity, using the actual wind turbine as a wind gauge. Wind measurements are not always sufficiently accurate [4], and since the turbine covers a much greater area than an actual anemometer, the estimated wind velocity will behave smoother than the actual measurements and be more representative to what wind velocity the entire turbine actually experienced. Since the estimation is dependent on measurements from the turbine behaviour, the rotational speed, mechanical power and pitch angle, the estimation will be altered if the turbine is rapidly forced out of optimal operation, for example during FFR. This makes the estimation currently unreliable while testing dynamic FFR during real operation, and can therefore not be used during the practical tests in this project, unless improved. However, the wind estimation is still useful during the simulations as it generates more realistic results than the actual wind velocity measurement, if the turbine measurements used to calculate the estimation are logged during common operation.

Estimate power calculates the available power P_{ref} in the wind based on assumptions on optimal operation and the estimated wind, and is a way of validating how accurate the simulation model is by comparing P_{ref} with P_{el}. Like the wind estimation, it is currently only helpful during simulations as the measurements during practical tests will be affected if the testing forces the turbine out of optimal operation.

A selection of data from the wind turbine is summarised in Table 2.1.

Table 2.1: A selection of data describing the wind turbine.

Parameter	**Value**	**Unit**	**Description**
b	0.1	$[\frac{Nm}{rad/s}]$	Damping constant
β_{opt}	2	$[°]$	Optimal pitch angle
η	0.89	$[-]$	Generator efficiency
J	1700	$[kgm^2]$	Moment of inertia
λ_{opt}	8.75	$[-]$	Optimal tip speed ratio
P_{nom}	25	$[kW]$	Rated generator power
ρ	1.225	$[\frac{kg}{m^3}]$	Air density
r	8	$[m]$	Turbine radius
ω_{nom}	7.33	$[\frac{rad}{s}]$	Rated rotational speed
ω_{min}	5.7	$[\frac{rad}{s}]$	Cut-in rotational speed
ω_{max}	7.85	$[\frac{rad}{s}]$	Cut-out rotational speed

2.1.3 Wind conditions

Depending on the wind conditions, the wind turbine might act differently based on how the operation is designed to work. This means that the wind conditions might affect the behaviour of the wind turbine while delivering ancillary services. Firstly, there has to be enough wind for the wind turbine to start spinning. If the wind velocity is low, it is possible to shift the torque-rotational speed curve, by decreasing the torque and increasing the rotational speed. Increasing the rotational speed has also been investigated to enable delivery of FFR [12]. In that way, more available rotational energy can be stored even in low wind velocity conditions. On the other hand, if the wind velocity is high, the wind turbine will reach rated rotational speed, and the pitch angle will increase to decrease the efficiency of the turbine. How the turbine will behave during activation of dynamic FFR is summarised in Table 2.2, if the optimal pitch angle is set to β_{opt}=2°. The activated reserve will affect the pitch angle or the rotational speed, or both. The parameter P_{FFR} is the power response due to activation of dynamic FFR, and can force the turbine to behave either up-regulating to increase the power output, or down-regulating to decrease the power output of the entity.

Table 2.2: How the wind turbine will behave from an added power response P_{FFR} due to dynamic FFR.

$\beta = 2°$, $\omega < \omega_{nom}$	ω will slow down if FFR is up-regulating. ω will speed up if FFR is down-regulating. τ_{NREL} is affected since ω is affected.
$\beta > 2°$, $\omega = \omega_{nom}$	β will decrease if FFR is up-regulating. β will increase if FFR is down-regulating. τ_{NREL} is not affected since ω is not affected.

On windy days when the rated wind velocity is exceeded, or if the turbine speeds up to rated rotational speed due to down-regulation, the pitch increases to not exceed the rated rotational speed. This also means that the angle can be increased to deliberately produce less power than what's actually available to extract from the wind. Even though mechanical power from the wind is wasted continuously by this action, the electrical production can be increased by decreasing the angle when desired. The increased angle creates margins to increase power production without affecting the stored rotational energy in the turbine. This is positive when up-regulating, but negative during down-regulation since the energy recovery is solely wasted if the pitch increases.

If the wind velocity gusts exceed certain velocities, the minimum pitch angle has to be increased to avoid that the rotational speed exceeds the cut-out speed and the turbine stops, according to the settings in Table 2.3.

Table 2.3: How the wind turbine pitch angle has to be adjusted during higher wind velocities.

Wind velocity of gusts [m/s]	Minimum pitch angle [°]
v < 13	$\beta_{min} = 2$
13 <= v < 14	$\beta_{min} = 8$
14 <= v < 16	$\beta_{min} = 14$

2.2 Frequency stability in the power system

This section describes the existing ancillary services and remedial action, and how variable resources can deliver these services.

2.2.1 Ancillary services and remedial actions

To mitigate frequency deviation in the power system, ancillary services and remedial actions were designed. The reserves that are most relevant for this project are described below.

Static Fast Frequency Reserve (FFR) is a remedial action which purpose is to act fast and decrease the magnitude of the first frequency dip during a disturbance. It is used when rotational energy in the power system is low [13]. Static FFR is currently only used for up-regulation, and comes in three different combinations of activation times and frequency trigger levels [3], summarised in Table 2.4.

Table 2.4: Combinations of activation times and frequency trigger levels for static FFR.

Activation time [s]	Frequency trigger [Hz]
1.3	49.7
1.0	49.6
0.7	49.5

Static FFR also has two alternatives for endurance, 5 seconds or 30 seconds, with different recovery behaviour, respectively [3].

Frequency Containment Reserve - Normal (FCR-N) has the purpose to stabilize the frequency during normal operation, through linear automatic activation in the frequency interval 49.9-50.1 Hz [14].

Frequency Containment Reserve - Disturbance (FCR-D) upwards has the purpose to counteract frequency deviation during large disturbances with under-frequency events, and stabilize the frequency. It is linearly actived automatically in the frequency interval 49.9-49.5 Hz, and 86% of its power capacity should be activated after 7.5 seconds [14]. FCR-D upwards can be both static and dynamic [14].

Frequency Containment Reserve - Disturbance (FCR-D) downwards has the purpose to counteract frequency deviation during large disturbances with over-frequency events, and stabilize the frequency. It is linearly actived automatically in the frequency interval 50.1-50.5 Hz, and 86% of its power capacity should be activated after 7.5 seconds [14]. FCR-D downwards can be both static and dynamic [14].

2.2.2 Variable resources as reserves

Variable resources, such as wind power, have additional challenges when providing ancillary services or remedial actions compared to other resources. To contribute with ancillary services from variable power production, a reference value is needed, which corresponds to the normal active power that would have been produced if the service was not active [15]. The reference value is necessary to determine the delivery of power from the entity, and the corresponding compensation for the service. The reference value can be determined following two different methods as specified by the Swedish Transmission System Operator (TSO) [15]:

Method 1 determines the reference value dynamically through reliable measurements by calculating the theoretically available power. For wind power, this could be done by using equation 2.1 and 2.6 together with measurements of the wind velocity and assuming values of β and λ based on optimal operation to obtain the theoretically available electric power as $P_{ref,dynamic}$. The difference between P_{el} and $P_{ref,dynamic}$ would then show the change in power delivered by the reserve. This is however under the conditions that the measurements and assumptions would be sufficiently reliable.

Method 2 determines the reference value by curtailing power to obtain a well-defined and constant power output, to which the reference value more easily can be estimated from. For wind power, this could be done by increasing the pitch angle β in advance to the activation of the reserve, and then continuously adjust to deliver constant power, which then would act as a static reference value $P_{ref,static}$. The difference between P_{el} and $P_{ref,static}$ during activation of the reserve would then account for the power delivery. However, this is as long as the produced power never decreases below the set static reference value.

2.2.3 NEM and AEM

Normal State Energy Management (NEM) and Alert State Energy Management (AEM) are used for Limited Energy Reservoir (LER) entities that provide FCR, since an entity with LER risks depletion of its reserve unless managed [14]. The reason for implementing NEM is to make sure that there exists margins to provide the reserve, and AEM makes sure that the FCR entity depletes as harmlessly as possible if unavoidable [14]. For FCR, the State of Charge (SOC) which represents the currently stored energy of the entity, defines when NEM and AEM shall be active [14].

Dynamic FFR from wind power would probably benefit from implementing similar energy managements such as NEM and AEM, since dynamic FFR risks depleting the wind power entity, making it LER. For wind power, SOC could be based on the stored rotational energy E_{rot}, or the rotational speed of the turbine ω_t. However, the behaviour of depletion and recovery will vary greatly with wind velocity as descriped in Chapter 2.1.3, indicating that SOC alone is not a sufficient measure. The current wind velocity might need to be considered as well.

2.3 Design of dynamic FFR

The proposed concept and designed control system of the reserve dynamic FFR is presented, and filters and stability are described.

2.3.1 Filters

Filters can be used to alter an input signal in a preferred manner. Two different types of filters, low-pass and high-pass, are illustrated in Figure 2.3.

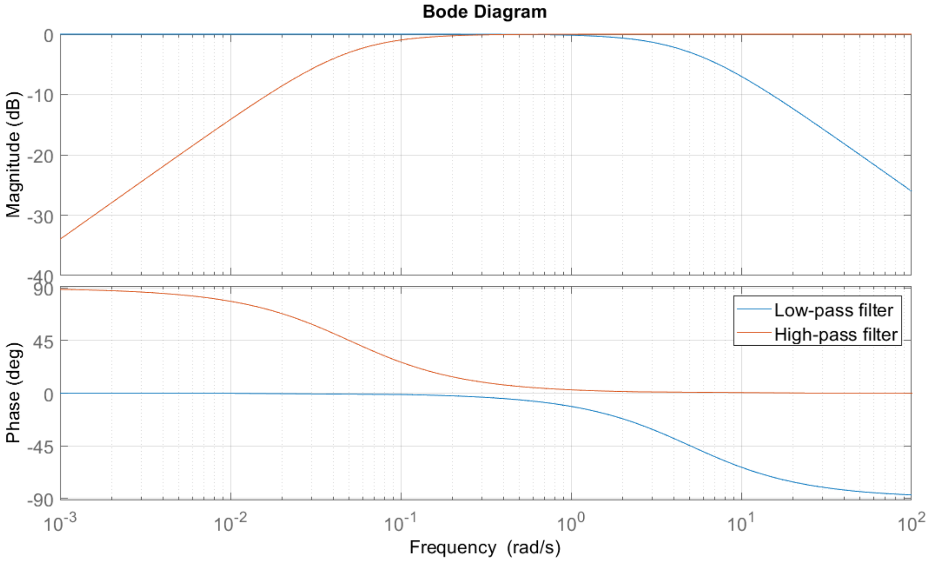

Figure 2.3: Bode plot of low-pass and high-pass filter. The time constants $\tau_{c,LP}$ and $\tau_{c,HP}$ are set to 0.2 and 20 seconds, respectively.

There exists a relationship between frequency and period such that

$$f_i = \frac{1}{T_i} \quad [Hz], \tag{2.9}$$

where f_i is the frequency in $[Hz]$ and T_i is the period in $[s]$. Both parameters are commonly used when studying filters.

A low-pass filter suppresses higher frequencies and leaves lower frequencies unaffected, which means that it can be used to filter out fast changes of an input signal. How much the filter suppresses higher frequencies depends on what time constant, or cut-off frequency, is used in the filter. Only digital filters will be utilised in this project, but for better understanding of the time constant, an example where it is derived from an analogue filter is described below.

The value of the time constant, or cut-off frequency, depends on the resistance R and capacitance C of the filter, and can be determined by analysing an AC RC-circuit representing a first order low-pass filter [16]. By using the $j\omega$-method, complex impedances and voltage division, it is possible to determine the ratio between the input and output [16], thus defining the low-pass filter as

$$\frac{V_{out}}{V_{in}} = \frac{1}{j\omega RC + 1} \tag{2.10}$$

The time constant τ_c will then be [16]

$$\tau_c = RC = \frac{1}{\omega_c} = \frac{1}{2\pi f_c} \quad [s], \tag{2.11}$$

where R is the resistance of the filter $[\Omega]$, C is the capacitance of the filter $[F]$, and ω_c $[\frac{rad}{s}]$ and f_c $[Hz]$ are the cut-off frequencies.

The time constant can be defined as the cut-off frequency f_c as

$$f_c = \frac{1}{2\pi\tau_c} \quad [Hz]. \tag{2.12}$$

The cut-off frequency f_c is the frequency where the input signal is attenuated by 3 dB, which corresponds to an amplitude ratio of 70.7%.

$$\frac{A_{out}}{A_{in}} = \sqrt{\frac{1}{2}} \approx 0.707, \tag{2.13}$$

where A_{out}, A_{in} are amplitudes.

A step response is commonly considered to have reached its final value (98.2%) when time corresponding to the value of the time constant τ_c has passed four times, and the response has reached 63.2% after time equivalent to one time constant [16].

The first order continuous low-pass filter can also be defined as a transfer function as

$$LP = \frac{1}{\tau_{c,LP}s + 1}. \tag{2.14}$$

The Laplace parameter s is a complex number, such that $s = \mu + j\omega$ [17], where μ is the real and ω the imaginary part, and $\tau_{c,LP}$ is a time constant $[s]$.

A high-pass filter on the other hand does the opposite from a low-pass filter, as it attenuates lower frequencies and leaves higher frequencies unaffected. For a step signal, the time constant in the high-pass filter determines for how long the signal will persist, since the only high-frequency part of the signal is when the step is taken. For sine signals, the frequency of the sine decides how much the signal is attenuated. The RC-circuit can represent a high-pass filter if the resistor and capacitor switch places [16], and can be derived in similar ways as the low-pass filter. The continuous transfer function is defined as

$$HP = \frac{\tau_{c,HP}s}{\tau_{c,HP}s + 1}, \tag{2.15}$$

where $\tau_{c,HP}$ is a time constant $[s]$.

Laplace-transforms enable simpler calculation of convolution [17], which means that equations 2.14 and 2.15 can simply be multiplied if put in series to construct a band-pass filter. The properties of the low-pass and high-pass filter are combined in the band-pass filter, enabling a certain range of frequencies to pass through, which can be seen in Figure 2.4 where a sine signal with increasing frequency illustrates how the band-pass filter will affect lower and higher frequencies.

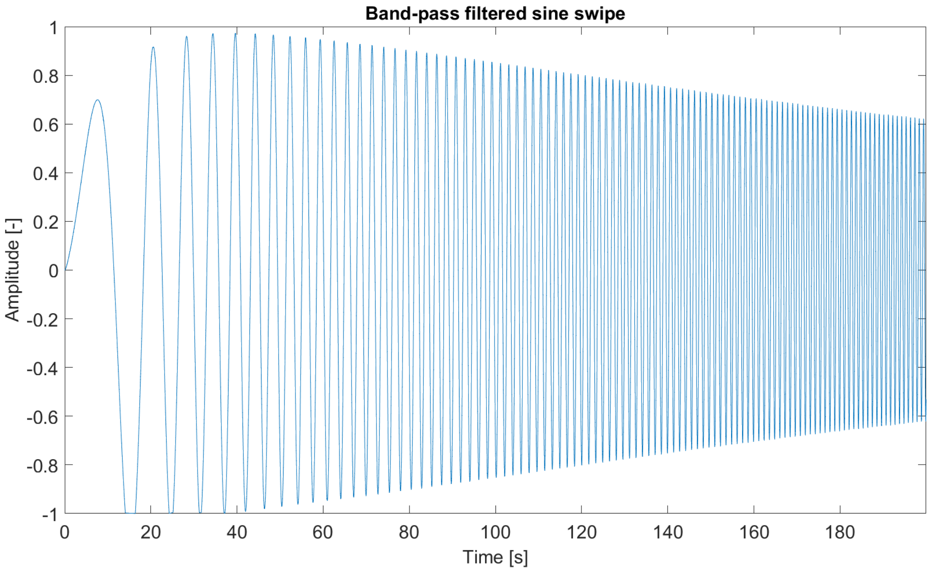

Figure 2.4: A swipe of sine signals with increasing frequency that are band-pass filtered.

2.3.2 Dynamic FFR concept

The purpose of dynamic FFR is to rapidly deliver a power response which counteracts the frequency deviation in the power system, most importantly the first big dip or peak during a large disturbance, by using the frequency change as input signal. The frequency signal is bandpass filtered, with time constants that are optimised to obtain the desired response. The signal is first low-pass filtered to decide how sensitive the reserve should be to fast changes in frequency, and then high-pass filtered which decides for how long the response shall remain. This ensures a dynamic response from the reserve, which adjusts for both frequency increase and decrease, and the concept is presented in Figure 2.5. In practice, this means to rapidly adjust the power output from the entity with an endurance of at least a few seconds during a disturbance, but preferably longer if possible. Since the output will adjust for positive and negative changes of frequency, the entity has the possibility to recover through the activation of the service, which could improve the entity's ability to stay active for a longer period.

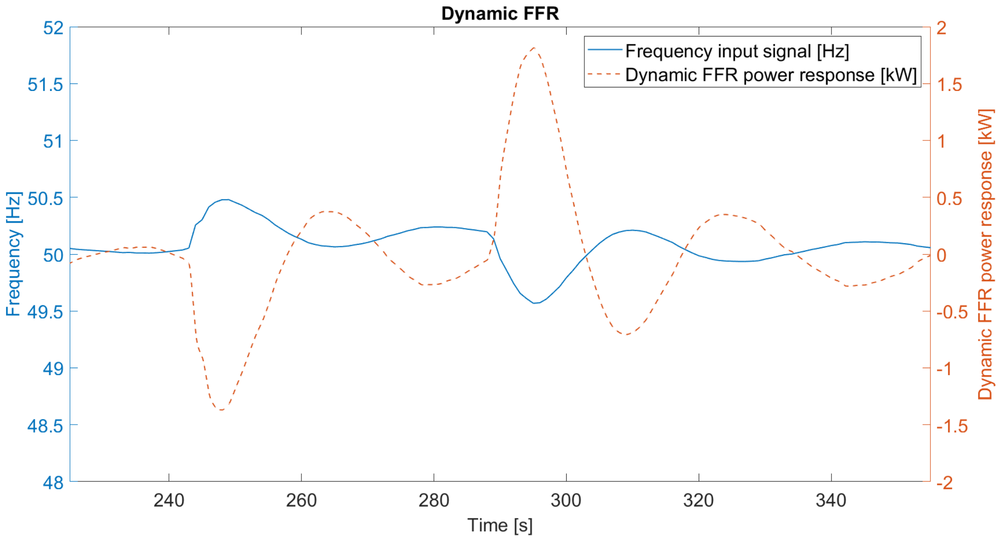

Figure 2.5: The concept of dynamic FFR. The power output of an entity will dynamically adjust to the frequency change.

2.3.3 Dynamic FFR model

A block representing a control system for dynamic FFR was provided and used during the project. The block constitutes of mainly a band-pass filter constructed from a low-pass filter and a high-pass filter in series, and is illustrated in Figure 2.6.

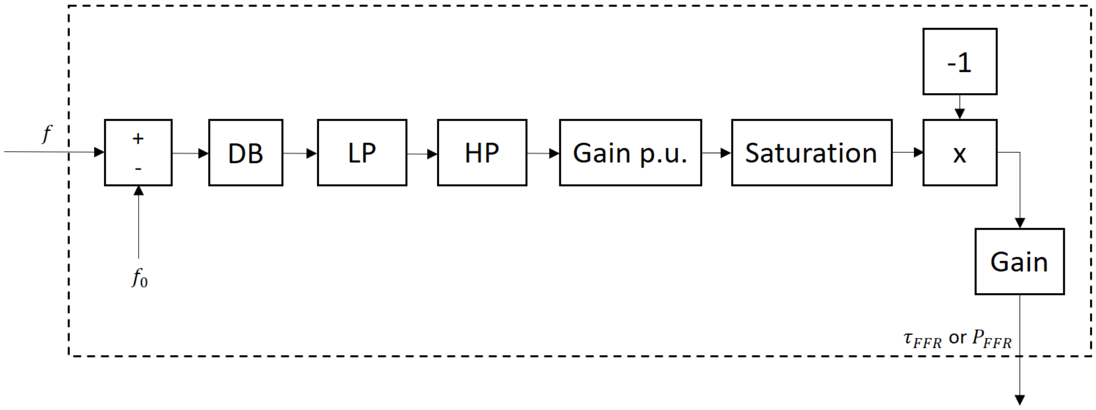

Figure 2.6: Scheme of the block containing the controller for the dynamic FFR signal. The block takes a frequency signal as input, and subtracts 50 Hz (f_0). The signal then passes through a deadband (DB), low-pass filter (LP), high-pass filter (HP), an internal per-unit gain (Gain p.u.), saturation and gain. The output response can be either a torque, τ_{FFR}, or a power P_{FFR}.

The block receives the frequency deviation from a reference value (50 Hz) as input signal. It is important to ensure that the design of the filter time constants is done in such a way that it does not cause stability problems in the power system, and also works well with the limitations of wind power. The block also contains deadband

and saturation, which can adjust in what range of frequency the reserve shall be active. Lastly, the signal from the block is multiplied with -1, and amplified to the desired level of power output.

2.3.4 Stability

Since the contribution from wind power is supposed to interact with the power system, it is necessary to ensure that it does so without compromising the stability in the grid. This can be ensured by studying stability through Bode plots of the behaviour of the wind turbine and the power system. An example based on calculations of a scenario for the Nordic power system is illustrated in Figure 2.7, with rotational energy E_k in the power system set to 100 GWs, showing a closed loop Bode plot comparing the Nordic power system with and without dynamic FFR, but with the dynamics from wind power excluded. The Bode plot shows that including dynamic FFR dampens the amplitude of the power system, and the greater time constant set in the high-pass filter, $\tau_{c,HP}$, the more attenuation occurs.

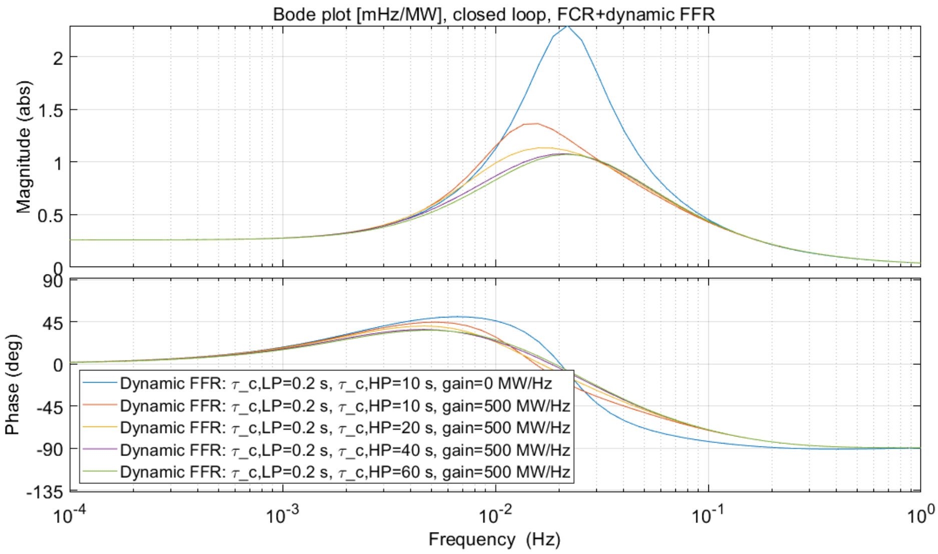

Figure 2.7: A closed loop Bode plot comparing the stability of a power system with and without dynamic FFR, but with wind power dynamics excluded. The rotational energy E_k in the power system is set to 100 GWs. The Bode plot shows that adding dynamic FFR dampens the amplitude of the power system, with increasing $\tau_{c,HP}$.

To construct a Bode plot, sine tests can be carried out to find the changes in magnitude and phase between the input and output signal [18]. For every sine test with a different period, a point can be generated in the Bode plot by computing the change in amplitude and phase from measurements of the sine shaped frequency input and power output signal. The magnitude is computed as the amplitude quota between the output and input signal as

$$M = \frac{A_{out}}{A_{in}} \quad [\frac{W}{Hz}], \tag{2.16}$$

where A_{out} is the amplitude of the power output signal, and A_{in} is the amplitude of the frequency input signal.

The phase change is the difference between the output and input phase as

$$\phi = (\phi_{out} - \phi_{in})\frac{360}{2\pi} \quad [^\circ], \tag{2.17}$$

where ϕ_{out} is the phase of the power output signal $[rad]$, and ϕ_{in} is the phase of the frequency input signal $[rad]$.

For FCR reserves, it is required to generate 10 points by using sine input signals with periods ranging from 10 and 300 seconds, during 2-5 periods depending on the period used [14].

2.3.5 POD-P

Power Oscillation Damping - active power (POD-P) is interesting to study while investigating dynamic FFR since they overlap in functionality area. POD-P is a fast function which is active for periods of 1-4 s and has the purpose to mitigate power oscillations, especially rotor angle oscillations. Dynamic FFR is also supposed to be fast, yet also have an even wider working area preferably between 1-60 s, which means that POD-P is incorporated in the functionality of dynamic FFR. Since there already exists stability requirements for POD-P in Sweden, it is suggested that dynamic FFR also fulfills these requirements. The requirements states ideally that

$$\phi \approx 0 \quad [^\circ], \tag{2.18}$$

and requires that

$$\phi \in [-90, 90] \quad [^\circ] \tag{2.19}$$

when $f \in [0.25, 1]$ Hz [19].

3
Methods

The methodology was divided into five parts: literature studies and education, preparations, development of prototypes through simulations and practical tests, Bode plots, and closed loop simulations with the prototypes in two different models. These parts are all elaborated in this chapter.

3.1 Literature study and education

Literature studies were conducted with literature provided by both Chalmers and Svenska kraftnät. Topics that were primarily studied were wind power theory and how the wind turbine used for practical tests in this project works, as well as static FFR, ancillary services, the power system, filters and stability. Articles and previous work related to emulated inertia from wind power were also researched. Education was also provided by Svenska kraftnät on relevant topics related to the project.

3.2 Preparations

Preparations described in this section were done by first training and testing with the models for better understanding, and then by integrating the dynamic FFR block in the wind turbine model. Suitable input signals were created by programming and modelling, and from data of real frequency disturbances. Lastly, test programs for practical tests were developed through simulations, and certain preparations prior to the practical tests were conducted.

3.2.1 Simulations and training

The dynamic FFR block described in Chapter 2.3.3 had to be integrated in the wind turbine model described in Chapter 2.1.2, which is shown in Figure 3.1, and was done in Simulink. In contrast to the real wind turbine that is studied in this project, the simulation model included a gear box with a ratio of 20.

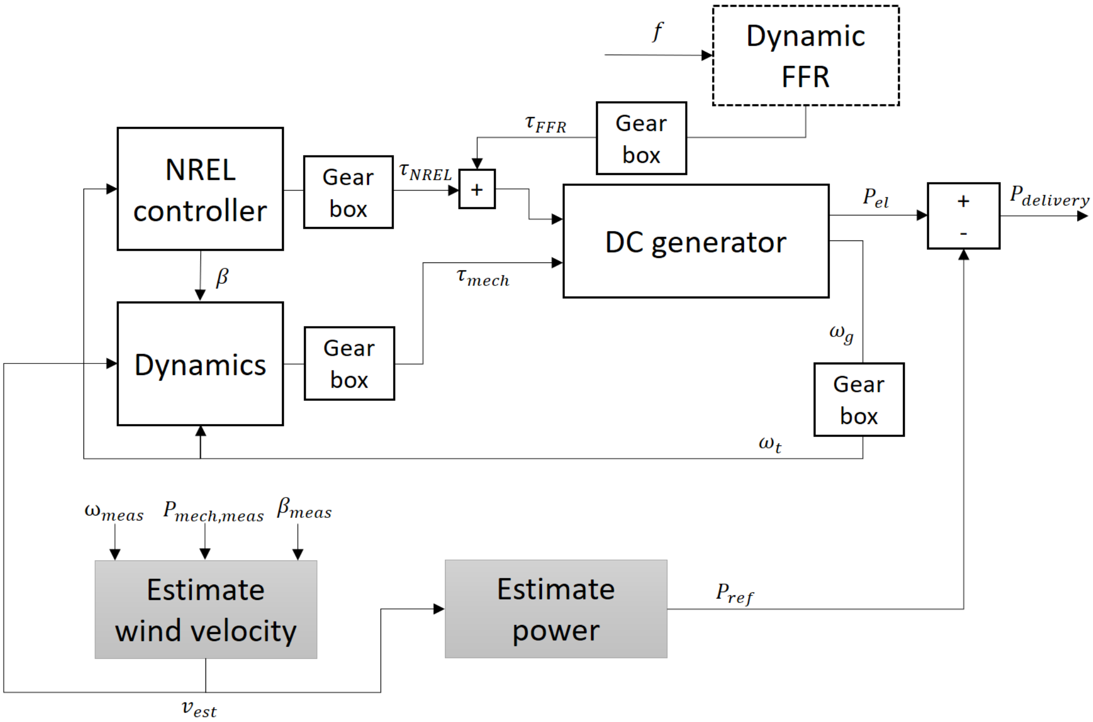

Figure 3.1: Scheme of wind turbine model with the dynamic FFR block included, used for simulations.

It was decided to integrate the dynamic FFR response as a torque addition, τ_{FFR}, to the optimal electrical torque estimated by the MPPT, τ_{NREL} as

$$\tau_{tot} = \tau_{NREL} + \tau_{FFR} \quad [Nm]. \tag{3.1}$$

The reason for adding the torque reponse τ_{FFR} to the torque estimated by the NREL controller was for the wind turbine control system to remain in control of operating the turbine. If the MPPT would be completely bypassed, the turbine would suffer larger risks of passing limits for cut-in and cut-out rotational speeds since the wind velocity can vary greatly even within the order of seconds. Keeping the MPPT active might however counteract the torque addition from dynamic FFR, as the NREL controller strives for optimal operation. Therefore, the MPPT should remain partly in control while delivering dynamic FFR, but not entirely.

3.2.2 Input signals

Four types of frequency input signals were prepared for tests with the simulation models and the real wind turbine. These were step, sine, grid frequency and logged large disturbance signals. The step and sine input signals are shown in Figure 3.2.

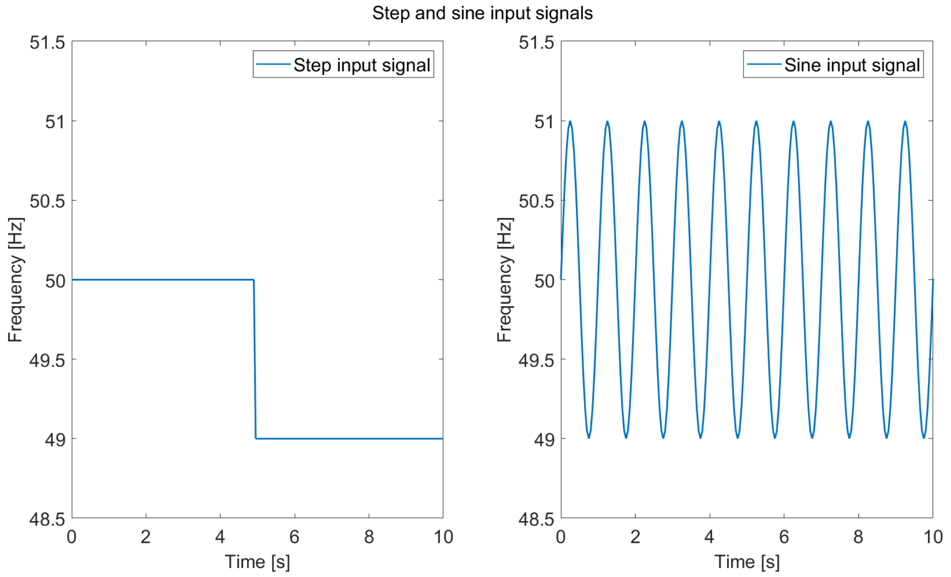

Figure 3.2: Input signals as step and sine. To the left, a step signal, and to the right, a sine signal with a period of 1 s.

The step signal goes between 50 Hz to 49 Hz, and the sine input signals were prepared with ten different period times, spread logarithmically even between $T_1 = 1$ s and $T_{10} = 100$ s, with an amplitude of 1. Table 3.1 summarises the periods used for the sine signals during simulations and practical tests, which differed due to limited precision during the practical tests.

Table 3.1: Periods and corresponding frequencies used for the sine input signals.

	Simulations		**Practical tests**	
	T [s]	**f [Hz]**	**T [s]**	**f [Hz]**
1	1	1	1	1
2	1.6681	0.5995	1.6949	0.59
3	2.7826	0.3594	2.7778	0.36
4	4.6416	0.2154	4.5455	0.22
5	7.7426	0.1292	7.6923	0.13
6	12.9155	0.0774	12.5	0.08
7	21.5443	0.0464	20.0	0.05
8	35.9381	0.0278	33.3333	0.03
9	59.9484	0.0167	50.0	0.02
10	100.0	0.01	100.0	0.01

Data on grid frequency during normal operation was used for the simulations, see Figure 3.3. During tests with the real turbine, real-time data of the grid frequency was used.

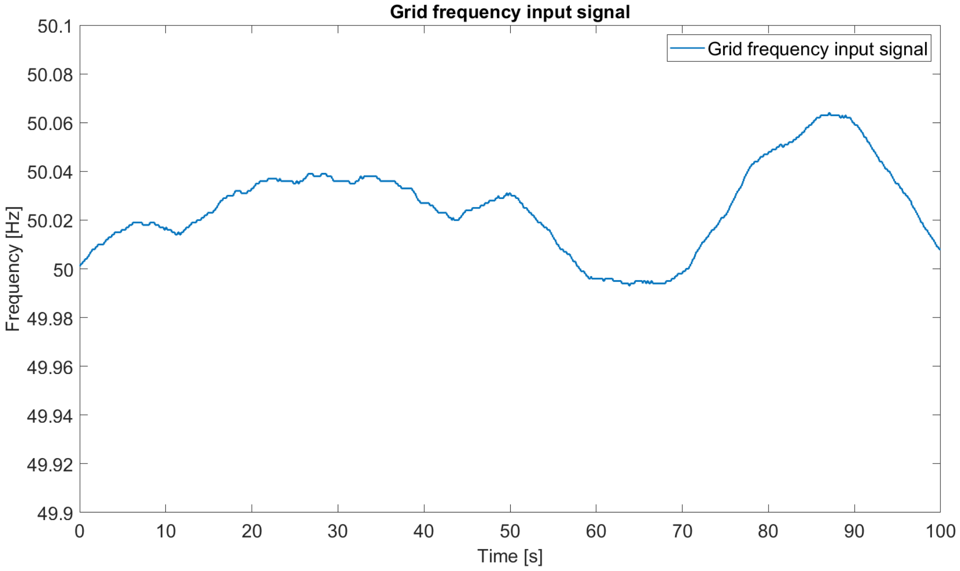

Figure 3.3: The grid frequency input signal during normal operation that was used during simulations.

Lastly, one recorded disturbance signal was used as frequency input signal for both simulations and practical tests, as shown in Figure 3.4.

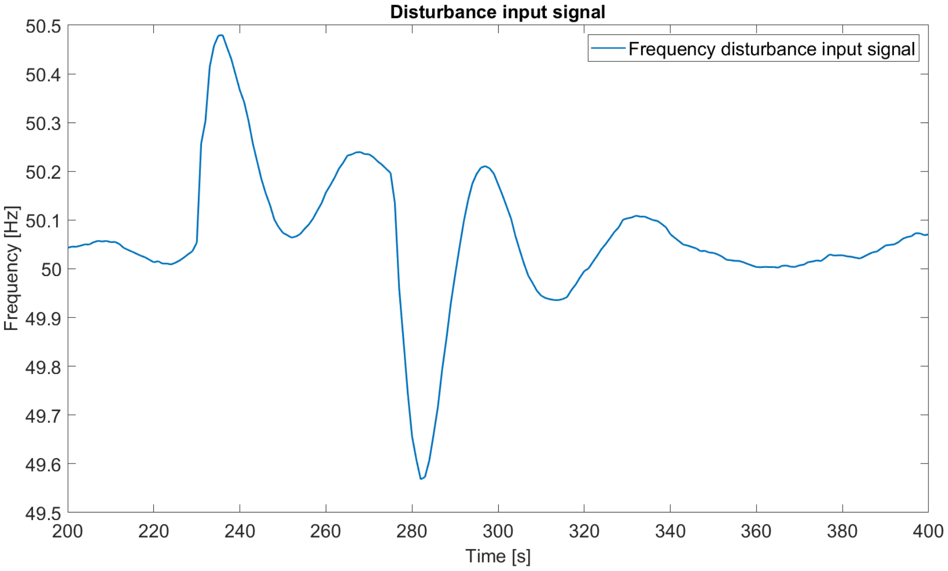

Figure 3.4: The disturbance signal that was used as frequency input signal during simulations and practical tests, from a real disturbance that occurred September 10:th, 2020.

3.2.3 Test programs

The prototypes were tested with different settings and input signals to understand the behaviour of dynamic FFR, as well as the wind turbine while providing the reserve. Tests that were considered interesting during simulations, in promising or bad behaviour, or for understanding of the wind turbine, were documented for future comparison and hypotheses on how the real turbine should behave. Test programs for the practical tests were based on the test documentations from the simulations, to investigate resemblance, find promising behaviour and understand the wind turbine better. The programs specified the practical testing procedure, including what tests to carry out, specific settings and parameters, which data that should be logged, priority of the tests, and any intermediate steps.

3.2.4 Practical tests

The prototypes had to be converted into another software in order to be compatible with the real wind turbine studied in the project. The conversion resulted in some changes compared to the simulation models. Filters had to be modelled in a discrete manner rather than the continuous transfer functions used in Simulink. This resulted in using Butterworth filters for the required filters. There were limitations on numbers of adjustable parameters that could be used in the real set-up, therefore the time constant $\tau_{c,LP}$ used in the low-pass filter in the dynamic FFR block was set to a constant value of 0.2 s, as it looked like a promising value in simulations. Since the estimated wind and power were not useful during the practical tests, they are excluded in Figure 3.5 which describes the initial set-up that was used during the practical tests, before the addition of dynamic FFR.

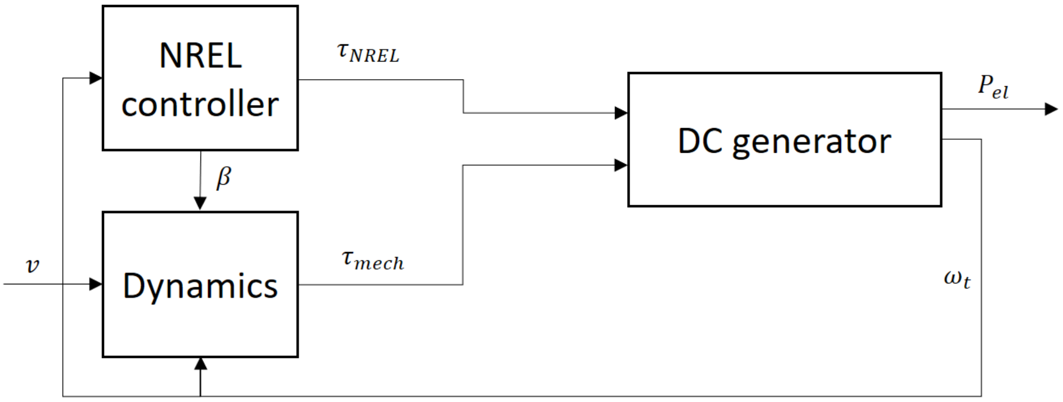

Figure 3.5: Scheme of the real wind turbine used for practical tests.

3.3 Prototypes

Two different types of solutions to adjust the speed control of the wind turbine to accommodate dynamic FFR were investigated in this project, referred to as prototype A and B.

3.3.1 Prototype A: slow down MPPT

The first solution was to add a low-pass filter to the torque from the NREL controller, to try to limit the effect that the MPPT wants to compensate for the torque addition due to dynamic FFR activation. This makes the first prototype rather simple. The scheme of the prototype A model is illustrated in Figure 3.6, and the Simulink model of prototype A is illustrated in Appendix A.1.1.

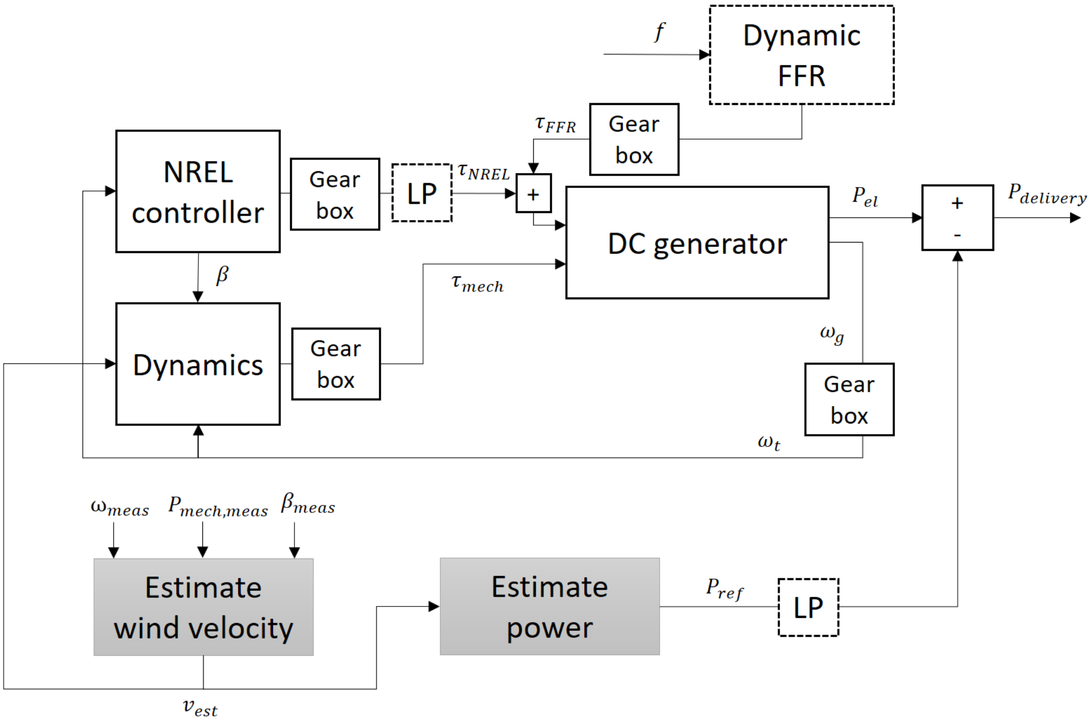

Figure 3.6: Scheme of prototype A of the wind turbine model, with included dynamic FFR block and additional low-pass filters surrounded by dashed lines, used for simulations.

The purpose of the added low-pass filter for τ_{NREL} is to slow down the counteracting behaviour from the MPPT because of the torque addition τ_{FFR}. A low-pass filter was also included for the estimated power P_{ref}, to delay it in the same manner as the torque from the MPPT.

Simulations were carried out with prototype A, focusing on trying different time constants for the high-pass filter in the dynamic FFR block and the added low-pass filters slowing down the MPPT and estimated power, as well as suitable gain of τ_{FFR} depending on these time constants. All prepared input signals were tested and test programs were prepared for the practical tests.

Figure 3.7 describes the used set-up during the practical tests with prototype A. Tests with step, sine, grid frequency and recorded disturbance as input signals were done according to the prepared test program, but tests were also adjusted in the moment to understand the behaviour better.

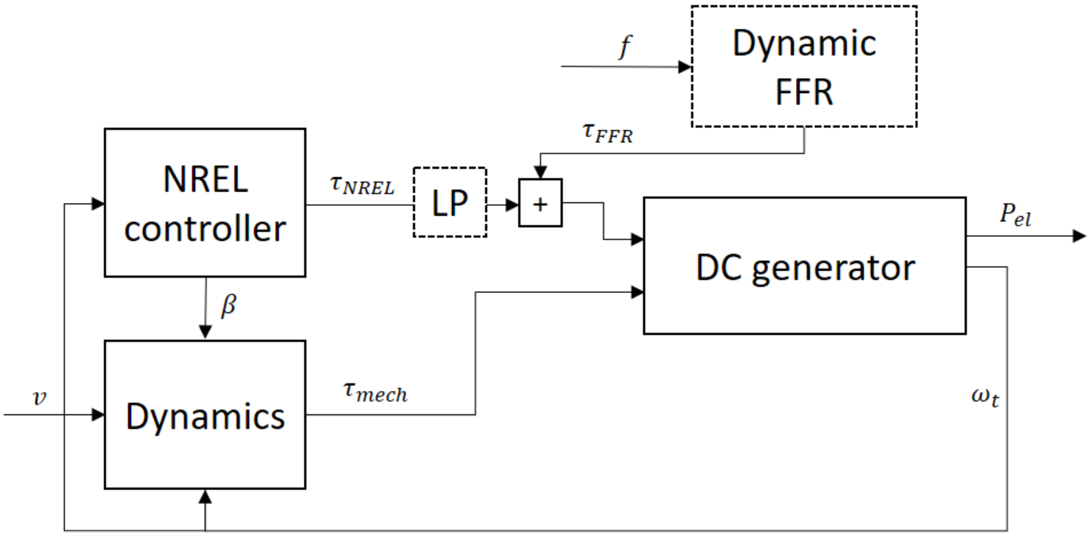

Figure 3.7: Scheme of the real wind turbine model, with included dynamic FFR block and additional low-pass filter surrounded by dashed lines, used during practical tests.

Several testing occasions suffered from poor wind conditions, as the wind velocity was either close to cut-in speed or cut-out speed. To be able to run tests during low wind velocities, the torque-rotational speed curve was adjusted by decreasing the torque from the NREL controller, and consequently increase the rotational speed, as described in section 2.1.3. This adjustment was done by multiplying τ_{NREL} with a curtailment factor, ranging between 0 to 1. During high wind velocites, the minimum pitch angle β_{min} had to be increased according to the settings in Table 2.3, described in section 2.1.3.

Generally during the first practical tests with prototype A, some differences between the simulation and reality were spotted. The appearance of the added torque τ_{FFR} looked different compared to in the simulations. Therefore, an experiment was done in Matlab to investigate if the problem could be caused by the used Butterworth filters. It was concluded that the order of the band-pass filter used in the dynamic FFR block for the practical tests had been incorrectly set to an order of 2, where it should have been set to 1, which is illustrated in Figure 3.8. This explained the differences between simulation and reality, as the response with order 2 looks like τ_{FFR} looked during the practical tests, in contrast to an order of 1 which resembles the appearance during simulations.

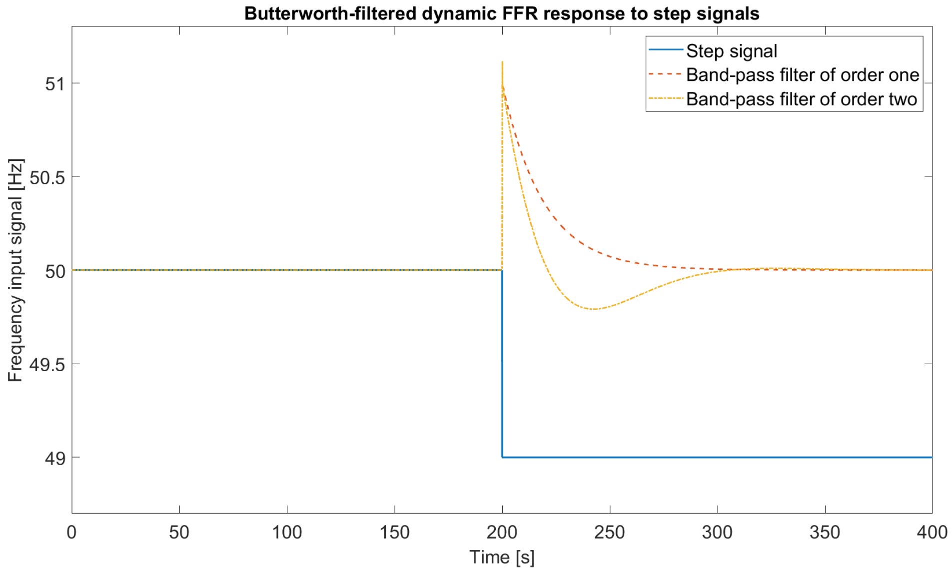

Figure 3.8: Experiment testing different orders of a Butterworth band-pass filter in Matlab. The experiment concluded that the band-pass filter during practical tests was mistakenly set to an order of 2, when it should have been set to an order of 1 to resemble the desired response used in simulations.

The fourth and last testing occasion was used to produce measurements for the final results, based on experience and measurements from previous occasions. The settings of the final measurements for the sine tests are summarised in Table 3.2. Due to the low wind velocity conditions during testing, a curtailment factor of 0.5 was used during these sine tests.

Table 3.2: Settings used for the final sine tests with prototype A.

Test-ID	$\tau_{c,LP}$ [s]	$\tau_{c,HP}$ [s]	$\tau_{c,NREL}$ [s]	$Gain$ [Nm/Hz]	Periods
$4.Si.A1$	0.2	20	20	400	$T_1 - T_{10}$
$4.Si.A2$	n.a.*	n.a.	20	400	$T_1 - T_{10}$
$4.Si.A3$	0.2	20	n.a.	400	$T_1 - T_{10}$
$4.Si.A4$	n.a.	n.a.	n.a.	400	$T_1 - T_{10}$

*n.a.: not active.

Step tests were carried out according to the settings in Table 3.3 for the final results. A curtailment factor of 0.25 was used during these step tests.

Table 3.3: Settings used for the final step tests with prototype A.

Test-ID	$\tau_{c,LP}$ [s]	$\tau_{c,HP}$ [s]	$\tau_{c,NREL}$ [s]	$Gain$ [Nm/Hz]
$4.St.A1$	0.2	10	10	200
$4.St.A2$	0.2	60	10	200
$4.St.A3$	0.2	20	20	200
$4.St.A4$	0.2	20	n.a.*	200
$4.St.A5$**	0.2	60	60	200

*n.a.: not active.
**only simulated.

Table 3.4 shows the settings used for final measurements using real grid frequency as input signal. The tests were carried out with a curtailment factor of 0.5. Observe that the gain was set much higher compared to the step tests, since the frequency changes in the input signal are very small. If a disturbance would occur while using the real grid frequency as input, the output would become much larger than intended and could worsen the disturbance. One way to avoid this problem, is to instead use the per unit gain in the dynamic FFR block, see Figure 2.6, together with the following saturation which would limit the output in case it got too big. These functions are definitely necessary for dynamic FFR, but were not prioritised to investigate further in this project to limit the variation of used settings, to keep the testing and readability of the results simpler.

Table 3.4: Settings used for the final grid frequency tests with prototype A.

Test-ID	$\tau_{c,LP}$ [s]	$\tau_{c,HP}$ [s]	$\tau_{c,NREL}$ [s]	$Gain$ [Nm/Hz]
$4.G.A1$	0.2	20	20	4000
$4.G.A2$	0.2	60	10	4000

Lastly, the final disturbance tests that were carried out with prototype A are summarised in Table 3.5, using a curtailment factor of 0.5.

Table 3.5: Settings used for the final tests using recorded frequency from a real disturbance with prototype A.

Test-ID	$\tau_{c,LP}$ [s]	$\tau_{c,HP}$ [s]	$\tau_{c,NREL}$ [s]	$Gain$ [Nm/Hz]
$4.D.A1$	0.2	10	10	800
$4.D.A2$	0.2	20	20	800
$4.D.A3$	0.2	60	20	800

3.3.2 Prototype B: estimate rotational speed to MPPT

The concept of prototype B was to estimate what the rotational speed would have been without activation of the reserve, and input this speed to the MPPT, rather than the actual rotational speed that is affected by the dynamic FFR activation, as illustrated in Figure 3.9. The Simulink model of this prototype is illustrated in Appendix A.1.2. This solution involves more steps, and is more complicated than prototype A.

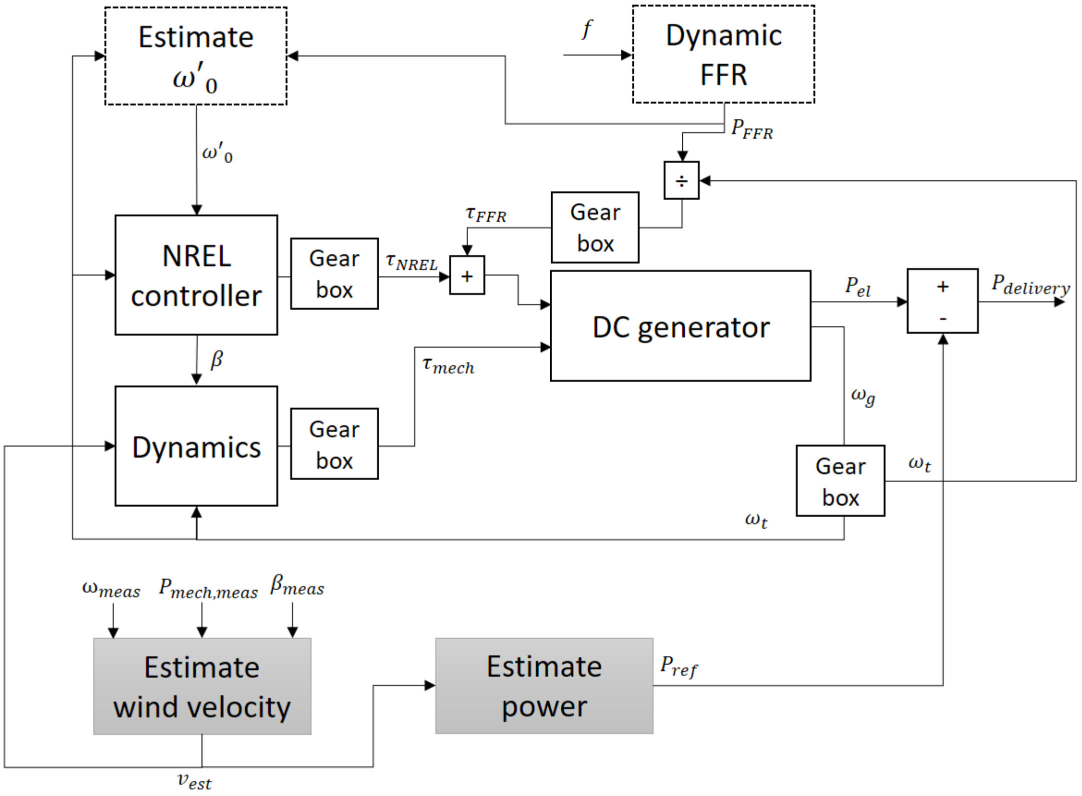

Figure 3.9: Scheme of prototype B, consisting of the wind turbine model with included dynamic FFR and estimate ω'_0 blocks that are surrounded by dashed lines, used for simulations.

The inside of the block estimate ω'_0 is illustrated in Figure 3.10.

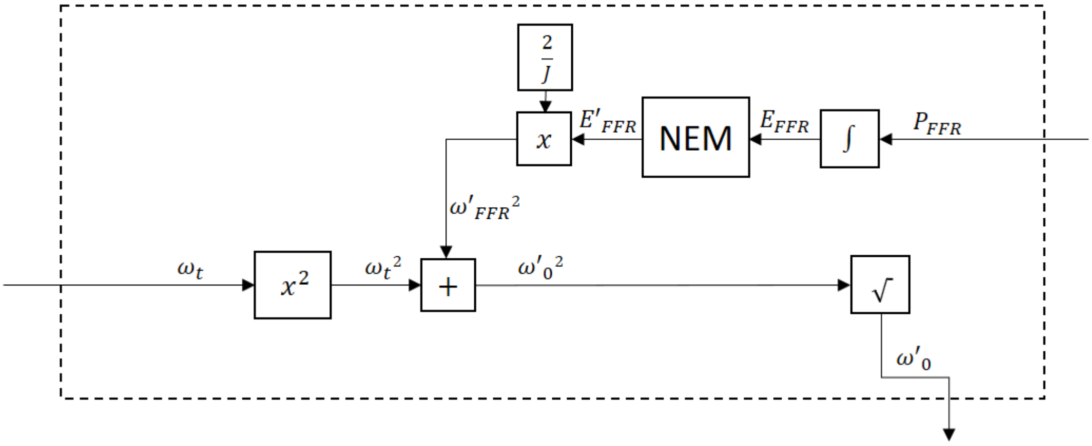

Figure 3.10: The inside of block estimate ω'_0, part of prototype B. P_{FFR} is the power response due to dynamic FFR, and E_{FFR} the energy. NEM is modelled as a high-pass filter which limits the magnitude of the energy to E'_{FFR}. The parameter ω'_{FFR} corresponds to change in rotational speed, while ω_t is the actual turbine rotational speed, and ω'_0 is the estimated rotational speed.

The mathematics behind the scheme in Figure 3.10 is mainly based on equation 2.7, which expresses the stored rotational energy in terms of rotational speed ω_t and moment of inertia J, and the integral of the kinetic power of the turbine in equation 2.8. If an addition of electric power due to dynamic FFR activation is defined as P_{FFR}, then the mechanical rotational energy that is used from the turbine can be defined as

$$E_{FFR} = \int_{t_0}^{T} P_{FFR}\,dt \quad [J]. \tag{3.2}$$

Since equation 3.2 is an integral, it could theoretically grow towards infinity. A NEM function was implemented as a high-pass filter to eventually force E_{FFR} towards zero as

$$E'_{FFR} = \frac{\tau_{c,NEM}s}{\tau_{c,NEM}s+1}E_{FFR} \quad [J], \tag{3.3}$$

where $\tau_{c,NEM}$ is a time constant. The parameter ω'_{FFR} corresponds to the change in rotational speed due to FFR delivery, but is restricted by the NEM function since it is based on E'_{FFR} according to equation 2.7 as

$$\omega'^2_{FFR} = \frac{2}{J}E'_{FFR} \quad [\frac{rad^2}{s^2}]. \tag{3.4}$$

The estimated rotational speed ω'_0 that would have occurred without FFR can then be calculated as

$$\omega'_0 = \sqrt{\omega_t^2 + \omega'^2_{FFR}} \quad [\frac{rad}{s}], \tag{3.5}$$

where ω_t is the real rotational speed of the turbine. The implementation of prototype B during practical tests is illustrated in Figure 3.11. To avoid stopping the turbine, the pitch controller, located in the NREL controller, still acted on the real rotational speed ω_t, while the estimated torque from NREL was based on the estimated ω'_0.

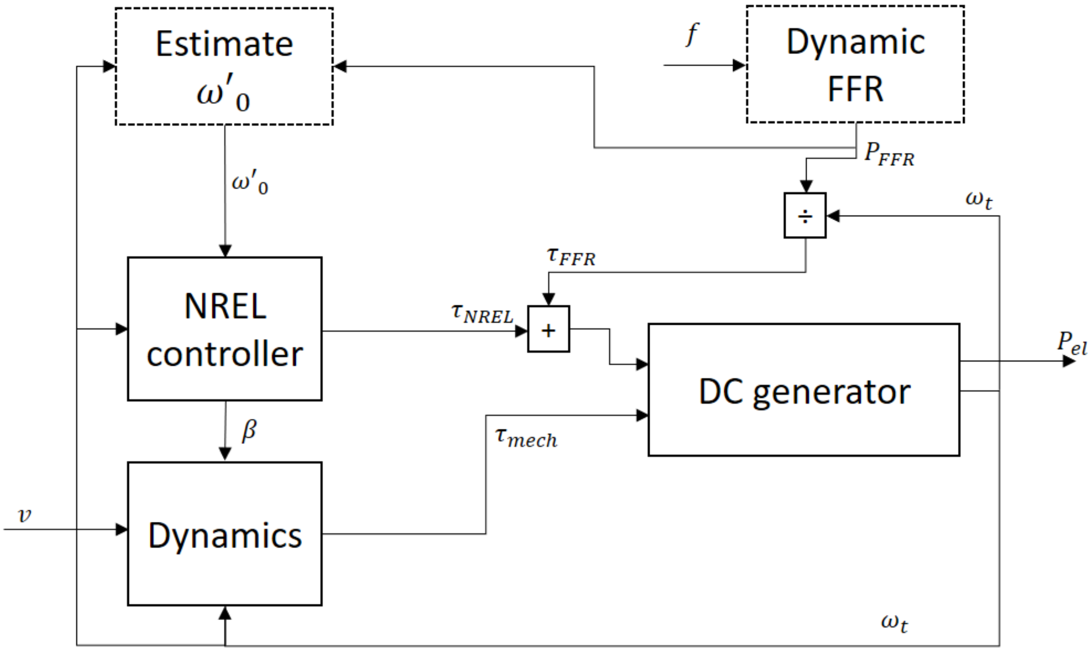

Figure 3.11: Scheme of prototype B, consisting of the wind turbine model with included dynamic FFR and estimate ω_0 blocks that are surrounded by dashed lines, used during practical tests.

Differences between reality and simulations were noted after analysing measurements that were logged from practical tests. One step test according to the settings in Table 3.6 was carried out to help illustrate the differences. A curtailment factor of 0.25 was used during the practical test.

Table 3.6: Settings for a step test with prototype B, used to illustrate differences between simulation and reality.

Test-ID	$\tau_{c,LP}$ [s]	$\tau_{c,HP}$ [s]	$\tau_{c,NEM}$ [s]	$Gain$ [W/Hz]
$4.St.B1$	0.2	10	10	1000

The estimated rotational speed ω'_0 did not behave as expected in reality, as it was very similar to ω_t, in contrast to in the simulation, see Figure 3.12 compared to simulation in Figure 3.13. This indicated that there existed an error in the calculations of ω'_0, either in the simulation or in the real set-up.

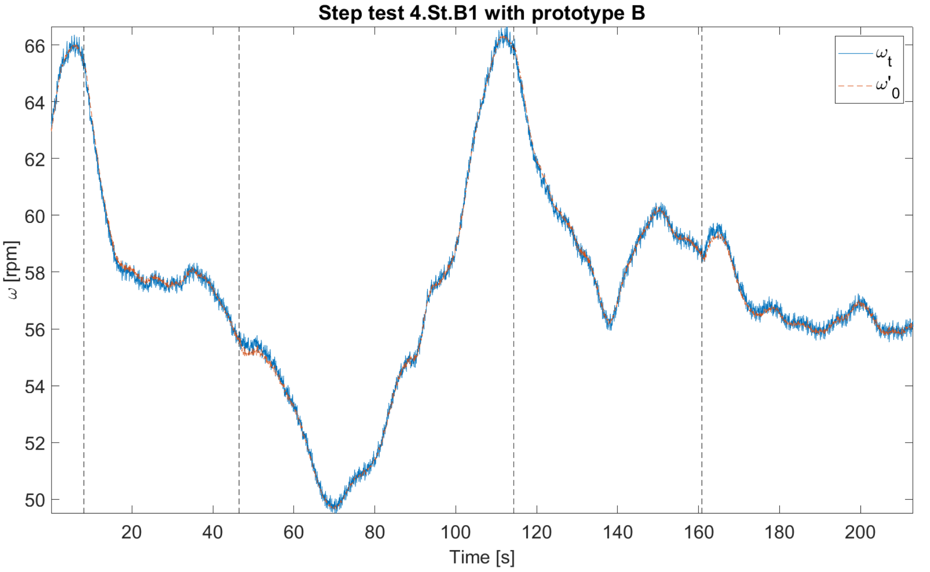

Figure 3.12: Experiment of step test 4.St.B1, with $\tau_{c,HP}$ = 10 s, $\tau_{c,NEM}$=10 s, and *gain* = 1000 W/Hz. Practical test.

Figure 3.13: Experiment of step test St.B1, with $\tau_{c,HP}$ = 10 s, $\tau_{c,NEM}$=10 s, and *gain* = 1000 W/Hz. Simulation.

To find the error, every signal in Figure 3.10 was investigated. It was found that the difference was in the parameter E'_{FFR}, see practical test in Figure 3.14 compared to simulation in Figure 3.15, indicating that the problem appeared in the NEM high-pass filter.

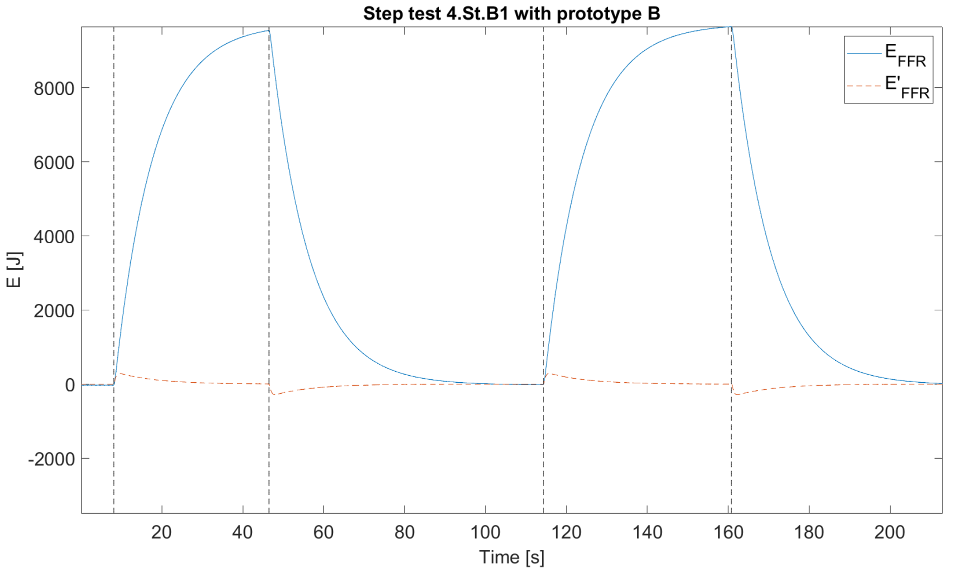

Figure 3.14: Experiment of step test 4.St.B1, with $\tau_{c,HP}$ = 10 s, $\tau_{c,NEM}$=10 s, and $gain$ = 1000 W/Hz. Parameter E'_{FFR} in real set-up.

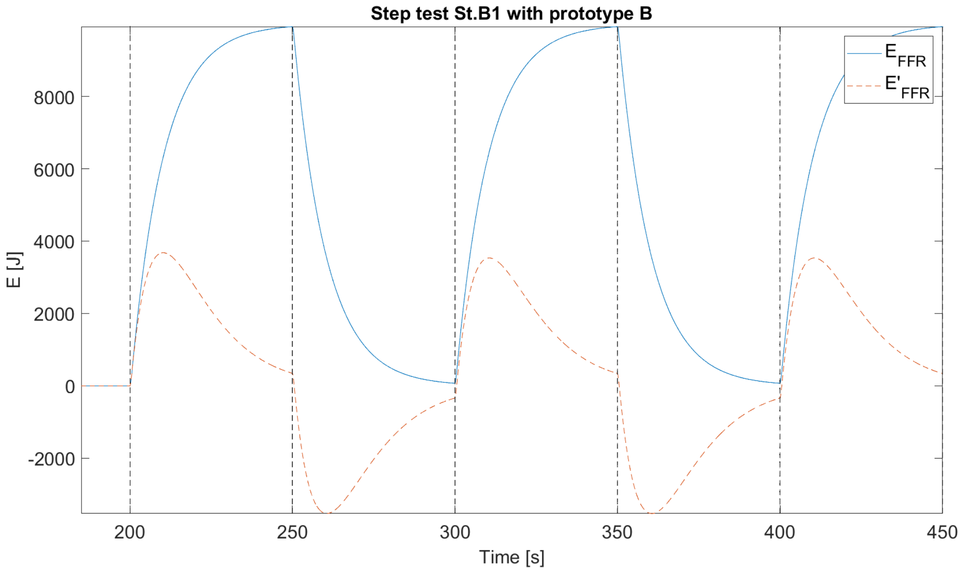

Figure 3.15: Experiment of step test St.B1, with $\tau_{c,HP}$ = 10 s, $\tau_{c,NEM}$=10 s, and $gain$ = 1000 W/Hz. Parameter E'_{FFR} in simulations.

An experiment was carried out to resolve if the error was in the simulation or real set-up. The signal E_{FFR}, logged from both simulation and real measurements, was manually high-pass filtered to compare with the logged E'_{FFR}, see practical test in Figure 3.16 and simulation in Figure 3.17. The experiment showed that the error was in the real set-up, as the manual calculation of E'_{FFR} from real measurements resembled how E'_{FFR} looked in simulations. The calculated and simulated E'_{FFR} were identical in the simulations.

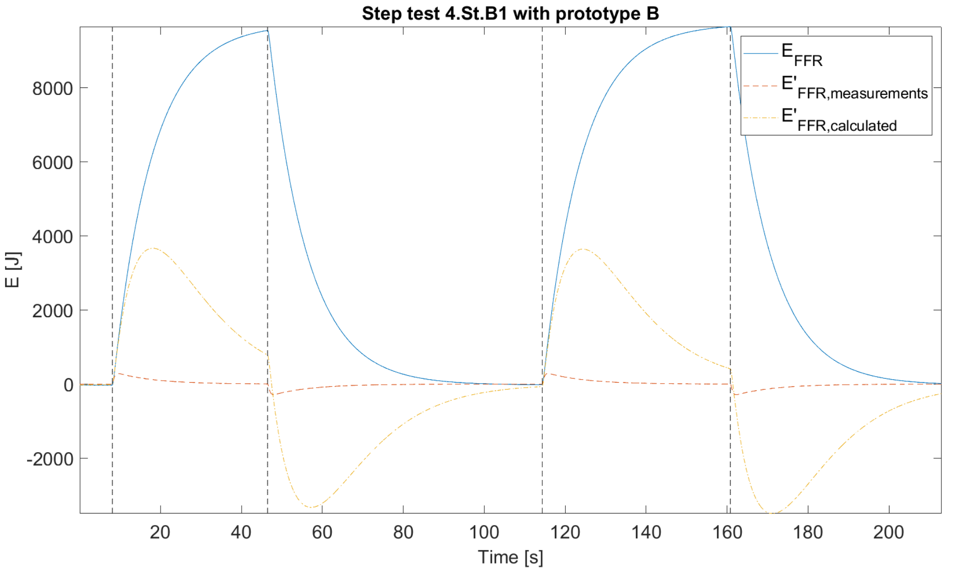

Figure 3.16: Experiment of step test 4.St.B1, with $\tau_{c,HP}$ = 10 s, $\tau_{c,NEM}$=10 s, and *gain* = 1000 W/Hz. Parameter E'_{FFR} is obtained by manually high-pass filtering the signal E_{FFR}. Practical test.

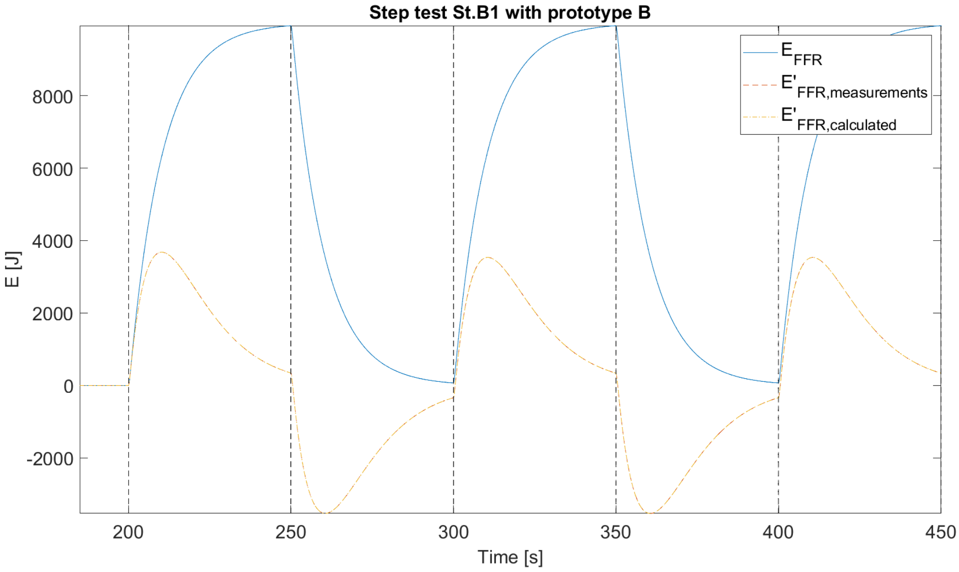

Figure 3.17: Experiment of step test St.B1, with $\tau_{c,HP}$ = 10 s, $\tau_{c,NEM}$=10 s, and *gain* = 1000 W/Hz. Parameter E'_{FFR} is obtained by manually high-pass filtering the signal E_{FFR}. Simulation.

By calculating ω'_0 from the calculated E'_{FFR}, Figure 3.18 shows how $\omega'_{0,calculated}$ differs from $\omega'_{0,measured}$ in the real set-up, and $\omega'_{0,calculated}$ looks more like what was expected. Figure 3.19 further confirms that the simulation seems valid, as $\omega'_{0,measured}$ and $\omega'_{0,calculated}$ both look similar to $\omega_{t,original}$ as intended.

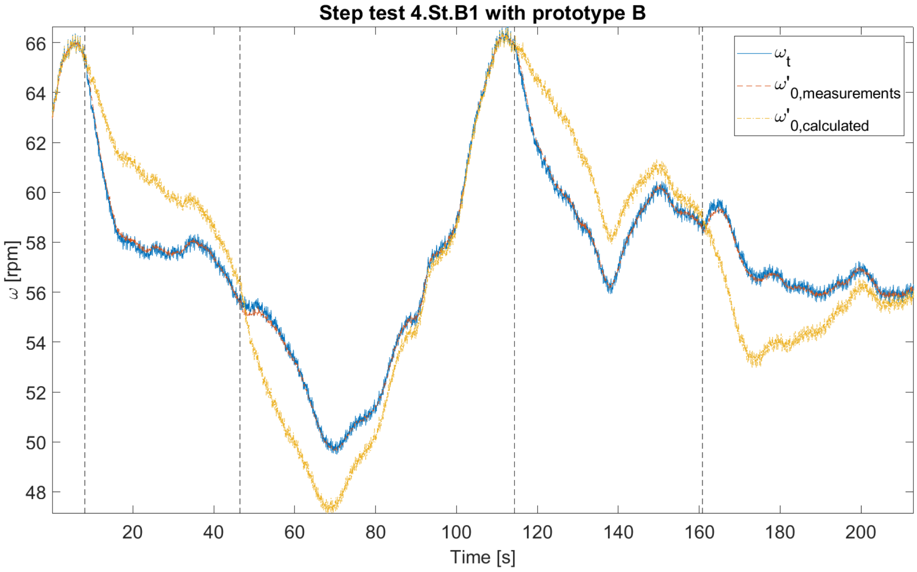

Figure 3.18: Experiment of step test 4.St.B1, with $\tau_{c,HP}$ = 10 s, $\tau_{c,NEM}$=10 s, and *gain* = 1000 W/Hz. Parameter ω'_0 is obtained from calculations based on $E'_{FFR,calculated}$. Practical test.

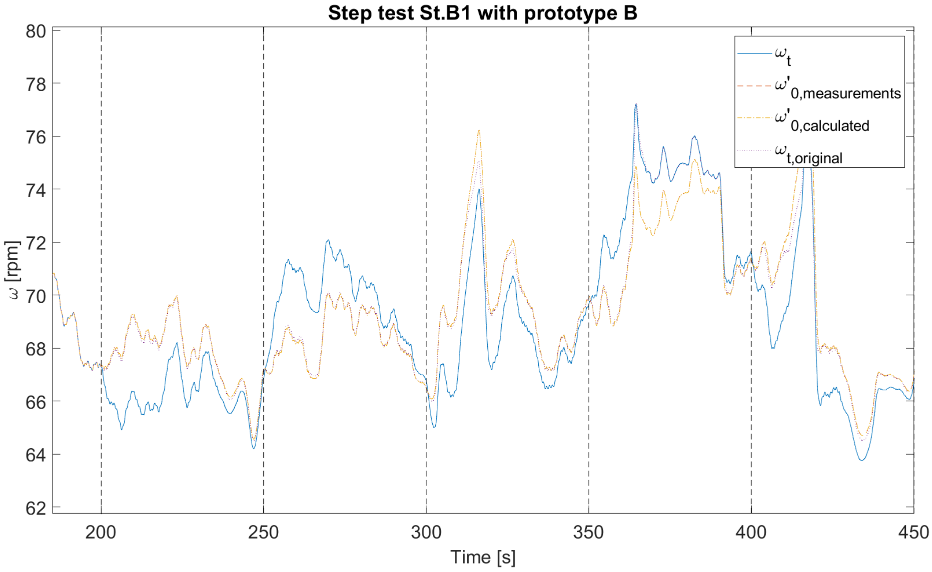

Figure 3.19: Experiment of step test St.B1, with $\tau_{c,HP}$ = 10 s, $\tau_{c,NEM}$=10 s, and *gain* = 1000 W/Hz. Parameter ω'_0 is obtained from calculations based on $E'_{FFR,calculated}$. Simulation.

In conclusion, this experiment confirmed that the difference appeared in the high-pass filter modelling NEM, and that the error was in the real set-up. Due to time and logistical constraints, the error in the real set-up could not be resolved until the very end of this project. The error was that the NEM filter did not initiate the assigned settings as it should have, but rather used some default values. Some last-minute step tests were done with the real set-up, but it was not possible to re-run all practical tests with prototype B. Therefore, most results for prototype B consist of simulations. The practical step tests that were done with prototype B after the error with the NEM filter was solved are summarised in Table 3.7. A curtailment factor of 0.5 was used during test 5.St.B4.

Table 3.7: Settings used for the final step tests with prototype B.

Test-ID	$\tau_{c,LP}$ [s]	$\tau_{c,HP}$ [s]	$\tau_{c,NEM}$ [s]	$Gain$ [W/Hz]
$5.St.B1$	0.2	10	10	3000
$5.St.B2$	0.2	60	10	1000
$5.St.B3$	0.2	10	60	1000
$5.St.B4$	0.2	60	60	1000
$5.St.B5$	0.2	20	20	1000

Another experiment was carried out through simulations to find the best estimation of ω'_0 while keeping ω_t below cut-out speed. Figure 3.20 shows step test St.B1 during varying wind velocity, and how the rotational speeds were affected if the pitch angle controller acted on ω'_0, while Figure 3.21 shows the behaviour if the pitching was based on ω_t. When ω'_0 controlled the pitching, the estimation of ω'_0 was more similar to the unaffected $\omega_{t,original}$. However, since the pitch controller did not act on the actual rotational speed behaviour, ω_t reached speeds above 80 rpm which is above cut-out speed and risks stopping the turbine. On the other hand, when the pitching was based on ω_t, the estimation of ω'_0 got worse during pitching, which can be seen between 350-400 seconds, where ω'_0 does not follow $\omega_{t,original}$.

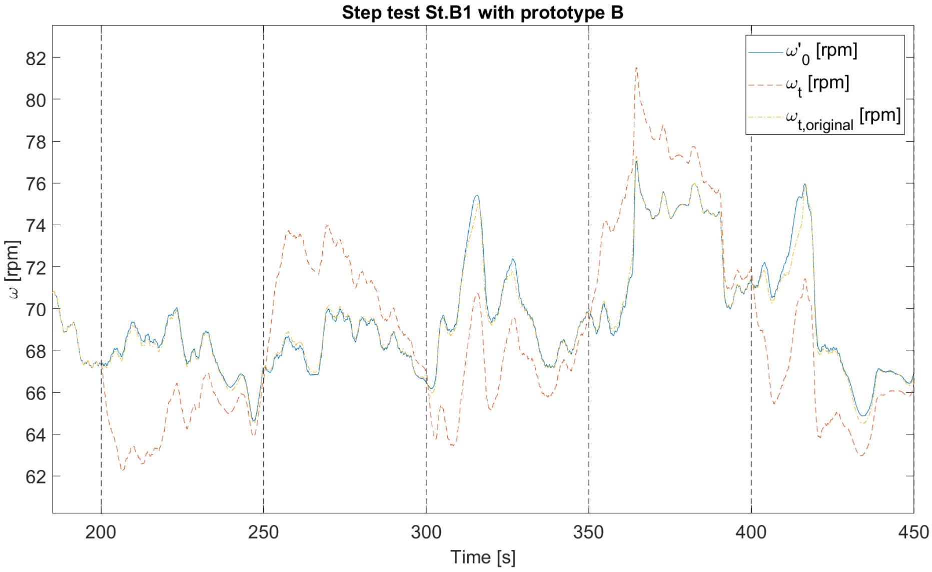

Figure 3.20: Step test St.B1, $\tau_{c,HP}$ = 10 s, $\tau_{c,NEM}$=10 s. Simulations with varying wind velocity and $gain$ = 2000 W/Hz. The pitching was based on ω'_0.

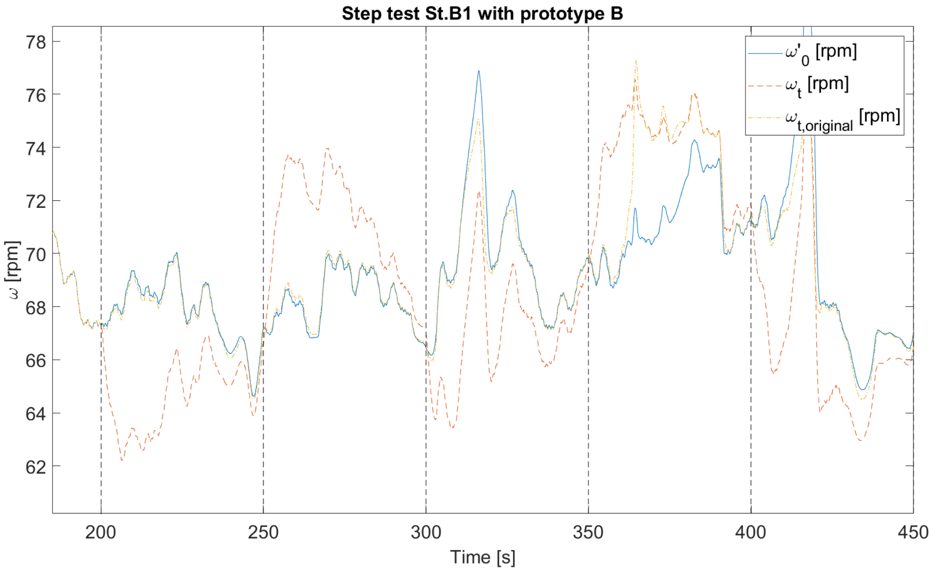

Figure 3.21: Step test St.B1, $\tau_{c,HP}$ = 10 s, $\tau_{c,NEM}$=10 s. Simulations with varying wind velocity and *gain* = 2000 W/Hz. The pitching was based on ω_t.

One simulation with constant velocity was also done to investigate how the pitch controller would act based on ω'_0 or ω_t. Figure 3.22 shows the rotational speed behaviour when pitching is based on ω'_0, and Figure 3.23 when pitching is based on ω_t, where both cases show similar behaviour as during varying wind velocity.

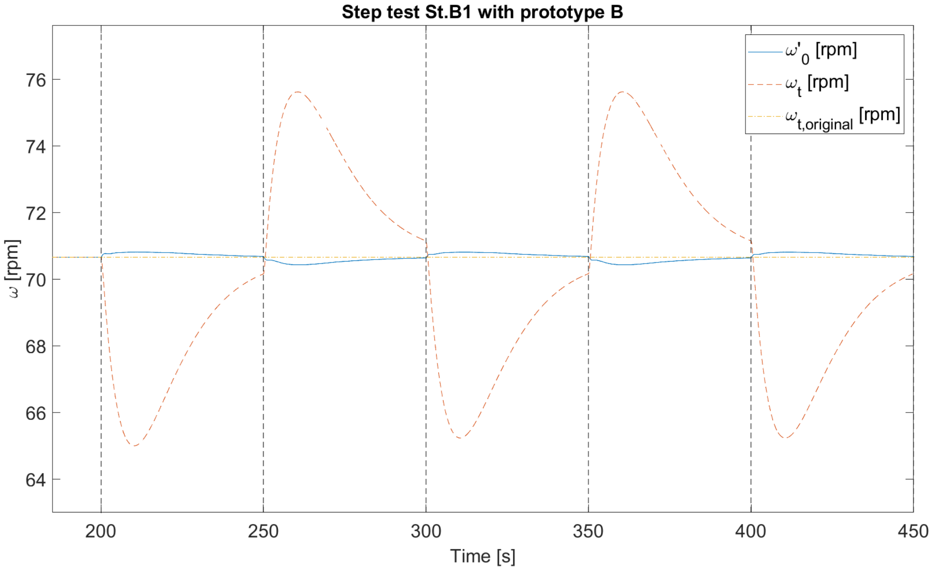

Figure 3.22: Step test St.B1, $\tau_{c,HP}$ = 10 s, $\tau_{c,NEM}$=10 s. Simulations with constant wind velocity and *gain* = 2000 W/Hz. The pitching is based on ω'_0.

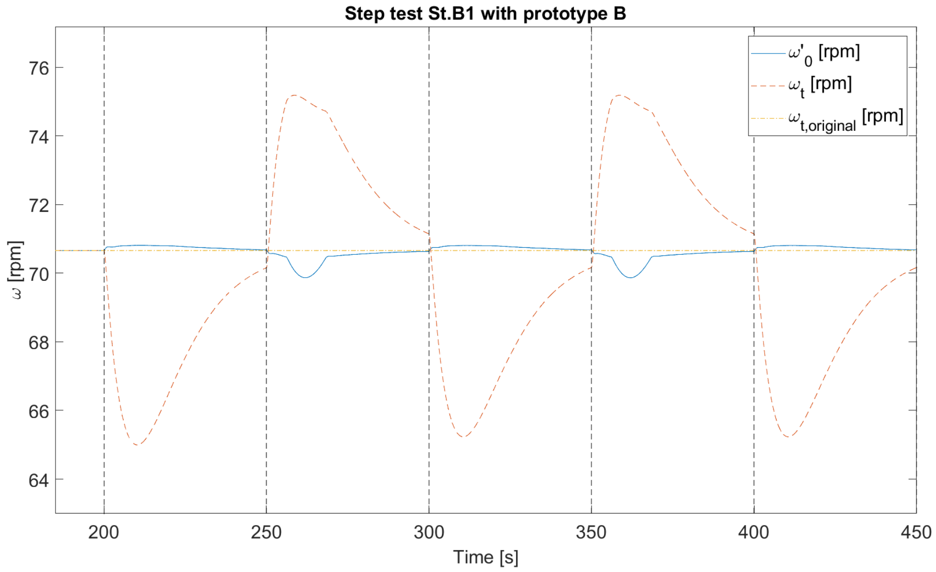

Figure 3.23: Step test St.B1, $\tau_{c,HP} = 10$ s, $\tau_{c,NEM}$=10 s. Simulations with constant wind velocity and *gain* = 2000 W/Hz. The pitching is based on ω_t.

A separate circuit of the wind turbine was then created, which did not restrict ω_t through pitching, to calculate the estimated ω'_0 with this unrestricted speed instead, see Figure 3.24. This allowed for both a better estimation of ω'_0 and to keep ω_t below cut-out speed, since the main circuit pitched based on the real ω_t.

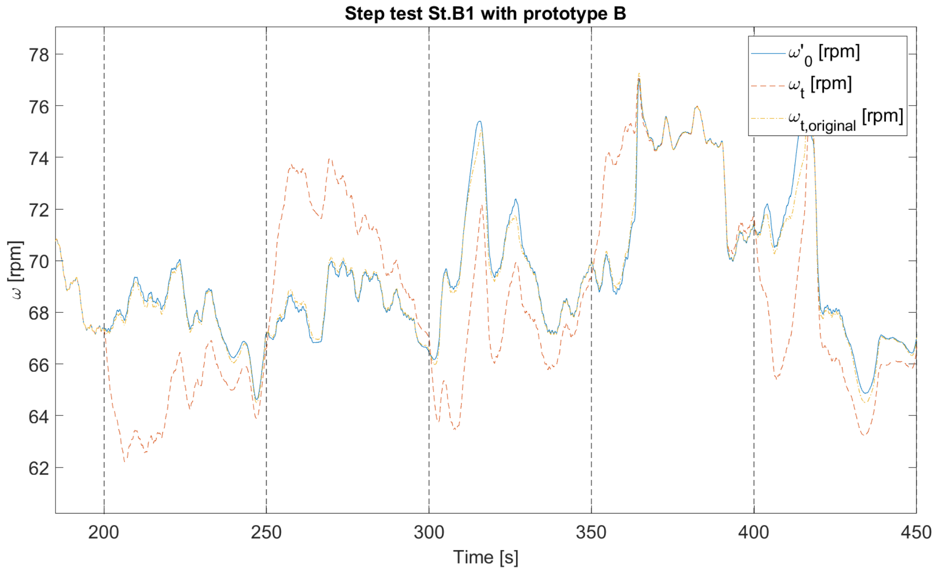

Figure 3.24: Step test St.B1, $\tau_{c,HP} = 10$ s, $\tau_{c,NEM}$=10 s. Simulation with varying wind velocity and *gain* = 2000 W/Hz. Pitching is based on the real rotational speed ω_t, while ω'_0 is calculated with ω_t from a separate curcuit that does not restrict the real rotational speed through pitching.

This indicated that the cause for the poorer estimation was that ω'_0 is based on

ω_t, see equation 3.5, and the estimation does not account for when ω_t is restricted in speed by the pitching. Since the turbine might stop if ω_t reaches cut-out or cut-in speed, it was decided to let the pitch controller act on this real rotational speed instead of the estimated, and calculate ω'_0 by using ω_t from a separate circuit where it is not restricted in speed by the pitching. Preferably, this should have been done by instead taking the curtailed energy into account in the estimation of ω'_0 to enable better estimation also during practical tests. The reason for why this was not further investigated in this project, was due to time contraints, and since it also was not possible to run practical tests with this prototype during most parts of the project due to issues with the real set-up. An AEM function should also have been implemented in addition to the NEM function to make sure that the wind turbine does not shut down in a bad way, but was also not implemented due to time constraints. The final step tests that were simulated are summarised with settings in Table 3.8.

Table 3.8: Settings used for the final simulated step tests with prototype B.

Test-ID	$\tau_{c,LP}$ [s]	$\tau_{c,HP}$ [s]	$\tau_{c,NEM}$ [s]	$Gain$ [W/Hz]
$St.B1$	0.2	10	10	1000
$St.B2$	0.2	60	10	1000
$St.B3$	0.2	10	60	1000
$St.B4$	0.2	60	60	1000

Table 3.9 shows the settings used for the final disturbance tests that were simulated with prototype B.

Table 3.9: Settings used for the final simulated tests using recorded frequency from a real disturbance with prototype B.

Test-ID	$\tau_{c,LP}$ [s]	$\tau_{c,HP}$ [s]	$\tau_{c,NEM}$ [s]	$Gain$ [W/Hz]
$D.B1$	0.2	10	10	6000
$D.B2$	0.2	20	20	6000
$D.B3$	0.2	20	40	6000
$D.B4$	0.2	40	20	6000
$D.B5$	0.2	40	40	6000

The settings used for the final grid frequency test that was simulated with prototype B are summarised in Table 3.10. Note that the gain was set very high since the frequency changes in the input signal are very small.

Table 3.10: Settings used for the final simulated grid frequency test with prototype B.

Test-ID	$\tau_{c,LP}$ [s]	$\tau_{c,HP}$ [s]	$\tau_{c,NEM}$ [s]	$Gain$ [W/Hz]
$G.B1$	0.2	20	20	80000

3.4 Bode plots

Bode plots were constructed from the practical sine tests done with prototype A in Table 3.2, by using the logged measurements of the sine-shaped frequency input signals with different periods and the corresponding electrical power output from the generator, P_{el}. A script was created to read the measurements and plot Bode plots from the different tests. The fluctuating wind velocity resulted in a lot of noise in particularly the electrical power output P_{el}, and a function was used to help approximate the sine shape present in the output, P_{fitted}. The output signal and the fitted output signal P_{fitted} were compared to confirm that the collected data points were relevant, and that P_{fitted} sufficiently resembled P_{el} in amplitude and phase. The input signal f was compared in the same way with a fitted input signal f_{fitted}, and the difference between these should be zero. If the fitted sine input and output matches the real input and output signals from a sine test with a certain period sufficiently, then the obtained point in the Bode plot from the test is considered valid.

3.5 Closed loop simulations of dynamic FFR in the power system

Prototype A and B were integrated in a simulation model representing the power system with FCR-D reserves and static FFR. FCR-N was deactivated during the simulations, and FRR was not included. The power response from static FFR was set to not deactivate, to model a worst-case-scenario of the frequency zenith. The kinetic energy E_k in the power system was set to 150 GWs. For prototype A, the time constants $\tau_{c,HP}$ and $\tau_{c,NREL}$ were set to 20 s, and the gain to 1000 Nm/Hz. For prototype B, the time constants $\tau_{c,HP}$ and $\tau_{c,NEM}$ were also set to 20 s, and the gain set to 5000 W/Hz. The simulations were done with varying wind velocity, and the dynamic FFR power responses from both prototypes were estimated by subtracting the output power of a separate circuit without dynamic FFR activation, $P_{el,original}$, from P_{el} of the main circuit with activated dynamic FFR. Both entities were amplified by the equivalent of 200 000 wind turbines, since the studied 25-kW wind turbine is small. The simulated 200 000 entities correspond to 2000 2.5-MW wind turbines.

To investigate how dynamic FFR from prototype A would affect the power system in a closed loop Bode plot, a different model was used. The gain and phase from the Bode plot of sine test 4.Si.A1 were expressed as complex numbers for each point in the plot as

$$G_{FFR,wind} = \frac{M_i}{max(M)}(cos(\phi_i) + jsin(\phi_i)), \tag{3.6}$$

where M_i is the quota of the output-input amplitudes $[\frac{W}{Hz}]$, ϕ_i is the phase $[rad]$, and j is a complex number. Transfer functions expressing the power system, G_{sys}, and FCR reserves, F_{FCR}, were expressed with the points of frequency that were used during the sine tests, to be compatible with $G_{FFR,wind}$. Furthermore, it was assumed that the gain was 0 and phase 90° for frequencies below 0.02 Hz. The function G_{sys} was expressed as

$$G_{sys} = \frac{1}{2Hj\omega_i + K_f f_0}, \tag{3.7}$$

where H is an inertia constant $[s]$, j is a complex number, ω_i are the frequencies that were used during the sine test of prototype A $[\frac{rad}{s}]$, K_f is a model parameter, and f_0 is the reference frequency set to 50 Hz. The inertia constant H can be expressed as

$$H = \frac{E_k}{S_n}, \tag{3.8}$$

where E_k is the rotational energy in the power system $[GWs]$, and S_n is the rated apparent power of the power system $[W]$. The function F_{FCR} was expressed as

$$F_{FCR} = FCR_{gain,scaling} \frac{K_p j\omega_i + K_i}{(E_p K_p + 1)j\omega_i + E_p K_i} \frac{1}{T_{servo} j\omega_i + 1} \frac{-T_w j\omega_i + 1}{\frac{T_w}{2} j\omega_i + 1}, \tag{3.9}$$

where K_p, K_i, E_p, T_{servo}, T_w are FCR controller parameters. Here, F_{FCR} only accounted for FCR-D volume upwards and downwards, FCR-N was not included. The parameter $FCR_{gain,scaling}$ scales the gain. The function for the power system with FCR and dynamic FFR was obtained as

$$G_{0,wind} = G_{sys}(FCR_{sys,scale} F_{FCR} + FFR_{sys,scale} G_{FFR,wind}), \tag{3.10}$$

where $FCR_{sys,scale}$ and $FFR_{sys,scale}$ scales the reserves to p.u, for $FCR_{sys,scale}$ this is done as

$$FCR_{sys,scale} = \frac{FCR_{volume} f_0}{f_{band} S_n}, \tag{3.11}$$

where f_{band} is the range of frequency FCR is active $[Hz]$, and FCR_{volume} is the reserve amount $[W]$. For $FFR_{sys,scale}$, this was done as

$$FFR_{sys,scale} = \frac{FFR_{volume} f_0}{S_n}, \tag{3.12}$$

where FFR_{volume} is the gain of dynamic FFR $[\frac{MW}{Hz}]$. The closed loop function from P to f was obtained as

$$G_{closed,wind} = \frac{G_{sys}}{1 + G_{0,wind}}. \tag{3.13}$$

Four different combinations of settings were investigated, by varying the rotational energy E_k and gain of dynamic FFR, see Table 3.11.

Table 3.11: Settings used for the closed loop Bode plots with the power system and FCR, with added dynamic FFR from prototype A.

E_k [GWs]	FFR_{volume} [MW/Hz]
150	1000
150	500
100	1000
100	500

4

Results & discussion

The results from simulations and practical tests are presented and discussed along the way in this chapter, first for prototype A, and then for prototype B. Lastly, results from closed loop simulations of the prototypes with two different models are presented and discussed.

4.1 Prototype A: slow down MPPT

Results from step tests, grid frequency tests, disturbance tests and Bode plots from sine tests with prototype A will be presented in this section. Simulations will be presented first, and then the practical test results.

4.1.1 Simulated step tests

Following step tests were simulated, with settings summarised in Table 3.3. First, shorter time constants are investigated, followed by increasing the high-pass filter time constant $\tau_{c,HP}$, and then using longer time constants in both the high-pass filter and NREL filter. Lastly, the effect of shorter and longer time constants are looked at by letting a step linger for a long time. Observe that the parameters denoted original are from a separate circuit without dynamic FFR, but the NREL controller is still delayed with the same time constant $\tau_{c,NREL}$, to enable better readability of what effect dynamic FFR has.

Step test St.A1 was simulated with both varying and constant wind velocity, and these simulations are presented in Figure 4.1-4.6. The behaviour of the electric power output P_{el} and torque addition τ_{FFR} are illustrated in Figure 4.1 with varying wind velocity, and Figure 4.2 when the wind velocity is constant. The simulated step test St.A1 in Figure 4.1-4.2 indicates that the torque addition of τ_{FFR} does initially increase and decrease the electric power output P_{el} as desired, but that the torque addition induces an undesired and oscillating behaviour of P_{el} during both varying and constant wind velocity. The intended increase and decrease in power declines much earlier than τ_{FFR}, which could be because the torque addition affects the efficiency of the wind turbine.

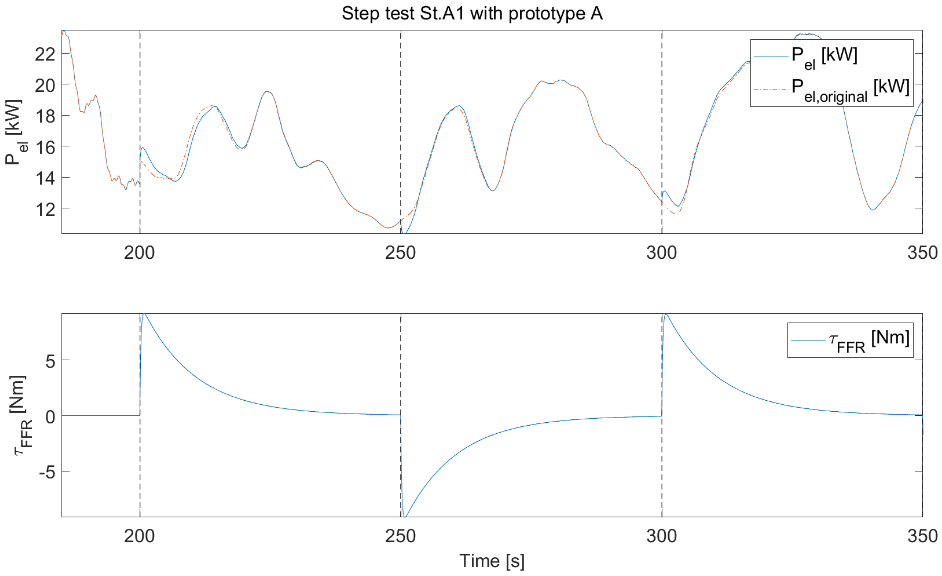

Figure 4.1: Step test St.A1, $\tau_{c,HP}$ = 10 s, $\tau_{c,NREL}$ = 10 s. Simulation with *gain* = 200 Nm/Hz, and varying wind velocity.

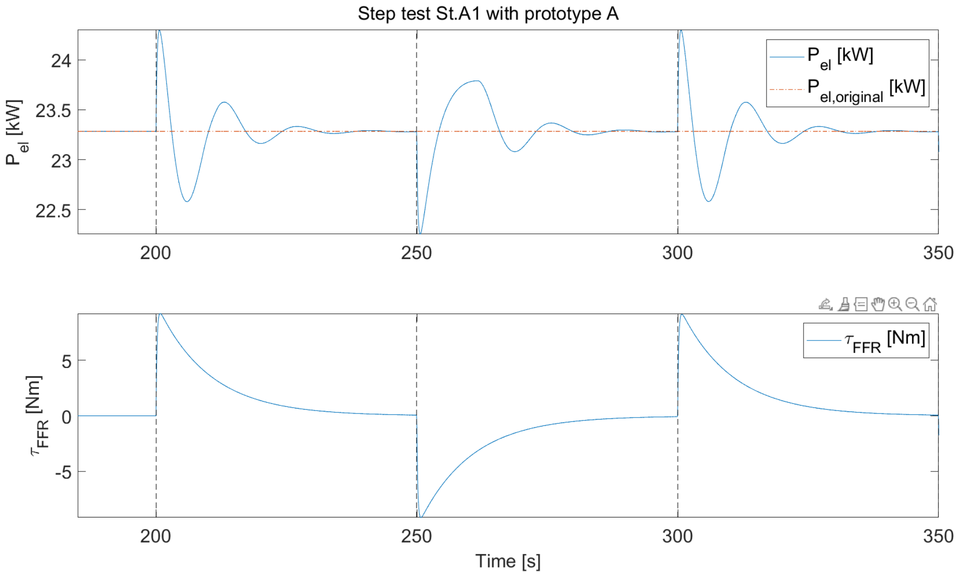

Figure 4.2: Step test St.A1, $\tau_{c,HP}$ = 10 s, $\tau_{c,NREL}$ = 10 s. Simulation with *gain* = 200 Nm/Hz, and constant wind velocity.

The input wind velocity and behaviour of the pitch angle during these simulations are shown in Figure 4.3 and Figure 4.4, and it is possible to recognize the varying wind velocity pattern in the power output shown in Figure 4.1.

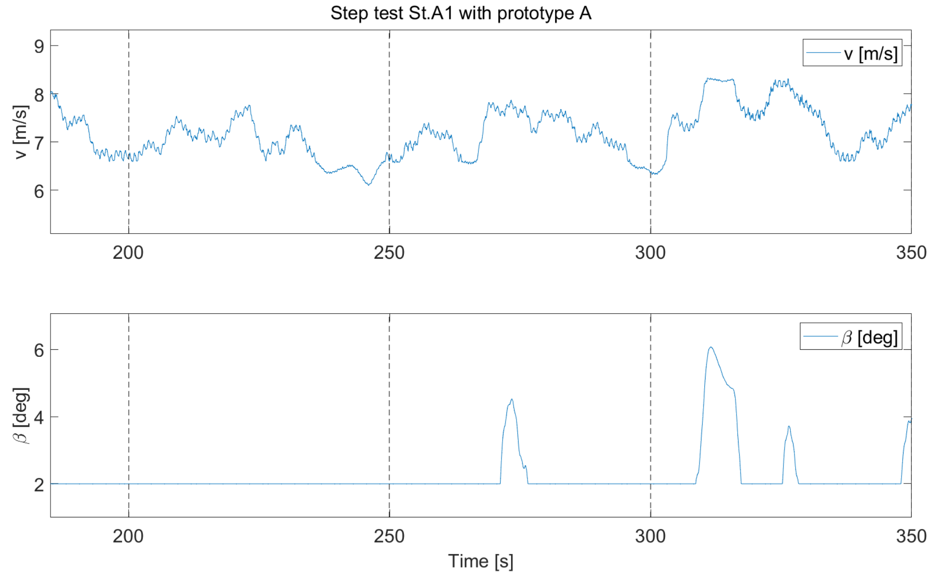

Figure 4.3: Step test St.A1, $\tau_{c,HP}$ = 10 s, $\tau_{c,NREL}$ = 10 s. Simulation with *gain* = 200 Nm/Hz, and varying wind velocity.

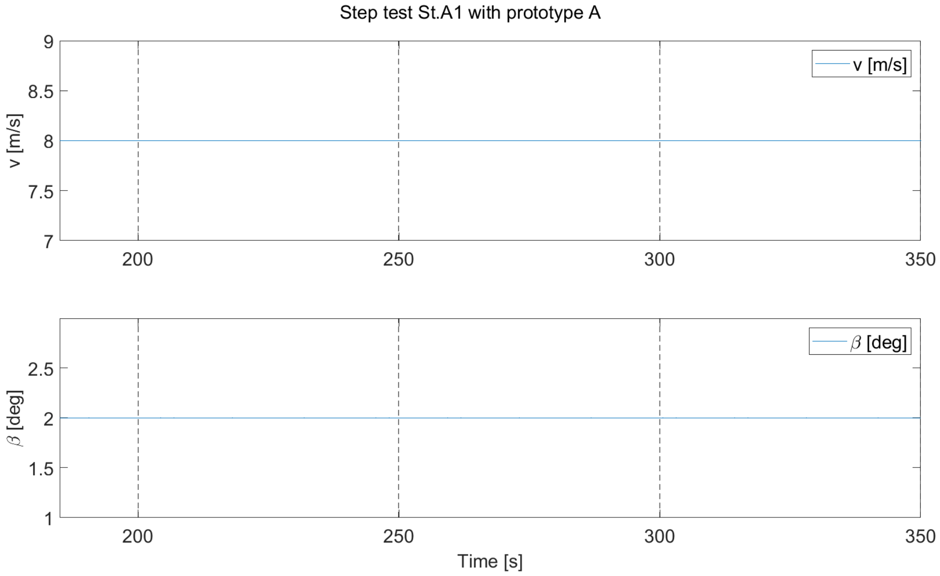

Figure 4.4: Step test St.A1, $\tau_{c,HP}$ = 10 s, $\tau_{c,NREL}$ = 10 s. Simulation with *gain* = 200 Nm/Hz, and constant wind velocity.

Figure 4.5 and Figure 4.6 shows the behaviour of the torque and rotational speed, where τ_{tot} is the sum of the torque response, τ_{FFR}, and the torque from the NREL controller, τ_{NREL}. The torque and rotational speed also show an oscillating behaviour just like P_{el}, indicating that the cause for the oscillations is the NREL controller which tries to return to optimal operation after the reserve activation. The behaviour during torque increase and decrease, as well as rotational speed decrease and increase, looks different in Figure 4.6, which is also seen in the behaviour of P_{el} in Figure 4.2. Both magnitude and endurance seem greater during power decrease, which could be explained by that the turbine gains momentum from the increased rotational speed.

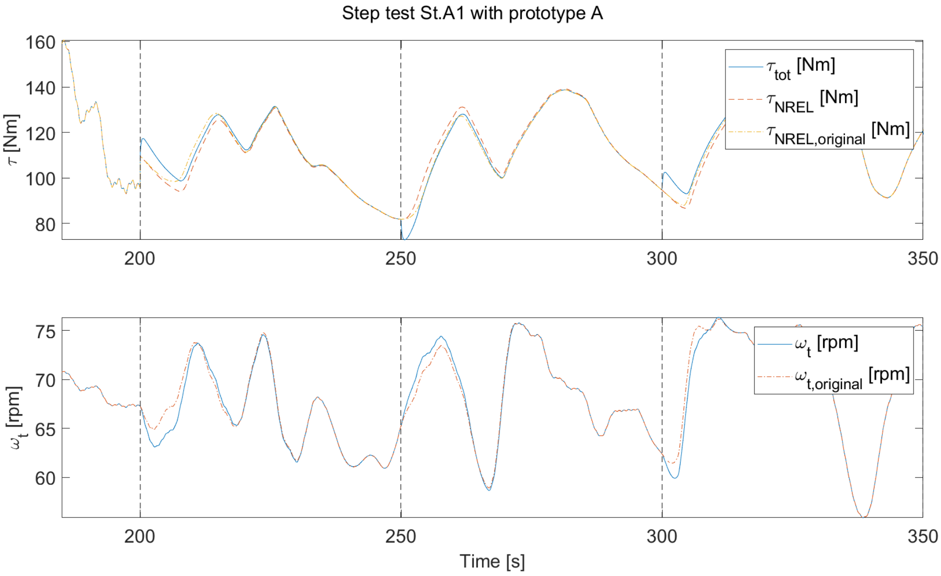

Figure 4.5: Step test St.A1, $\tau_{c,HP}$ = 10 s, $\tau_{c,NREL}$ = 10 s. Simulation with *gain* = 200 Nm/Hz, and varying wind velocity.

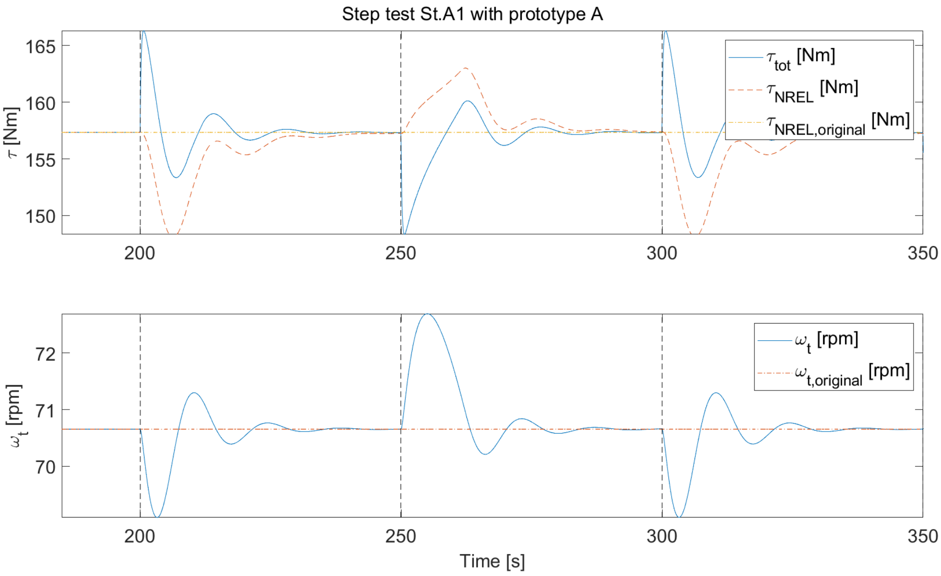

Figure 4.6: Step test St.A1, $\tau_{c,HP}$ = 10 s, $\tau_{c,NREL}$ = 10 s. Simulation with *gain* = 200 Nm/Hz, and constant wind velocity.

Step test St.A2 was also simulated, increasing the time constant $\tau_{c,HP}$ to 60 s while keeping $\tau_{c,NREL}$ to 10 s, and can be seen in Figure 4.7 and Figure 4.8, using varying and constant wind velocity respectively. The results indicate that increasing $\tau_{c,HP}$, while $\tau_{c,NREL}$ is set to a smaller value, has a little impact on the electric power output P_{el}, as P_{el} looks similar to step test St.A1 shown in Figure 4.1-4.2. During constant velocity, it is noted that P_{el} behaves differently compared to St.A1, especially when the torque decreases and rotational speed increases, as P_{el} looks flatter with increased endurance during the first zenith after the dip.

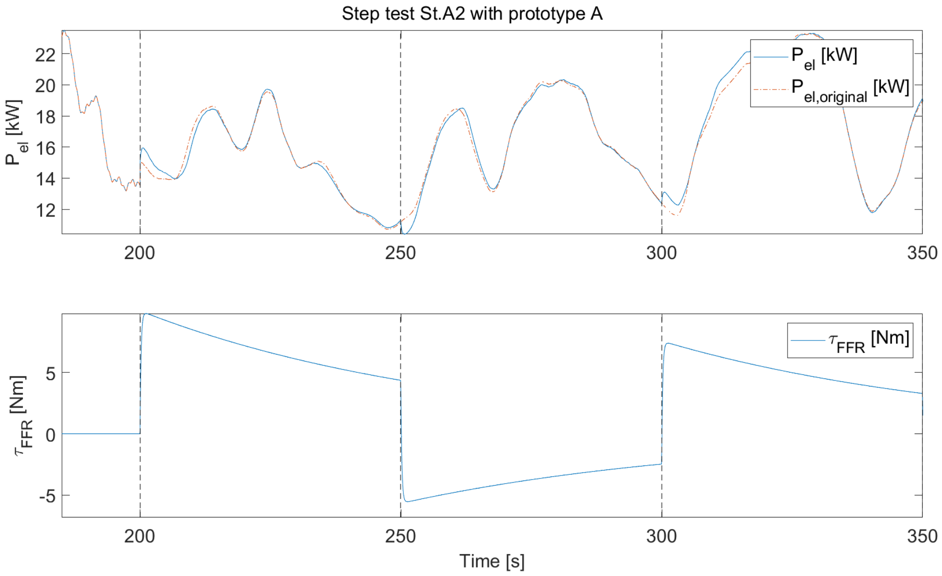

Figure 4.7: Step test St.A2, $\tau_{c,HP} = 60$ s, $\tau_{c,NREL} = 10$ s. Simulation with *gain* = 200 Nm/Hz, and constant wind velocity.

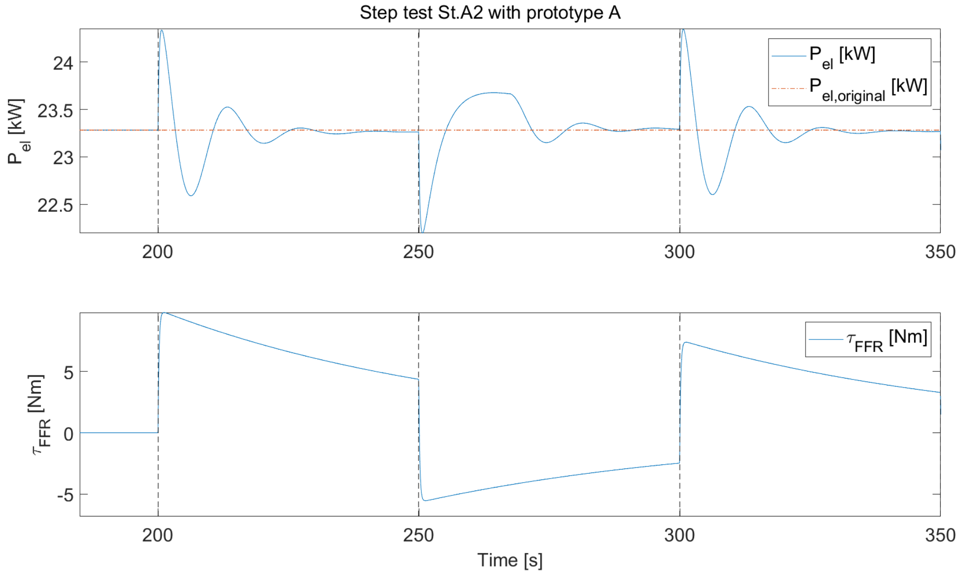

Figure 4.8: Step test St.A2, $\tau_{c,HP} = 60$ s, $\tau_{c,NREL} = 10$ s. Simulation with *gain* = 200 Nm/Hz, and constant wind velocity.

Both $\tau_{c,HP}$ and $\tau_{c,NREL}$ were set to 60 s and simulated in step test St.A5, which is illustrated in Figure 4.9-4.11. Note how P_{el} initially dips during constant wind velocity in Figure 4.10, as the low-pass filter slowing down the NREL controller is activated when the first step starts.

In contrast to Figure 4.7-4.8, the torque addition in Figure 4.9-4.10 has a much greater effect on the power output P_{el}, as it now seems to linger for a longer period of time as intended. This indicates that $\tau_{c,NREL}$ limits the effects of the high-pass filter in the dynamic FFR block. Furthermore, setting both time constants to higher values seems to mitigate the amplitude of the oscillating behaviour that was seen in Figure 4.1-4.2.

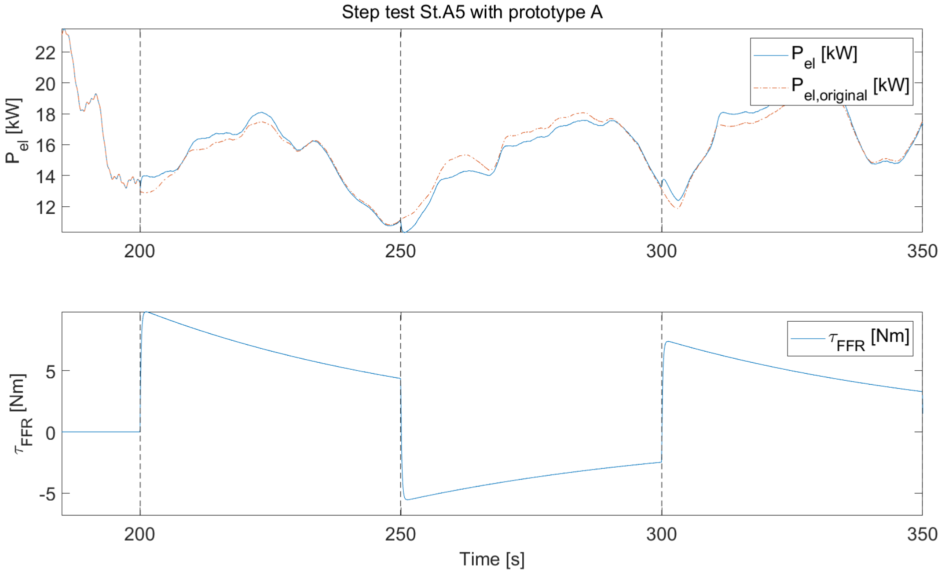

Figure 4.9: Step test St.A5, $\tau_{c,HP} = 60$ s, $\tau_{c,NREL} = 60$ s. Simulation with *gain* = 200 Nm/Hz, and varying wind velocity.

Figure 4.10 also shows a more long lasting overshoot of P_{el} during intended power decrease compared to power increase. Furthermore, the overshoot is also more long lasting compared with simulations St.A1 and St.A2, which showed similar behaviour. The greater time constants in test St.A5, together with the fact that the turbine gains momentum from the rotational speed increase during power decrease, could explain this behaviour.

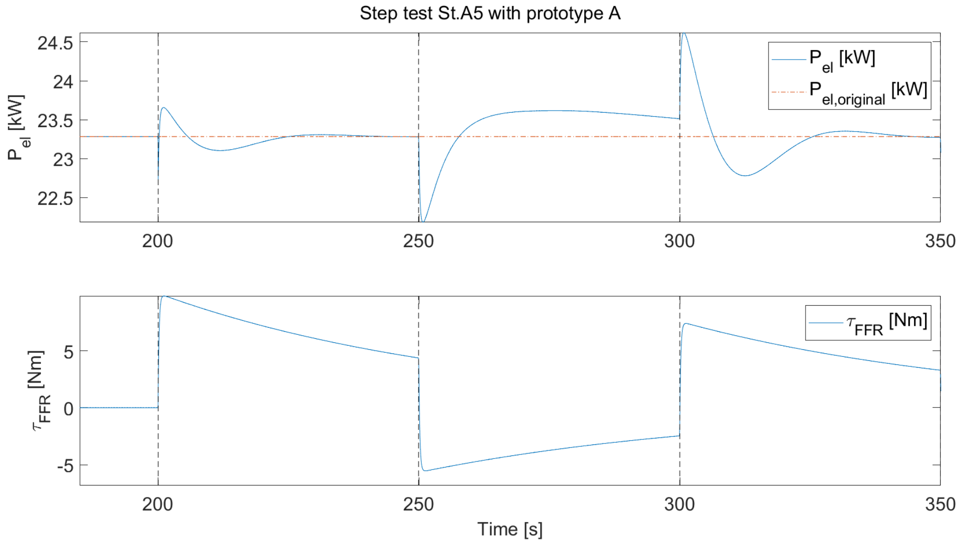

Figure 4.10: Step test St.A5, $\tau_{c,HP}$ = 60 s, $\tau_{c,NREL}$ = 60 s. Simulation with *gain* = 200 Nm/Hz, and constant wind velocity.

Figure 4.11 shows the behaviour of the torque during varying wind velocity, where τ_{tot} shows a significantly better endurance compared to in test St.A1 in Figure 4.5.

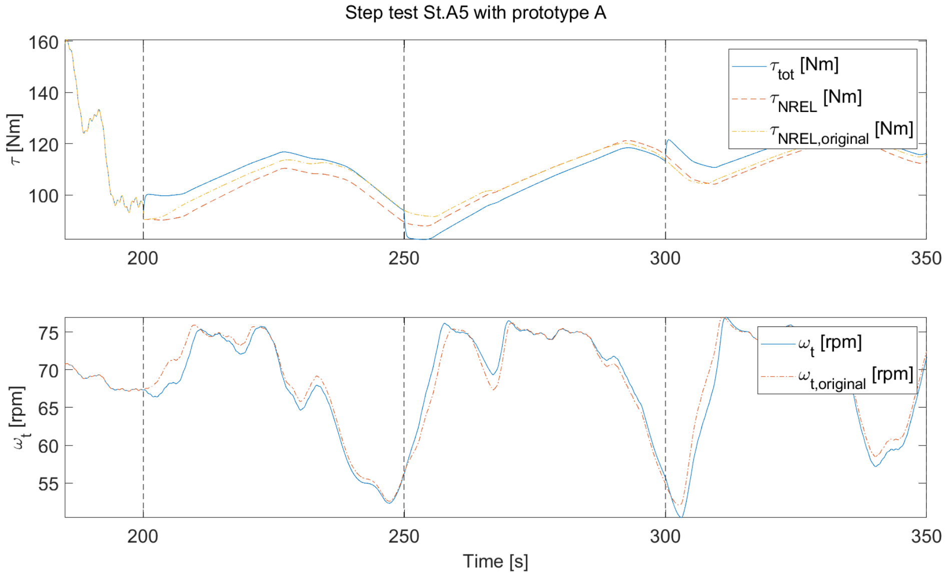

Figure 4.11: Step test St.A5, $\tau_{c,HP}$ = 60 s, $\tau_{c,NREL}$ = 60 s. Simulation with *gain* = 200 Nm/Hz and varying wind velocity.

However, if the step simulated in step test St.A5 gets to linger for 250 seconds instead of 50 seconds as in previous simulations, the turbine stops, while doing the same with step test St.A1 keeps the turbine spinning, which is shown in Figure 4.12 and Figure 4.13, respectively. These results show that it is not feasible to delay τ_{NREL} too much, at least without other measures.

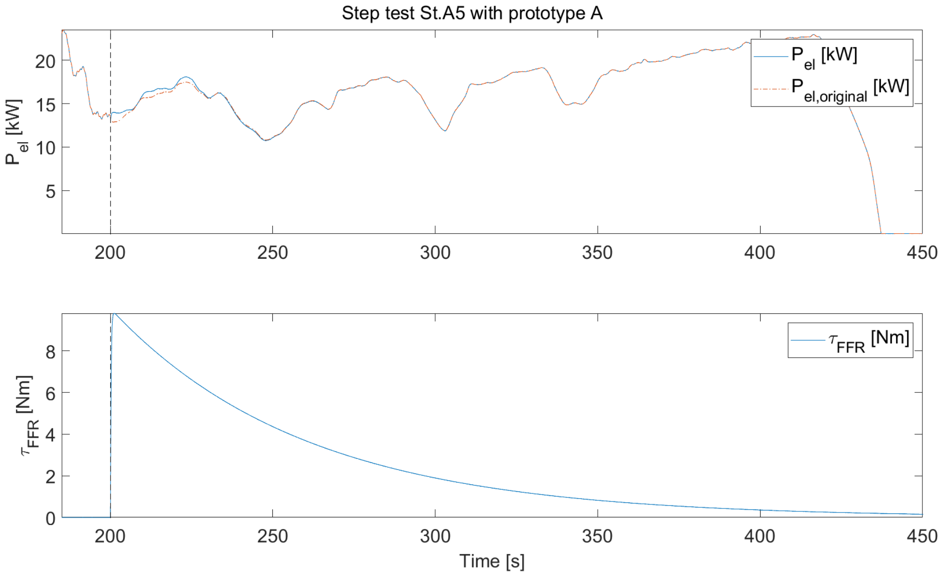

Figure 4.12: Step test St.A5, with $\tau_{c,HP} = 60$ s, and $\tau_{c,NREL} = 60$ s. Simulation with $gain = 200$ Nm/Hz and varying wind velocity.

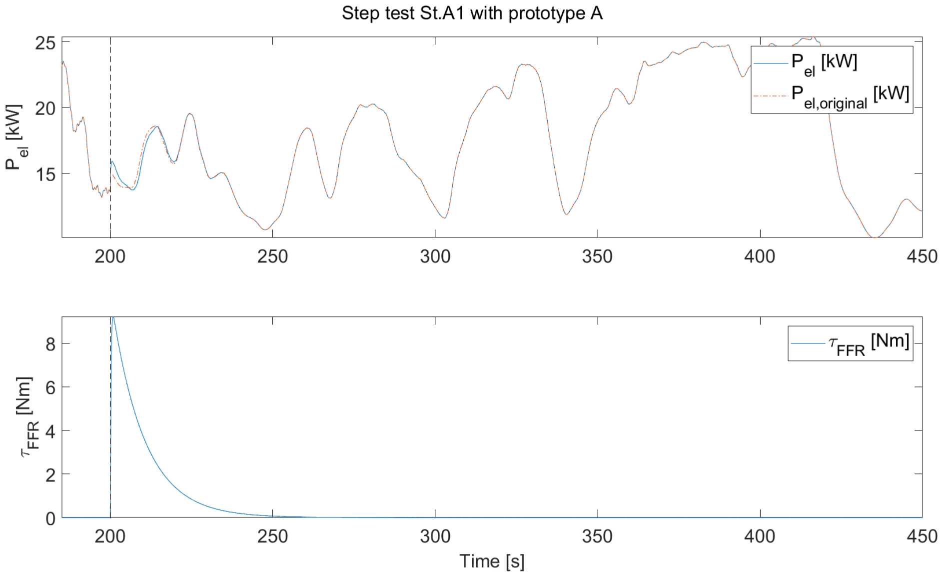

Figure 4.13: Step test St.A1, $\tau_{c,HP} = 10$ s and $\tau_{c,NREL} = 10$ s. Simulation with $gain = 200$ Nm/Hz and varying wind velocity.

4.1.2 Step tests

Following step tests are from real measurements, and the settings for the tests are summarised in Table 3.3. Firstly, shorter time constants are explored, followed by increasing the high-pass filter time constant $\tau_{c,HP}$. Then, longer and equal time constants are investigated, and finally the effect of the NREL filter is explored by de-activating the filter.

The results from step test 4.St.A1 are presented from two different measurements with the same settings, as step test 4.St.A1a in Figure 4.14-4.16, and as 4.St.A1b in Figure 4.17-4.19. Note that τ_{FFR} differs by a factor of 20 in contrast to in simulation St.A1, corresponding to the gear box ratio since the real wind turbine lacks a gear box. Another difference to the simulation was that a curtailment factor had to be used due to the low wind velocity conditions during testing. Step test 4.St.A1a in Figure 4.14 shows a softer and more ideal behaviour of P_{el}, compared to the simulations illustrated in Figure 4.1-4.2 where P_{el} showed an oscillating behaviour.

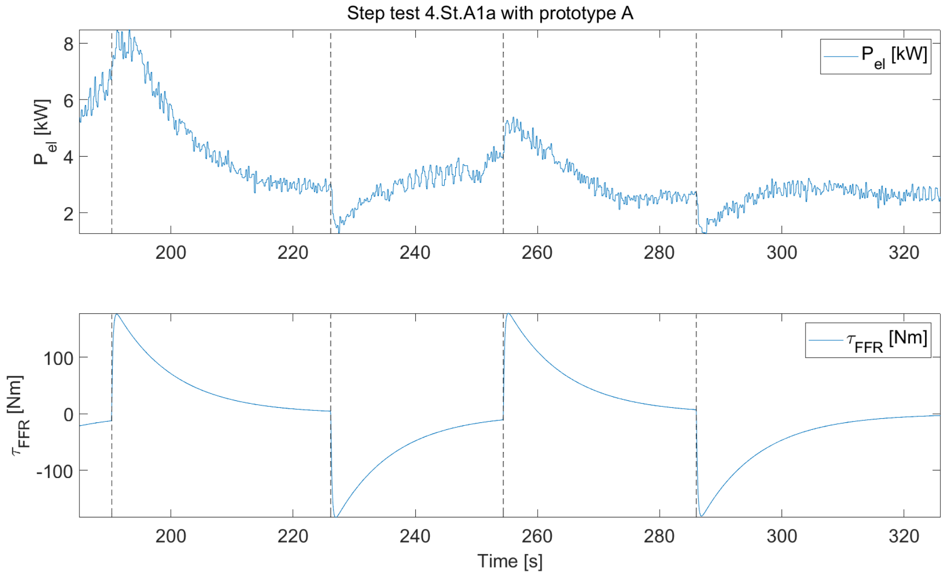

Figure 4.14: Step test 4.St.A1a, $\tau_{c,HP} = 10$ s, $\tau_{c,NREL} = 10$ s. Practical test with $gain = 200$ Nm/Hz and curtailment factor of 0.25.

The first power increase seems greater than the second one in Figure 4.14, which probably is because the wind velocity was initially greater and followed the pattern of the first torque addition, see Figure 4.15. The behaviour of P_{el} is interesting since the wind velocity overall behaved rather smooth and with small variations, indicating that the oscillating behaviour seen in the simulation might not be present in the practical test 4.St.A1a.

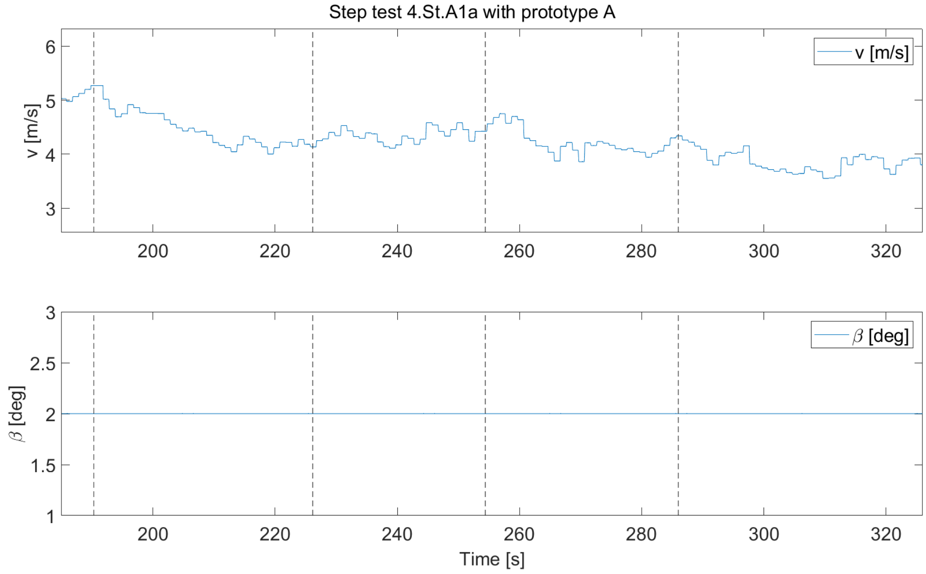

Figure 4.15: Step test 4.St.A1a, $\tau_{c,HP} = 10$ s, $\tau_{c,NREL} = 10$ s. Practical test with $gain = 200$ Nm/Hz and curtailment factor of 0.25.

The behaviour of the torque and rotational speed in Figure 4.16 also looks less oscillating compared to the simulations in Figure 4.5-4.6. On the other hand, the decrease of rotational speed seems to have a better endurance here, in contrast to the simulation where the increase had better endurance. The reason for worse endurance during rotational speed increase could be because of the low wind velocity conditions during the practical test, making it more difficult to gain speed. Furthermore, the low wind velocity also makes it easier for the turbine to drop in speed.

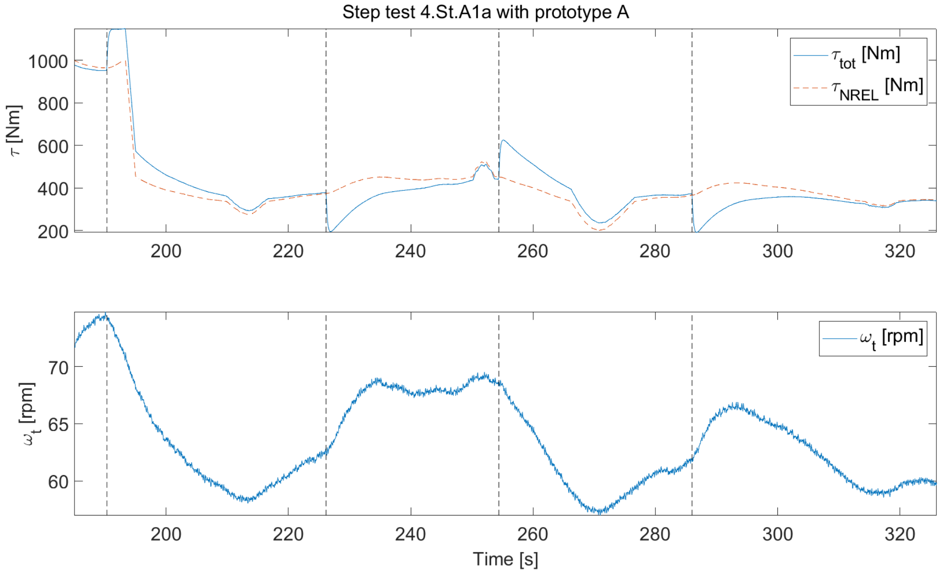

Figure 4.16: Step test 4.St.A1a, $\tau_{c,HP} = 10$ s, $\tau_{c,NREL} = 10$ s. Practical test with $gain = 200$ Nm/Hz and curtailment factor of 0.25.

The results from step test 4.St.A1b are illustrated in Figure 4.17-4.19. P_{el} shows a slightly different behaviour in Figure 4.17 compared to 4.St.A1a in Figure 4.14, as it fluctuates more during the third and sixth step.

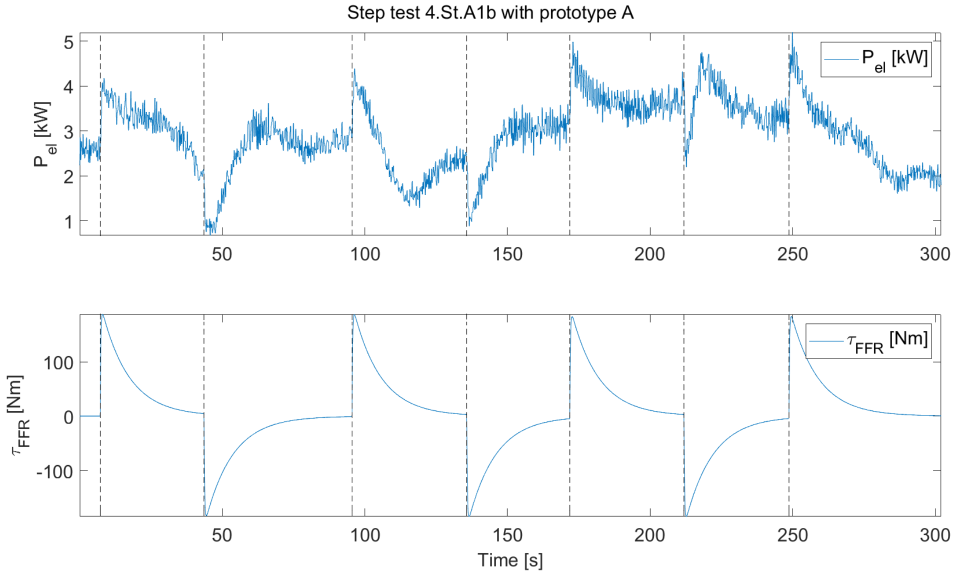

Figure 4.17: Step test 4.St.A1b, $\tau_{c,HP} = 10$ s, $\tau_{c,NREL} = 10$ s. Practical test with $gain = 200$ Nm/Hz and curtailment factor of 0.25.

The wind velocity varied slightly more compared to during step test 4.St.A1a, see Figure 4.18, but it looks rather constant during the third and sixth step.

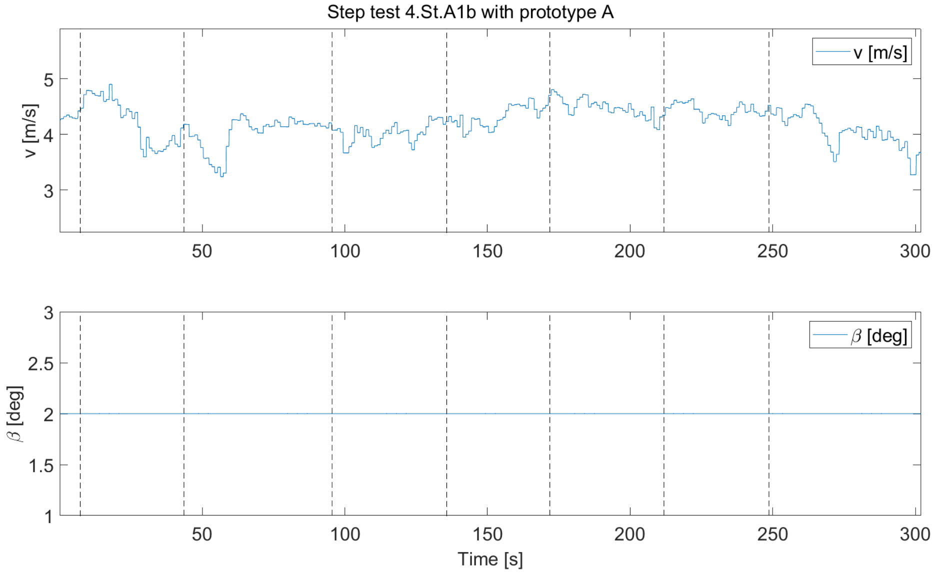

Figure 4.18: Step test 4.St.A1b, $\tau_{c,HP} = 10$ s, $\tau_{c,NREL} = 10$ s. Practical test with $gain = 200$ Nm/Hz and curtailment factor of 0.25.

The torque and rotational speed for test St.A1b is illustrated in Figure 4.19.

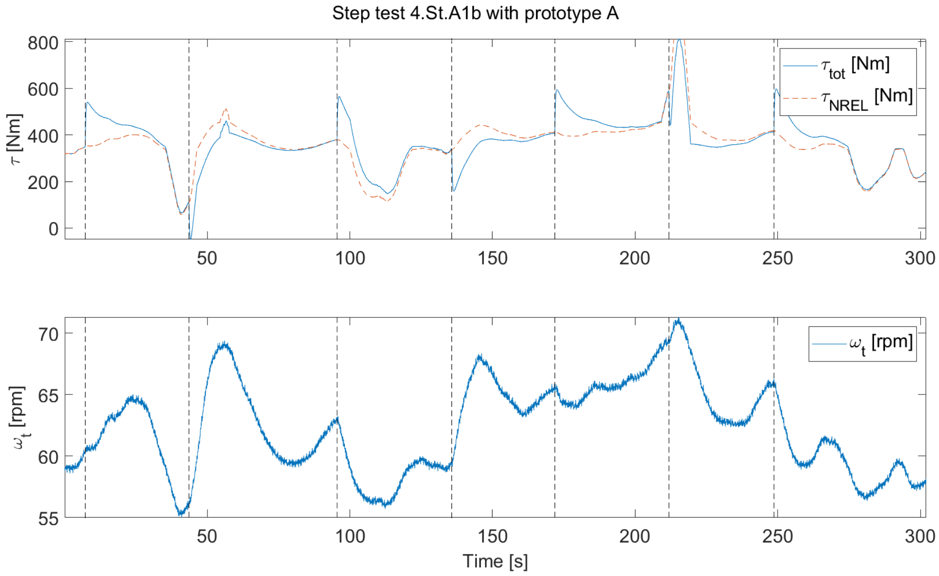

Figure 4.19: Step test 4.St.A1b, $\tau_{c,HP}$ = 10 s, $\tau_{c,NREL}$ = 10 s. Practical test with *gain* = 200 Nm/Hz and curtailment factor of 0.25.

The results from step test 4.St.A2 are presented in Figure 4.20-4.22. The power P_{el} shows a very oscillating behaviour in Figure 4.20, in contrast to previous tests 4.St.A1a and 4.St.A1b. Since the time constant $\tau_{c,HP}$ was increased to 60 s in this test, τ_{FFR} was set to linger for at least around 100 seconds.

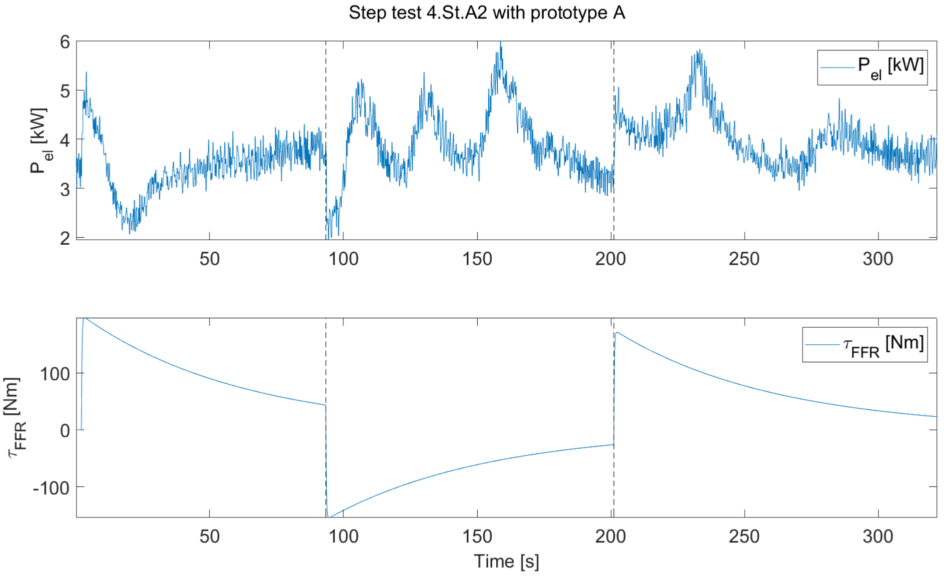

Figure 4.20: Step test 4.St.A2, $\tau_{c,HP}$ = 60 s, $\tau_{c,NREL}$ = 10 s. Practical test with *gain* = 200 Nm/Hz and curtailment factor of 0.25.

The wind velocity in Figure 4.21 seem rather constant during the test, and cannot explain the oscillating behaviour of P_{el}. However, the oscillating behaviour is also seen in the torque τ_{NREL} and rotational speed ω_t in Figure 4.22, which explains the behaviour of P_{el}. This indicates that the MPPT causes this behaviour, trying to compensate for τ_{FFR}, but in a delayed way due to the added low-pass filter. The time constant $\tau_{c,NREL}$ is set much smaller than $\tau_{c,HP}$, which means that the MPPT will try to compensate for the torque contribution more frequently when the steps also lingers for a longer time, compared to in test 4.St.A1. This result shows that it is probably not beneficial to set $\tau_{c,NREL}$ smaller than $\tau_{c,HP}$.

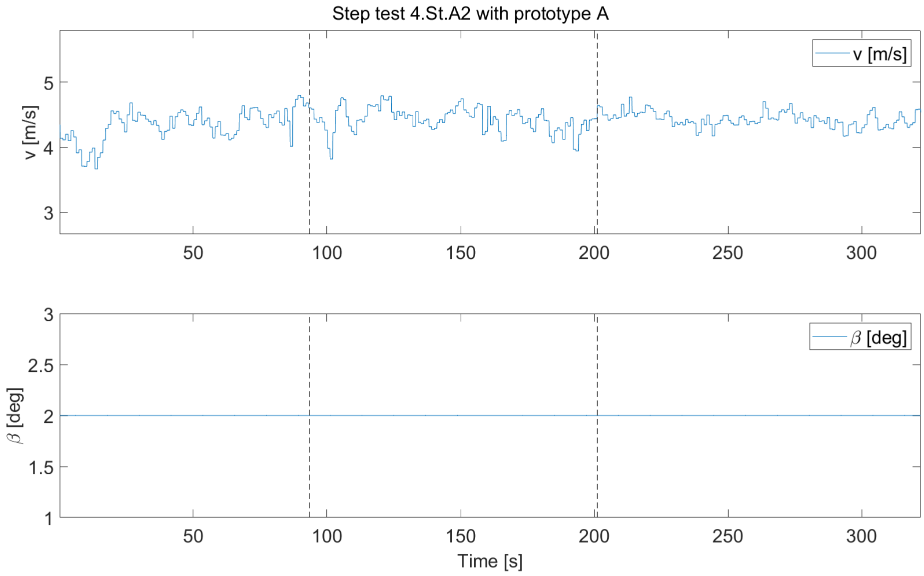

Figure 4.21: Step test 4.St.A2, $\tau_{c,HP} = 60$ s, $\tau_{c,NREL} = 10$ s. Practical test with $gain = 200$ Nm/Hz and curtailment factor of 0.25.

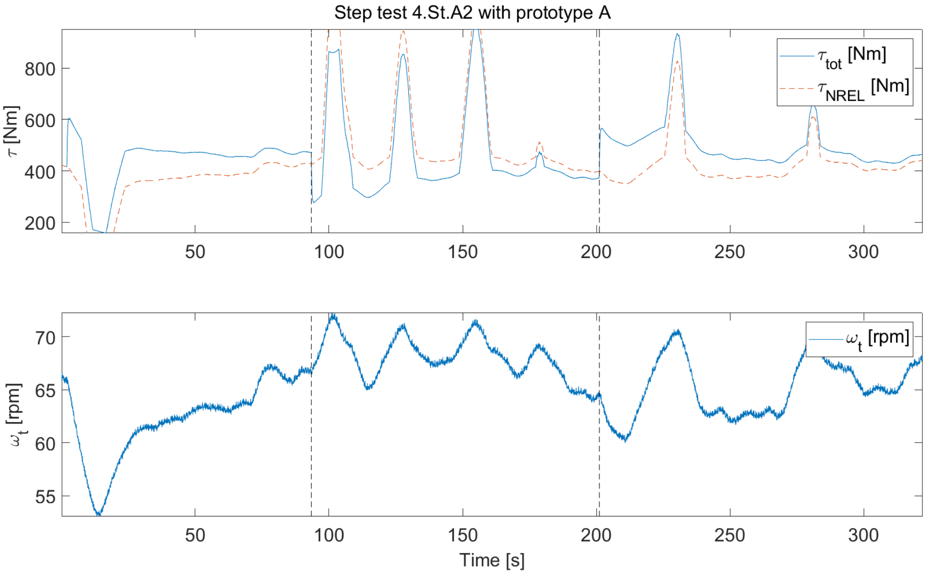

Figure 4.22: Step test 4.St.A2, $\tau_{c,HP} = 60$ s, $\tau_{c,NREL} = 10$ s. Practical test with $gain = 200$ Nm/Hz and curtailment factor of 0.25.

The reason why the behaviour of the torque is so steep in Figure 4.22, could be because of the design of the NREL controller, as the torque reaches a steeper region in the rotational speed-torque curve when the rotational speed exceeds around 70 rpm. Figure 4.23-4.25 show the results from step test 4.St.A3 where both time constants are set to 20 s. The power P_{el} appears to behave smoother in Figure 4.23 compared to test 4.St.A2, which could be because the time constants are set to be equal. The wind velocity is rather stable, see Figure 4.24.

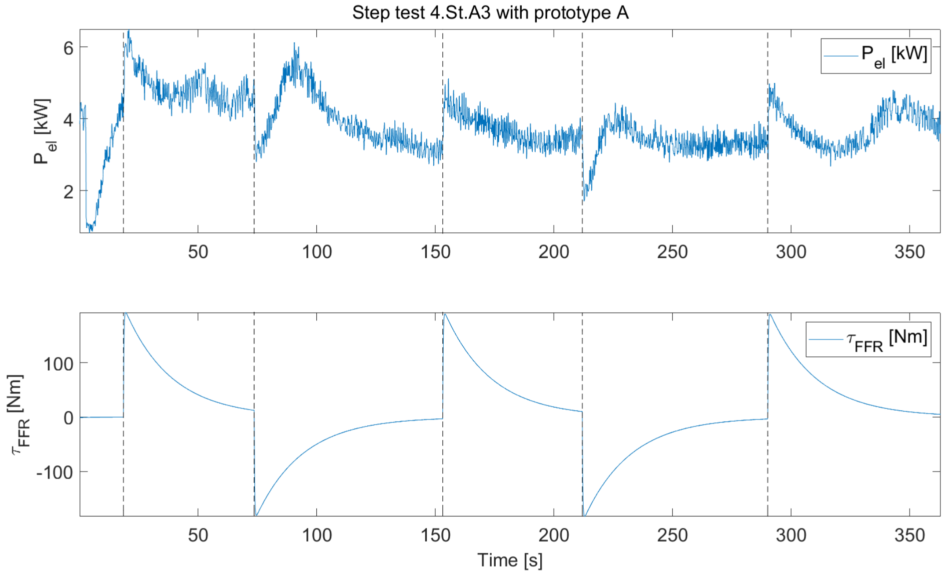

Figure 4.23: Step test 4.St.A3, $\tau_{c,HP} = 20$ s, $\tau_{c,NREL} = 20$ s. Practical test with $gain = 200$ Nm/Hz and curtailment factor of 0.25.

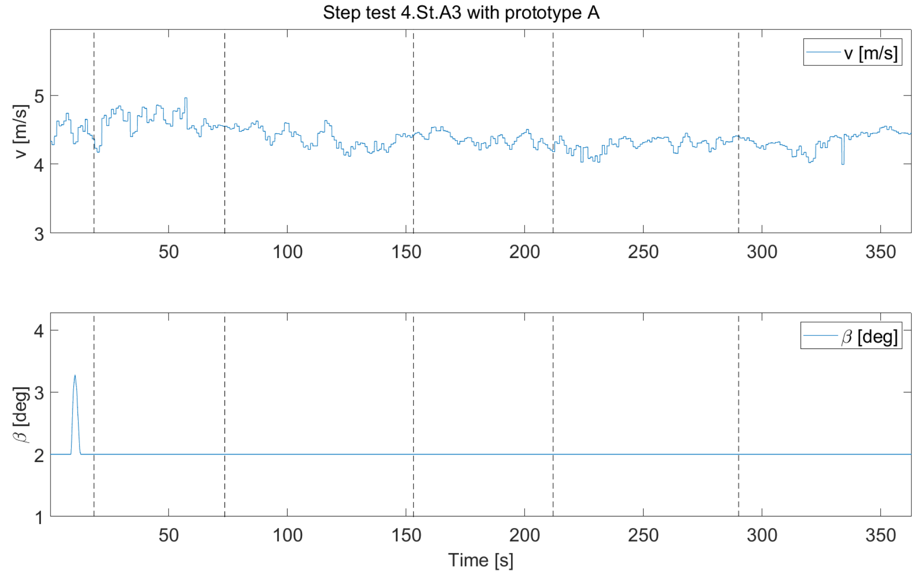

Figure 4.24: Step test 4.St.A3, $\tau_{c,HP} = 20$ s, $\tau_{c,NREL} = 20$ s. Practical test with $gain = 200$ Nm/Hz and curtailment factor of 0.25.

Figure 4.24 also shows that the pitch angle increases slightly for a moment after 10 seconds, to compensate for the rotational speed exceeding the rated speed, which can be seen in Figure 4.25.

Figure 4.25 shows that the torque τ_{NREL} and rotational speed ω_t still oscillates occasionally despite rather stable wind velocity. This oscillating behaviour was not apparent in test 4.St.A1a and 4.St.A1b where $\tau_{c,NREL}$ was set to 10 s, which means that the greater delay of the MPPT with $\tau_{c,NREL}$ set to 20 s could explain the oscillations. The results proposes that delaying the MPPT too much can create an unintended and oscillating behaviour of the entity.

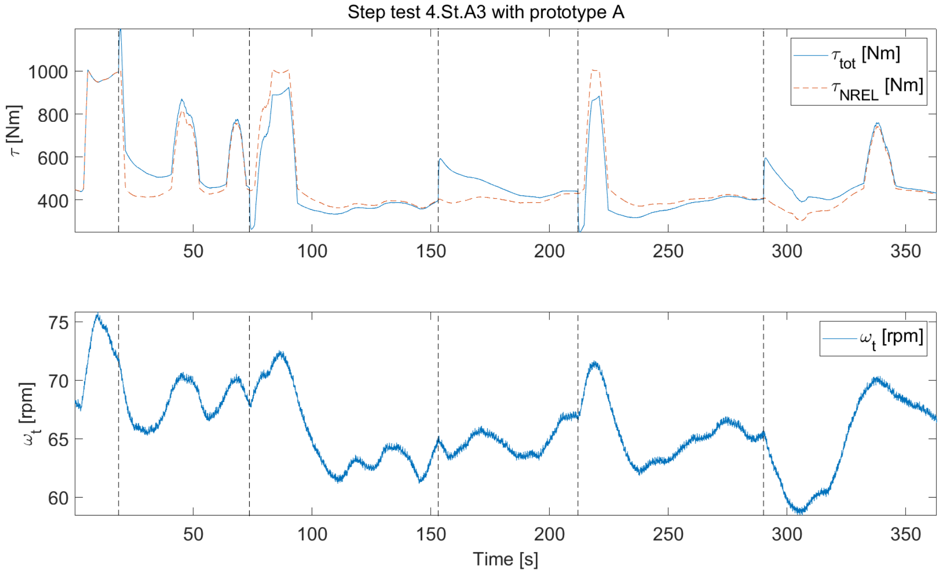

Figure 4.25: Step test 4.St.A3, $\tau_{c,HP} = 20$ s, $\tau_{c,NREL} = 20$ s. Practical test with $gain = 200$ Nm/Hz and curtailment factor of 0.25.

The results from step test 4.St.A4 show how the wind turbine behaves without the low-pass filter slowing down the MPPT in Figure 4.26. The power P_{el} increases and decreases according to the torque addition, but the endurance of the power responses is much shorter compared to tests 4.St.A1-4.St.A3.

The torque and rotational speed does not behave in an oscillating way without the low-pass filter slowing down the MPPT, see Figure 4.27. Notable is also that the rotational speed is significantly less affected by the added step signals, as it only changes around 1 rpm, compared to in test 4.St.A1a, see Figure 4.16, where it dropped around 15 rpm during power increase, and test 4.St.A3 in Figure 4.25, where it dropped around 5 rpm.

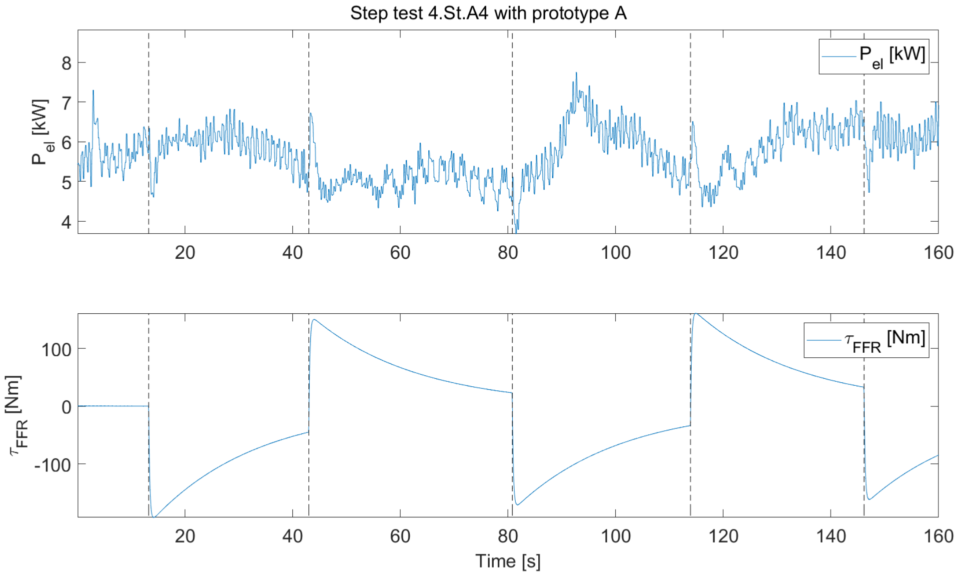

Figure 4.26: Step test 4.St.A4, $\tau_{c,HP} = 20$ s, $\tau_{c,NREL}$ not active. Practical test with *gain* = 200 Nm/Hz and curtailment factor of 0.25.

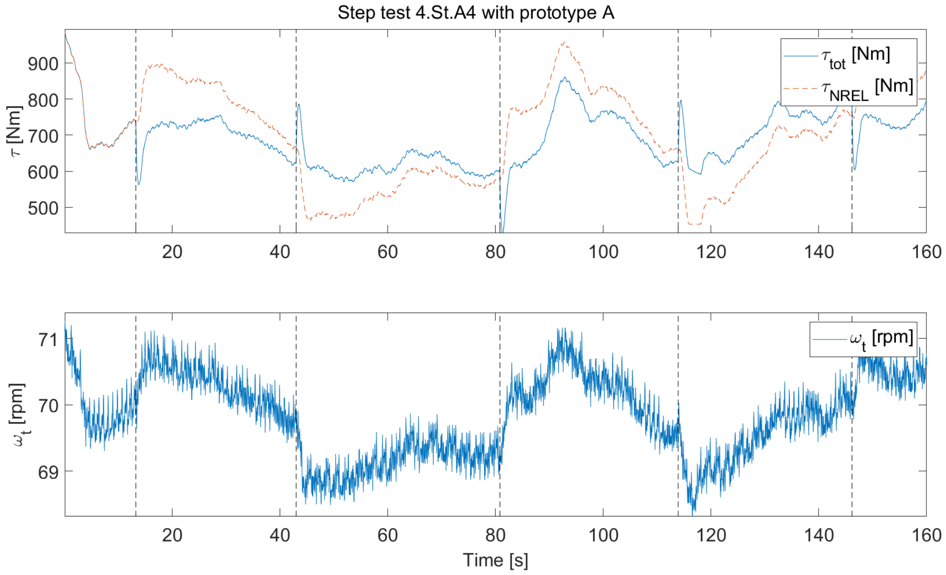

Figure 4.27: Step test 4.St.A4, $\tau_{c,HP} = 20$ s, $\tau_{c,NREL}$ not active. Practical test with *gain* = 200 Nm/Hz and curtailment factor of 0.25.

4.1.3 Large disturbance tests

Following results present practical disturbance tests that were carried out with prototype A, summarised with settings in Table 3.5. Figure 4.28-4.30 show results from these tests, 4.D.A1-4.D.A3, where the first test uses shorter and equal time constants, the second test uses longer and equal time constants, and the third test uses a longer time constant in the dynamic FFR high-pass filter. Figure 4.28 shows how the power output P_{el} behaves during test 4.D.A1, and it looks like P_{el} follows the torque addition τ_{FFR} relatively well, but peaks slightly earlier than τ_{FFR}.

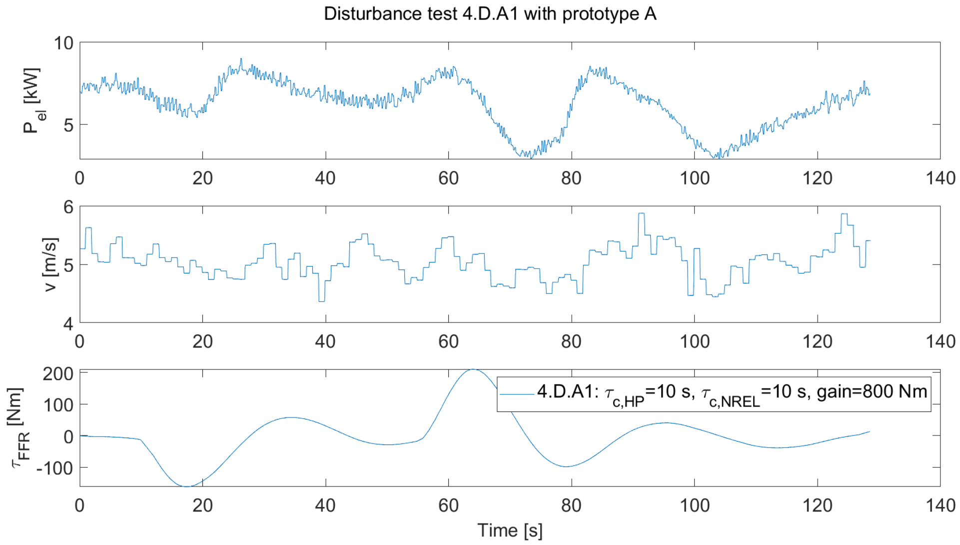

Figure 4.28: Disturbance test 4.D.A1. Practical test with $\tau_{c,HP} = 10$ s, $\tau_{c,NREL} = 10$ s, $gain = 800$ Nm/Hz and curtailment factor of 0.5.

Figure 4.29 shows results from test 4.D.A2, where both time constants are increased to 20 s. The power output P_{el} seems to follow τ_{FFR} better with these settings since the peaks for P_{el} and τ_{FFR} align better, compared to test 4.D.A1, shown in Figure 4.28. However, the shape of the overall response looked better in test 4.D.A1, which used smaller time constants for both filters. The decreasing wind velocity between 40 and 70 seconds could explain why P_{el} does not increase in power as intended around 65 seconds.

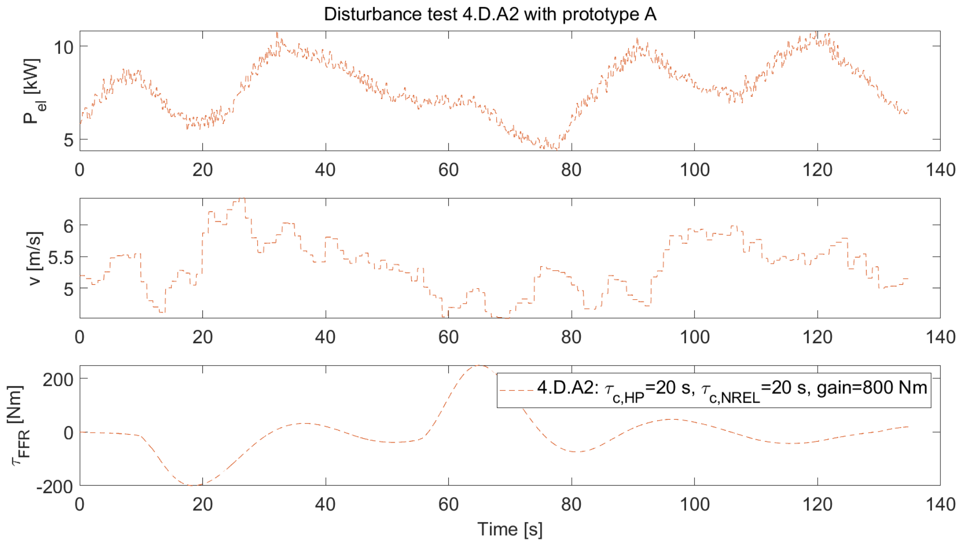

Figure 4.29: Disturbance test 4.D.A2. Practical test with $\tau_{c,HP} = 20$ s, $\tau_{c,NREL} = 20$ s, $gain = 800$ Nm/Hz and curtailment factor of 0.5.

The results from test 4.D.A3 are shown in Figure 4.30, where $\tau_{c,HP}$ is increased to 60 s. The power P_{el} seems to have greater difficulties following τ_{FFR} with these settings.

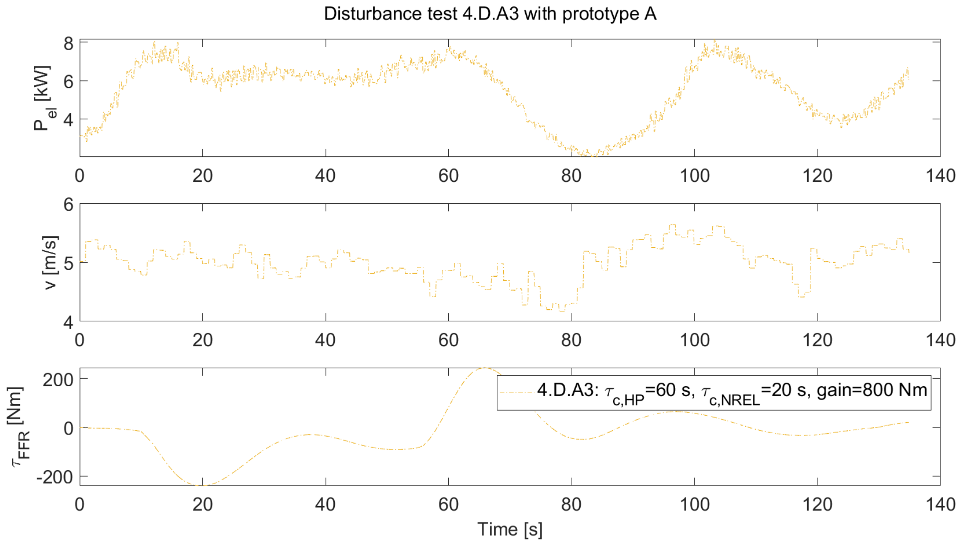

Figure 4.30: Disturbance test 4.D.A3. Practical test with $\tau_{c,HP} = 60$ s, $\tau_{c,NREL} = 20$ s, *gain* $= 800$ Nm/Hz and curtailment factor of 0.5.

Figure 4.31 shows how τ_{tot} behaves during tests 4.D.A1-4.D.A3, and it looks like τ_{tot} is least affected during test 4.D.A1, which is expected since it used the smallest $\tau_{c,NREL}$.

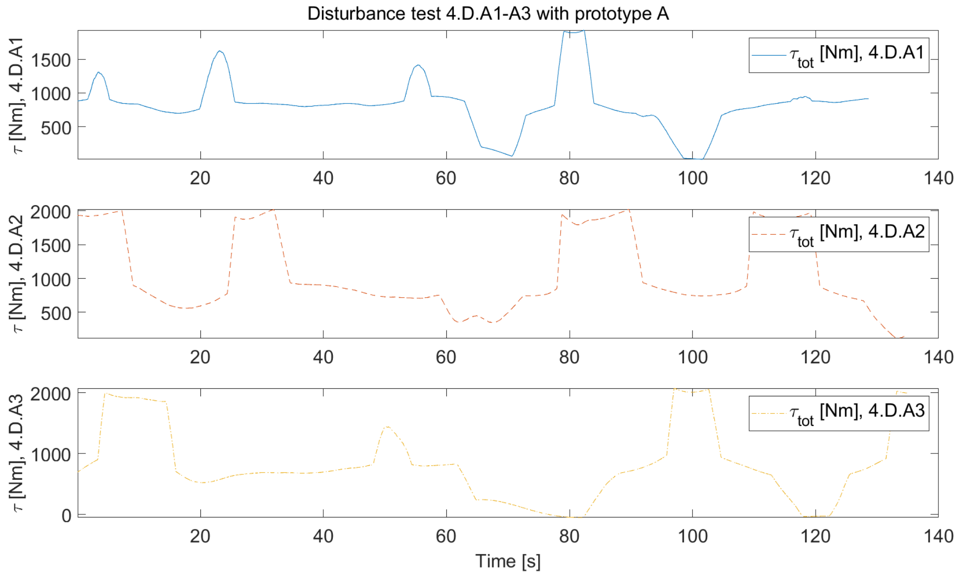

Figure 4.31: Disturbance tests 4.D.A1-4.D.A3. Practical tests with *gain* $= 800$ Nm/Hz and curtailment factor of 0.5.

The rotational speeds for tests 4.D.A1-4.D.A3 are presented in Figure 4.32. The rotational speeds for tests 4.D.A1 and 4.D.A2 look rather similar, taking into account that the wind velocity decreased between 40 and 60 seconds during test 4.D.A2, where ω_t was intended to recover speed.

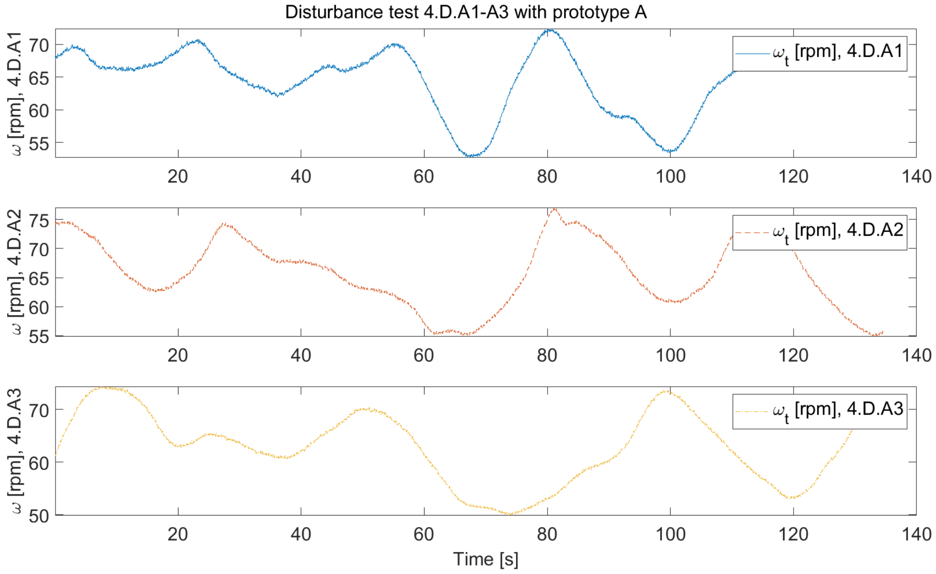

Figure 4.32: Disturbance tests 4.D.A1-4.D.A3. Practical tests with $gain = 800$ Nm/Hz and curtailment factor of 0.5.

4.1.4 Grid frequency tests

This section presents practical grid frequency tests that were done according to settings summarised in Table 3.4. Firstly, equal time constants of 20 s are used, followed by increasing the high-pass filter time constant while keeping the NREL filter time constant short.

The results from test 4.G.A1 are illustrated in Figure 4.33-4.35. Figure 4.33 shows that the electric power output P_{el} seems to approximately follow the pattern according to the added torque τ_{FFR} but lack in endurance.

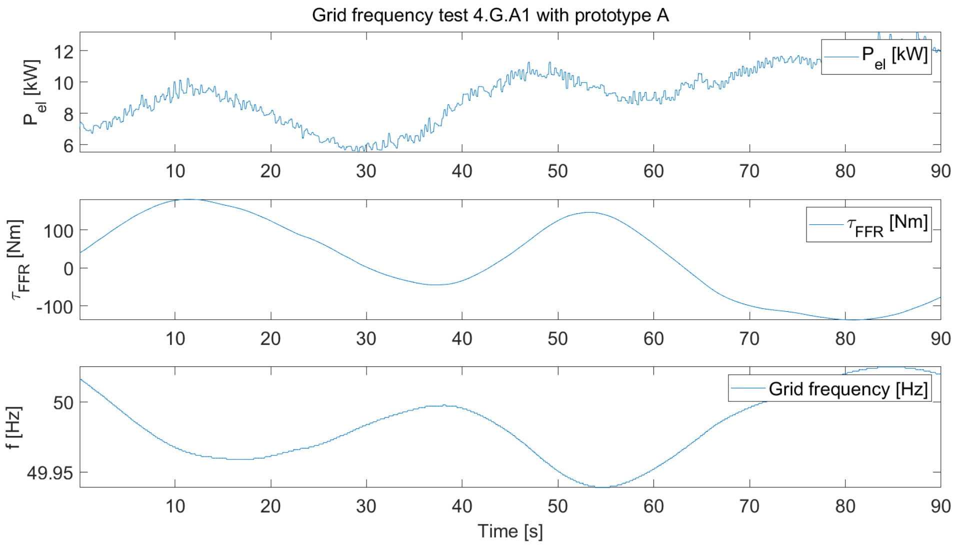

Figure 4.33: Grid frequency test 4.G.A1, $\tau_{c,HP} = 20$ s, $\tau_{c,NREL} = 20$ s. Practical test with $gain = 4000$ Nm/Hz and curtailment factor of 0.5.

Figure 4.34 shows that the wind velocity was rather stable during the test, apart from at the end, which contributes to that P_{el} increased at the end in Figure 4.33.

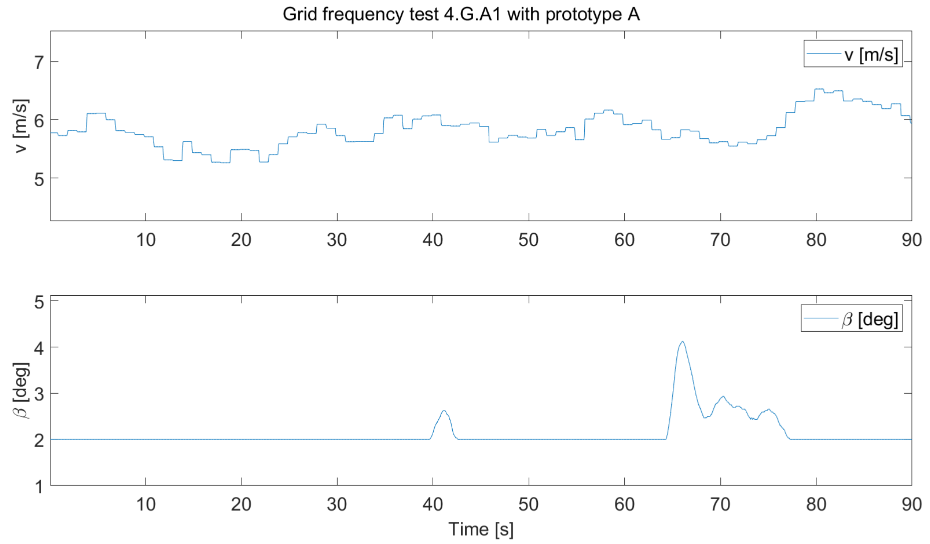

Figure 4.34: Grid frequency test 4.G.A1, $\tau_{c,HP} = 20$ s, $\tau_{c,NREL} = 20$ s. Practical test with $gain = 4000$ Nm/Hz and curtailment factor of 0.5.

The torque and rotational speed is shown in Figure 4.35. The rotational speed does not as distinctively decrease when P_{el} increases compared to during the step tests, which could be because the grid frequency input signal is much smoother than the step signal.

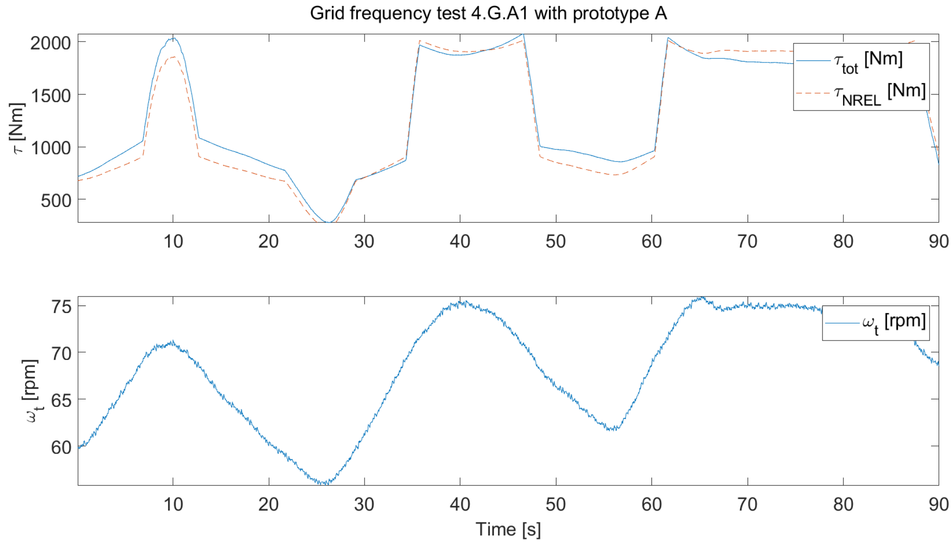

Figure 4.35: Grid frequency test 4.G.A1, $\tau_{c,HP} = 20$ s, $\tau_{c,NREL} = 20$ s. Practical test with $gain = 4000$ Nm/Hz and curtailment factor of 0.5.

Grid frequency test 4.G.A2 illustrated in Figure 4.36-4.38 shows a less desirable behaviour as P_{el} does not seem to resemble the shape of τ_{FFR} that well, which could be because the NREL controller is faster than the high-pass filter, due to its smaller time constant.

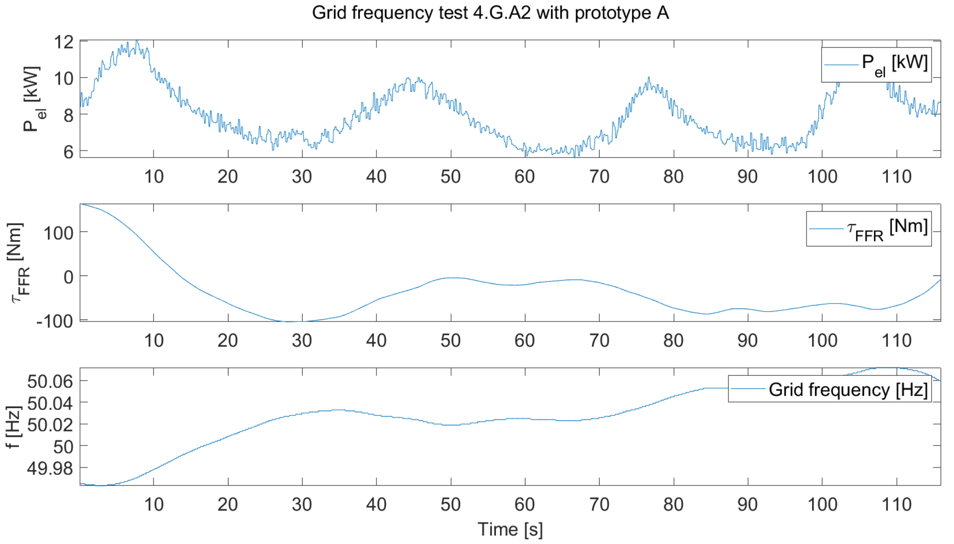

Figure 4.36: Grid frequency test 4.G.A2, $\tau_{c,HP} = 60$ s, $\tau_{c,NREL} = 10$ s. Practical test with $gain = 4000$ Nm/Hz and curtailment factor of 0.5.

Figure 4.37 shows the wind velocity and pitch angle during the test.

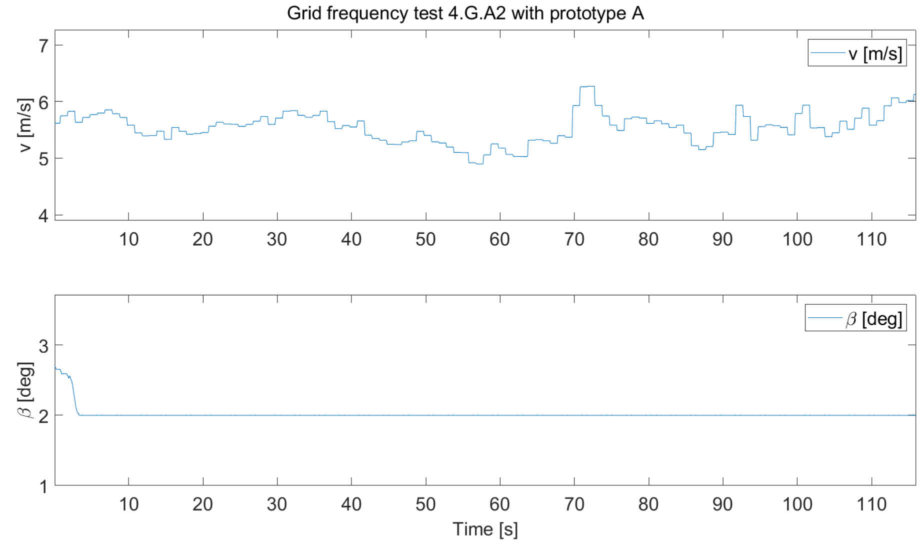

Figure 4.37: Grid frequency test 4.G.A2, $\tau_{c,HP} = 60$ s, $\tau_{c,NREL} = 10$ s. Practical test with $gain = 4000$ Nm/Hz and curtailment factor of 0.5.

The rotational speed in Figure 4.38 behaves more as expected during this test compared to test 4.G1, which could be explained by that $\tau_{c,NREL}$ was set to a smaller value.

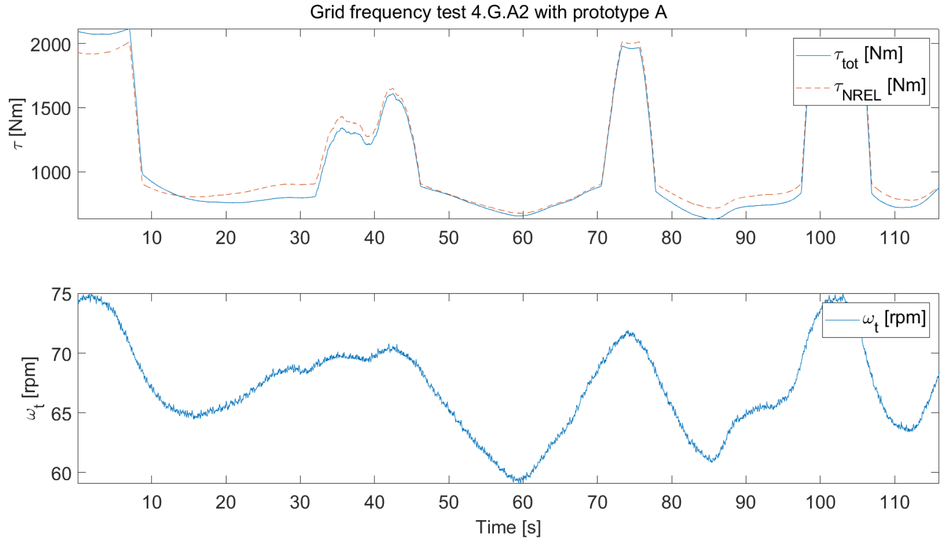

Figure 4.38: Grid frequency test 4.G.A2, $\tau_{c,HP} = 60$ s, $\tau_{c,NREL} = 10$ s. Practical test with $gain = 4000$ Nm/Hz and curtailment factor of 0.5.

4.1.5 Sine tests

Bode plots between the frequency input signal f and the electric power output P_{el} from four practical sine tests done according to settings presented in Table 3.2, will be presented in this section. The sine tests investigate the effects of the different filters by varying having the dynamic FFR high-pass filter and NREL filter activated or de-activated.

The Bode plot from sine test 4.Si.A1, with both band-pass filter and low-pass filter slowing down NREL activated, is shown in Figure 4.39. Plots showing the input signals and output signals that were used constructing the points in the Bode plot, together with corresponding fitted sines are found in Appendix A.2.1. The sine shape is clearly present in P_{el} until the lowest frequency, $f_{10} = 0.01$ Hz, where it starts deforming. Therefore, the Bode plot should be valid in the frequency range f_1-f_9. It appears from the Bode plot in Figure 4.39 that lower and higher frequencies are attenuated as intended by the band-pass filter. The Bode plot indicates that the POD-P requirements described in section 2.3.5 are almost fulfilled, as the phase angle is -100° at $f_1 = 1$ Hz, were it should not be below -90°.

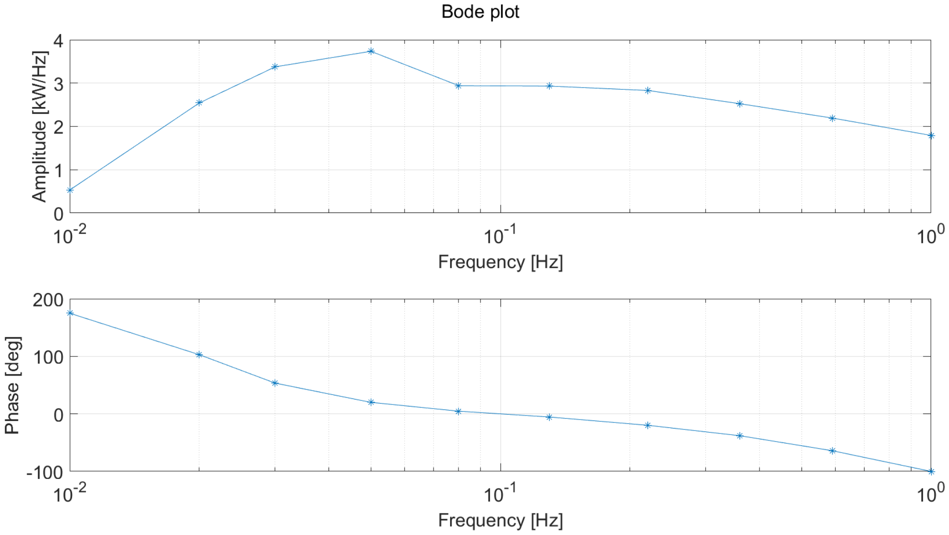

Figure 4.39: Sine test 4.Si.A1, $\tau_{c,HP} = 20$ s, $\tau_{c,NREL} = 20$ s. Practical test with $gain = 400$ Nm/Hz and curtailment factor of 0.5.

Figure 4.40 shows the Bode plot from sine test 4.Si.A2, with de-activated band-pass filter yet still activated low-pass filter slowing down NREL. Plots showing the signals used to construct the Bode plot together with fitted sines are found in Appendix A.2.2, and the sine shape is clear until the last point $f_{10} = 0.01$ Hz, like in sine test 4.Si.A1. By comparing the Bode plots from test 4.Si.A1 and 4.Si.A2, it appears that the frequencies that were attenuated in Figure 4.39 have greater amplitude in Figure 4.40, which is reasonable. This can be seen by comparing for example points $f_1 = 1$ Hz and $f_9 = 0.02$ Hz in Figures 4.39 and 4.40. The phase shift is also smaller in Figure 4.40 compared to Figure 4.39, which is expected without the band-pass filter.

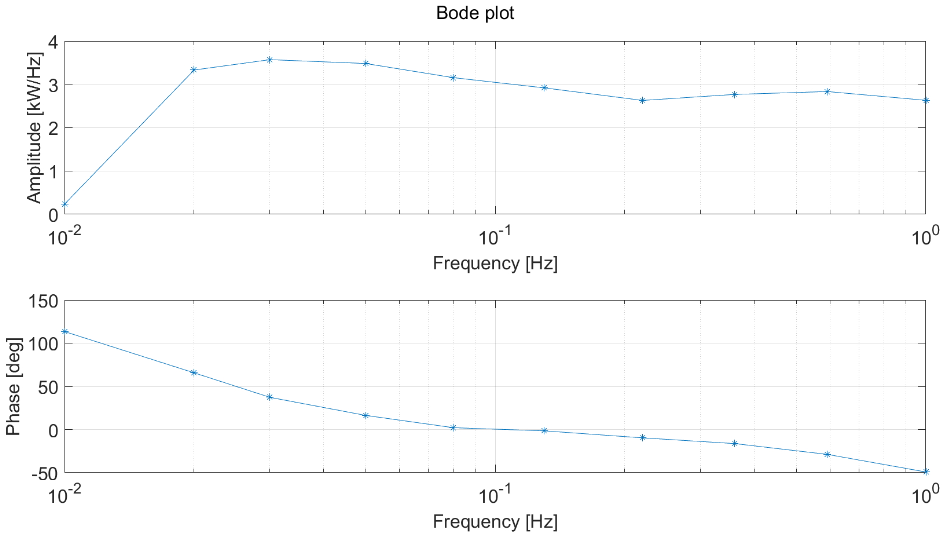

Figure 4.40: Sine test 4.Si.A2, $\tau_{c,HP}$ not active, $\tau_{c,NREL}$ = 20 s. Practical test with *gain* = 400 Nm/Hz and curtailment factor of 0.5.

The Bode plots from sine test 4.Si.A3 and 4.Si.A4 are illustrated together in Figure 4.41.

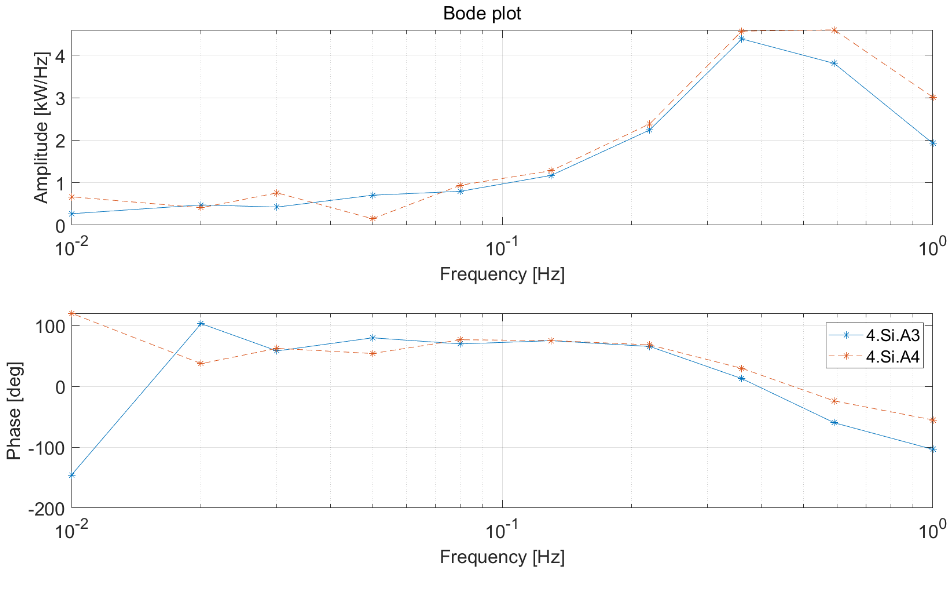

Figure 4.41: Sine tests 4.Si.A3, $\tau_{c,HP}$ = 20 s, $\tau_{c,NREL}$ not active, and 4.Si.A4, $\tau_{c,HP}$ not active, $\tau_{c,NREL}$ not active. Practical tests with *gain* = 400 Nm/Hz and curtailment factor of 0.5.

Sine test 4.Si.A3 had the band-pass filter activated, but not the low-pass filter slowing down the MPPT, while test 4.Si.A4 had none of the filters activated. Plots of the signals used to construct the Bode plots together with corresponding fitted sines are found in Appendix A.2.3 for test 4.Si.A3, and in Appendix A.2.4 for 4.Si.A4. The sine shape in the power output P_{el} becomes quite deformed already at f_5 =

0.13 Hz for both sine tests. Both sine tests in Figure 4.41 indicate that the MPPT suppresses frequencies lower than $f_3 = 0.36$ Hz. The sine test 4.Si.A3 shows a more attenuated $f_1 = 1$ Hz in contrast to test 4.Si.A4, which is reasonable. Overall, the sine tests with prototype A show that it is evident that the low-pass filter slowing down MPPT has a large effect on the behaviour of the wind turbine.

4.2 Prototype B: estimate rotational speed to MPPT

Results from simulated and practical step tests, and simulated disturbance and grid frequency tests with prototype B are presented and discussed in this section.

4.2.1 Simulated step tests

Simulated step tests with prototype B are presented in this section, with settings summarised in Table 3.8. Firstly, short and equal time constants are used, followed by increasing the time constants $\tau_{c,HP}$ and $\tau_{c,NEM}$ each at a time, while keeping the other time constant short. Finally, both time constants are increased. Figure 4.42 shows results from step test St.B1. The power initially increases and decreases as desired. Plots showing the wind velocity and pitch angle behaviour are found in Appendix A.3.1.

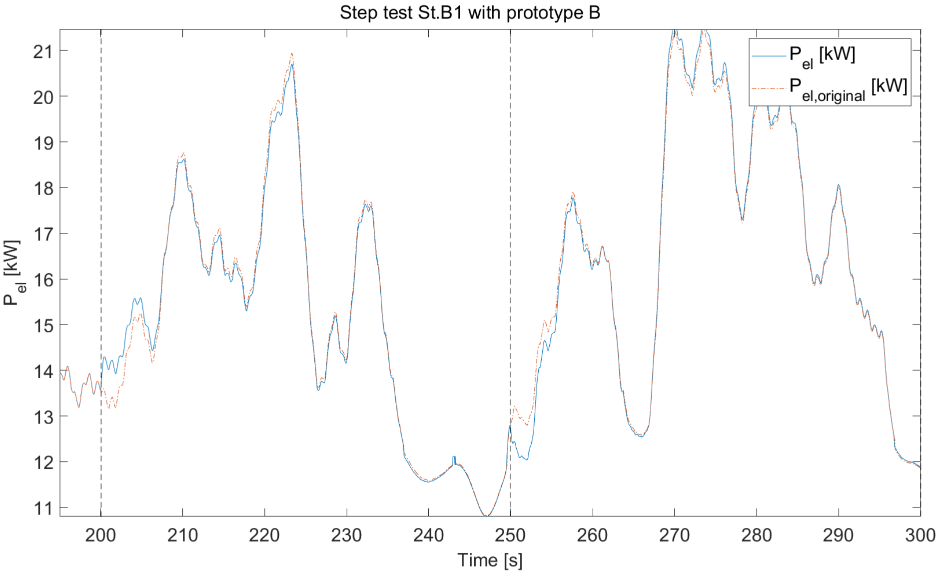

Figure 4.42: Step test St.B1, $\tau_{c,HP} = 10$ s, $\tau_{c,NEM} = 10$ s. Simulation with varying wind velocity and $gain = 1000$ W/Hz.

A close-up of the power output is shown in Figure 4.43 to see when P_{el} becomes less than $P_{el,original}$ after the forced power increase. For test St.B1 the endurance is about 8 seconds.

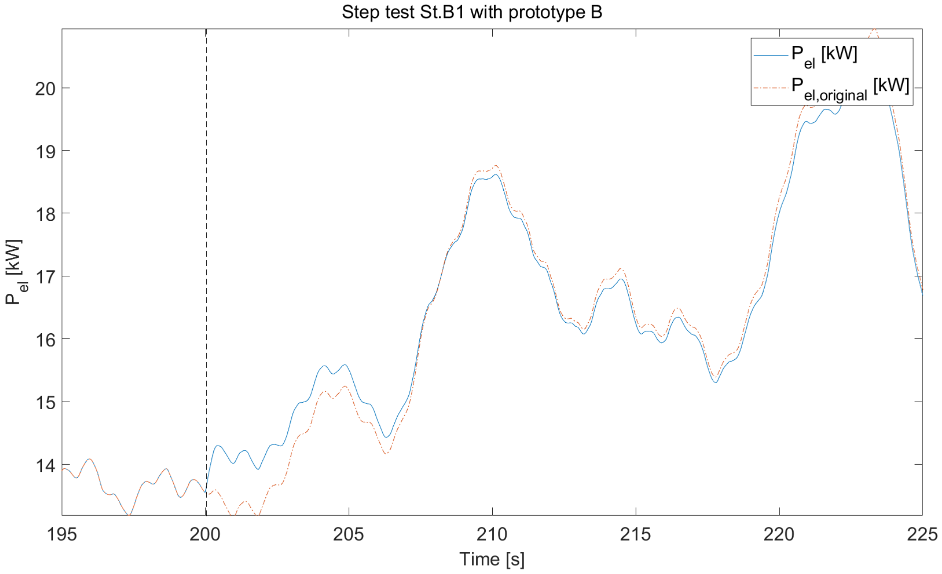

Figure 4.43: Step test St.B1, $\tau_{c,HP} = 10$ s, $\tau_{c,NEM} = 10$ s. Simulation with varying wind velocity and $gain = 1000$ W/Hz.

Figure 4.44 shows the behaviour of the torque and the rotational speed. The torque behaves as desired, and in contrast to the simulated step tests with prototype A, the oscillating behaviour of the torque is not present, probably because the MPPT is not delayed in prototype B.

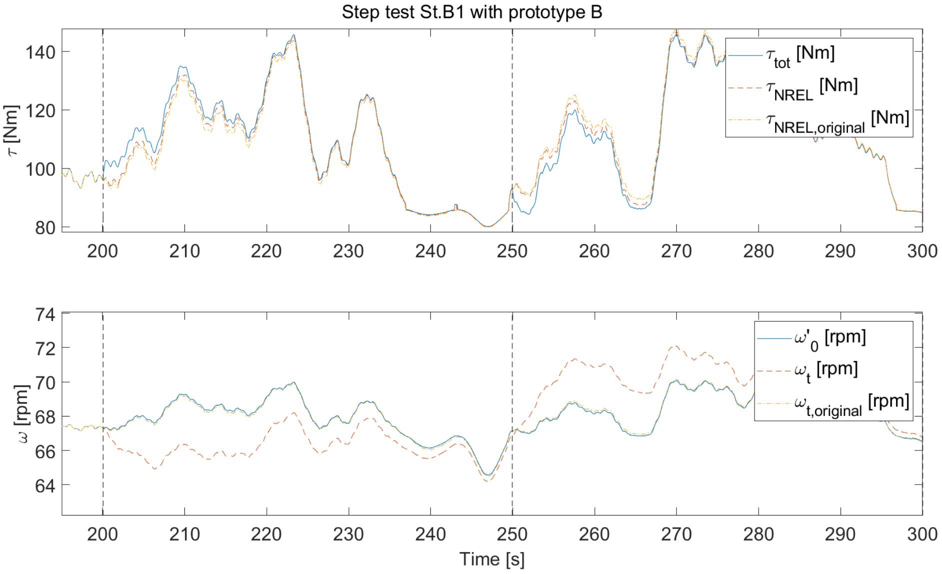

Figure 4.44: Step test St.B1, $\tau_{c,HP} = 10$ s, $\tau_{c,NEM} = 10$ s. Simulation with varying wind velocity and $gain = 1000$ W/Hz.

A simulation with constant wind velocity was also carried out, where the power output is shown in Figure 4.45, and torque and rotational speed behaviour in Figure 4.46. Both figures show that it is obvious that prototype B is does not have the oscillating behaviour that was seen in test St.A1 with prototype A, see Figure 4.2 and 4.6 for comparison. Figure 4.46 also shows how τ_{NREL} contributes to the desired behaviour of τ_{tot}, which was not intended with the design of prototype B, and it is not certain why the torque τ_{NREL} shows this behaviour.

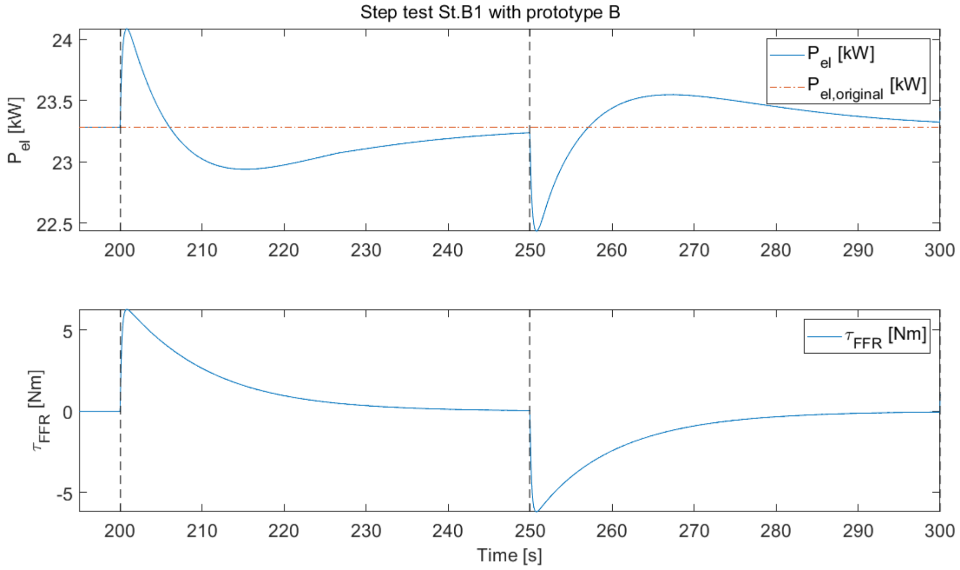

Figure 4.45: Step test St.B1, $\tau_{c,HP} = 10$ s, $\tau_{c,NEM} = 10$ s. Simulation with constant wind velocity and *gain* = 1000 W/Hz.

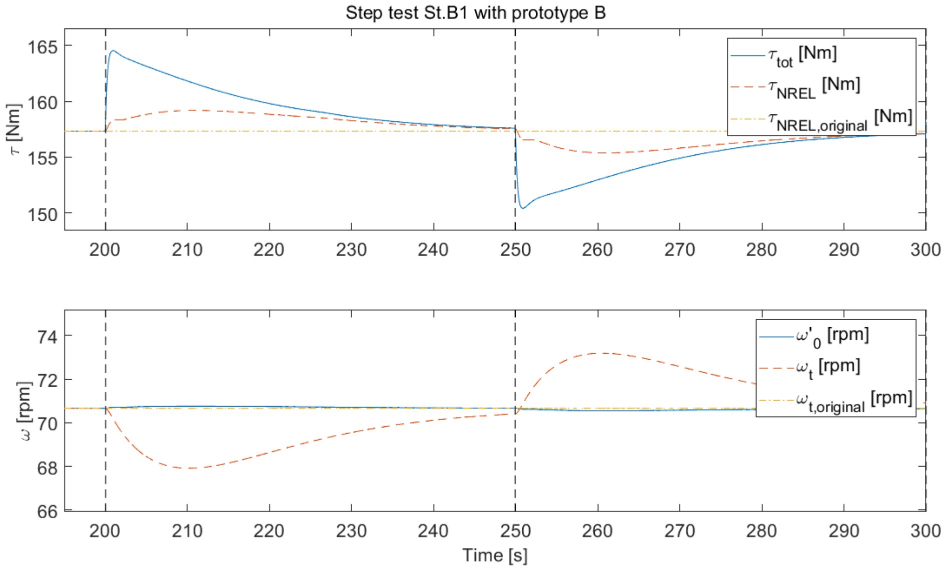

Figure 4.46: Step test St.B1, $\tau_{c,HP} = 10$ s, $\tau_{c,NEM} = 10$ s. Simulation with constant wind velocity and *gain* = 1000 W/Hz.

Figure 4.47 shows a close-up of test St.B2, and Figure 4.48 shows test St.B3. The results from these tests indicate that there is no big difference in the behaviour of

P_{el} despite setting different time constants in the NEM and dynamic FFR filters. Plots showing a greater time span of P_{el}, as well as the behaviour of the torque, rotational speeds, wind velocity and pitch angle are found in Appendix A.3.2 for St.B2, and in Appendix A.3.3 for St.B3. The torque τ_{tot} shows greater endurance during test St.B2 compared to St.B3.

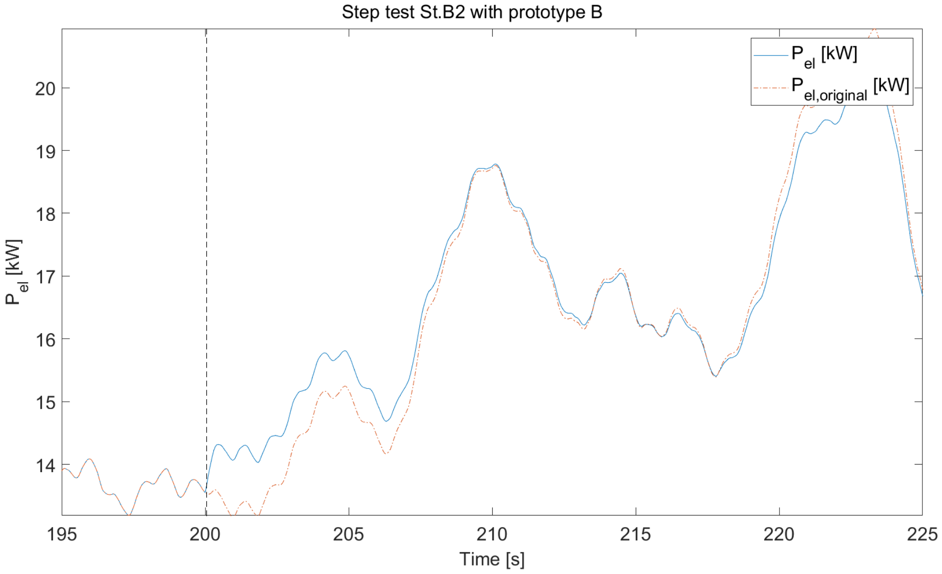

Figure 4.47: Step test St.B2, $\tau_{c,HP} = 60$ s, $\tau_{c,NEM} = 10$ s. Simulation with varying wind velocity and $gain = 1000$ W/Hz.

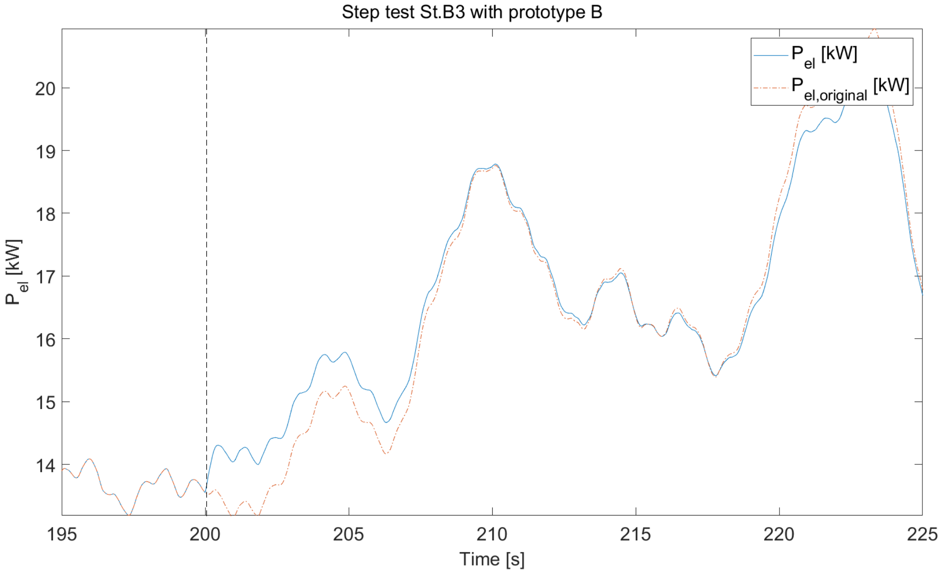

Figure 4.48: Step test St.B3, $\tau_{c,HP} = 10$ s, $\tau_{c,NEM} = 60$ s. Simulation with varying wind velocity and $gain = 1000$ W/Hz.

Figure 4.49 shows test St.B4, and compared to Figure 4.47 and 4.48, the result indicates that the smaller time constant seems to limit the effect of the greater time constant. Furthermore, the endurance of P_{el} increased to about 16 seconds, compared to 8 seconds in test St.B1. The behaviour of the wind velocity and pitch angle are found in Appendix A.3.4.

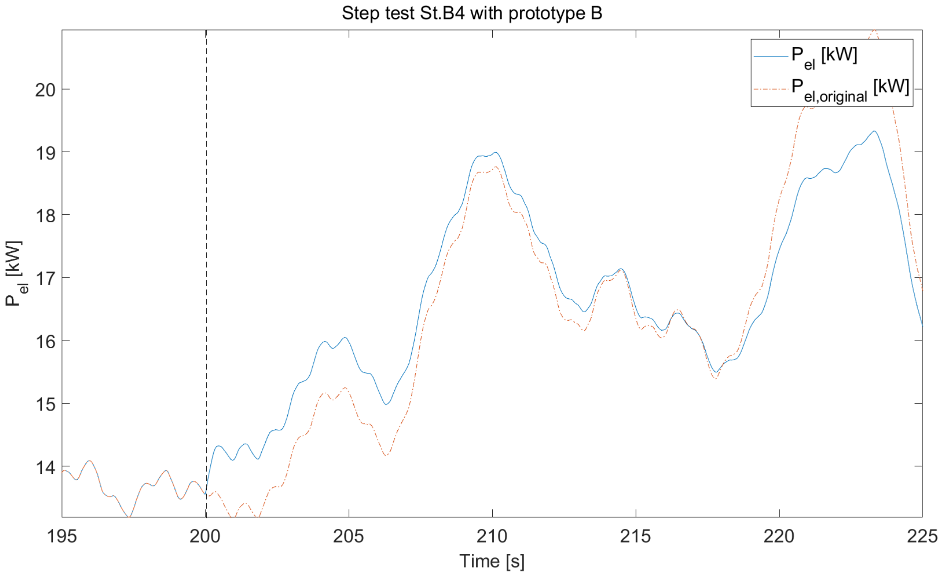

Figure 4.49: Step test St.B4, $\tau_{c,HP} = 60$ s, $\tau_{c,NEM} = 60$ s. Simulation with varying wind velocity and *gain* = 1000 W/Hz.

How two steps in opposite direction affect P_{el} is shown in Figure 4.50. The endurance looks better during power decrease, but worse during power increase, as seen in Figure 4.42. This could be, like in the case of prototype A, because the forced change in torque decreases the efficiency as optimal operation is not achieved.

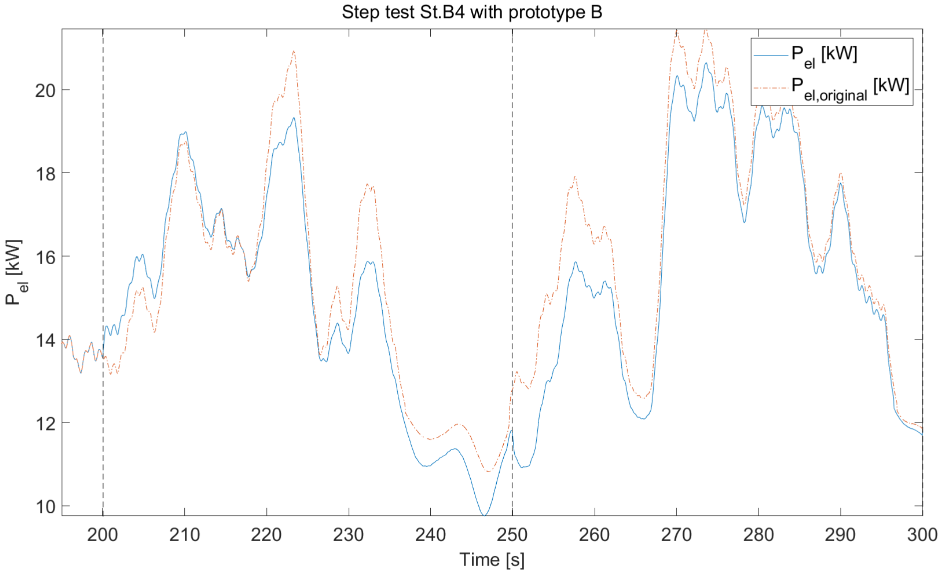

Figure 4.50: Step test St.B4, $\tau_{c,HP} = 60$ s, $\tau_{c,NEM} = 60$ s. Simulation with varying wind velocity and *gain* = 1000 W/Hz.

The torque and rotational speed are illustrated in Figure 4.51. Compared to test St.B1, the magnitude of the torque seems more amplified, and the estimation of ω'_0 seems worse, with greater time constants.

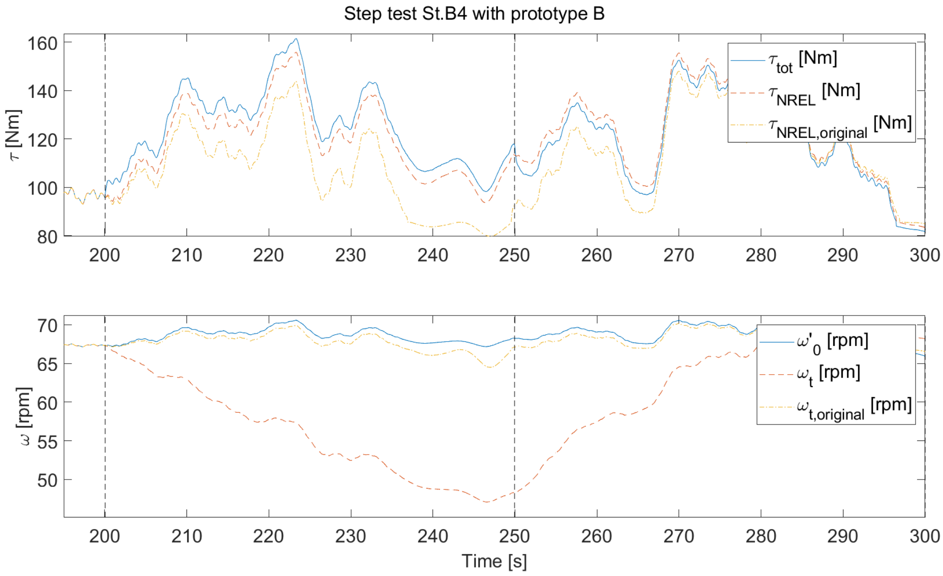

Figure 4.51: Step test St.B4, $\tau_{c,HP} = 60$ s, $\tau_{c,NEM} = 60$ s. Simulation with varying wind velocity and *gain* = 1000 W/Hz.

Figure 4.52-4.53 show test St.B4 but with constant wind velocity.

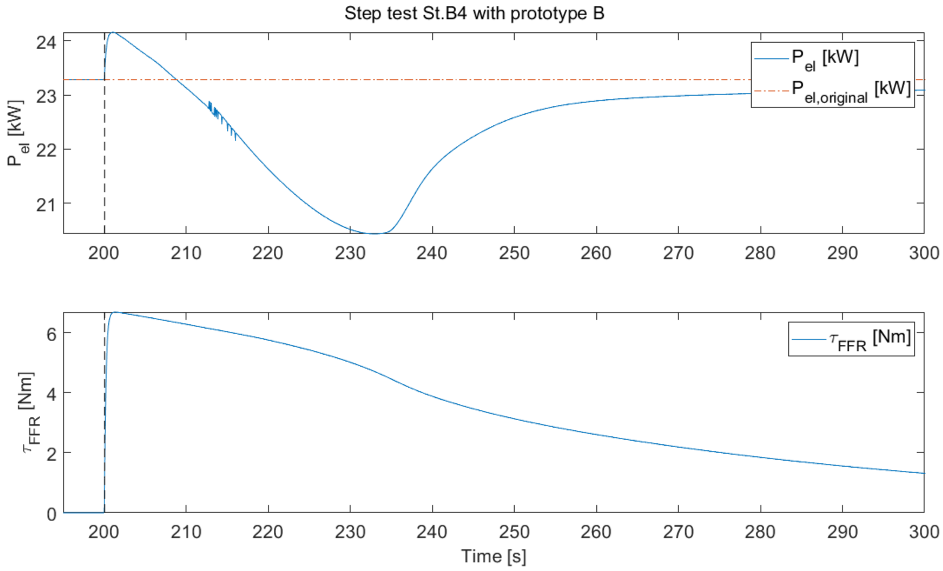

Figure 4.52: Step test St.B4, $\tau_{c,HP} = 60$ s, $\tau_{c,NEM} = 60$ s. Simulation with constant wind velocity and *gain* = 1000 W/Hz.

It is possible to see a dramatic decrease in P_{el} after the initial power increase in Figure 4.52, possible due to decreased efficiency, compared to St.B1 shown in Figure 4.45. The greater time constants seem to be the cause for this behaviour, and affect the estimation of ω'_0 negatively compared with test St.B1.

The torque and rotational speed in Figure 4.53 do not behave as anticipated, and do not resemble the behaviour seen in previous tests. This indicates that the larger time constants might be the cause for the different behaviour.

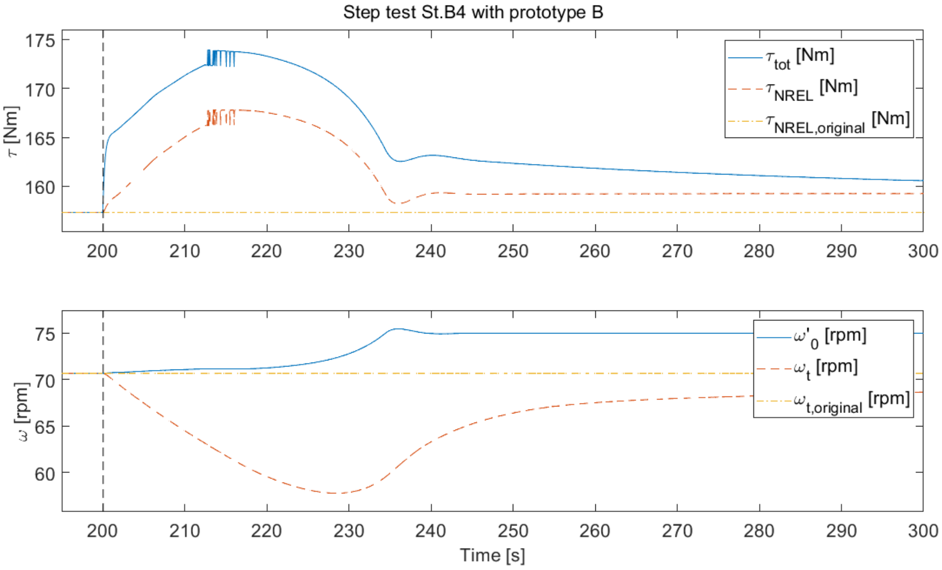

Figure 4.53: Step test St.B4, $\tau_{c,HP} = 60$ s, $\tau_{c,NEM} = 60$ s. Simulation with constant wind velocity and *gain* = 1000 W/Hz.

4.2.2 Step tests

This section presents practical step tests with prototype B, with settings summarised in Table 3.7. Shorter time constants are first explored, and then varying using one longer time constant in the different filters, and then setting them both to longer time constants. Lastly, equal time constants of 20 s are used. Figure 4.54 shows test 5.St.B1, showing initial power increase and decrease as intended.

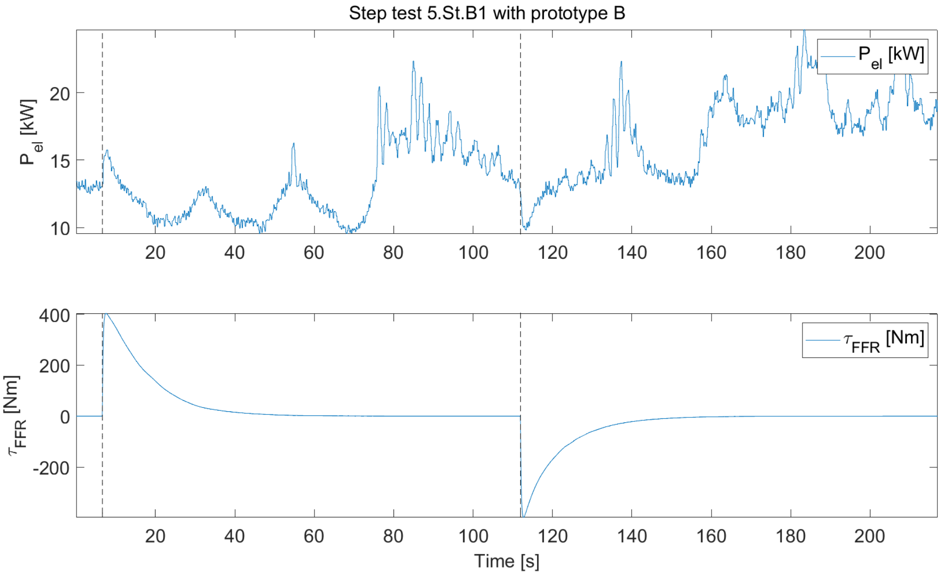

Figure 4.54: Step test 5.St.B1, $\tau_{c,HP} = 10$ s, $\tau_{c,NEM} = 10$ s. Practical test with $gain = 3000$ W/Hz.

Figure 4.55 shows the pitch and wind behaviour during test 5.St.B1. Compared to the smooth wind conditions during test 4.St.A1a, see Figure 4.15, the wind varied more. Furthermore, the wind pattern is recognisable in P_{el} in Figure 4.54.

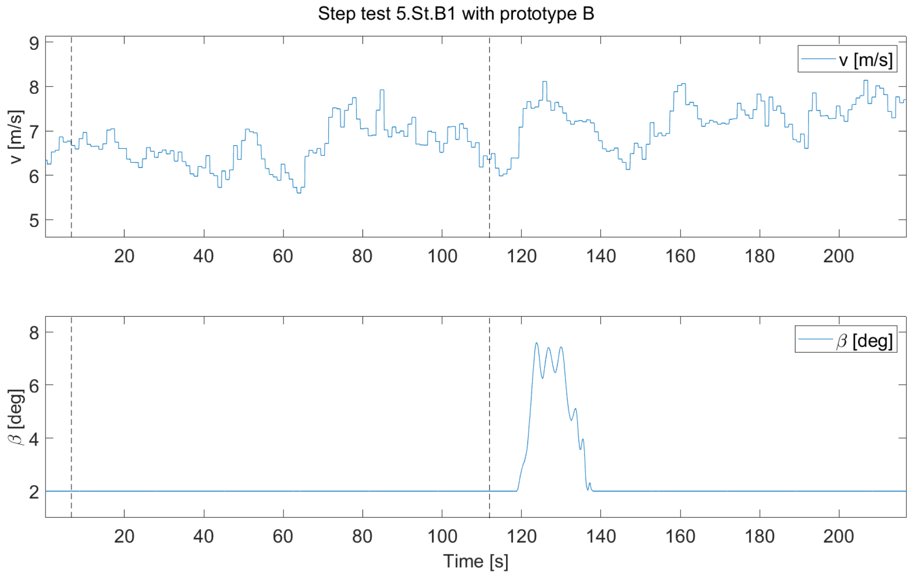

Figure 4.55: Step test 5.St.B1, $\tau_{c,HP} = 10$ s, $\tau_{c,NEM} = 10$ s. Practical test with $gain = 3000$ W/Hz.

Figure 4.56 shows the torque and rotational speed during test 5.St.B1. The torque increases and decreases as intended. The estimated speed ω'_0 seems rather unaffected as intended, and the real rotational speed changes as intended. The real rotational speed reaches very low speeds, indicating that it is not possible to increase the gain.

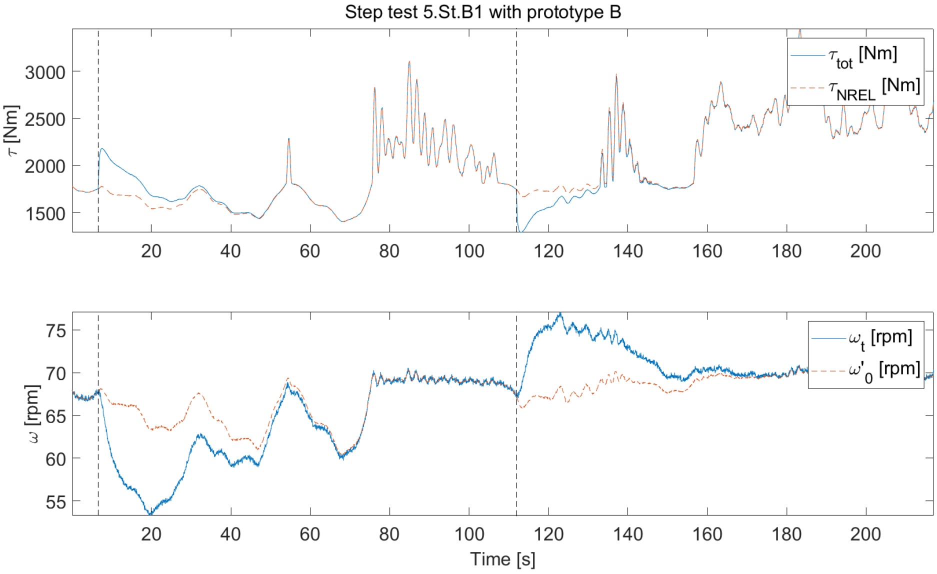

Figure 4.56: Step test 5.St.B1, $\tau_{c,HP} = 10$ s, $\tau_{c,NEM} = 10$ s. Practical test with *gain* = 3000 W/Hz.

The power output from test 5.St.B2, where $\tau_{c,HP}$ was increased to 60 s, is shown in Figure 4.57. Behaviours of wind velocity and pitch are found in Appendix A.3.5. The intended power changes are not that visible in P_{el}, which could be because the gain had to be decreased due to the wind conditions at testing.

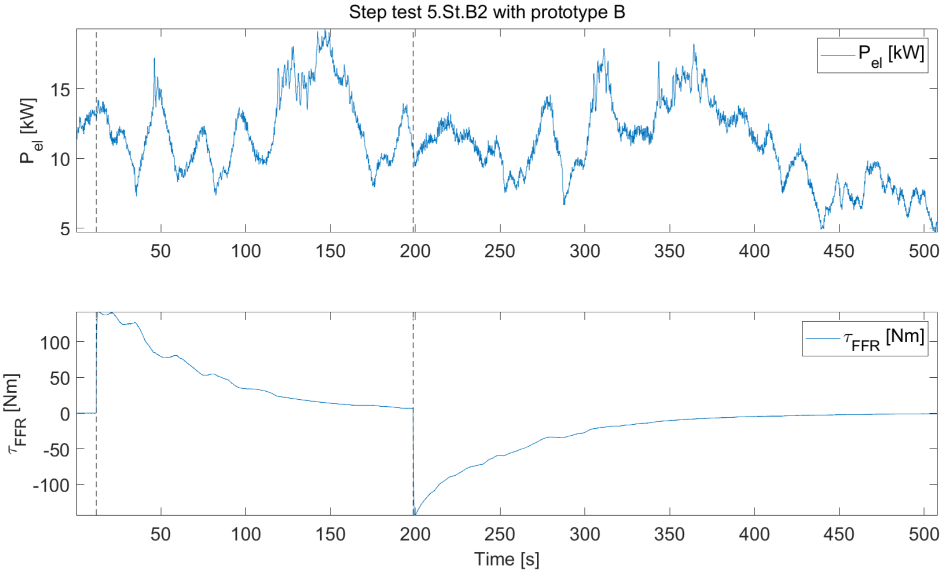

Figure 4.57: Step test 5.St.B2, $\tau_{c,HP} = 60$ s, $\tau_{c,NEM} = 10$ s. Practical test with *gain* = 1000 W/Hz.

Figure 4.58 shows P_{el} from test 5.St.B3, where instead $\tau_{c,NEM}$ was increased to 60 s, while $\tau_{c,HP}$ was kept at 10 s. The power increase of P_{el} is there, but not apparent, like in the previous test. How wind velocity and pitch behaves during test 5.St.B3 is found in Appendix A.3.6.

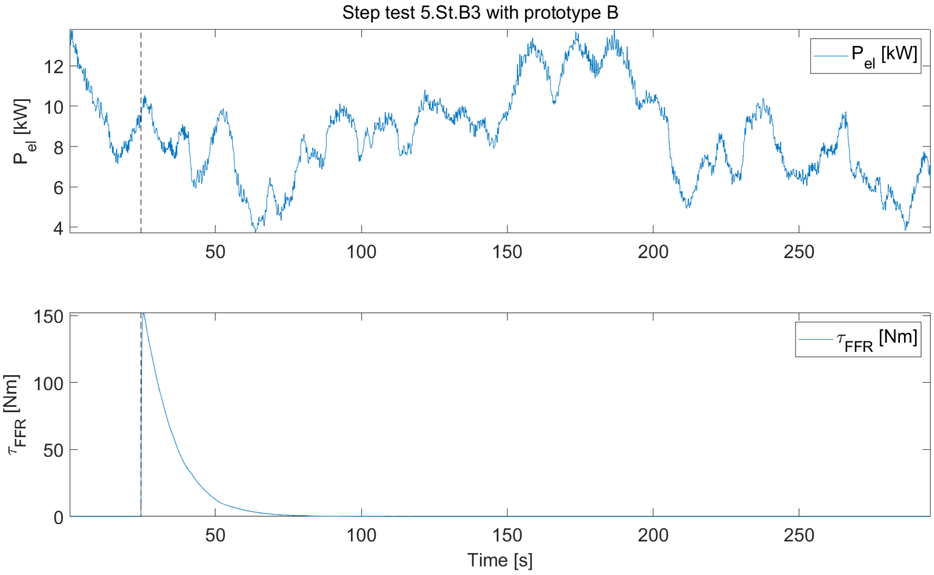

Figure 4.58: Step test 5.St.B3, $\tau_{c,HP}$ = 10 s, $\tau_{c,NEM}$ = 60 s. Practical test with *gain* = 1000 W/Hz.

Figure 4.59 and Figure 4.60 show how the torque and rotational speeds behaves during test 5.St.B2 and 5.St.B3.

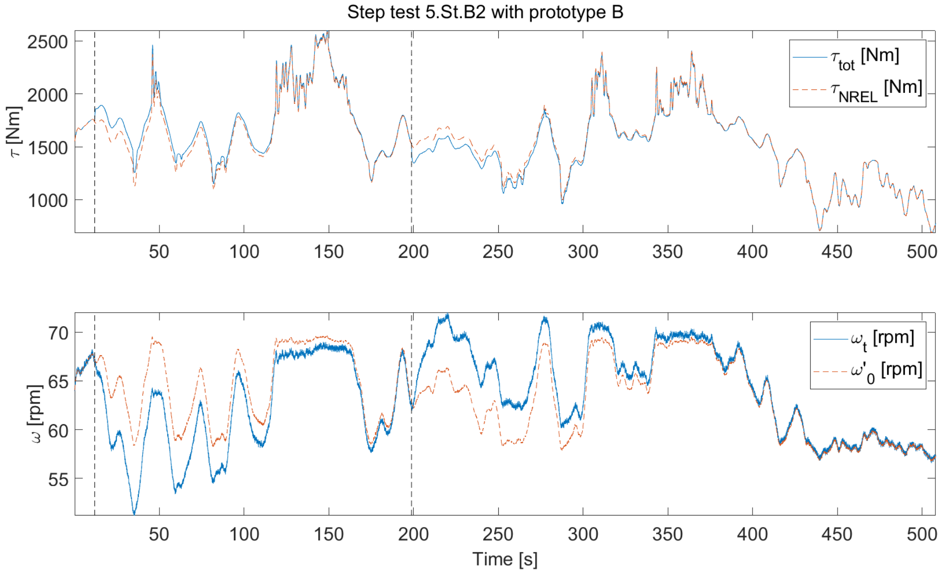

Figure 4.59: Step test 5.St.B2, $\tau_{c,HP}$ = 60 s, $\tau_{c,NEM}$ = 10 s. Practical test with *gain* = 1000 W/Hz.

It is possible to see a greater endurance of τ_{tot} during test 5.St.B2 compared to 5.St.B3, while the difference between estimated and real rotational speed seems greater for test 5.St.B3 compared to 5.St.B2. The endurance of the estimated speed also looks slightly longer for 5.St.B3.

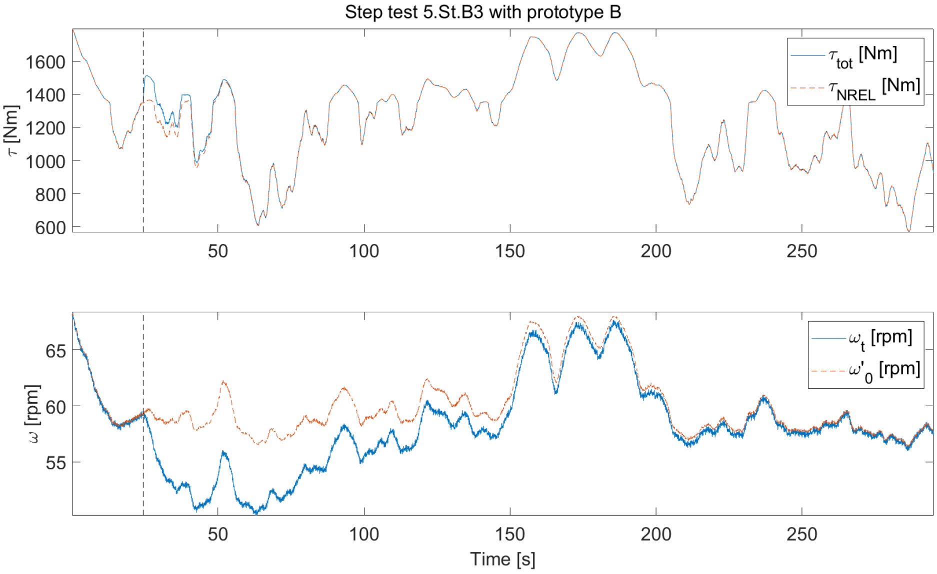

Figure 4.60: Step test 5.St.B3, $\tau_{c,HP}$ = 10 s, $\tau_{c,NEM}$ = 60 s. Practical test with *gain* = 1000 W/Hz.

Test 5.St.B4, were both time constants are increased to 60 s, is shown in Figure 4.61.

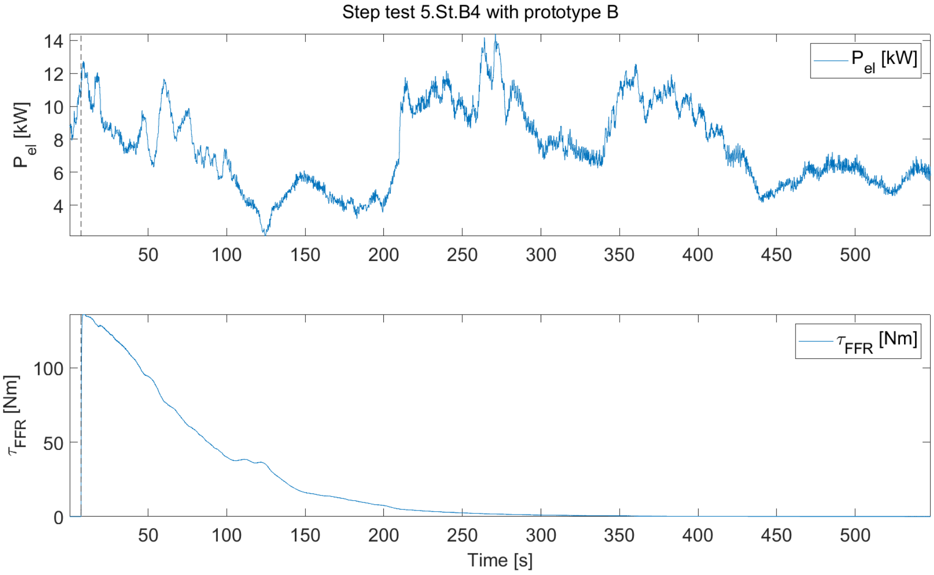

Figure 4.61: Step test 5.St.B4, $\tau_{c,HP}$ = 60 s, $\tau_{c,NEM}$ = 60 s. Practical test with *gain* = 1000 W/Hz. A curtailment factor of 0.5 was used.

The output power initially increases with the addition of τ_{FFR} in Figure 4.61, and then show a decreasing behaviour until 200 seconds. The wind velocity does also decrease from 6 m/s to 5 m/s between 0 and 200 seconds, see Appendix A.3.7. Simulation St.B4 with the same settings and constant wind velocity showed a dramatic efficiency decrease, see Figure 4.52, indicating that a decrease in efficiency could explain most of the appearance of P_{el} in Figure 4.61.

On the other hand, it is possible to see in Figure 4.62 that the rotational speed seems to decrease for about 50 seconds, from 70 rpm to 50 rpm, which show both much greater endurance and speed decrease than previous practical step tests with prototype B. It also shows that a smaller time constant limits a greater one, since the torque and rotational speed show a more altered behaviour here compared to in tests 5.St.B2 and 5.St.B3.

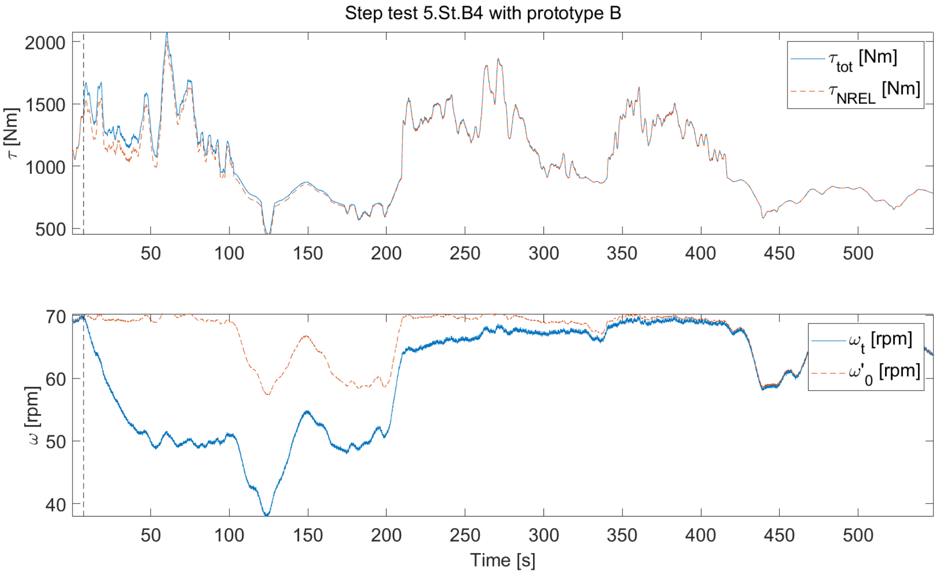

Figure 4.62: Step test 5.St.B4, $\tau_{c,HP} = 60$ s, $\tau_{c,NEM} = 60$ s. Practical test with $gain = 1000$ W/Hz. A curtailment factor of 0.5 was used.

The output power from test 5.St.B5 is shown in Figure 4.63, and how the torque, rotational speed, wind and pitch acts during the test is shown in Appendix A.3.8. The power increase is more distinct compared to tests 5.St.B2-4.

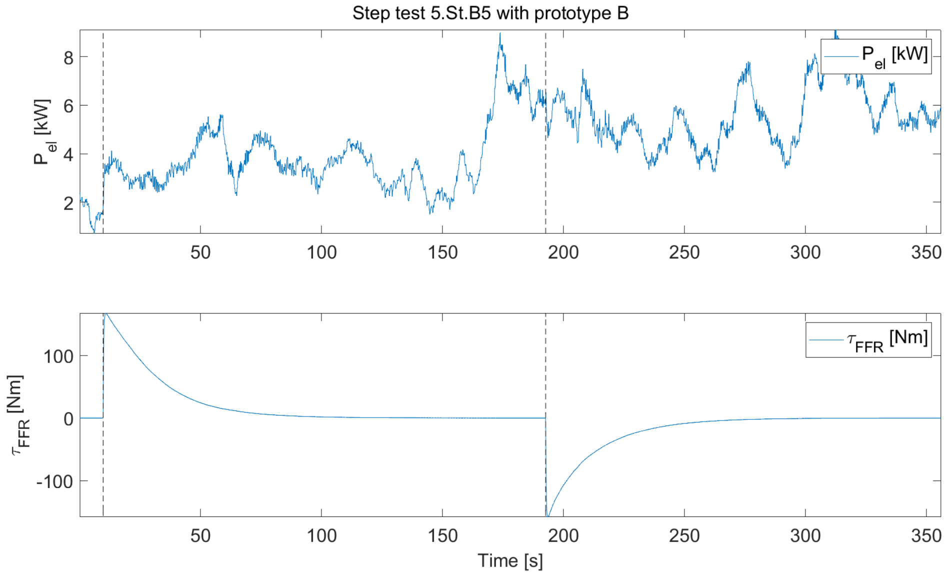

Figure 4.63: Step test 5.St.B5, $\tau_{c,HP} = 20$ s, $\tau_{c,NEM} = 20$ s. Practical test with $gain = 1000$ W/Hz.

4.2.3 Simulated large disturbance tests

This section presents simulated disturbance tests, with settings summarised in Table 3.9. First, equal time constants of 10 s followed by 20 s are used, followed by increasing one of the time constants, while keeping the other time constant shorter. Finally, both time constants are increased. Figure 4.64 shows disturbance test D.B1. The power P_{el} seems to follow τ_{FFR} rather well.

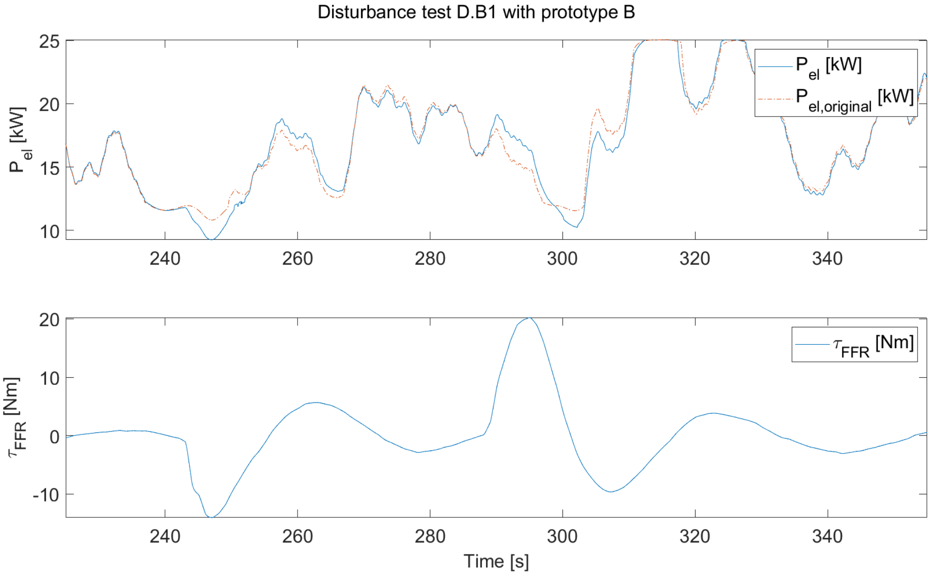

Figure 4.64: Disturbance test D.B1, $\tau_{c,HP} = 10$ s, $\tau_{c,NEM} = 10$ s. Simulation with varying wind velocity and $gain = 6000$ W/Hz.

The behaviour of the torque and rotational speed for test D.B1 is shown in Figure 4.65. The estimated rotational speed ω'_0 is very similar to $\omega_{t,original}$.

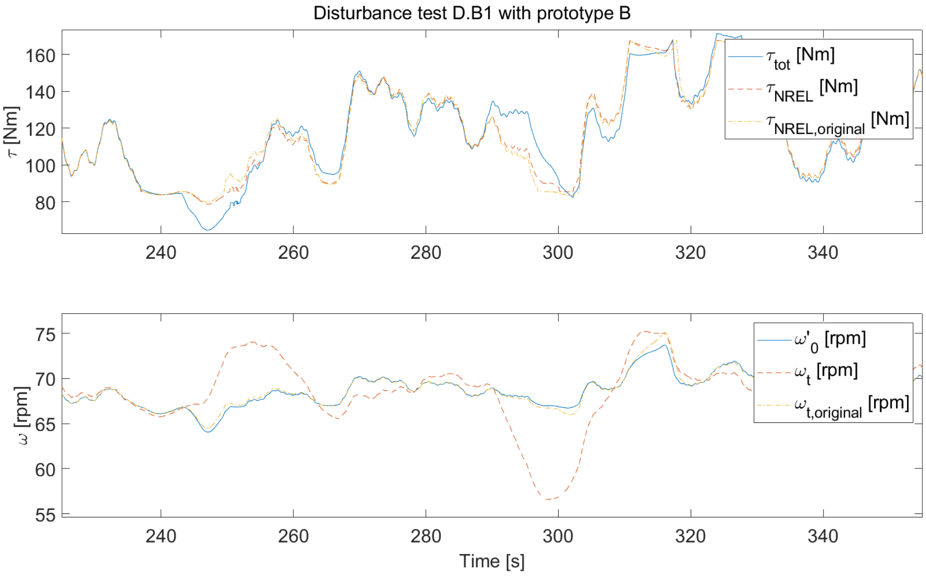

Figure 4.65: Disturbance test D.B1, $\tau_{c,HP} = 10$ s, $\tau_{c,NEM} = 10$ s. Simulation with varying wind velocity and $gain = 6000$ W/Hz.

Test D.B2 is shown in Figure 4.66, and it looks like P_{el} follows τ_{FFR} quite well here as well.

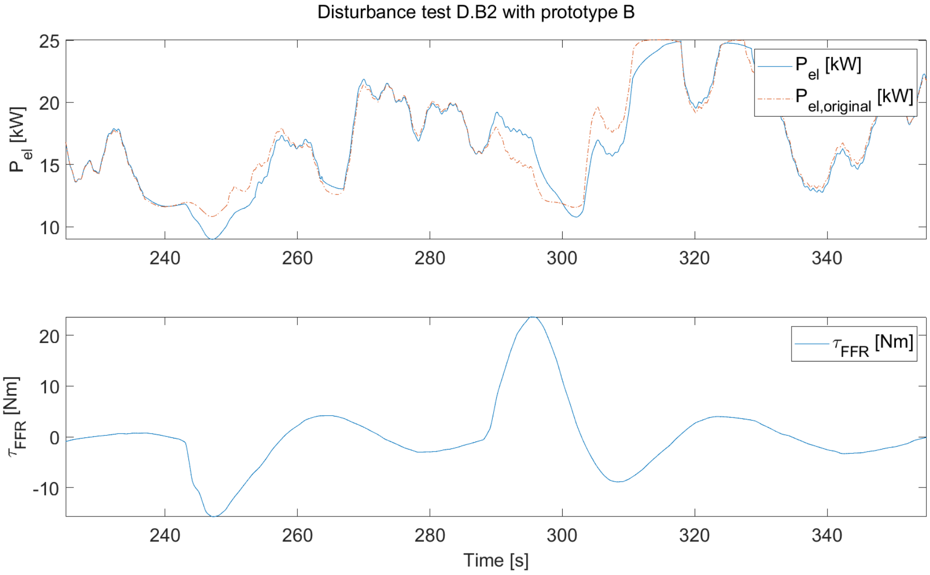

Figure 4.66: Disturbance test D.B2, $\tau_{c,HP} = 20$ s, $\tau_{c,NEM} = 20$ s. Simulation with varying wind velocity and $gain = 6000$ W/Hz.

Figure 4.67 shows the torque and rotational speed during test D.B2. Compared to test D.B1, the estimation of ω'_0 is less alike $\omega_{t,original}$.

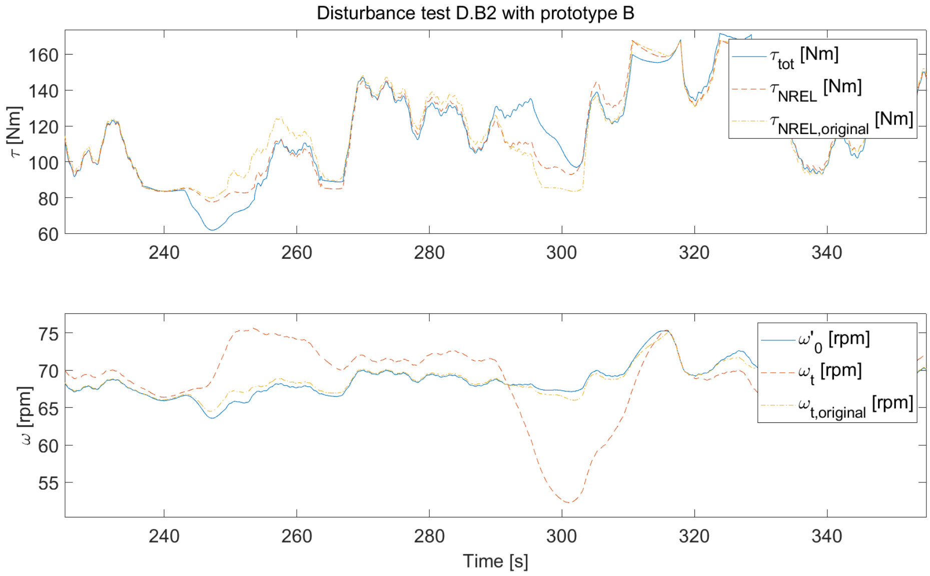

Figure 4.67: Disturbance test D.B2, $\tau_{c,HP} = 20$ s, $\tau_{c,NEM} = 20$ s. Simulation with varying wind velocity and $gain = 6000$ W/Hz.

Figure 4.68-4.69 show test D.B2 with constant velocity, and it looks like P_{el} follows the shape of τ_{FFR} quite well in Figure 4.68, but the zenith and nadir differ a bit in time. Figure 4.69 shows that the rotational speed behaves as expected, as it decreases when the torque increases, and increases when the torque decreases.

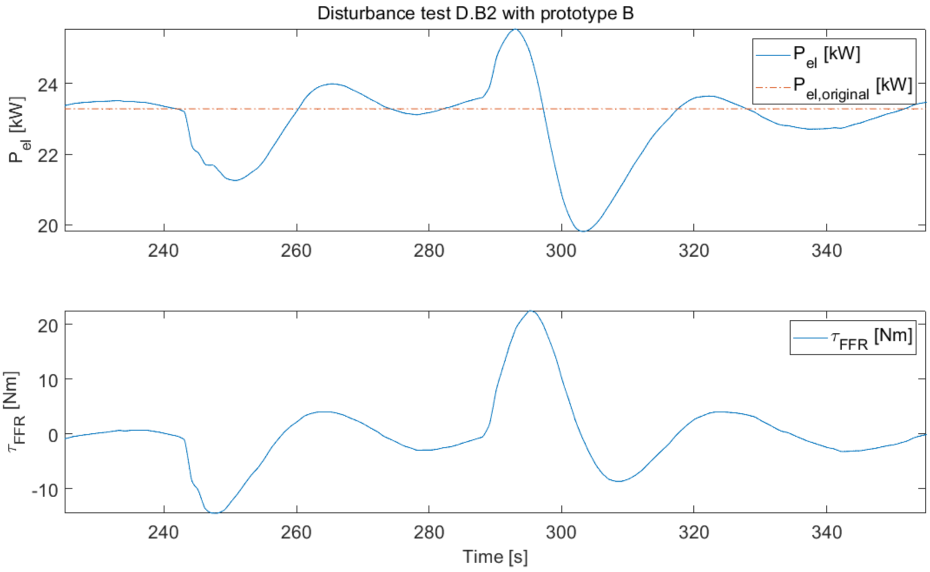

Figure 4.68: Disturbance test D.B2, $\tau_{c,HP} = 20$ s, $\tau_{c,NEM} = 20$ s. Simulation with constant wind velocity and $gain = 6000$ W/Hz.

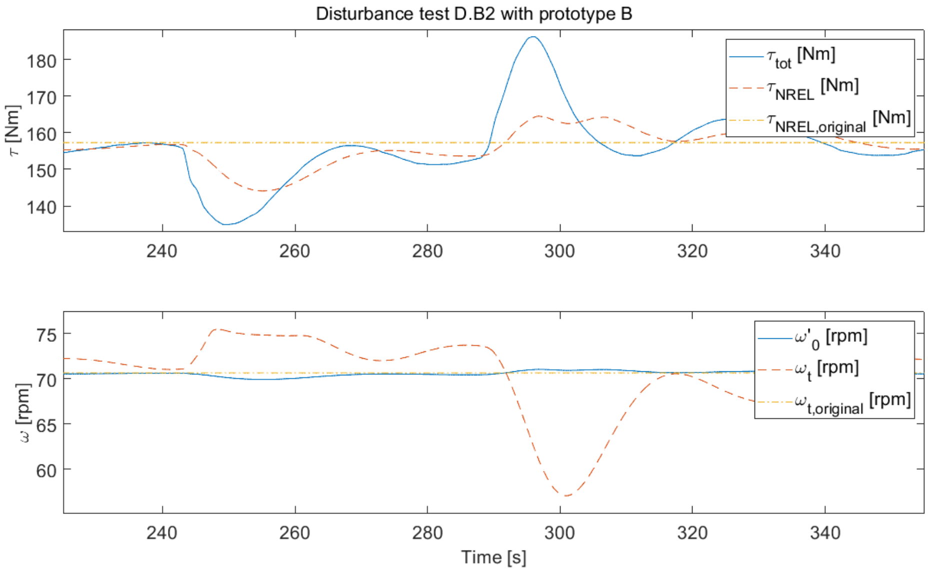

Figure 4.69: Disturbance test D.B2, $\tau_{c,HP} = 20$ s, $\tau_{c,NEM} = 20$ s. Simulation with constant wind velocity and *gain* = 6000 W/Hz.

Figures showing disturbance test D.B3, with $\tau_{c,HP} = 20$ s and $\tau_{c,NEM} = 40$ s, are found in Appendix A.3.9, and test D.B4, using $\tau_{c,HP} = 40$ s and $\tau_{c,NEM} = 20$ s, in Appendix A.3.10. The differences between the tests are small, like with step tests St.B2 and St.B3, and therefore it seems more reasonable to use the same constant for $\tau_{c,HP}$ and $\tau_{c,NEM}$. Figure 4.70 shows disturbance test D.B5, where P_{el} is not greater than $P_{el,original}$ during the first zenith in τ_{FFR}, compared to tests D.B1-D.B4.

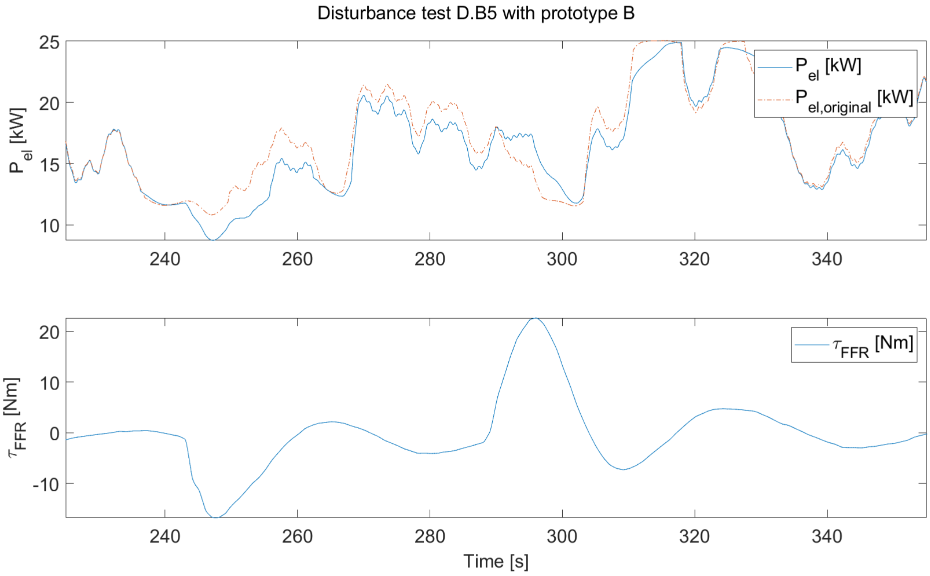

Figure 4.70: Disturbance test D.B5, $\tau_{c,HP} = 40$ s, $\tau_{c,NEM} = 40$ s. Simulation with varying wind velocity and *gain* = 6000 W/Hz.

Figure 4.71 shows the torque and rotational speed during test D.B5. In contrast to test D.B2, the estimation of ω'_0 is less alike $\omega_{t,original}$, and the endurance of the torque is much greater.

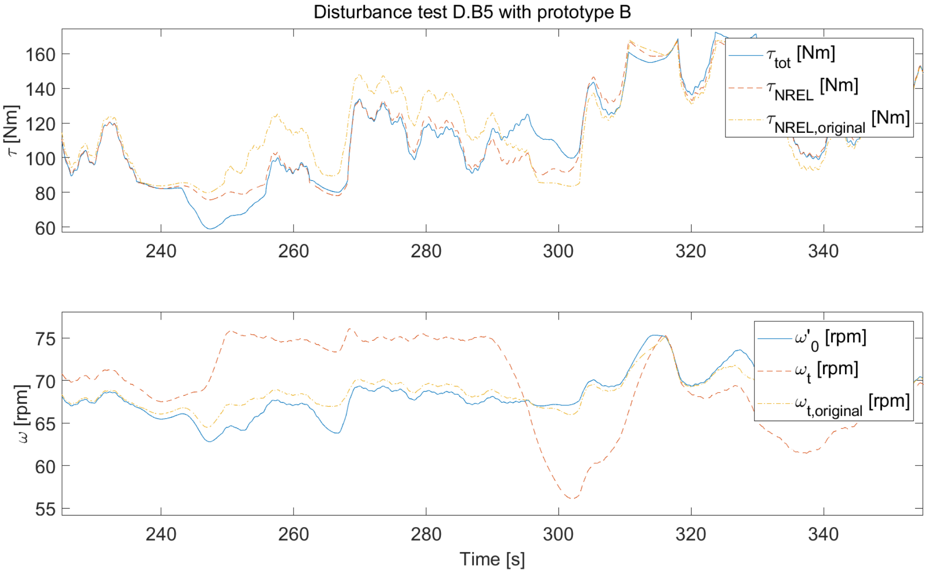

Figure 4.71: Disturbance test D.B5, $\tau_{c,HP} = 40$ s, $\tau_{c,NEM} = 40$ s. Simulation with varying wind velocity and $gain = 6000$ W/Hz.

Figure 4.72-4.73 show test D.B5 with constant velocity. It is more obvious here compared to the simulation with varying velocity that P_{el} is less than $P_{el,original}$ during the first zenith in τ_{FFR}, compared to test D.B2 shown in Figure 4.68. This indicates that the time constants might be set too large to be feasible, since a power increase was intended during the first zenith, and achieved with the previous disturbance tests using smaller time constants.

It is possible to see a phase shift between τ_{tot} and τ_{NREL} in Figure 4.73, which can also be seen in the simulation of test D.B2 with constant velocity. The torque τ_{NREL} looks more delayed than τ_{tot}. The delay could be because τ_{NREL} is based on ω'_0 which partly is based on P_{FFR} that passes through an integral and the NEM filter, and the integral itself is expected to induce a phase shift of 90°. The torque τ_{tot} have apart from τ_{NREL} also contribution of τ_{FFR}, which does not pass through the integral and NEM filter.

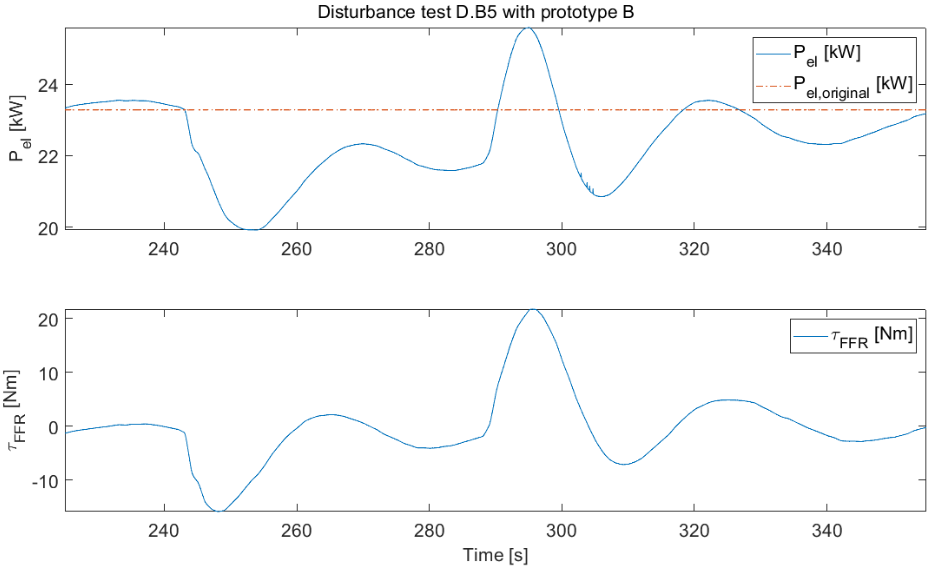

Figure 4.72: Disturbance test D.B5, $\tau_{c,HP} = 40$ s, $\tau_{c,NEM} = 40$ s. Simulation with constant wind velocity and $gain = 6000$ W/Hz.

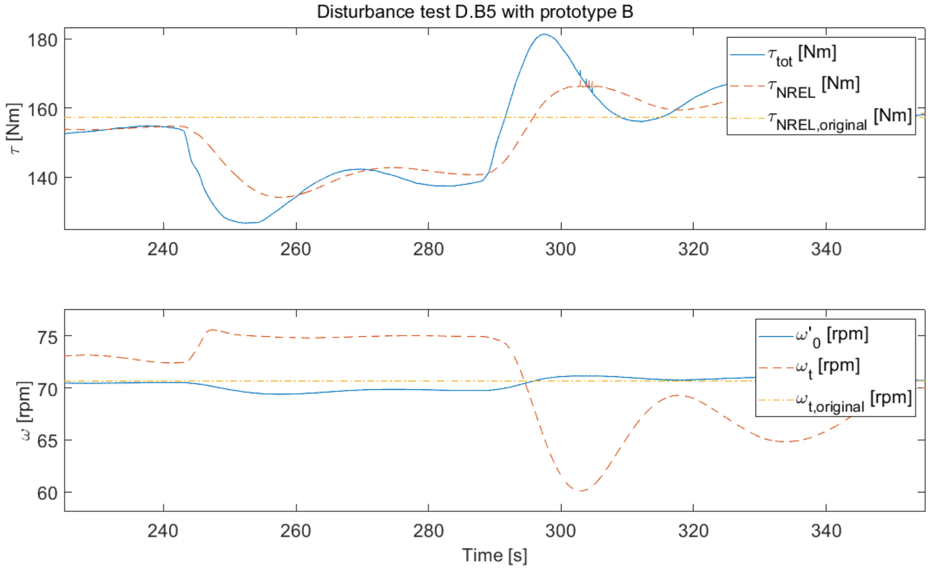

Figure 4.73: Disturbance test D.B5, $\tau_{c,HP} = 40$ s, $\tau_{c,NEM} = 40$ s. Simulation with constant wind velocity and $gain = 6000$ W/Hz.

4.2.4 Simulated grid frequency tests

Figure 4.74 shows the simulated test G.B1, as described in Table 3.10, which used grid frequency as input. Equal time constants are used in the test. It looks like the power output P_{el} follows τ_{FFR} well. Note that the gain is set very high since the changes in frequency are very small compared to the step and disturbance tests.

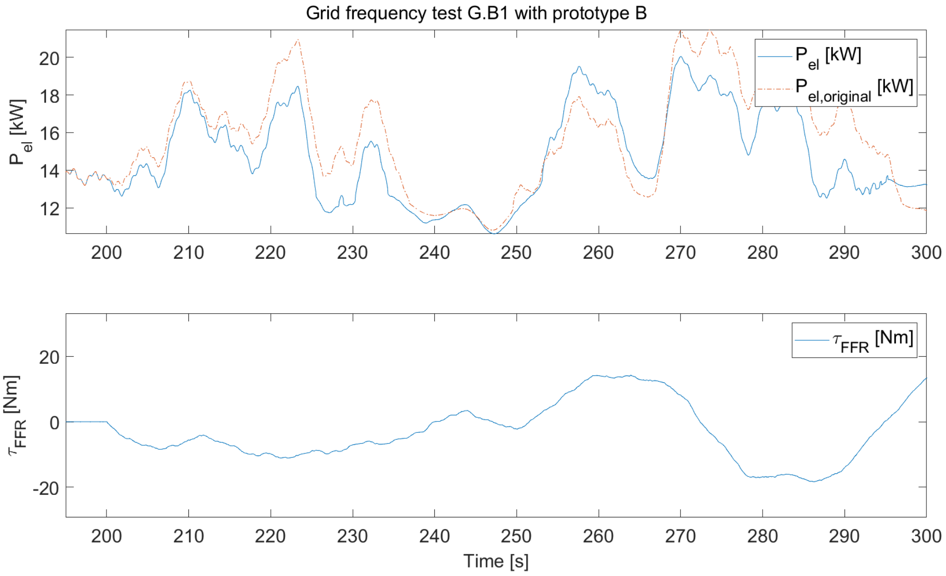

Figure 4.74: Grid frequency test G.B1, $\tau_{c,HP} = 20$ s, $\tau_{c,NEM} = 20$ s. Simulation with varying wind velocity and $gain = 80000$ W/Hz.

The torque and rotational speed are illustrated in Figure 4.75. The real rotational speed behaves as expected, by first increasing and later decreasing around 260 seconds. The estimated speed is alike $\omega_{t,original}$ for most part of the simulation, but differs quite a bit around 230-250 seconds.

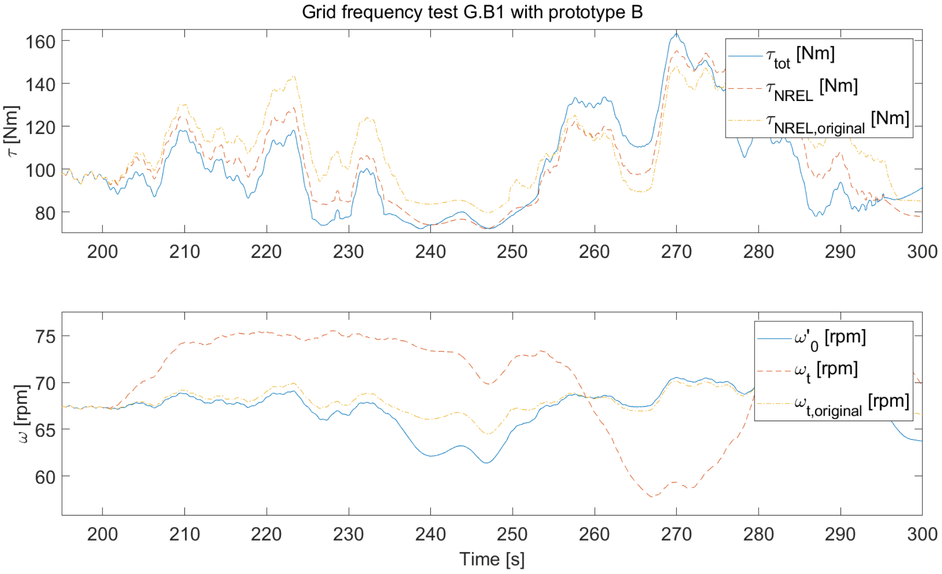

Figure 4.75: Grid frequency test G.B1, $\tau_{c,HP} = 20$ s, $\tau_{c,NEM} = 20$ s. Simulation with varying wind velocity and $gain = 80000$ W/Hz.

4.3 Closed loop simulations of dynamic FFR in the power system

This section first presents results from closed loop simulations when adding dynamic FFR responses from each prototype respectively to a power system model, and secondly closed loop Bode plots when adding dynamic FFR from prototype A to another model.

Figure 4.76 shows a closed loop simulation without dynamic FFR. The frequency nadir reaches below 49.0 Hz which is considered as emergency system state in the Nordic power system [20]. The frequency zenith reaches above 50.25 Hz which is considered as alert system state unless decreased within 5 minutes [20].

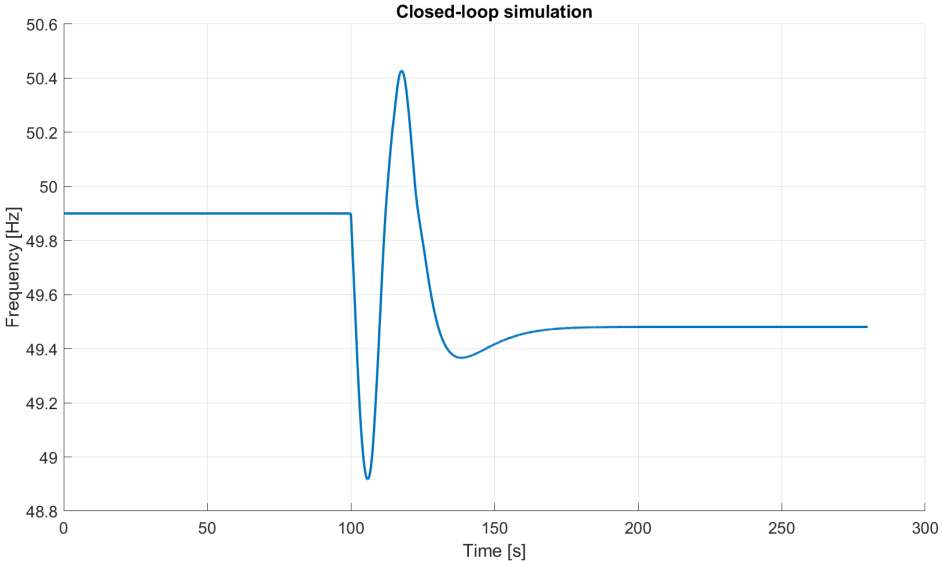

Figure 4.76: Closed loop simulation, without dynamic FFR.

Figure 4.77 shows a closed loop simulation with dynamic FFR provided by prototype A. The frequency nadir is pushed above 49.2 Hz, which is considered as normal system state if the frequency increases above 49.5 Hz within 60 seconds [20]. Dynamic FFR had the biggest impact on the frequency zenith, which was decreased by almost 0.6 Hz.

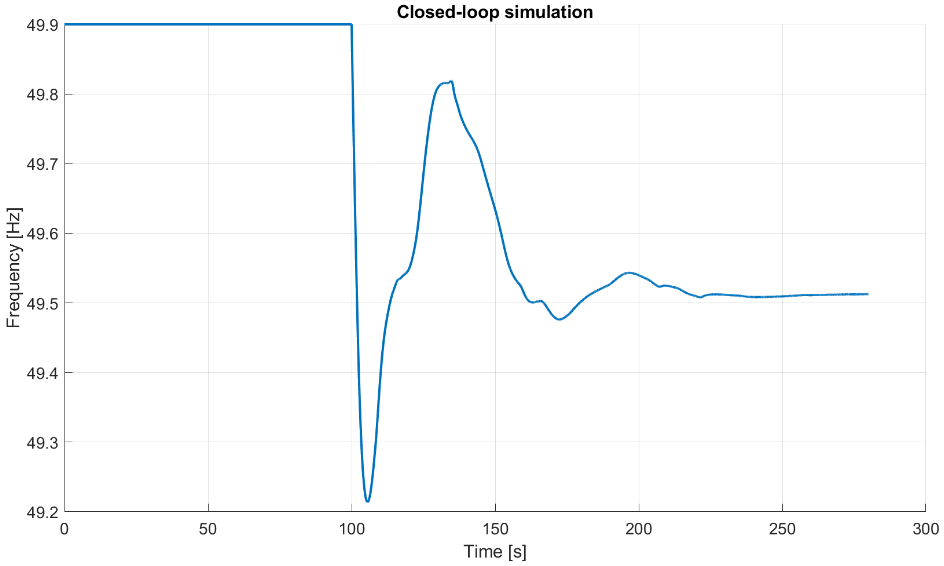

Figure 4.77: Closed loop simulation, with dynamic FFR from prototype A, with $\tau_{c,HP} = \tau_{c,NREL} = 20$ s and gain = 1000 Nm/Hz. The signal from the single 25 kW wind power plant is amplified to the equivalent of 200 000 plants, corresponding to 2000 2.5-MW turbines.

Figure 4.78 shows the dynamic FFR power response provided by prototype A during the closed loop simulation shown in Figure 4.77.

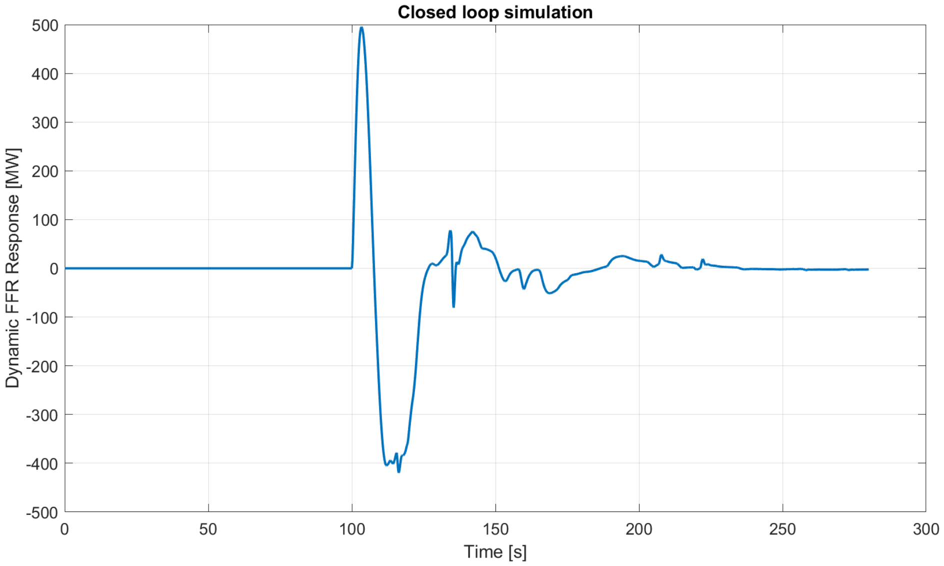

Figure 4.78: Closed loop simulation, dynamic FFR response from prototype A.

Figure 4.79 shows a closed loop simulation with dynamic FFR provided by prototype B. Similarly as with prototype A, the frequency nadir was pushed above 49.2 Hz. The frequency zenith was decreased more than in the case of prototype A, by 0.7 Hz.

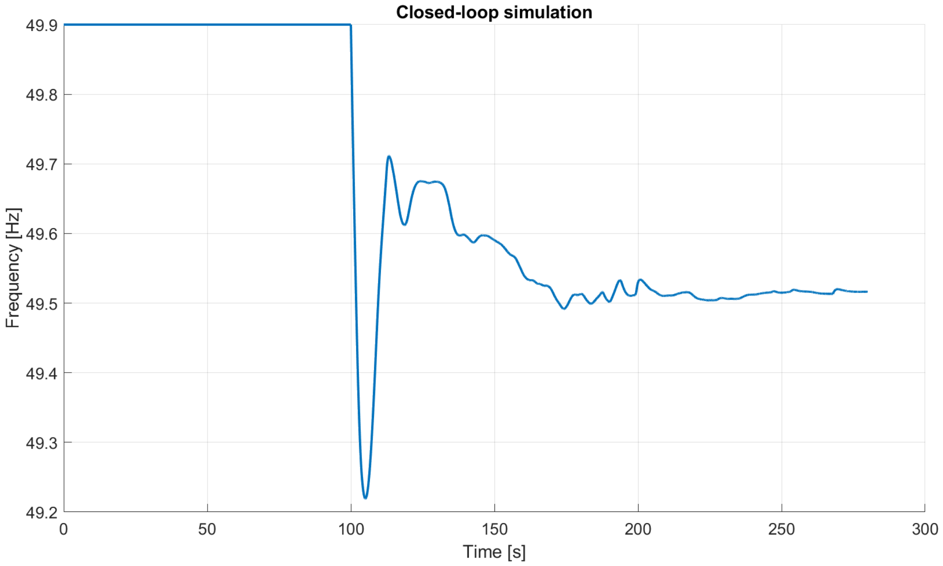

Figure 4.79: Closed loop simulation, with dynamic FFR from prototype B, with $\tau_{c,HP} = \tau_{c,NEM} = 20$ s and gain $= 5000$ W/Hz. The signal from the single 25 kW wind power plant is amplified to the equivalent of 200 000 plants, corresponding to 2000 2.5-MW turbines.

Figure 4.80 shows the dynamic FFR power response provided by prototype B during closed loop simulation shown in Figure 4.79. Compared to the response from prototype A shown in Figure 4.78, the response is less smooth, which could be because of the NREL low-pass filter used in prototype A.

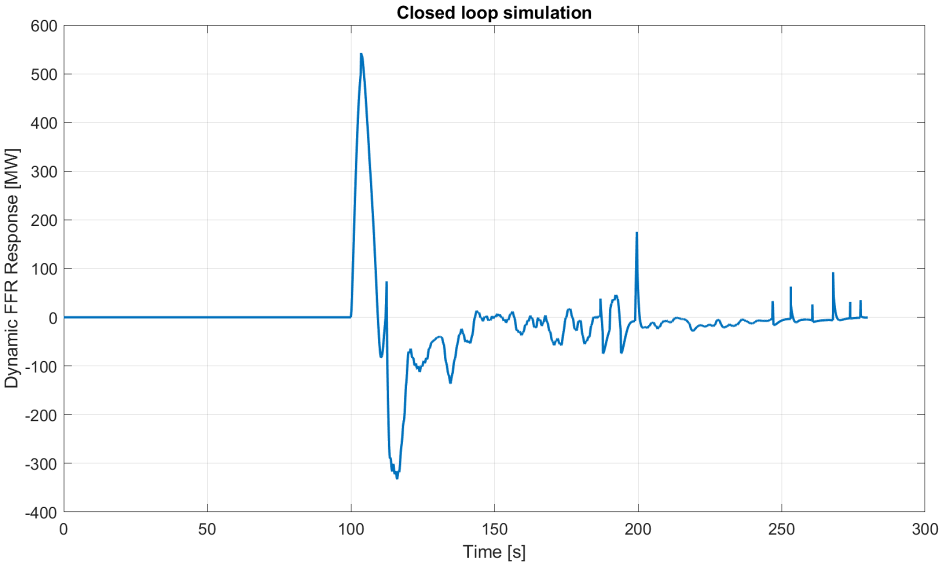

Figure 4.80: Closed loop simulation, dynamic FFR response from prototype B.

Both entities were amplified by the equivalent of 200 000 25-kW wind turbines, making the amplified gain 200 MNm/Hz for prototype A and 1000 MW/Hz for prototype B, and corresponding to 2000 2.5-MW wind turbines. Put into perspective, there were 5 497 installed wind turbines with an installed capacity of 16 224 MW in Sweden 2023 [21].

Additionally, results from another model is presented below as closed loop Bode plots of the power system and FCR, with and without dynamic FFR from prototype A, using time constants $\tau_{c,HP} = \tau_{c,NREL} = 20$ s. Four variations of settings are used, by using two different amounts of inertia in the power system, and two different volumes of dynamic FFR, as summarised in Table 3.11. Note that the gain of dynamic FFR is assumed to be 0 for frequencies at 0.01 Hz and lower in these Bode plots, which might be optimistic, as the wind turbine might need more energy from the power system for recovery at these frequencies. Figure 4.81 shows how the results from the Bode plot with prototype A, shown in Figure 4.39, affects the power system with FCR in a closed loop Bode plot, when the rotational energy in the power system E_k is set to 150 GWs and the dynamic FFR gain is set to 1000 MW/Hz. The plot shows that dynamic FFR seems to attenuate the amplitude of the power system with FCR, especially between 0.01-0.05 Hz, given the used settings.

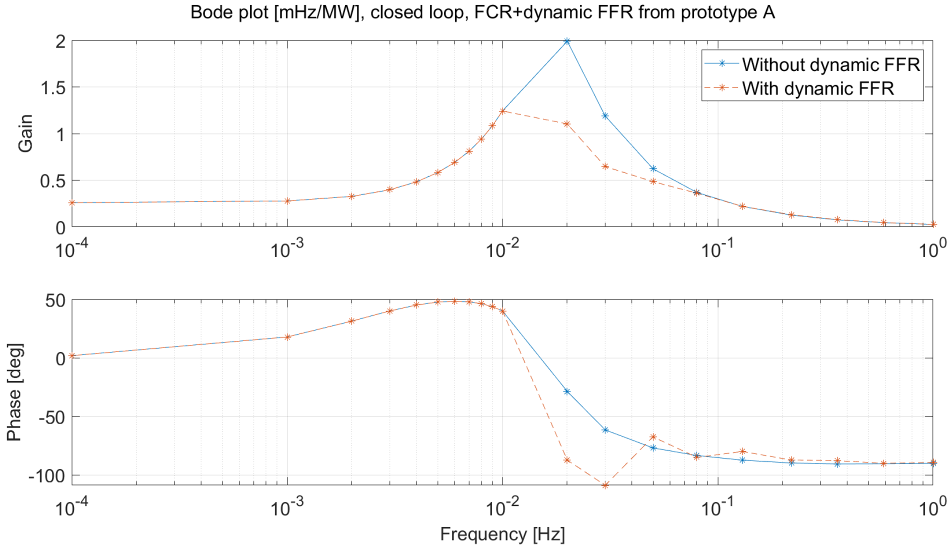

Figure 4.81: Closed loop Bode plot of the power system including FCR, comparison of with and without dynamic FFR from prototype A, using time constants $\tau_{c,HP} = \tau_{c,NREL} = 20$ s. Dynamic FFR gain = 1000 MW/Hz and $E_k = 150$ GWs.

Keeping E_k to 150 GWs while decreasing the gain of dynamic FFR to 500 MW/Hz, it is possible to see that the amplitude of the power system with FCR is less attenuated compared to when the gain was set to 1000 MW/Hz, see Figure 4.82, especially between 0.01-0.03 Hz.

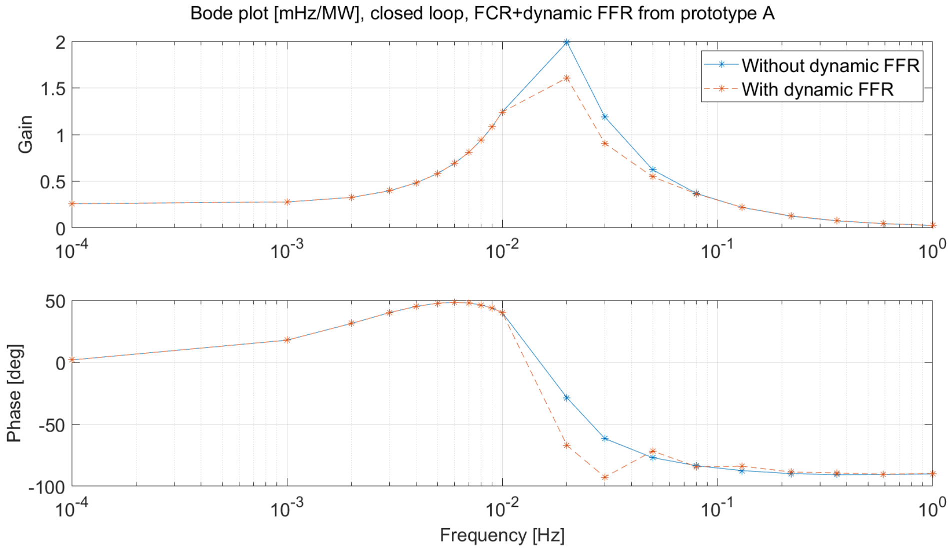

Figure 4.82: Closed loop Bode plot of the power system including FCR, comparison of with and without dynamic FFR from prototype A, using time constants $\tau_{c,HP} = \tau_{c,NREL} = 20$ s. Dynamic FFR gain = 500 MW/Hz and E_k = 150 GWs.

If instead decreasing the rotational energy E_k to 100 GWs and keeping the gain at 1000 MW/Hz, Figure 4.83 shows that the amplitude of the power system with FCR increases. Adding dynamic FFR with gain 1000 MW/Hz seems to attenuate the amplitude, especially between 0.01-0.05 Hz.

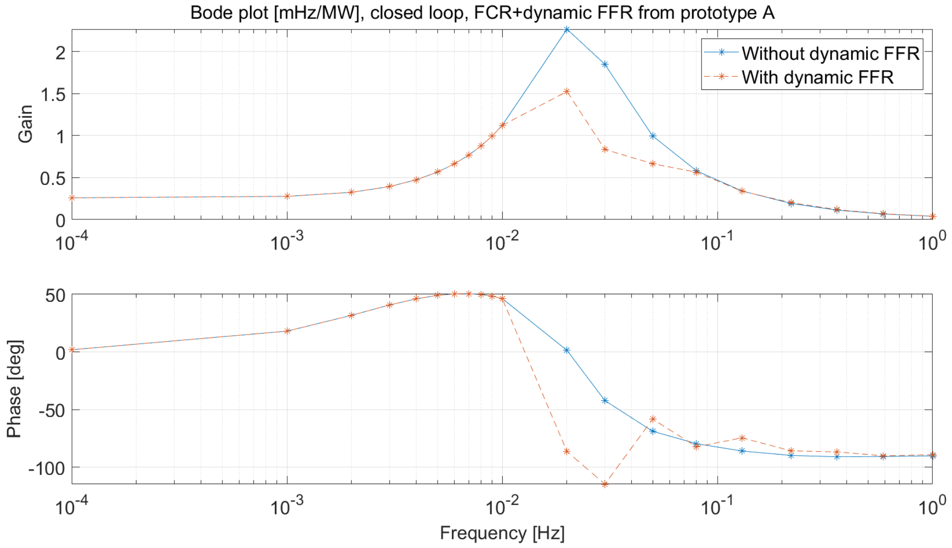

Figure 4.83: Closed loop Bode plot of the power system including FCR, comparison of with and without dynamic FFR from prototype A, using time constants $\tau_{c,HP} = \tau_{c,NREL} = 20$ s. Dynamic FFR gain = 1000 MW/Hz and E_k = 100 GWs.

Lastly, if E_k is kept at 100 GWs while the dynamic FFR gain is decreased to 500 MW/Hz, Figure 4.84 shows that dynamic FFR instead amplifies the existing amplitude of the power system with FCR at 0.02 Hz, while still attenuating the amplitude a bit between 0.03-0.05 Hz. The results indicate that the gain of dynamic FFR from prototype A, using time constants $\tau_{c,HP} = \tau_{c,NREL} = 20$ s, must be sufficiently large, as it otherwise risks amplifying the existing amplitude of the power system with FCR instead of attenuating it, especially when the rotational energy in the power system is lower. Comparing with Figure 2.7 which shows how dynamic FFR without the wind dynamics is expected to behave, using the same $E_k = 100$ GWs, gain = 500 MW/Hz and time constant $\tau_{c,HP} = 20$ s, the behaviour is quite different. The ideal case does not show amplification of the power system at 0.02 Hz, indicating that the amplification at 0.02 Hz in Figure 4.84 could be caused by the added wind dynamics. However, it is not certain why this amplification occurs.

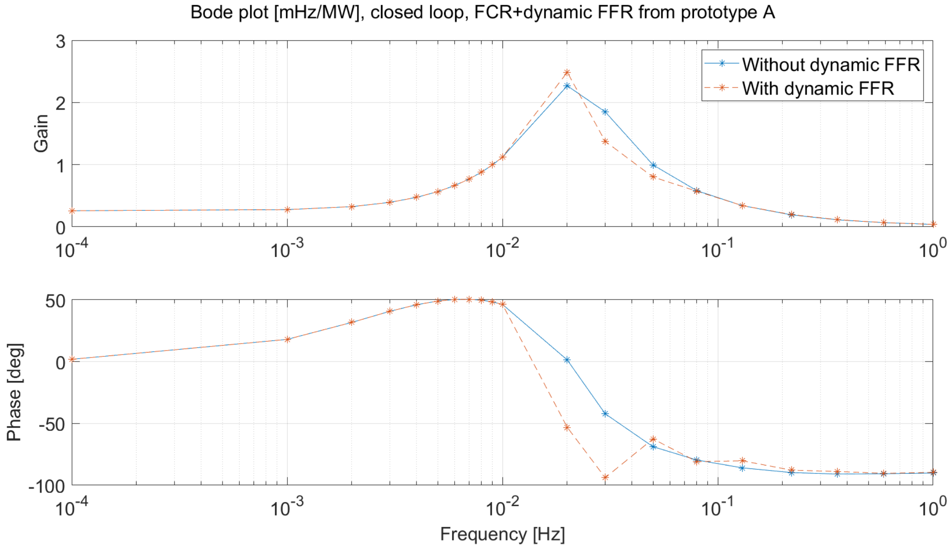

Figure 4.84: Closed loop Bode plot of the power system including FCR, comparison of with and without dynamic FFR from prototype A, using time constants $\tau_{c,HP} = \tau_{c,NREL} = 20$ s. Dynamic FFR gain = 500 MW/Hz and $E_k = 100$ GWs.

5

Conclusions

As most aspects have already been discussed in the results & discussion chapter, the most important findings are concluded in this chapter for prototype A, prototype B and closed loop simulations with the power system. Finally, a summarising conclusion is drawn to answer the precision of the problem stated in the introduction, and future works are recommended.

5.1 Prototype A

It could be concluded that it seems reasonable to use the same time constant for $\tau_{c,HP}$ and $\tau_{c,NREL}$ for prototype A, since a greater time constant of $\tau_{c,HP}$ compared to $\tau_{c,NREL}$ seems to induce oscillating behaviour of τ_{NREL}. Furthermore, it is probably not feasible do delay the NREL filter more than $\tau_{c,NREL} = 20$ s, as the greater the time constant, the greater the risks are of stopping the turbine. In summary, this could, at least for the studied wind turbine in this project, limit the time constants to $\tau_{c,HP} = \tau_{c,NREL} \leq 20$ s. Setting $\tau_{c,NREL}$ to 20 s might however still cause oscillating behaviours of the torque, but since the studied turbine is small and uses a look-up table for the NREL controller, this might not generalise for a conventional wind turbine. The Bode plots of prototype A show that dynamic FFR definitely affects the power output about as intended. The NREL low-pass filter makes a great difference, as without it, the effect from the band-pass filter is attenuated. The Bode plots also show that dynamic FFR from prototype A almost fulfils the POD-P requirement, as $f_1 = 1$ Hz induces a phase shift of -100°, which is a bit below the requirement -90°. The advantage with prototype A is that it is much simpler than the other prototype, as it only requires an additional low-pass filter apart from the dynamic FFR block. Disadvantage would be that the band-pass filter is restricted by how much the NREL controller is slowed down, and that the turbine suffer greater risks of stopping depending on how great this delay is set to be. Another drawback is that the NREL controller is delayed at all times, as it does not account for whether dynamic FFR is delivered or not.

5.2 Prototype B

For prototype B, it could also be reasonable to use the same time constant for $\tau_{c,HP}$ and $\tau_{c,NEM}$, as setting one smaller time constant seem to limit the effect of the greater time constant. Like with prototype A, $\tau_{c,HP} = \tau_{c,NEM} \leq 20$ s could be reasonable. Greater time constants seem to alter the estimation of ω'_0 and the power response in an undesired way, at least in simulations with the studied wind turbine. However, optimisation of the time constants must be further studied with practical tests. It was not possible to run sufficiently many practical tests with prototype B due to faulty behaviour in the NEM-filter used in the practical set-up. The step tests that were done in the real set-up after the error was resolved, indicated that the model now works as anticipated. The unaffected behaviour of the estimated rotational speed could be observed in both simulations and reality. The simulations indicate that the torque from the NREL controller does not oscillate at all with prototype B, in contrast to prototype A. An advantage with prototype B is that the risks of stopping the turbine are smaller, if implemented together with well-suited NEM and AEM functions. Furthermore, it is probably easier to increase the time constants as the NREL controller is not delayed in this prototype, which could be more beneficial for the power system if the performance is still acceptable. There are however still risks of stoppping the turbine, if the NEM function is not sufficiently restrictive. Disadvantages would be that the design is more complicated than prototype A.

5.3 Closed loop simulations of dynamic FFR in the power system

Both prototypes seem to work about as intended in the power system, as they both limit the frequency nadir and zenith during closed loop simulations with the power system. The closed loop Bode plots with the power system indicate that dynamic FFR from prototype A using $\tau_{c,HP} = \tau_{c,NREL} = 20$ s can attenuate the existing amplitude in the power system with FCR in situations with inertia down to 100 GWs.

5.4 Summarising conclusion

It can be concluded that dynamic FFR from both prototypes seem promising, and both designs seem to work as intended. The time constants for both prototypes are probably feasible to be equal, and $\tau_{c,HP} = \tau_{c,NREL} = \tau_{c,NEM} \leq 20$ s seem promising, at least for the studied wind turbine. For increased stability in the power system, it is best if the time constants are as great as possible in this specified interval. However, feasible time constants for prototype B, and the prototype overall behaviour, should be investigated further, especially with practical tests. The variety of carried out tests seemed to capture the behaviour quite well, but the results were much more difficult to interpret while doing grid frequency and disturbance tests, which on the other hand are the most realistic applications. The step and sine tests seem most feasible, as the step test more clearly shows anticipated effects in power output and rotational speed despite the varying wind velocity, and the sine tests enable Bode plots and a more holistic understanding of the system and different filters. There are restrictions regarding endurance and altered efficiency, but since the studied wind turbine is small, it might not be as big an issue with conventional wind turbines which have greater moment of inertia. Neither might it be an issue since the lack in endurance as well as efficiency was generally observed during step tests, which is not the thought application for dynamic FFR. The dynamic response seems to suit wind power rather well, as it allows for natural energy recovery. Despite different wind conditions, it is in many cases possible to adjust the pitch angle or the torque-rotational speed curve which can adapt the wind turbine to still be able to deliver dynamic FFR. The greatest challenge may lie in estimating a sufficiently accurate reference value, and establishing technical requirements that enables wind power on the ancillary service market despite its intermittent behaviour.

5.5 Future works

Practical tests with prototype B should be carried out, in particular sine tests to construct Bode plots to understand the behaviour of how NEM interacts better, and to further validate the simulation model. The design of prototype B can be further developed and improved, for example by implementing an AEM function, and taking the curtailed energy into account while estimating ω'_0. Optimisation of parameters should be investigated more thoroughly, and stability of the prototypes incorporated into the power system should also be explored more. Closed loop Bode plots of prototype A and the power system with FCR should especially be investigated further, by adding more points in the Bode plot to better understand the characteristics of dynamic FFR from this prototype. Furthermore, a sufficiently accurate reference value is required for wind power to deliver ancillary services, and is therefore necessary to estimate if wind power shall deliver dynamic FFR. Practical tests with a conventional wind turbine or wind power park should be carried out, since the studied wind turbine is very small and is probably not entirely representative.

Bibliography

[1] "System Development Plan 2022-2031 (In Swedish: Systemutvecklingsplan 2022-2031)," Svenska kraftnät, Sundbyberg, Sweden, 2021. [Online]. Available: $https://www.svk.se/siteassets/om-oss/rapporter/2021/svk_systemutvecklingsplan_2022-2031.pdf$ (accessed on: 2024-05-23)

[2] E. Ørum et al., "Future System Inertia 2," ENTSO-E, Brussels, Belgium, 2018. [Online]. Available: $https://www.statnett.no/globalassets/for-aktorer-i-kraftsystemet/utvikling-av-kraftsystemet/nordisk-frekvensstabilitet/future-system-inertia-phase-2.pdf$ (accessed on: 2024-05-23)

[3] "Technical Requirements for Fast Frequency Reserve Provision in the Nordic Synchronous Area - External document," ENTSO-E, Brussels, Belgium, 2021. [Online]. Available: $https://www.svk.se/siteassets/english/stakeholder-portal/prequalification/technical-requirements-for-ffr-v1.1.pdf$ (accessed on: 2024-05-23)

[4] P. Godin, M. Fischer, H. Röttgers, A. Mendonca and S. Engelken, "Wind Power Plant Level Testing of Inertial Response with Optimized Recovery Behaviour," in *IET Renewable Power Generation*, vol. 13, Mar. 2019, doi: $http://dx.doi.org/10.1049/iet-rpg.2018.5232$

[5] IRENA, "Critical materials," n.d.. [Online]. Available: $https://www.irena.org/Energy-Transition/Technology/Critical-materials$ (accessed on: 2024-02-08)

[6] M. Dreidy, H. Mokhlis and S. Mekhilef. (2017). "Inertia response and frequency control techniques for renewable energy sources: A review," in *Renewable and Sustainable Energy Reviews*, vol. 69, pp. 144-155, doi: $https://doi.org/10.1016/j.rser.2016.11.170$

[7] R. Vennell. (2013). "Exceeding the Betz limit with tidal turbines," in *Renewable Energy*, vol. 55, pp. 277-285, doi: $https://doi.org/10.1016/j.renene.2012.12.016$

[8] W. J. Farmer and A. J. Rix, "Modelling a wind turbine as a low-pass filter for wind to electrical power calculations," in *2020 International SAUPEC/RobMech/PRASA Conference*, Cape Town, South Africa, 2020, pp. 1-6, doi: $10.1109/SAUPEC/RobMech/PRASA48453.2020.9041077$.

[9] R. Neves, J. Silva and V. Teodoro. (2013). "Integrating Computational Modelling in Science, Technology, Engineering and Mathematics Education," in *Educational interfaces between mathematics and industry*, vol. 16 (pp. 375-383), doi: $10.1007/978-3-319-02270-3_38$

[10] J. Jonkman, S. Butterfield, W. Musial and G. Scott, "Definition of a 5-MW Reference Wind Turbine for Offshore System Development," NREL, Golden, CL, USA, TP-500-38060, 2009. [Online]. Available: *https://www.nrel.gov/docs/fy09osti/38060.pdf* (accessed on: 2024-04-07)

[11] M. Eriksson, "Frequency control with wind power (In Swedish: Frekvensstyrning med vindkraft)," Department of Electrical Engineering, Chalmers University of Technology, Gothenburg, Sweden, 2022.

[12] "Wind power's potential and costs to provide system services to the power grid (In Swedish: Vindkraftens potential och kostnader för att tillhandahålla systemtjänster till elnätet)," RISE, Borås, Sweden, 2021. [Online]. Available: *https://www.ri.se/sites/default/files/2021-07/Slutrapport-Vindkraftens%20potential%20och%20kostnader%20f%C3%B6r%20systemtj%C3%A4nster%20.pdf* (accessed on: 2024-05-23)

[13] N. Modig et al., "FFR Design of Requirements - External document," ENTSO-E, Brussels, Belgium, 2020. [Online]. Available: *https://energinet.dk/media/rwbbyspn/1c-ffr-design-requirements-external-document.pdf* (accessed on: 2024-04-07)

[14] "Technical requirements for Frequency Containment Reserve Provision in the Nordic Synchronous Area," ENTSO-E, Brussels, Belgium, 2023. [Online]. Available: *https://www.svk.se/siteassets/aktorsportalen/bidra-med-reserver/om-olika-reserver/fcr/fcr-technical-requirements-may-23.pdf* (accessed on: 2024-04-06)

[15] "Guidance for variable resources to deliver ancillary services and remedial actions (In Swedish: Vägledning för variabla resurser för att leverera stödtjänster och avhjälpande åtgärder)," Svenska kraftnät, Sundbyberg, Sverige, 2023. [Online]. Available: *https://www.svk.se/siteassets/aktorsportalen/bidra-med-reserver/forkvalificering/vagledning-for-variabla-resurser-for-att-leverera-stodtjanster-och-avhjalpande-atgarder.pdf*, p. 4

[16] D. G. Alciatore, *Introduction to mechatronics and measurements systems.* 5th ed., New York, NY, USA: McGraw-Hill Education, 2019.

[17] B. Lennartson, *The basics of automatic control (In Swedish: Reglerteknikens grunder).* Lund, Sweden: Studentlitteratur AB, 2011.

[18] R. Eriksson, N. Modig, A. Westberg, "FCR-N Design of requirements," ENTSO-E, Brussels, Belgium, 2017. [Online]. Available: *https://www.svk.se/contentassets/e5a38b7a16a443b290f5d49d42ea03c0/3---fcr-n-design-of-requirements.pdf* (accessed on: 2024-04-06)

[19] *The Swedish Energy Markets Inspectorate's regulations on establishing generally applicable requirements for grid connection of generators (In Swedish: Energimarknadsinspektionens föreskrifter om fastställande av generellt tillämpliga krav för nätanslutning av generatorer.)*, EIFS 2018:2, Energimarknadsinspektionen., Eskilstuna, Sweden: G. Morén, Dec. 2018. [Online]. Available: *https://ei.se/om-oss/publikationer/publikationer/foreskrifter-el/2018/foreskrift-eifs-20182*

[20] N. Modig, R. Eriksson, P. Ruokolainen, J. Nerbø Ødegård, S. Weizenegger, T. Dalgas Fechtenburg. "Overview of Frequency Control in the Nordic Power System," ENTSO-E, Brussels, Belgium, 2022. [Online].

Available: *https://www.statnett.no/globalassets/for-aktorer-i-kraftsystemet/systemansvaret/reservemarkeder/overview-of-frequency-control-in-the-nordic-power-system.pdf* (accessed on: 2024-05-23)

[21] Swedish Energy Agency, "Wind power statistics (In Swedish: Vindkraftsstatistik)," 2024. [Online]. Available: *https://www.energimyndigheten.se/statistik/den-officiella-statistiken/statistikprodukter/vindkraftsstatistik/* (accessed on: 2024-05-23)

A

Appendix

Additional illustrations and results are presented in this chapter.

A.1 Simulink prototypes

Illustrations of the prototypes in Simulink are provided in this section.

A.1.1 Simulink model of prototype A

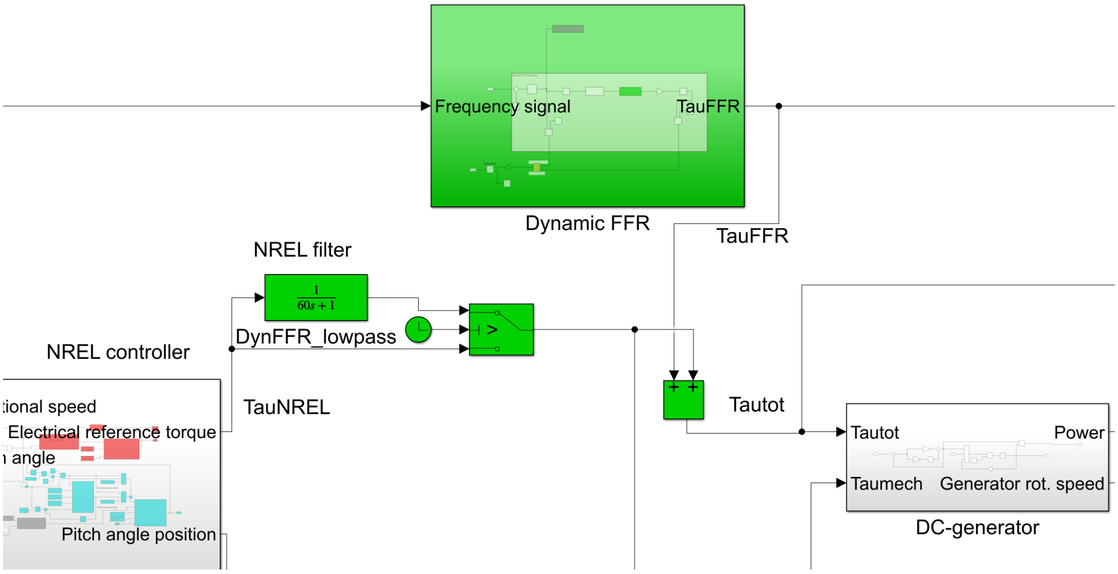

Figure A.1: Prototype A: The dynamic FFR block integrated in the wind power model, by adding the torque response τ_{FFR} to τ_{NREL}, and added low-pass filter to delay the NREL controller.

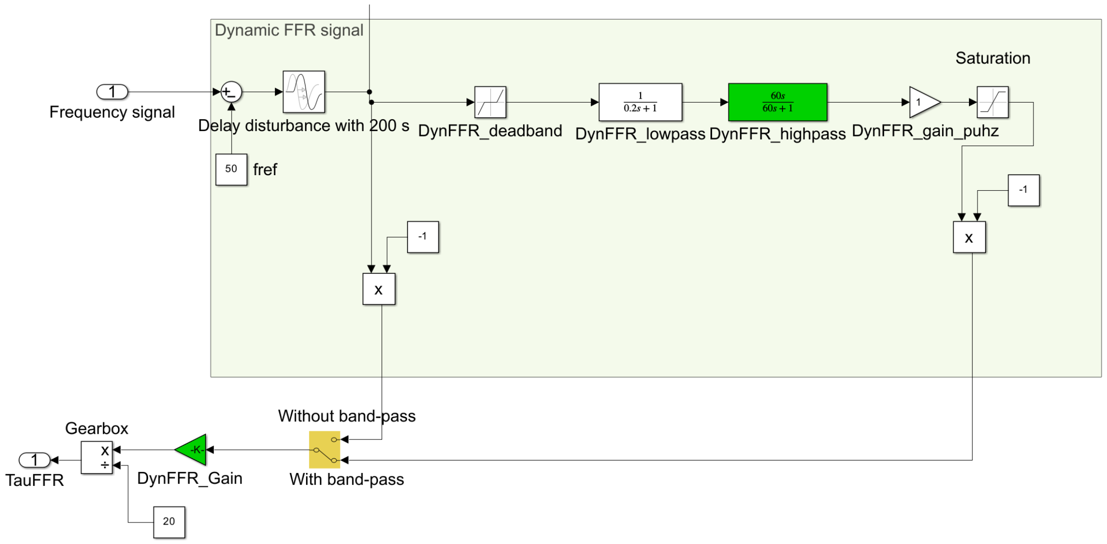

Figure A.2: Prototype A: The dynamic FFR block that delivers a torque response τ_{FFR}.

A.1.2 Simulink model of prototype B

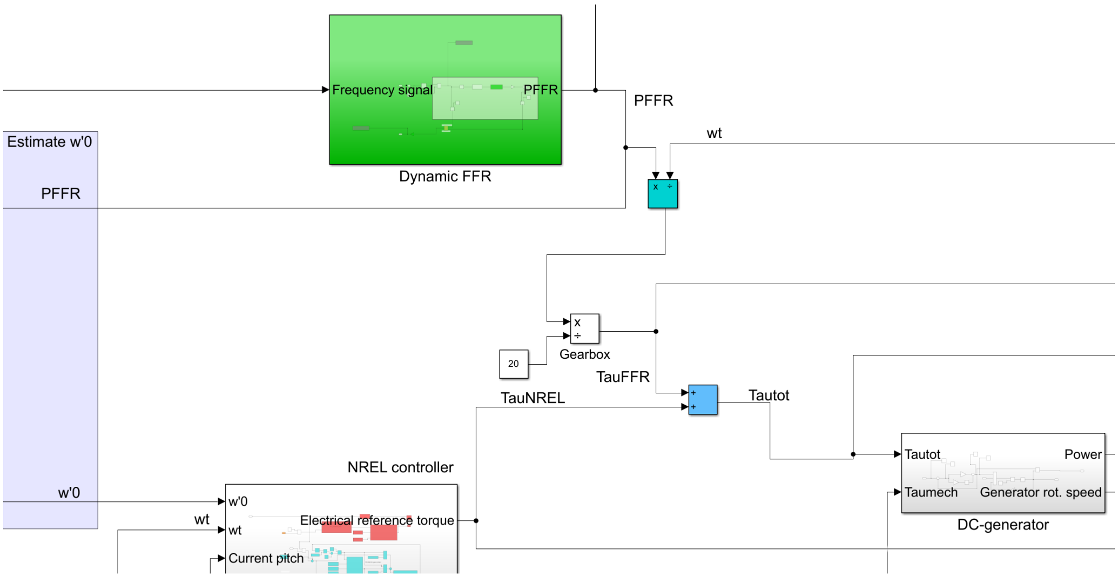

Figure A.3: Prototype B: The dynamic FFR block integrated in the wind power model, delivering a power response P_{FFR}. The torque response τ_{FFR} is calculated from the power response, and then added to the electrical reference torque τ_{NREL}. The power response P_{FFR} is used to estimate the unaffected rotational speed ω'_0.

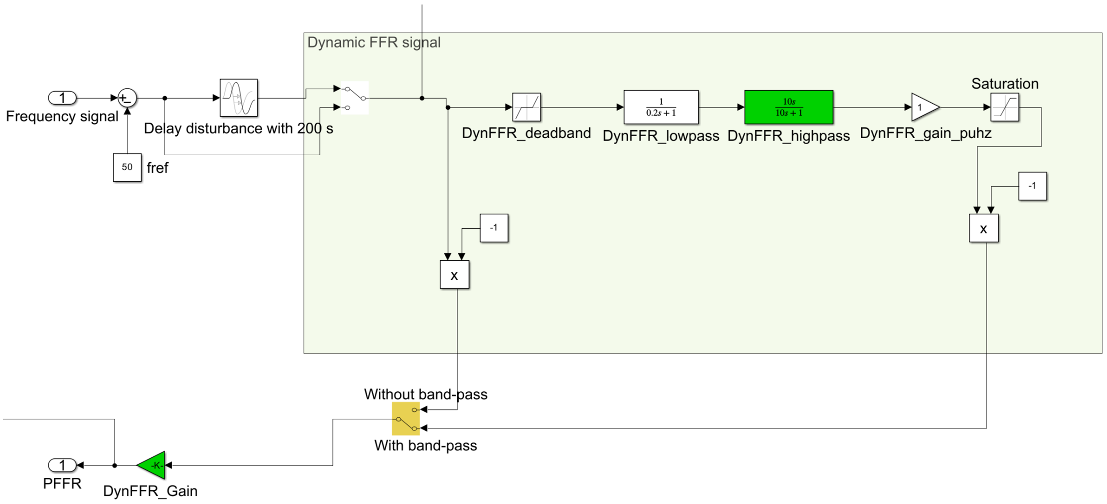

Figure A.4: Prototype B: The dynamic FFR block that delivers a power response P_{FFR}.

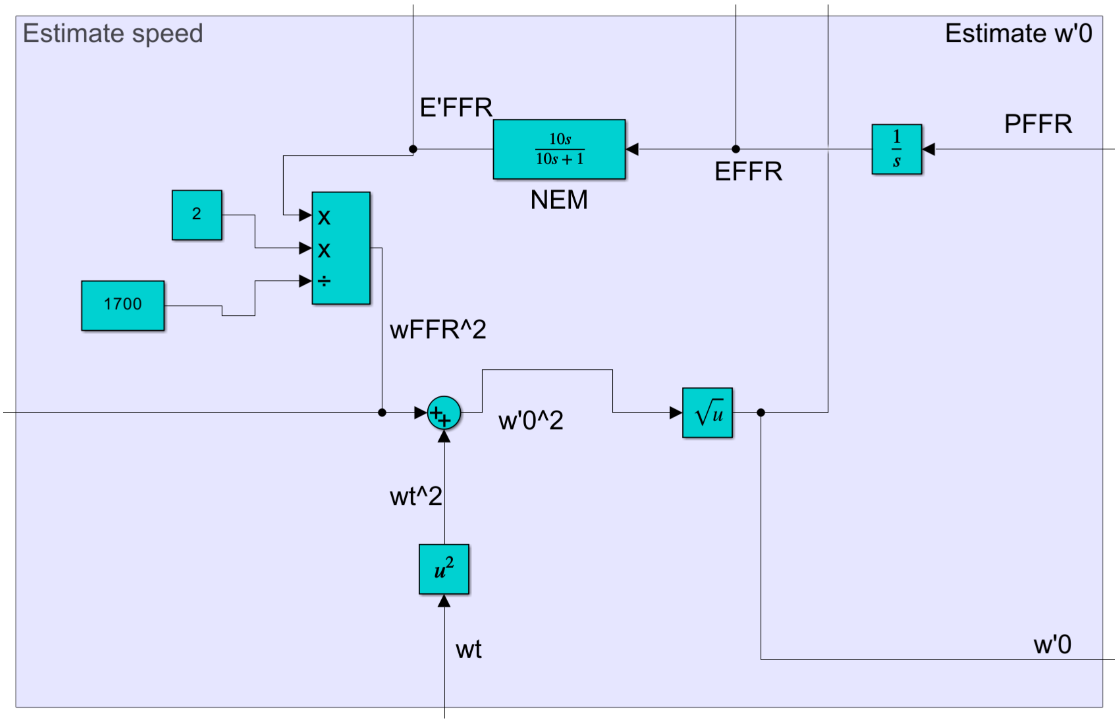

Figure A.5: Prototype B: the unaffected speed ω'_0 is estimated from the power response P_{FFR}.

A.2 Prototype A

Additional results from protoype A are illustrated in this section.

A.2.1 Sine test 4.Si.A1

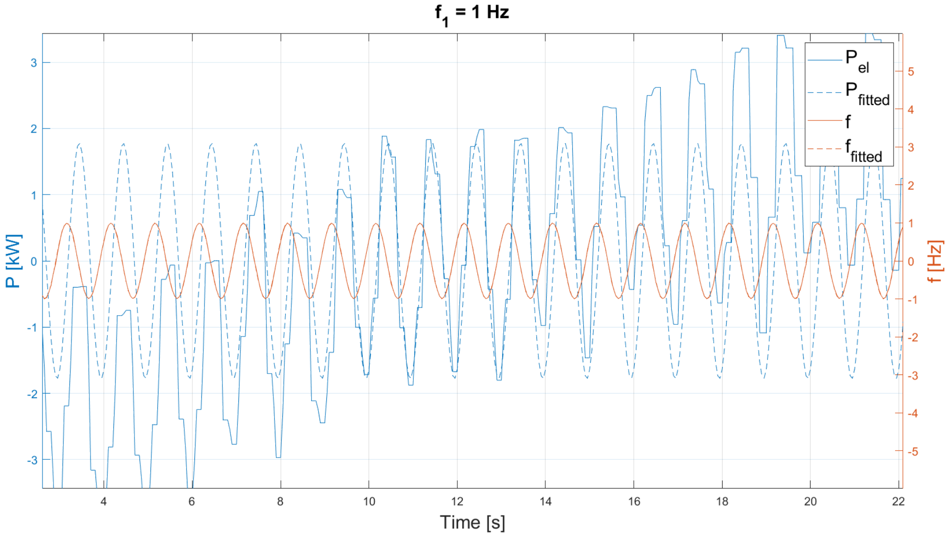

Figure A.6: Fitted sine with f_1, sine test 4.Si.A1, $\tau_{c,HP} = 20$ s, $\tau_{c,NREL} = 20$ s. Practical test with $gain = 400$ Nm/Hz and curtailment factor of 0.5.

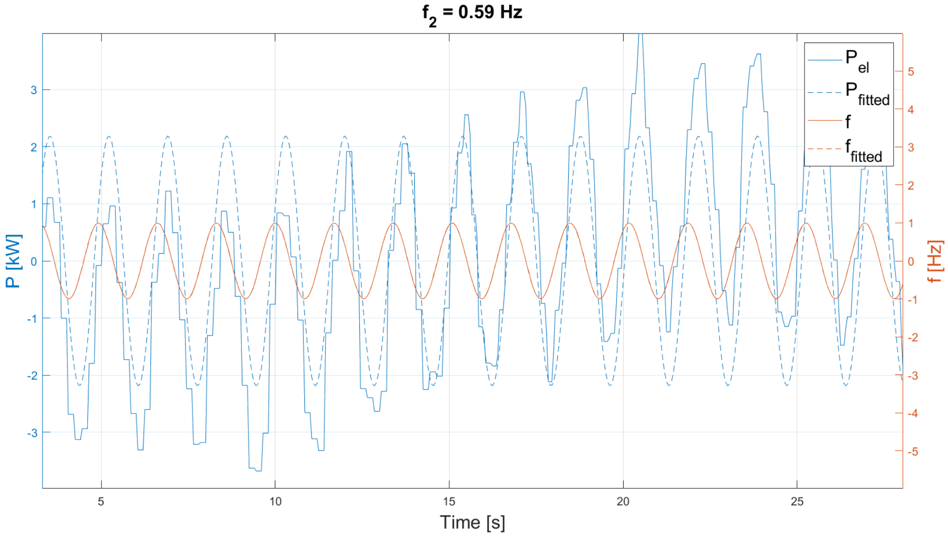

Figure A.7: Fitted sine with f_2, sine test 4.Si.A1, $\tau_{c,HP} = 20$ s, $\tau_{c,NREL} = 20$ s. Practical test with $gain = 400$ Nm/Hz and curtailment factor of 0.5.

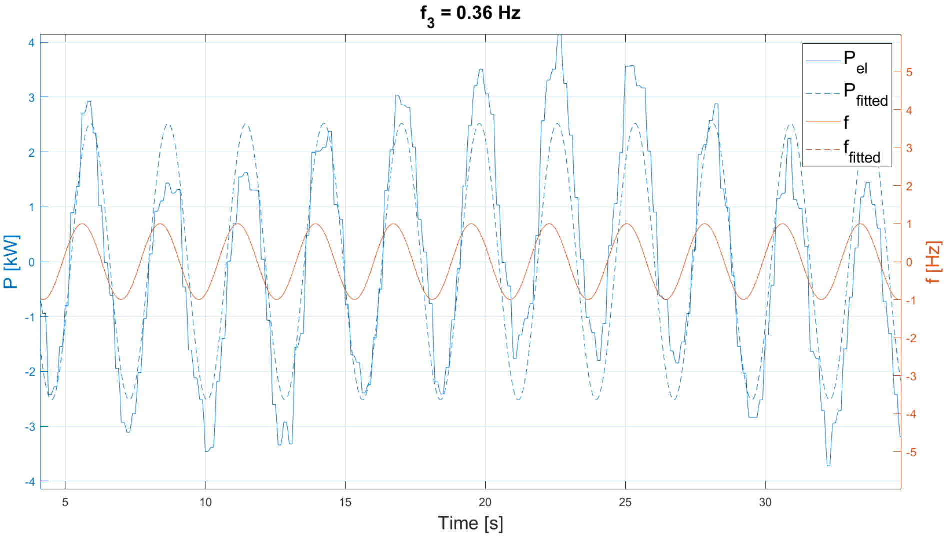

Figure A.8: Fitted sine with f_3, sine test 4.Si.A1, $\tau_{c,HP} = 20$ s, $\tau_{c,NREL} = 20$ s. Practical test with $gain = 400$ Nm/Hz and curtailment factor of 0.5.

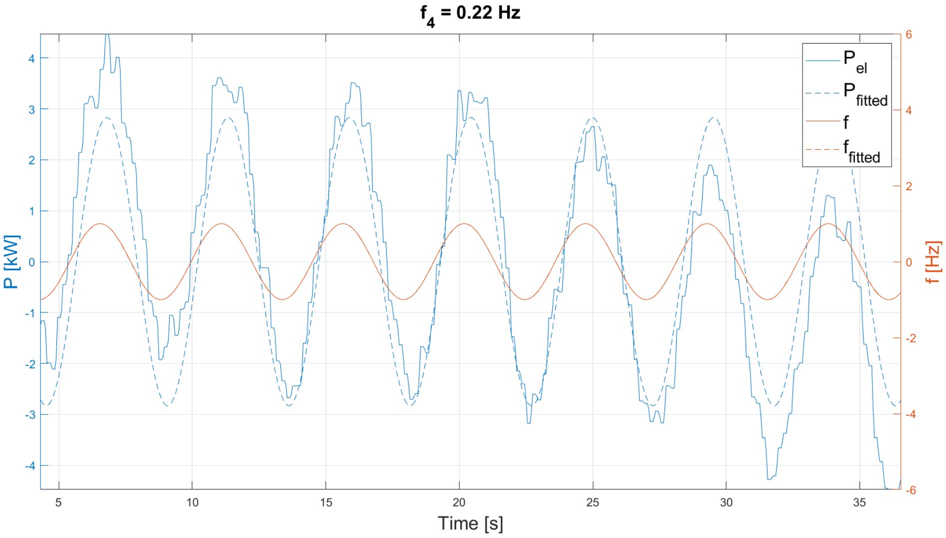

Figure A.9: Fitted sine with f_4, sine test 4.Si.A1, $\tau_{c,HP} = 20$ s, $\tau_{c,NREL} = 20$ s. Practical test with $gain = 400$ Nm/Hz and curtailment factor of 0.5.

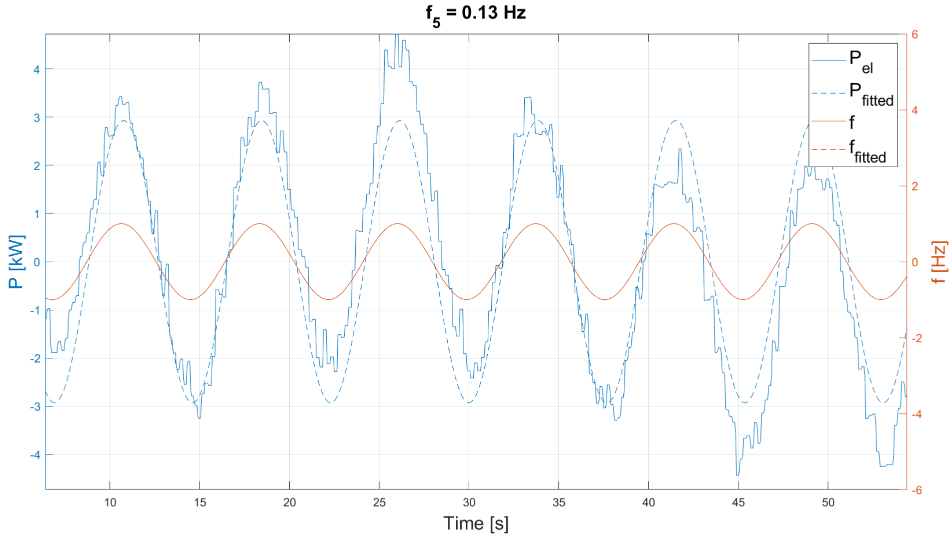

Figure A.10: Fitted sine with f_5, sine test 4.Si.A1, $\tau_{c,HP} = 20$ s, $\tau_{c,NREL} = 20$ s. Practical test with *gain* = 400 Nm/Hz and curtailment factor of 0.5.

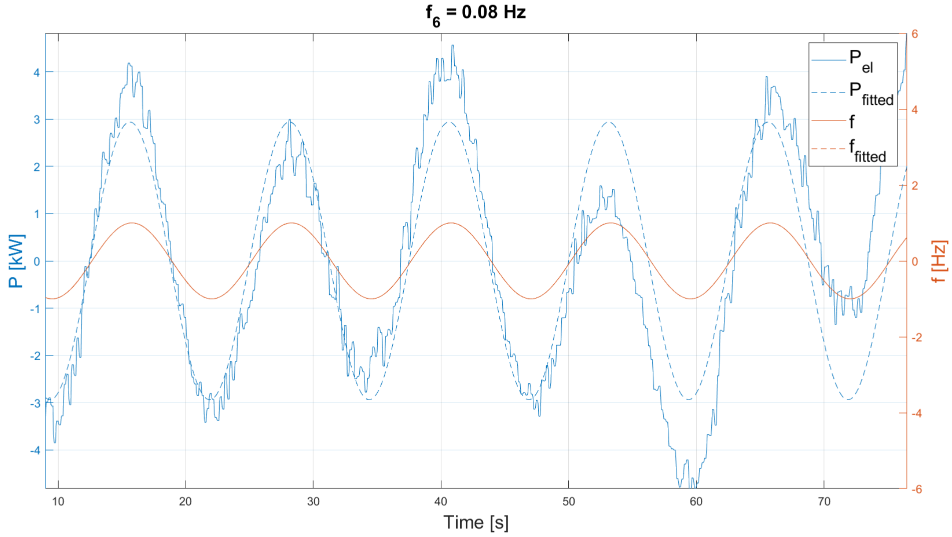

Figure A.11: Fitted sine with f_6, sine test 4.Si.A1, $\tau_{c,HP} = 20$ s, $\tau_{c,NREL} = 20$ s. Practical test with *gain* = 400 Nm/Hz and curtailment factor of 0.5.

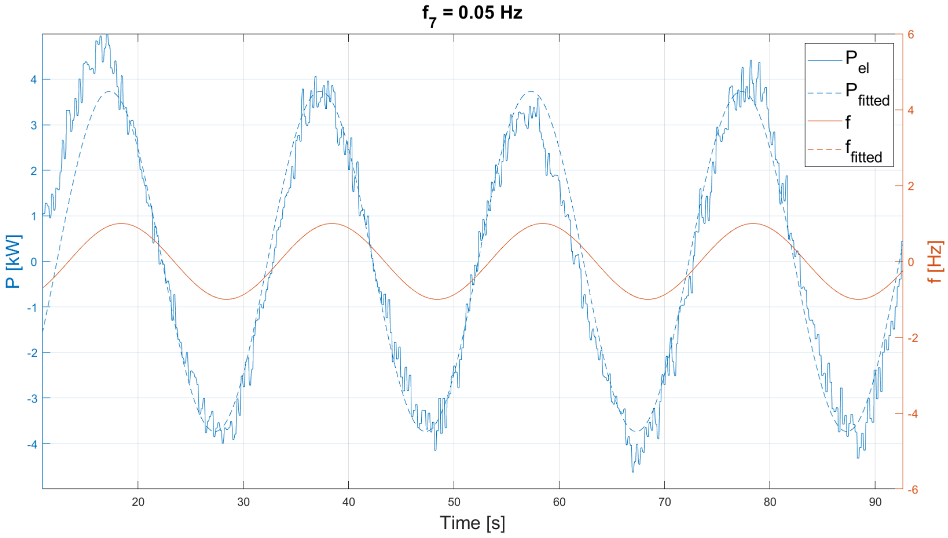

Figure A.12: Fitted sine with f_7, sine test 4.Si.A1, $\tau_{c,HP} = 20$ s, $\tau_{c,NREL} = 20$ s. Practical test with $gain = 400$ Nm/Hz and curtailment factor of 0.5.

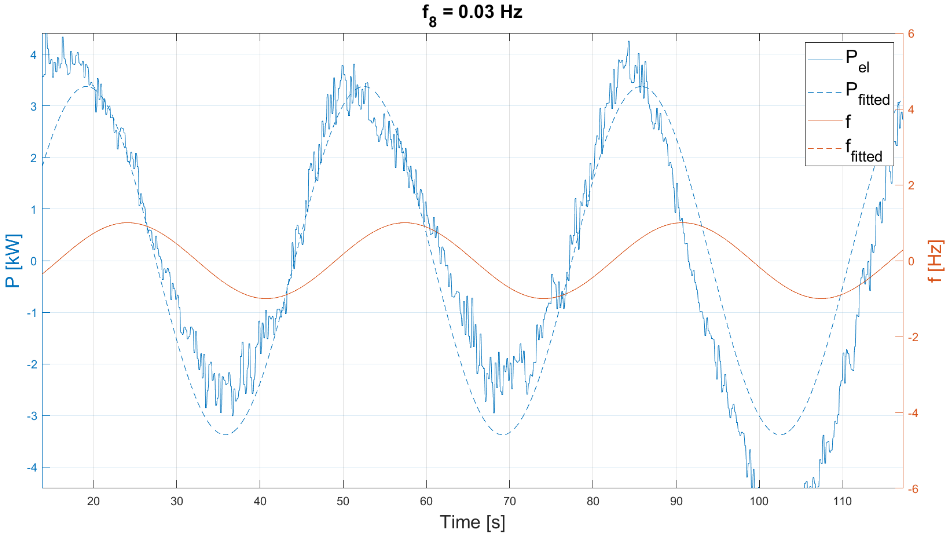

Figure A.13: Fitted sine with f_8, sine test 4.Si.A1, $\tau_{c,HP} = 20$ s, $\tau_{c,NREL} = 20$ s. Practical test with $gain = 400$ Nm/Hz and curtailment factor of 0.5.

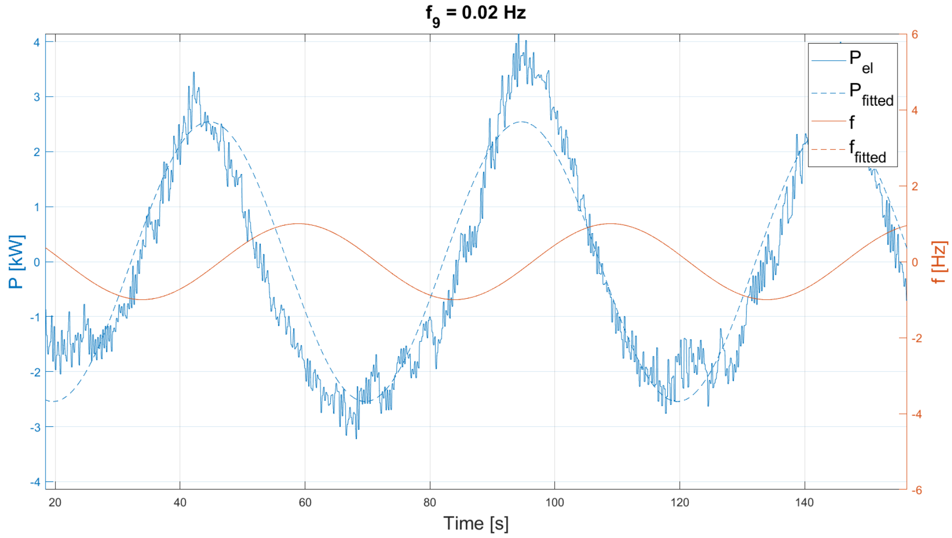

Figure A.14: Fitted sine with f_9, sine test 4.Si.A1, $\tau_{c,HP} = 20$ s, $\tau_{c,NREL} = 20$ s. Practical test with $gain = 400$ Nm/Hz and curtailment factor of 0.5.

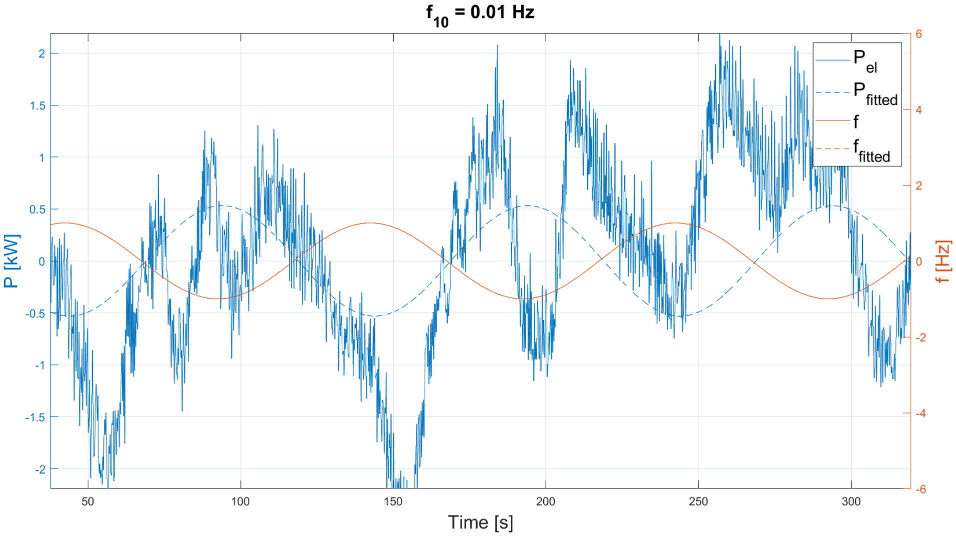

Figure A.15: Fitted sine with f_{10}, sine test 4.Si.A1, $\tau_{c,HP} = 20$ s, $\tau_{c,NREL} = 20$ s. Practical test with $gain = 400$ Nm/Hz and curtailment factor of 0.5.

A.2.2 Sine test 4.Si.A2

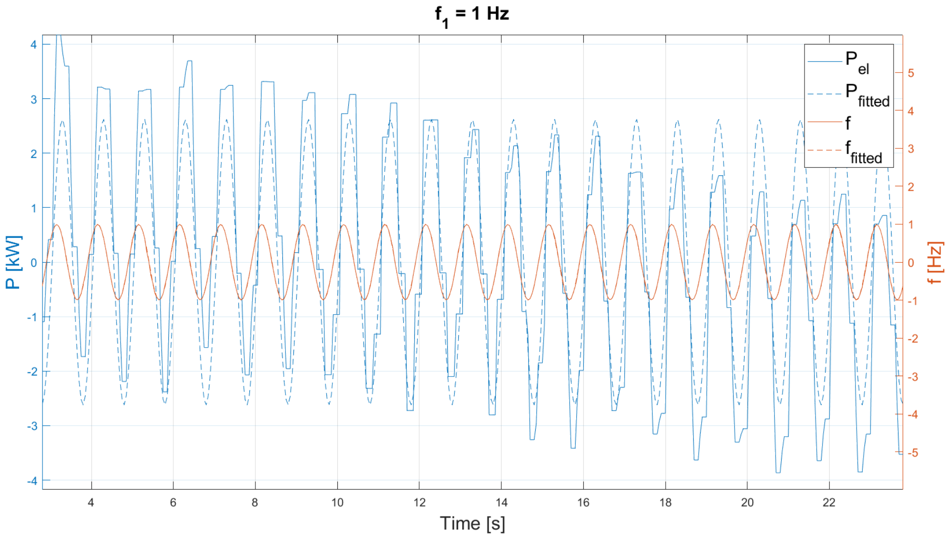

Figure A.16: Fitted sine with f_1, sine test 4.Si.A2, $\tau_{c,HP}$ not active, $\tau_{c,NREL} = 20$ s. Practical test with $gain = 400$ Nm/Hz and curtailment factor of 0.5.

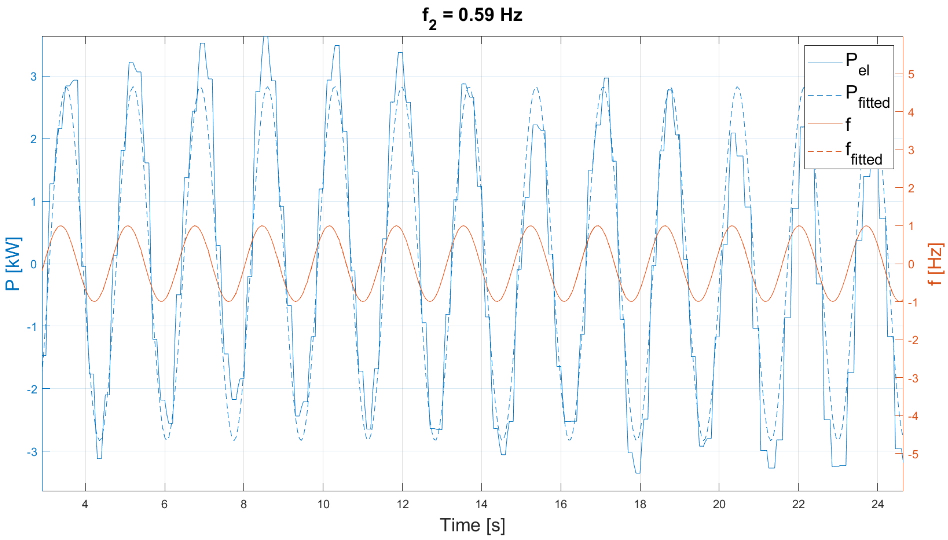

Figure A.17: Fitted sine with f_2, sine test 4.Si.A2, $\tau_{c,HP}$ not active, $\tau_{c,NREL} = 20$ s. Practical test with $gain = 400$ Nm/Hz and curtailment factor of 0.5.

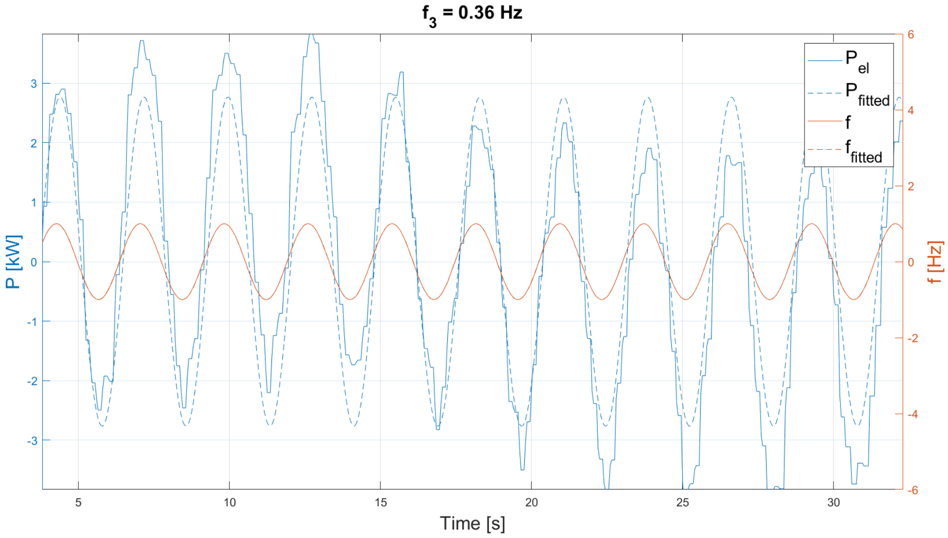

Figure A.18: Fitted sine with f_3, sine test 4.Si.A2, $\tau_{c,HP}$ not active, $\tau_{c,NREL} = 20$ s. Practical test with *gain* = 400 Nm/Hz and curtailment factor of 0.5.

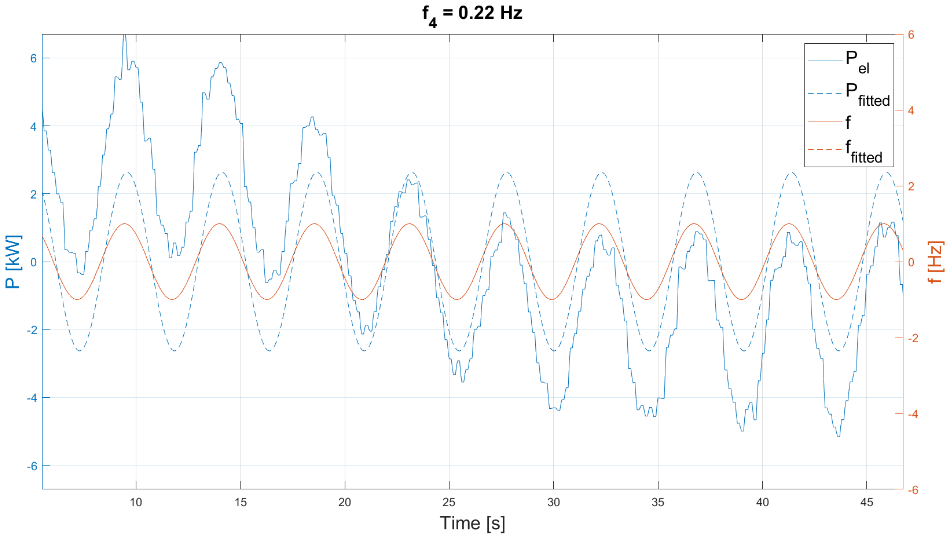

Figure A.19: Fitted sine with f_4, sine test 4.Si.A2, $\tau_{c,HP}$ not active, $\tau_{c,NREL} = 20$ s. Practical test with *gain* = 400 Nm/Hz and curtailment factor of 0.5.

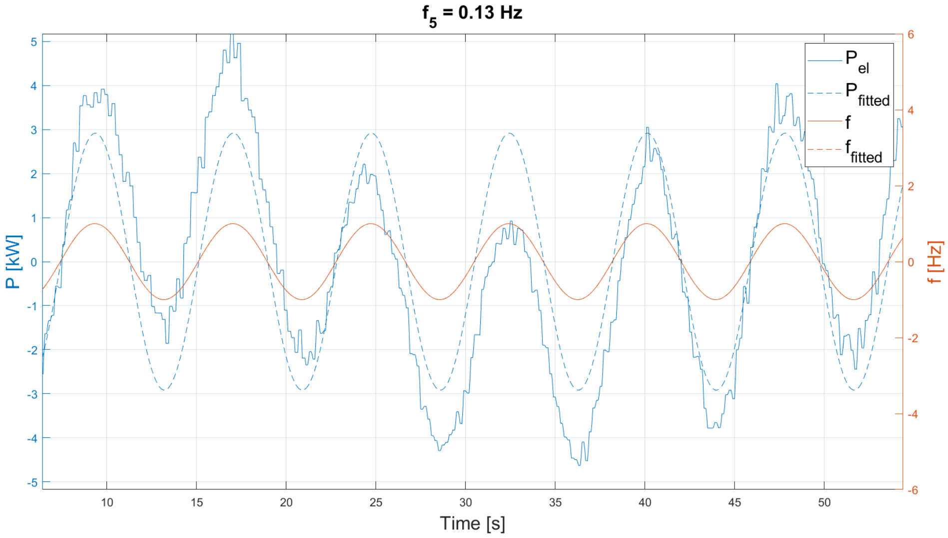

Figure A.20: Fitted sine with f_5, sine test 4.Si.A2, $\tau_{c,HP}$ not active, $\tau_{c,NREL} = 20$ s. Practical test with $gain = 400$ Nm/Hz and curtailment factor of 0.5.

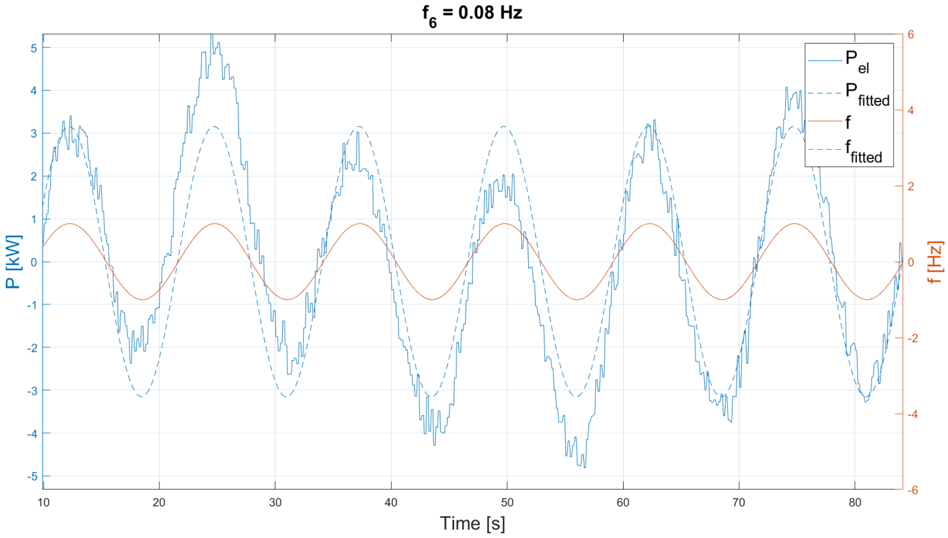

Figure A.21: Fitted sine with f_6, sine test 4.Si.A2, $\tau_{c,HP}$ not active, $\tau_{c,NREL} = 20$ s. Practical test with $gain = 400$ Nm/Hz and curtailment factor of 0.5.

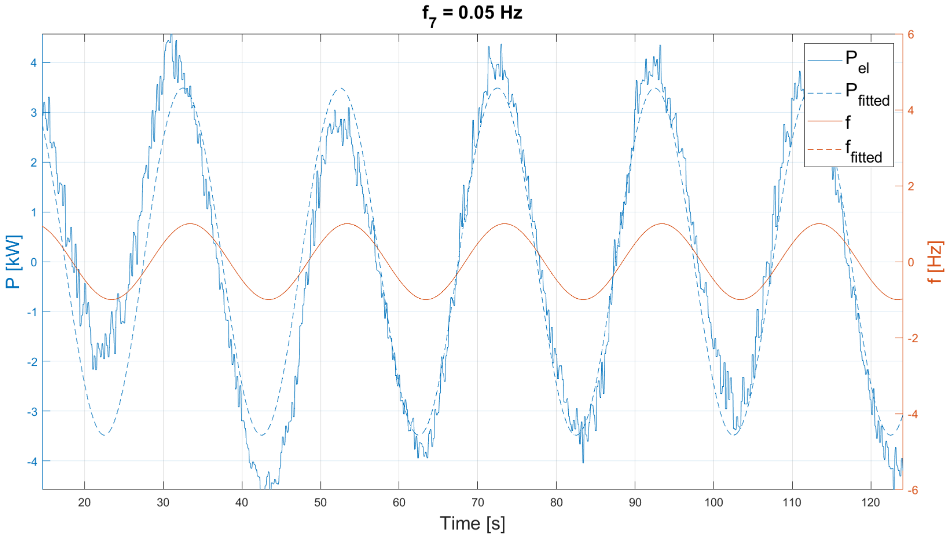

Figure A.22: Fitted sine with f_7, sine test 4.Si.A2, $\tau_{c,HP}$ not active, $\tau_{c,NREL} = 20$ s. Practical test with $gain = 400$ Nm/Hz and curtailment factor of 0.5.

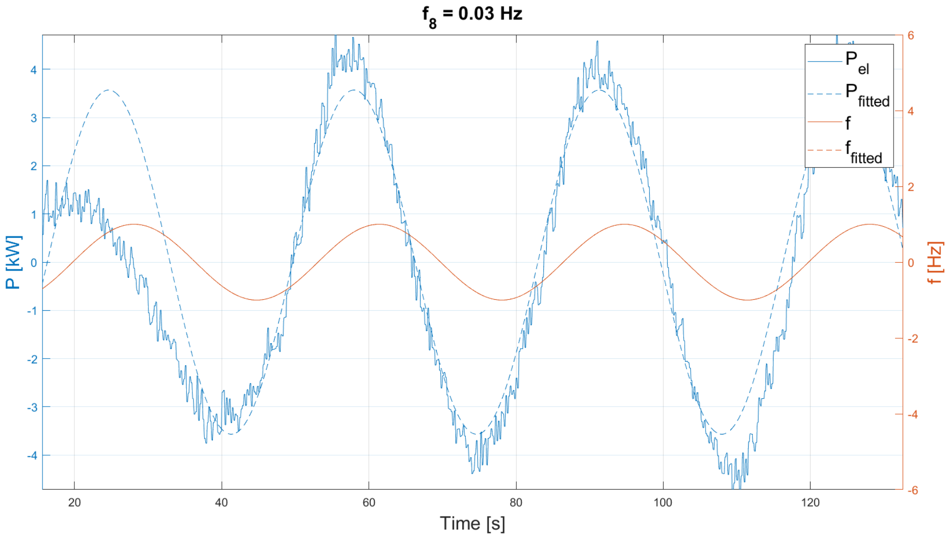

Figure A.23: Fitted sine with f_8, sine test 4.Si.A2, $\tau_{c,HP}$ not active, $\tau_{c,NREL} = 20$ s. Practical test with $gain = 400$ Nm/Hz and curtailment factor of 0.5.

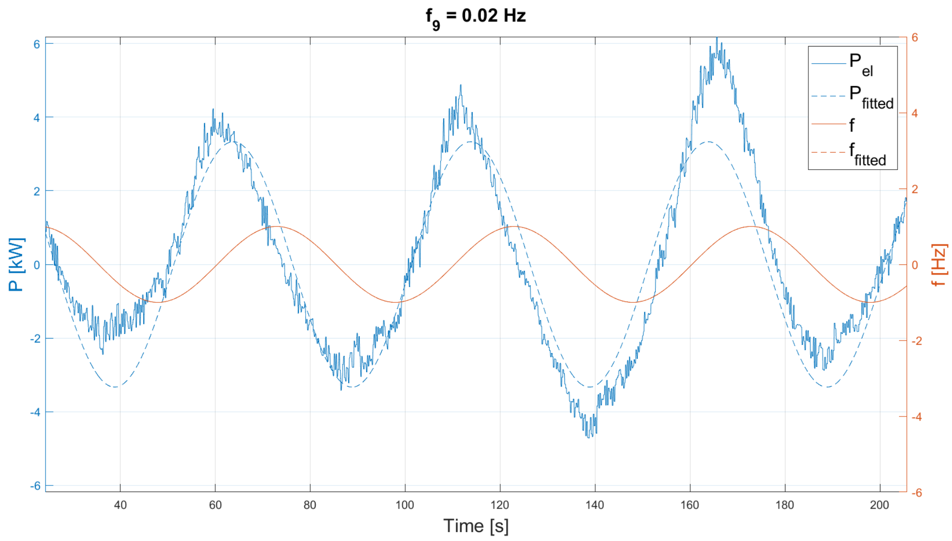

Figure A.24: Fitted sine with f_9, sine test 4.Si.A2, $\tau_{c,HP}$ not active, $\tau_{c,NREL} = 20$ s. Practical test with $gain = 400$ Nm/Hz and curtailment factor of 0.5.

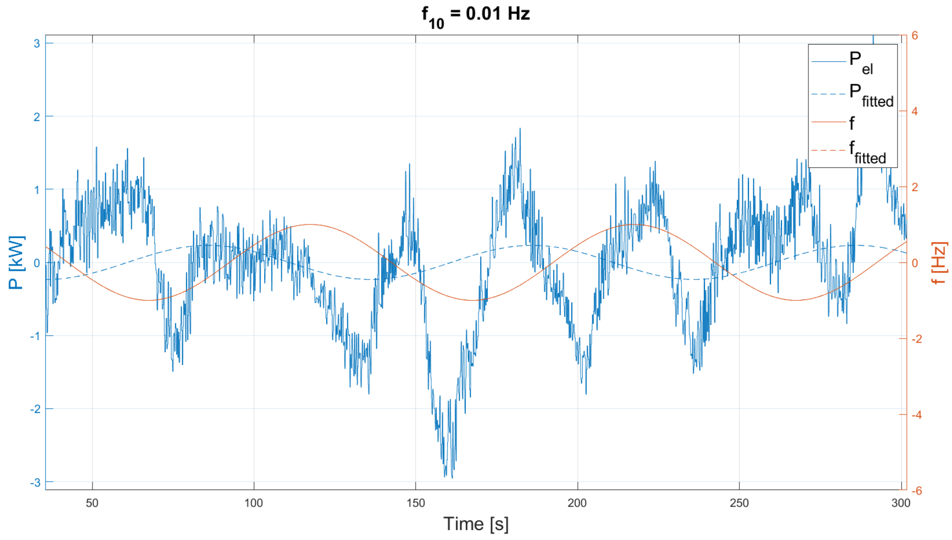

Figure A.25: Fitted sine with f_{10}, sine test 4.Si.A2, $\tau_{c,HP}$ not active, $\tau_{c,NREL} = 20$ s. Practical test with $gain = 400$ Nm/Hz and curtailment factor of 0.5.

A.2.3 Sine test 4.Si.A3

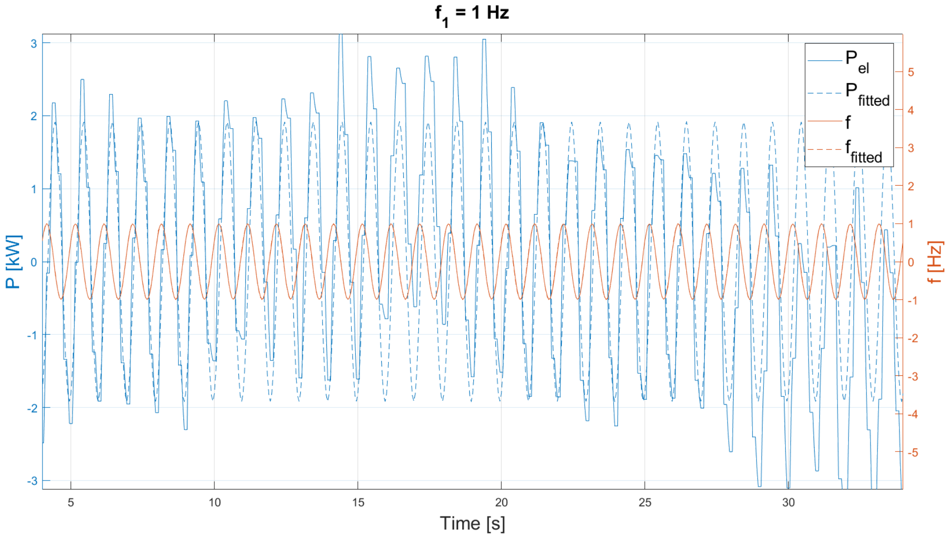

Figure A.26: Fitted sine with f_1, sine test 4.Si.A3, $\tau_{c,HP} = 20$ s, $\tau_{c,NREL}$ not active. Practical test with *gain* = 400 Nm/Hz and curtailment factor of 0.5.

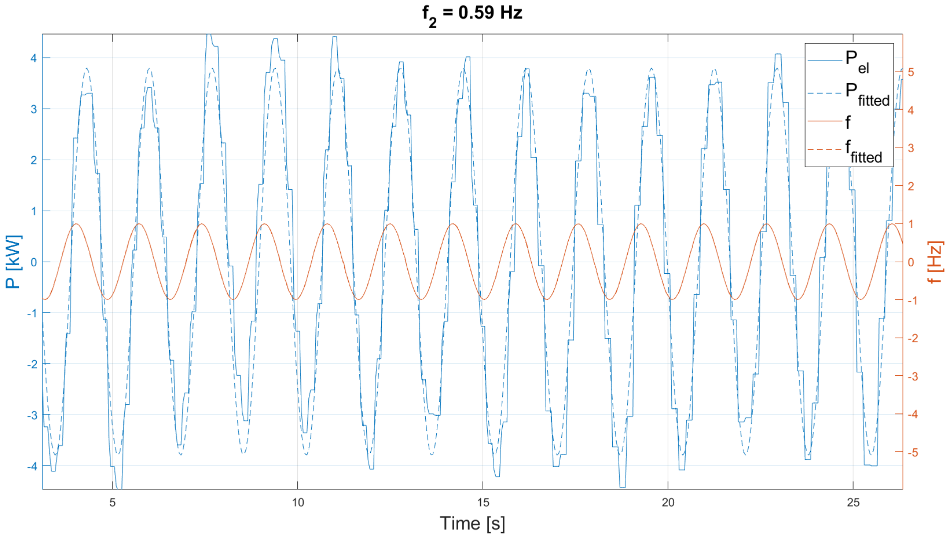

Figure A.27: Fitted sine with f_2, sine test 4.Si.A3, $\tau_{c,HP} = 20$ s, $\tau_{c,NREL}$ not active. Practical test with *gain* = 400 Nm/Hz and curtailment factor of 0.5.

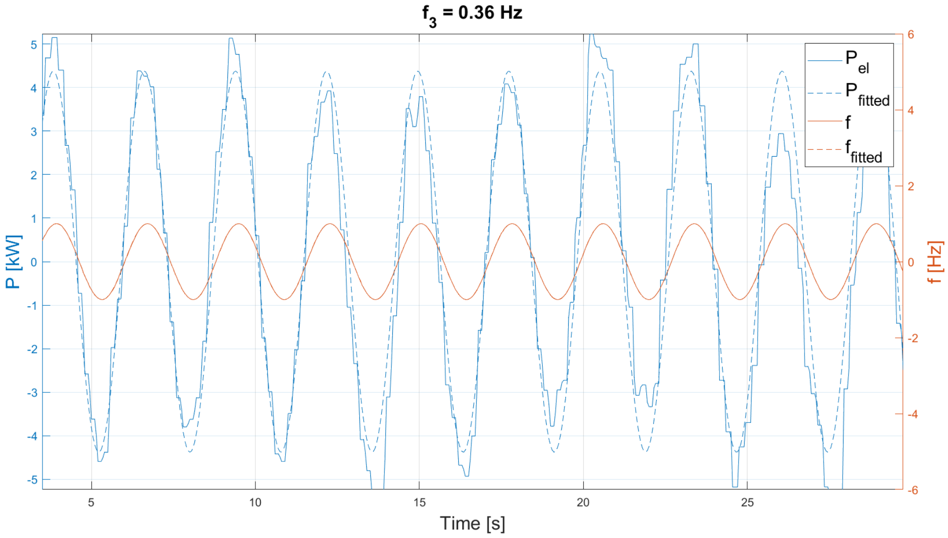

Figure A.28: Fitted sine with f_3, sine test 4.Si.A3, $\tau_{c,HP} = 20$ s, $\tau_{c,NREL}$ not active. Practical test with *gain* = 400 Nm/Hz and curtailment factor of 0.5.

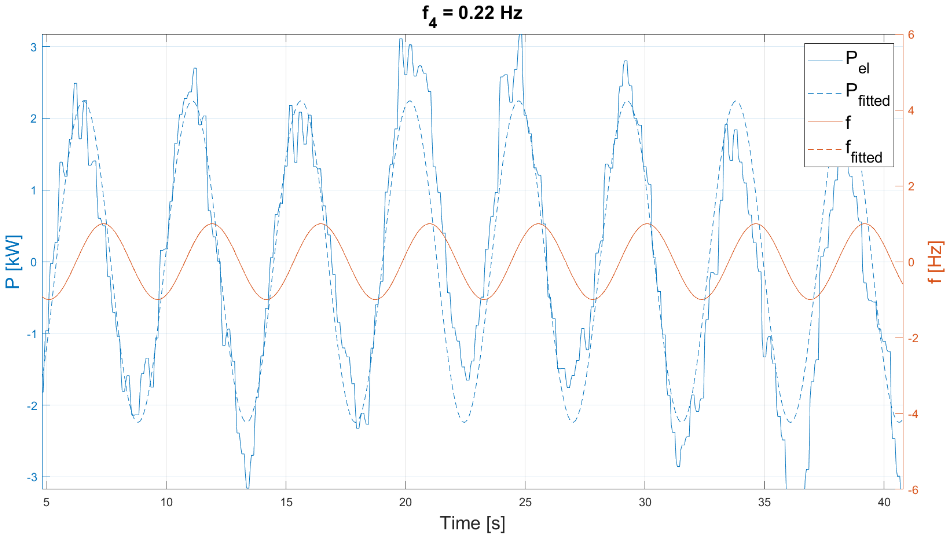

Figure A.29: Fitted sine with f_4, sine test 4.Si.A3, $\tau_{c,HP} = 20$ s, $\tau_{c,NREL}$ not active. Practical test with *gain* = 400 Nm/Hz and curtailment factor of 0.5.

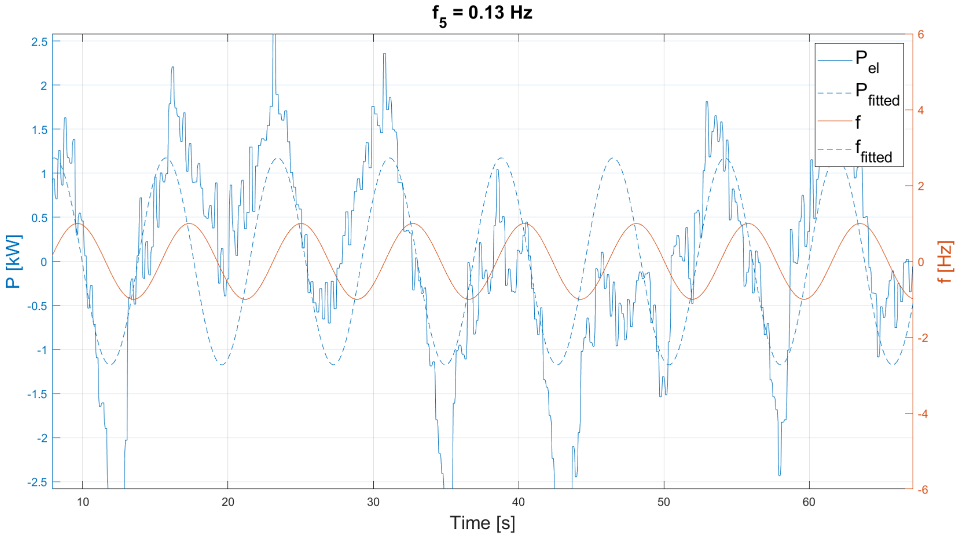

Figure A.30: Fitted sine with f_5, sine test 4.Si.A3, $\tau_{c,HP} = 20$ s, $\tau_{c,NREL}$ not active. Practical test with $gain = 400$ Nm/Hz and curtailment factor of 0.5.

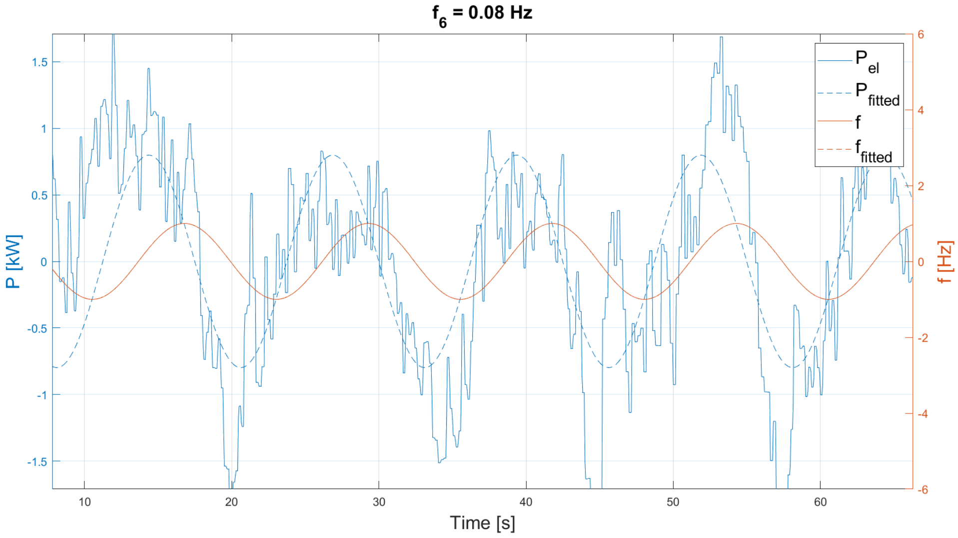

Figure A.31: Fitted sine with f_6, sine test 4.Si.A3, $\tau_{c,HP} = 20$ s, $\tau_{c,NREL}$ not active. Practical test with $gain = 400$ Nm/Hz and curtailment factor of 0.5.

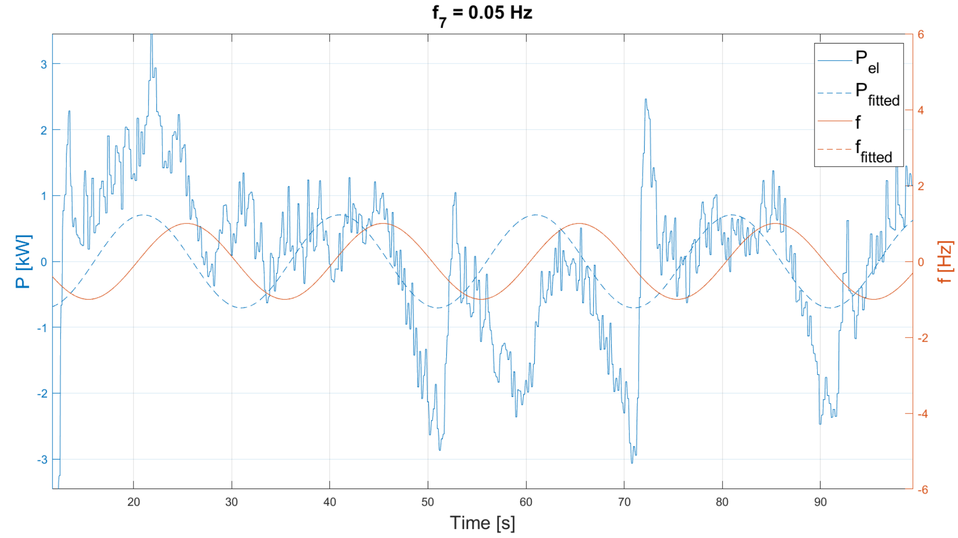

Figure A.32: Fitted sine with f_7, sine test 4.Si.A3, $\tau_{c,HP} = 20$ s, $\tau_{c,NREL}$ not active. Practical test with $gain = 400$ Nm/Hz and curtailment factor of 0.5.

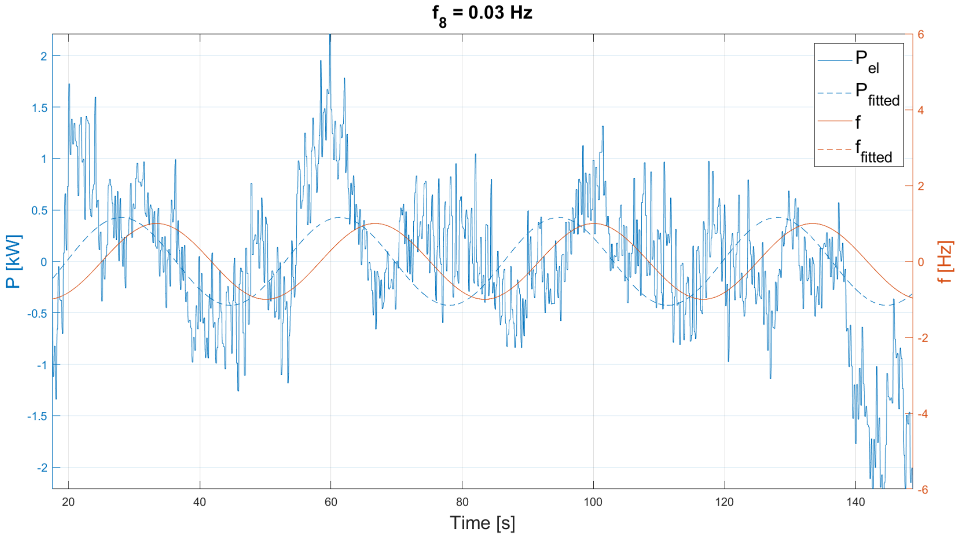

Figure A.33: Fitted sine with f_8, sine test 4.Si.A3, $\tau_{c,HP} = 20$ s, $\tau_{c,NREL}$ not active. Practical test with $gain = 400$ Nm/Hz and curtailment factor of 0.5.

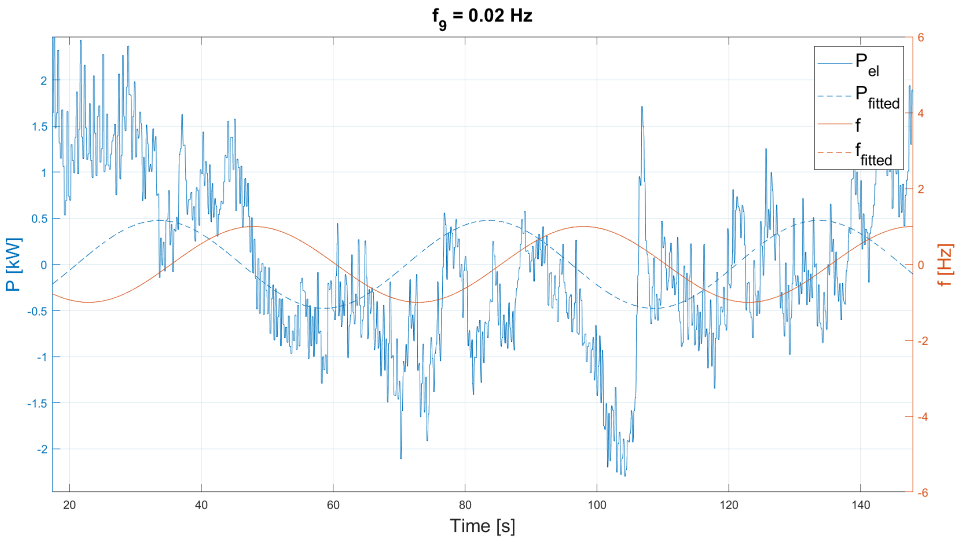

Figure A.34: Fitted sine with f_9, sine test 4.Si.A3, $\tau_{c,HP} = 20$ s, $\tau_{c,NREL}$ not active. Practical test with *gain* = 400 Nm/Hz and curtailment factor of 0.5.

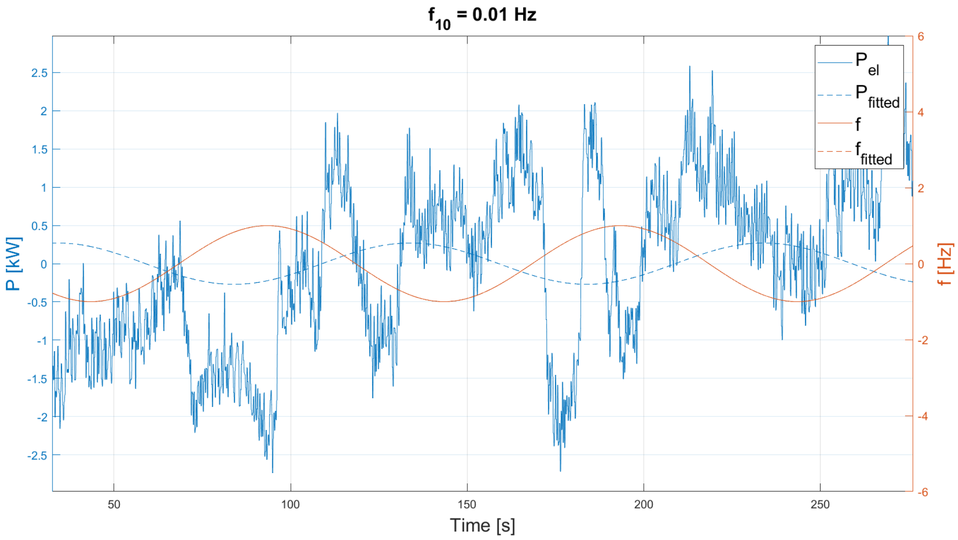

Figure A.35: Fitted sine with f_{10}, sine test 4.Si.A3, $\tau_{c,HP} = 20$ s, $\tau_{c,NREL}$ not active. Practical test with *gain* = 400 Nm/Hz and curtailment factor of 0.5.

A.2.4 Sine test 4.Si.A4

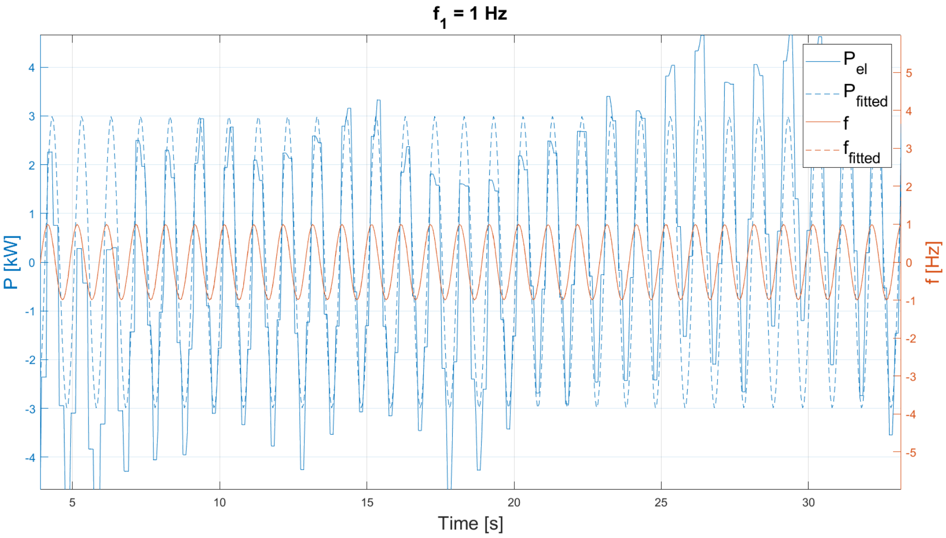

Figure A.36: Fitted sine with f_1, sine test 4.Si.A4, $\tau_{c,HP}$ not active, $\tau_{c,NREL}$ not active. Practical test with $gain$ = 400 Nm/Hz and curtailment factor of 0.5.

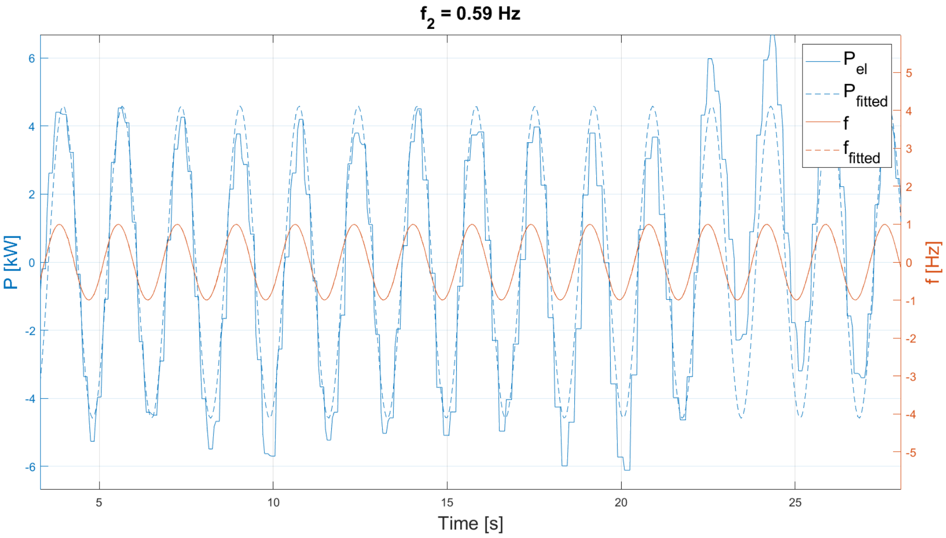

Figure A.37: Fitted sine with f_2, sine test 4.Si.A4, $\tau_{c,HP}$ not active, $\tau_{c,NREL}$ not active. Practical test with $gain$ = 400 Nm/Hz and curtailment factor of 0.5.

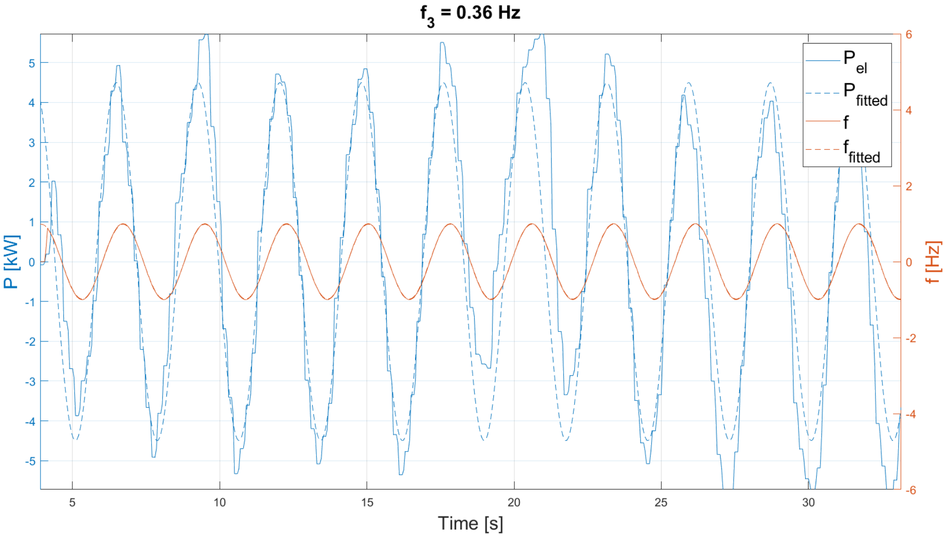

Figure A.38: Fitted sine with f_3, sine test 4.Si.A4, $\tau_{c,HP}$ not active, $\tau_{c,NREL}$ not active. Practical test with $gain$ = 400 Nm/Hz and curtailment factor of 0.5.

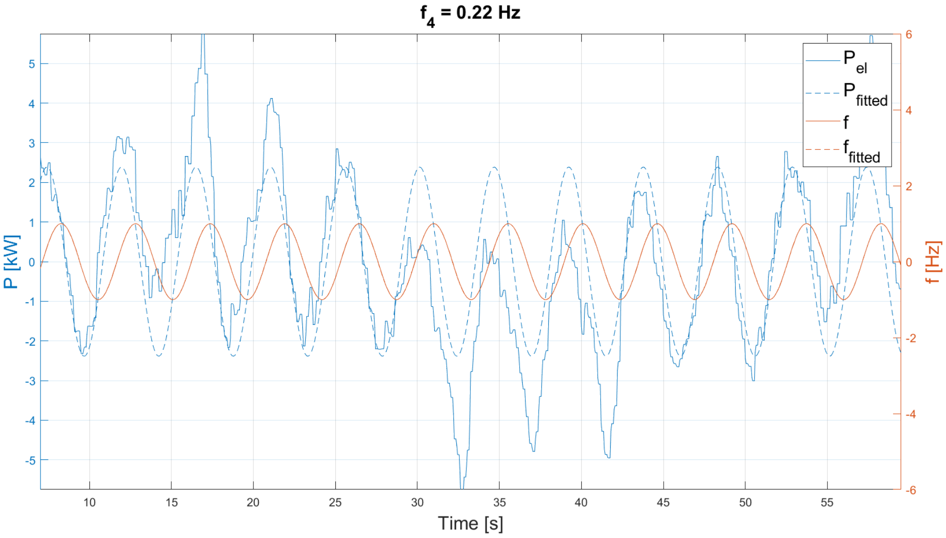

Figure A.39: Fitted sine with f_4, sine test 4.Si.A4, $\tau_{c,HP}$ not active, $\tau_{c,NREL}$ not active. Practical test with $gain$ = 400 Nm/Hz and curtailment factor of 0.5.

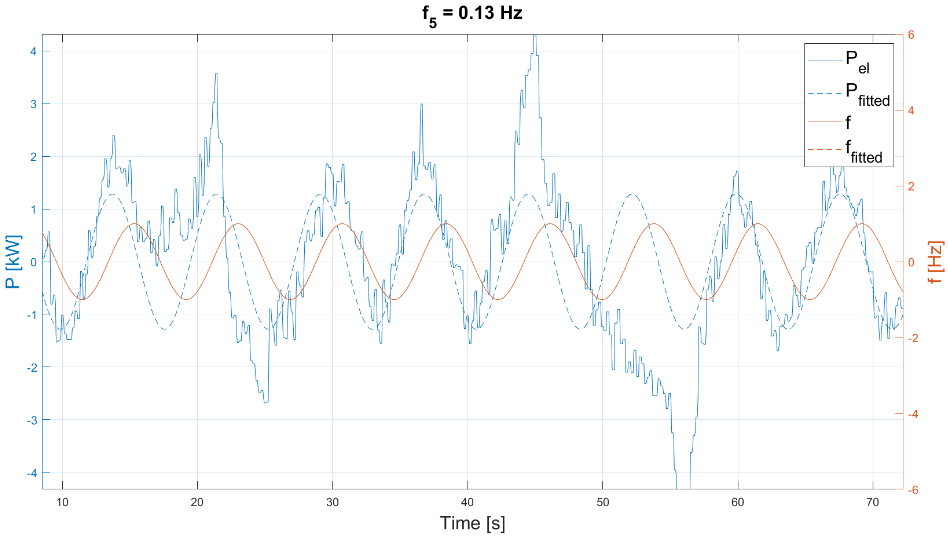

Figure A.40: Fitted sine with f_5, sine test 4.Si.A4, $\tau_{c,HP}$ not active, $\tau_{c,NREL}$ not active. Practical test with $gain = 400$ Nm/Hz and curtailment factor of 0.5.

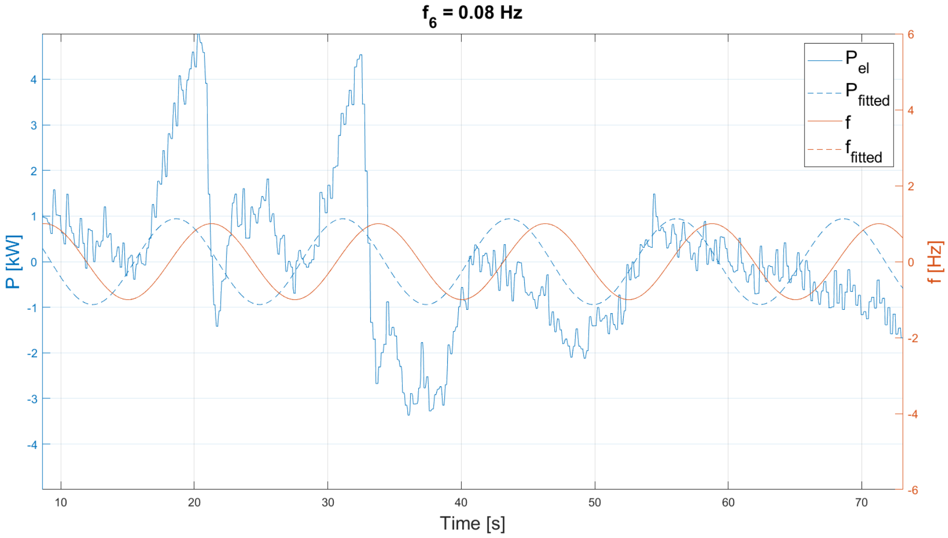

Figure A.41: Fitted sine with f_6, sine test 4.Si.A4, $\tau_{c,HP}$ not active, $\tau_{c,NREL}$ not active. Practical test with $gain = 400$ Nm/Hz and curtailment factor of 0.5.

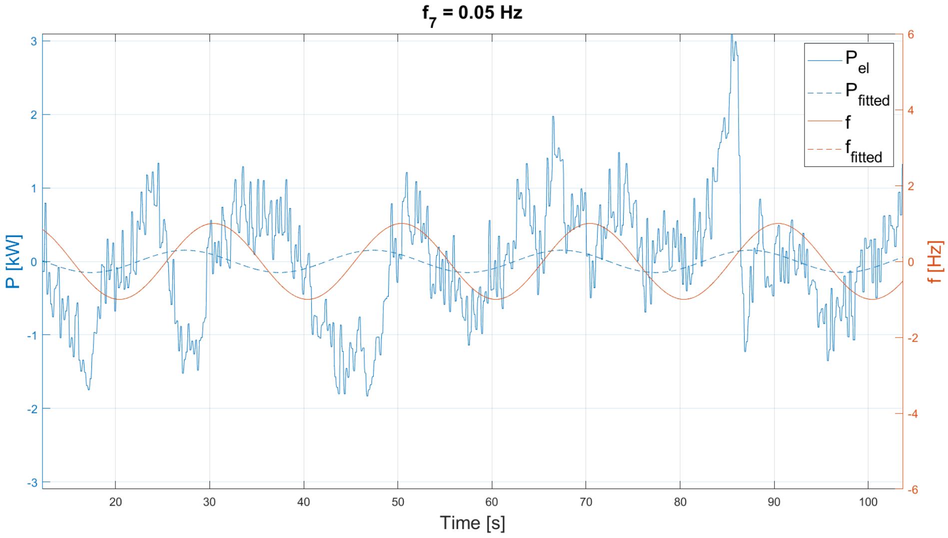

Figure A.42: Fitted sine with f_7, sine test 4.Si.A4, $\tau_{c,HP}$ not active, $\tau_{c,NREL}$ not active. Practical test with $gain = 400$ Nm/Hz and curtailment factor of 0.5.

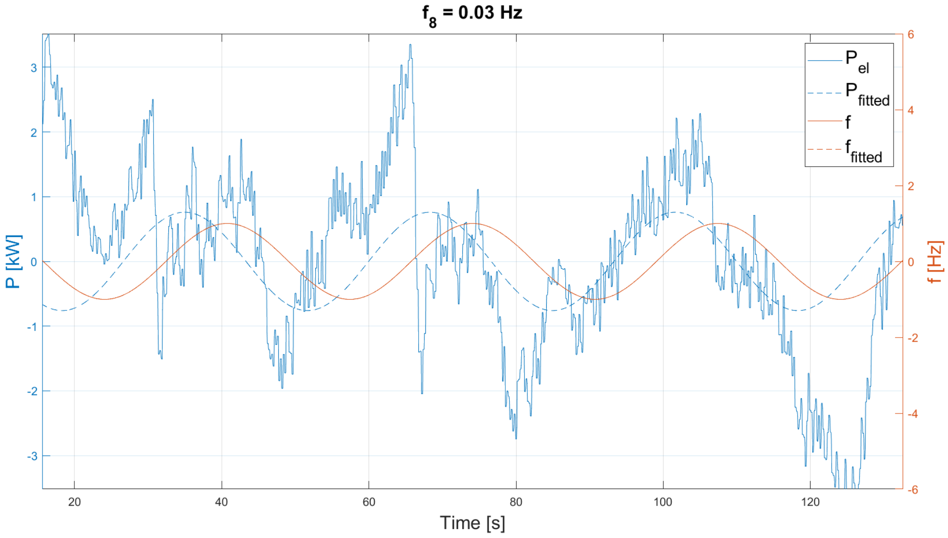

Figure A.43: Fitted sine with f_8, sine test 4.Si.A4, $\tau_{c,HP}$ not active, $\tau_{c,NREL}$ not active. Practical test with $gain = 400$ Nm/Hz and curtailment factor of 0.5.

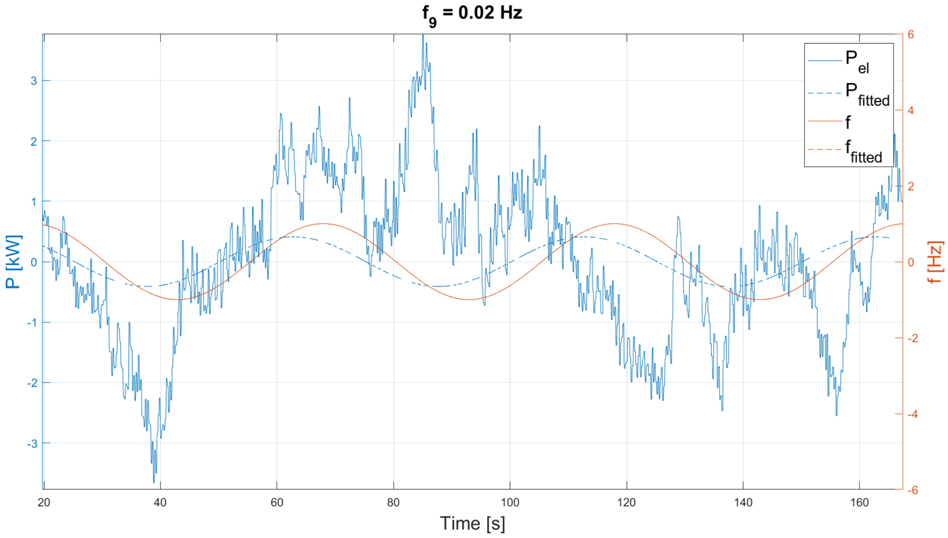

Figure A.44: Fitted sine with f_9, sine test 4.Si.A4, $\tau_{c,HP}$ not active, $\tau_{c,NREL}$ not active. Practical test with *gain* = 400 Nm/Hz and curtailment factor of 0.5.

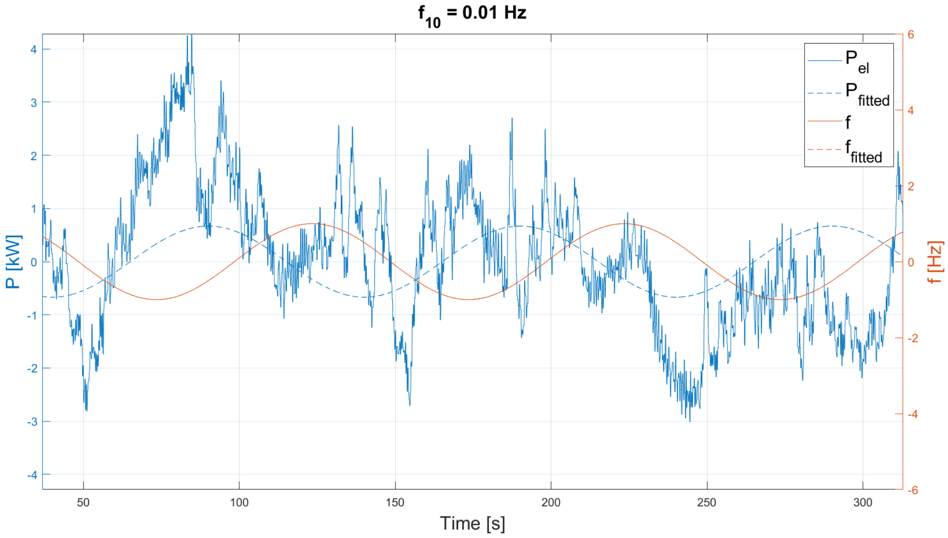

Figure A.45: Fitted sine with f_{10}, sine test 4.Si.A4, $\tau_{c,HP}$ not active, $\tau_{c,NREL}$ not active. Practical test with *gain* = 400 Nm/Hz and curtailment factor of 0.5.

A.3 Prototype B

Additional results from protoype B are illustrated in this section.

A.3.1 Step test St.B1

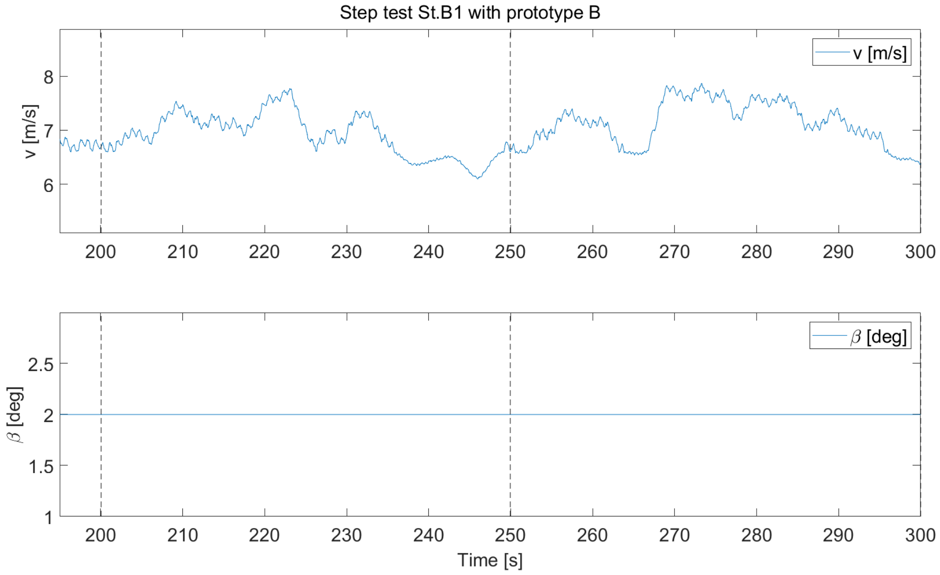

Figure A.46: Step test St.B1, $\tau_{c,HP} = 10$ s, $\tau_{c,NEM} = 10$ s. Simulation with varying wind velocity and *gain* = 1000 W/Hz.

A.3.2 Step test St.B2

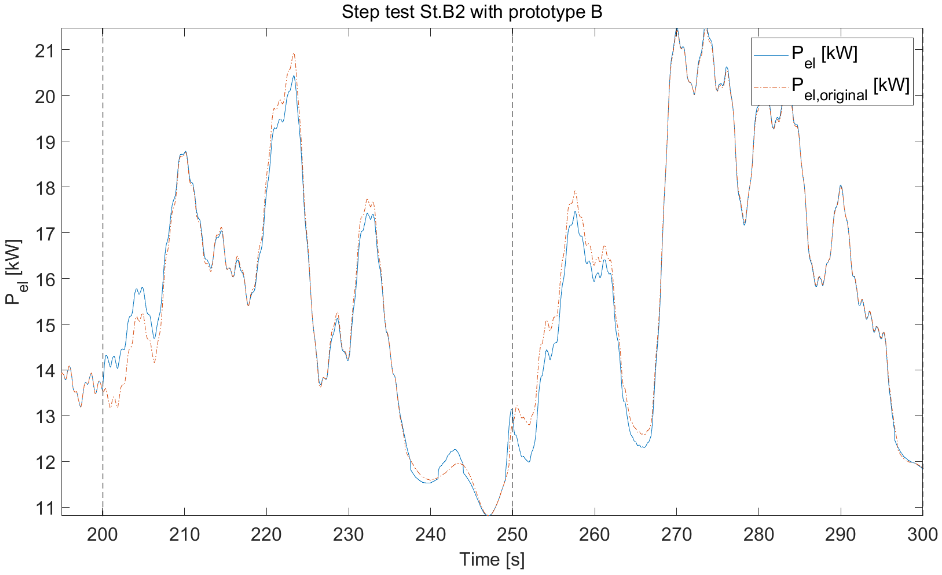

Figure A.47: Step test St.B2, $\tau_{c,HP} = 60$ s, $\tau_{c,NEM} = 10$ s. Simulation with varying wind velocity and *gain* = 1000 W/Hz.

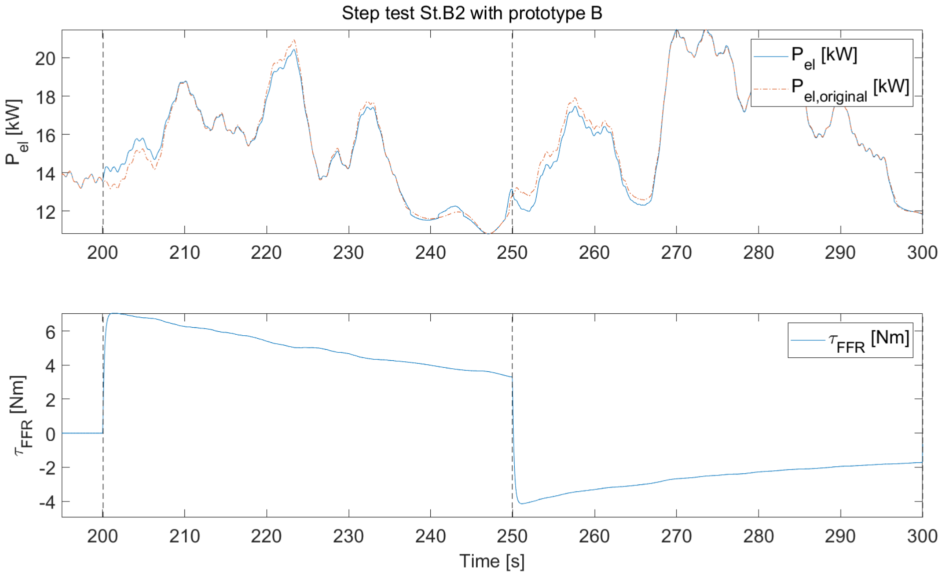

Figure A.48: Step test St.B2, $\tau_{c,HP} = 60$ s, $\tau_{c,NEM} = 10$ s. Simulation with varying wind velocity and *gain* = 1000 W/Hz.

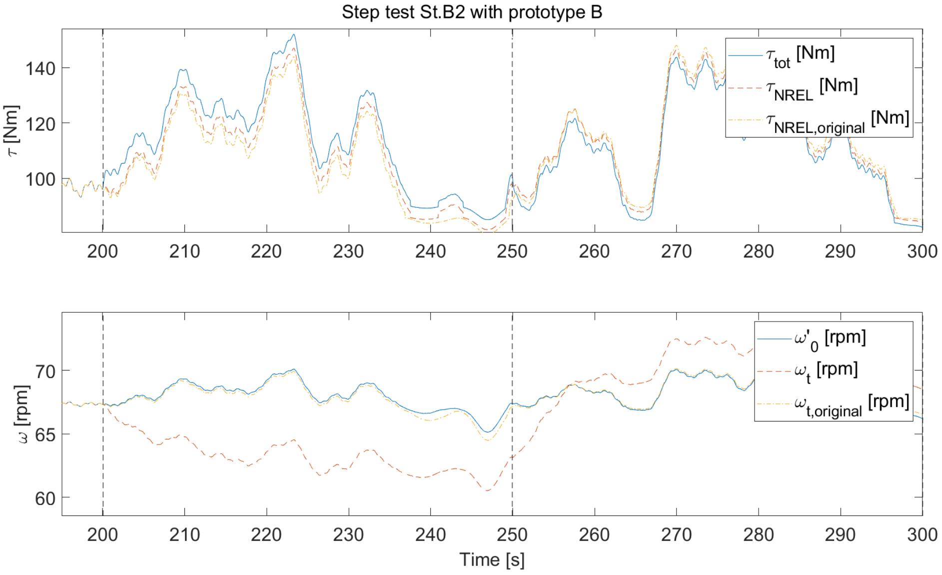

Figure A.49: Step test St.B2, $\tau_{c,HP} = 60$ s, $\tau_{c,NEM} = 10$ s. Simulation with varying wind velocity and *gain* = 1000 W/Hz.

A.3.3 Step test St.B3

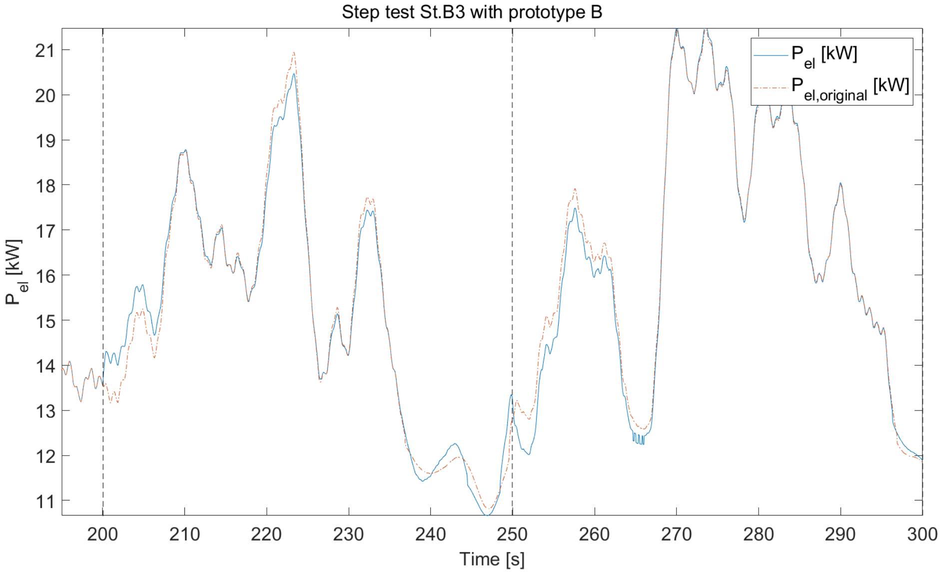

Figure A.50: Step test St.B3, $\tau_{c,HP} = 10$ s, $\tau_{c,NEM} = 60$ s. Simulation with varying wind velocity and *gain* = 1000 W/Hz.

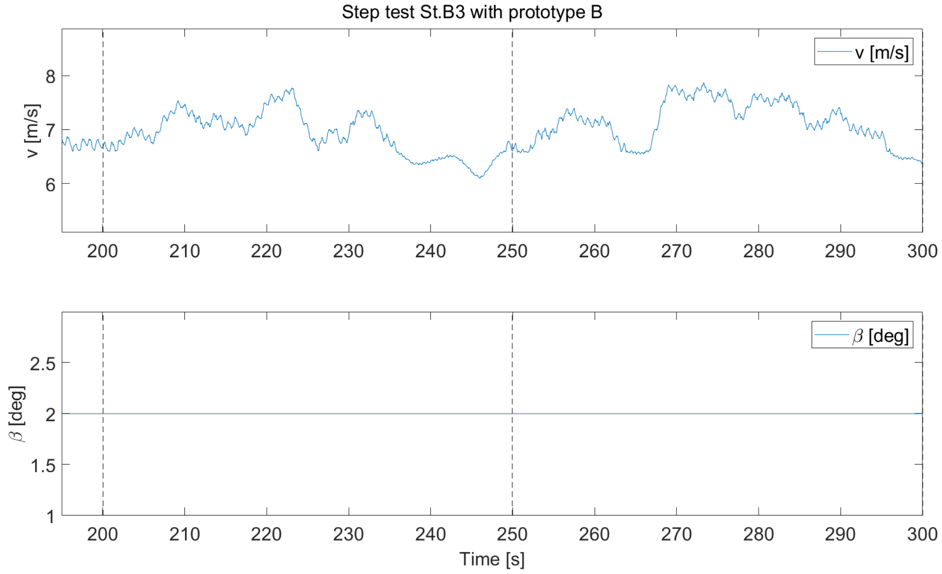

Figure A.51: Step test St.B3, $\tau_{c,HP} = 10$ s, $\tau_{c,NEM} = 60$ s. Simulation with varying wind velocity and *gain* = 1000 W/Hz.

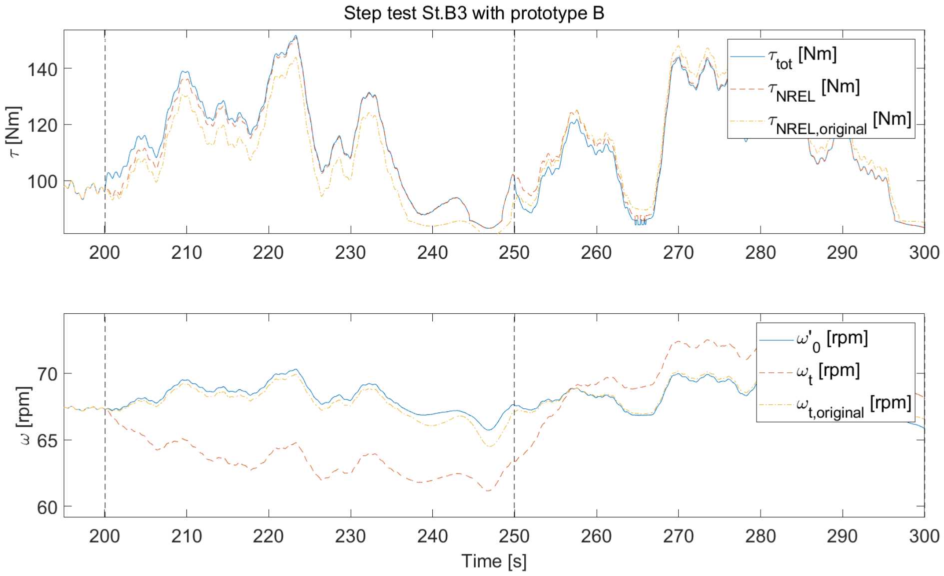

Figure A.52: Step test St.B3, $\tau_{c,HP} = 10$ s, $\tau_{c,NEM} = 60$ s. Simulation with varying wind velocity and *gain* = 1000 W/Hz.

A.3.4 Step test St.B4

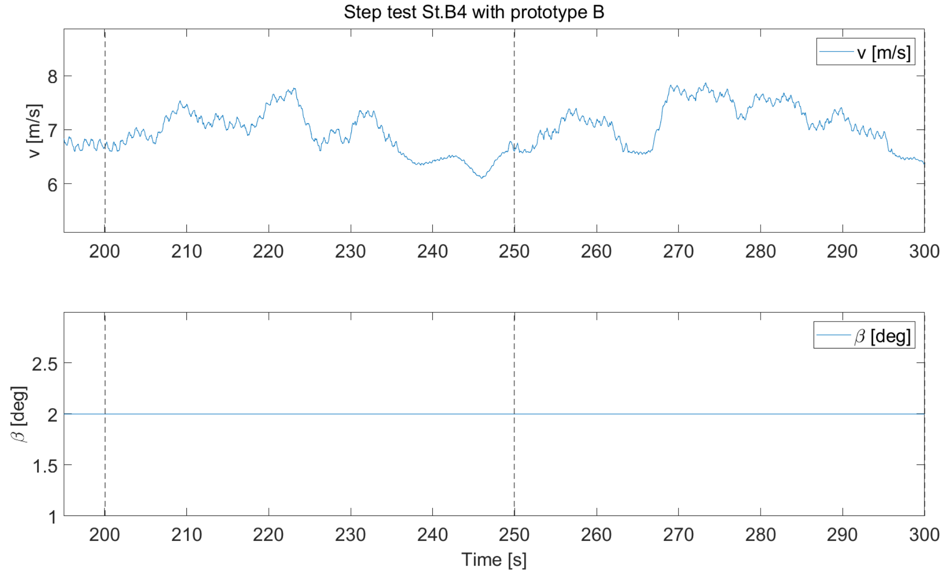

Figure A.53: Step test St.B4, $\tau_{c,HP} = 60$ s, $\tau_{c,NEM} = 60$ s. Simulation with varying wind velocity and *gain* = 1000 W/Hz.

A.3.5 Step test 5.St.B2

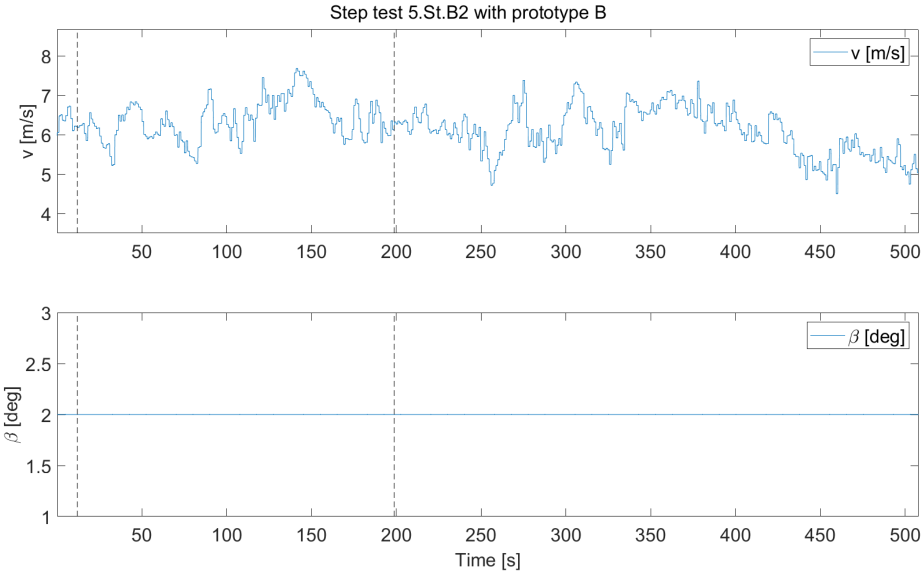

Figure A.54: Step test 5.St.B2, $\tau_{c,HP} = 60$ s, $\tau_{c,NEM} = 10$ s. Practical test with $gain = 1000$ W/Hz.

A.3.6 Step test 5.St.B3

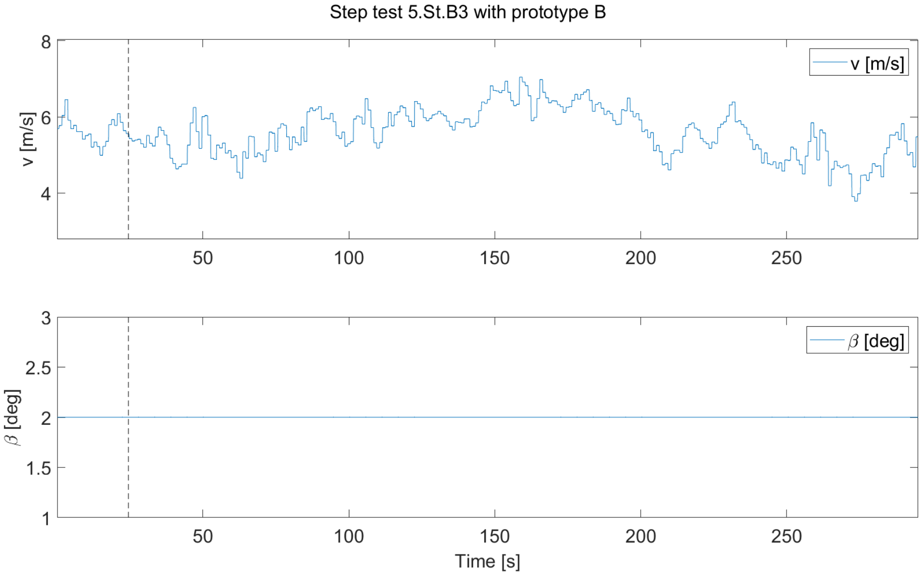

Figure A.55: Step test 5.St.B3, $\tau_{c,HP} = 10$ s, $\tau_{c,NEM} = 60$ s. Practical test with $gain = 1000$ W/Hz.

A.3.7 Step test 5.St.B4

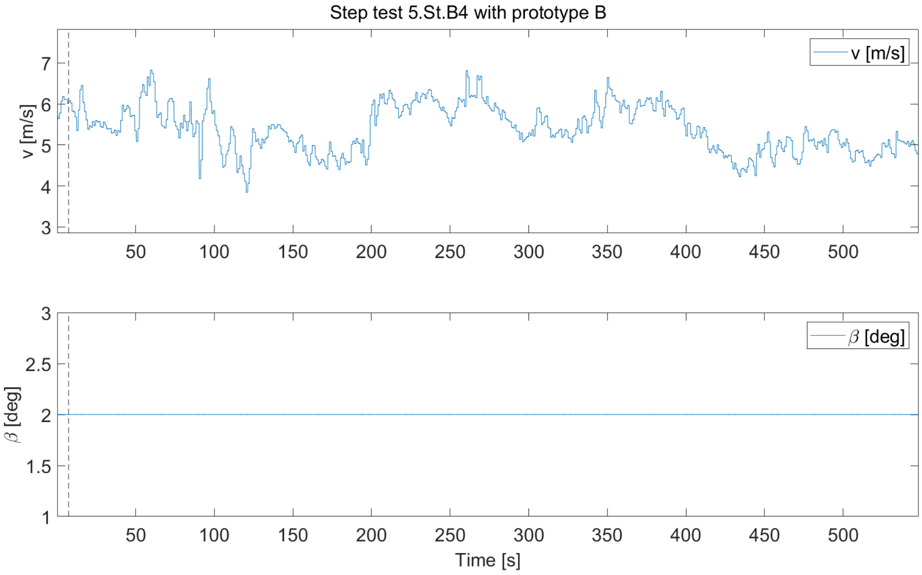

Figure A.56: Step test 5.St.B4, $\tau_{c,HP} = 60$ s, $\tau_{c,NEM} = 60$ s. Practical test with *gain* = 1000 W/Hz. A curtailment factor of 0.5 was used.

A.3.8 Step test 5.St.B5

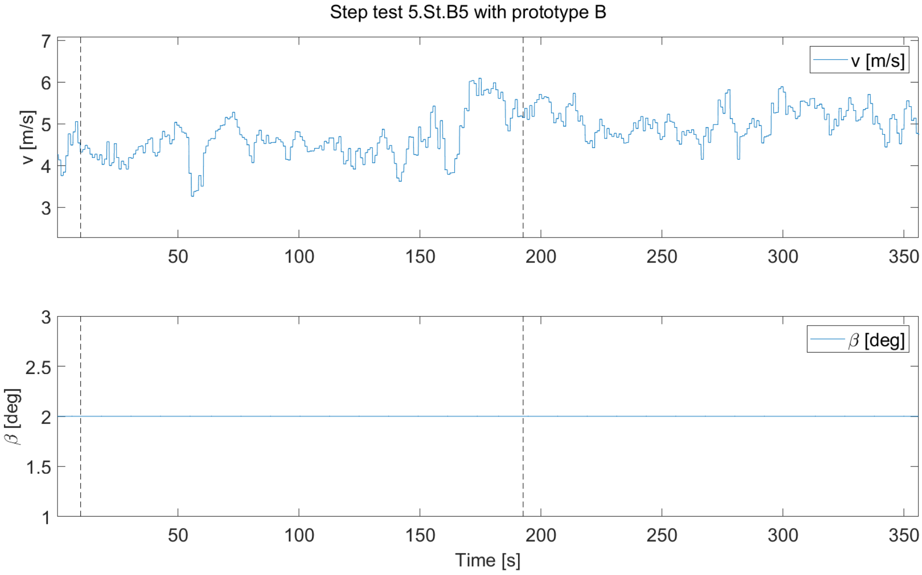

Figure A.57: Step test 5.St.B5, $\tau_{c,HP} = 20$ s, $\tau_{c,NEM} = 20$ s. Practical test with *gain* = 1000 W/Hz.

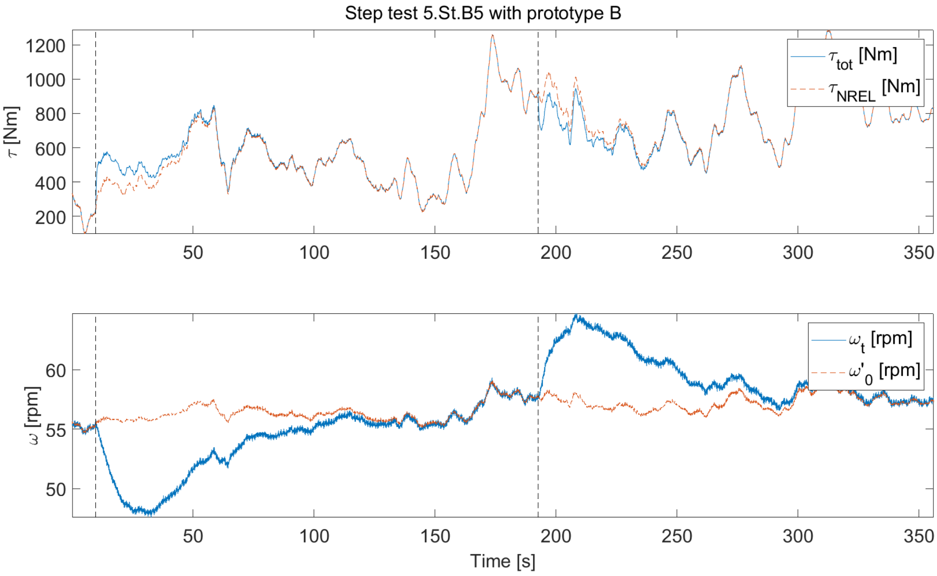

Figure A.58: Step test 5.St.B5, $\tau_{c,HP} = 20$ s, $\tau_{c,NEM} = 20$ s. Practical test with $gain = 1000$ W/Hz.

A.3.9 Disturbance test D.B3

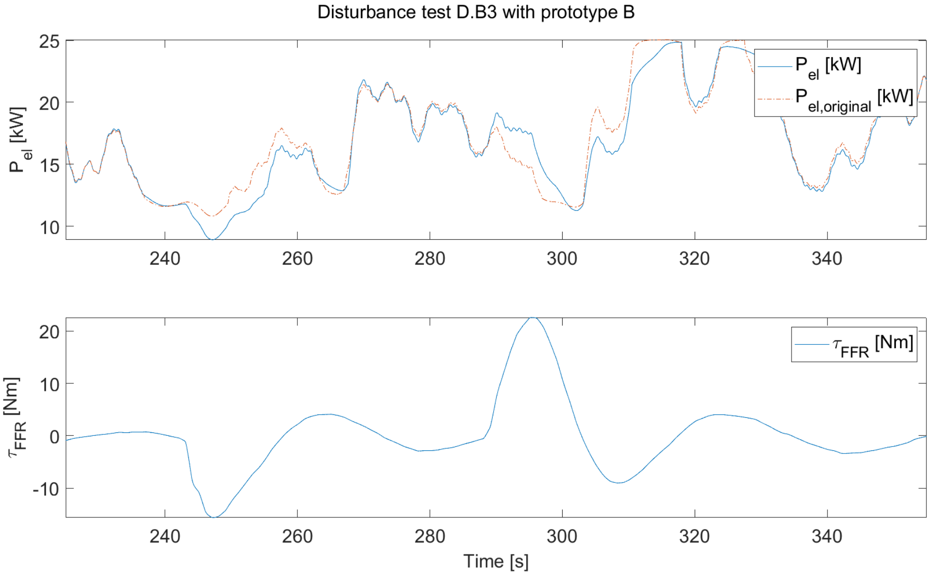

Figure A.59: Disturbance test D.B3, $\tau_{c,HP} = 20$ s, $\tau_{c,NEM} = 40$ s. Simulation with varying wind velocity and $gain = 6000$ W/Hz.

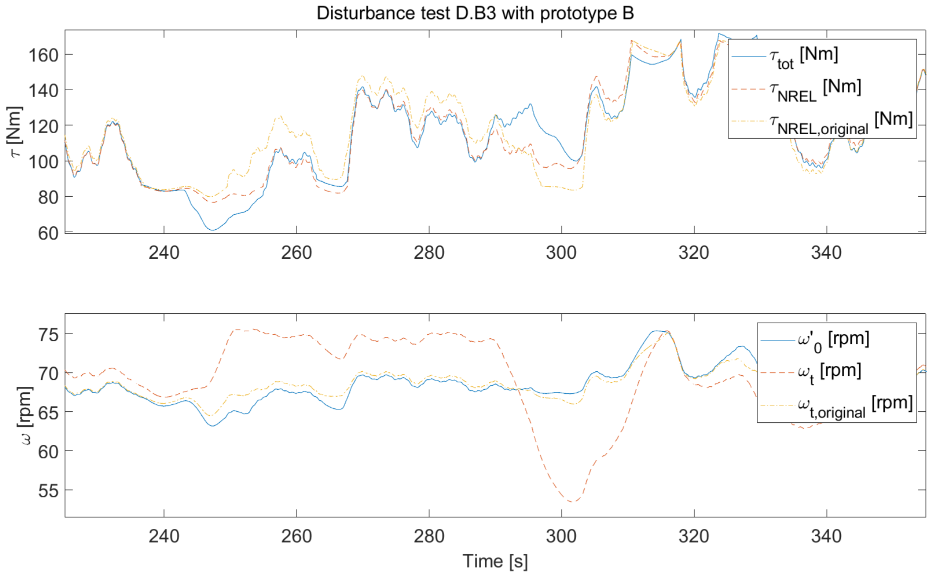

Figure A.60: Disturbance test D.B3, $\tau_{c,HP} = 20$ s, $\tau_{c,NEM} = 40$ s. Simulation with varying wind velocity and $gain = 6000$ W/Hz.

A.3.10 Disturbance test D.B4

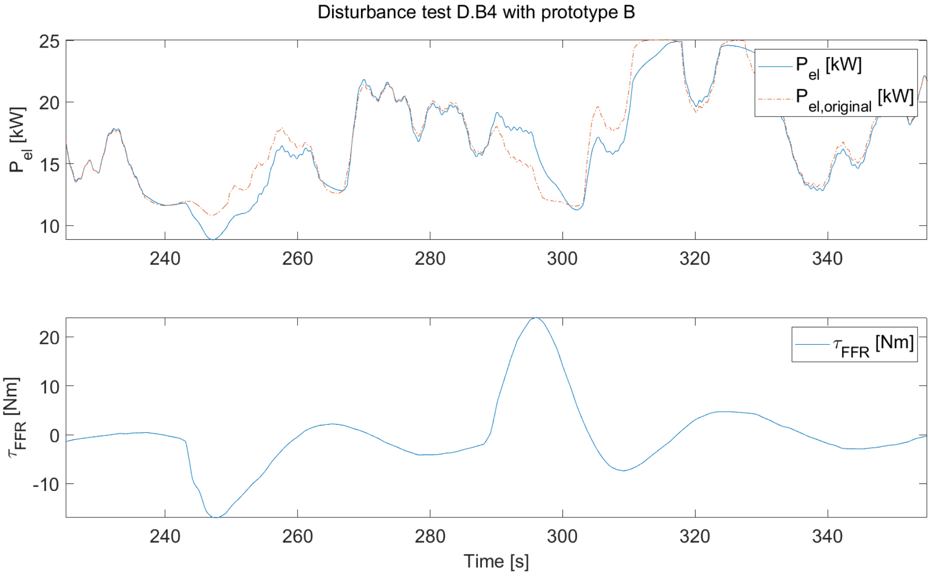

Figure A.61: Disturbance test D.B4, $\tau_{c,HP} = 40$ s, $\tau_{c,NEM} = 20$ s. Simulation with varying wind velocity and $gain = 6000$ W/Hz.

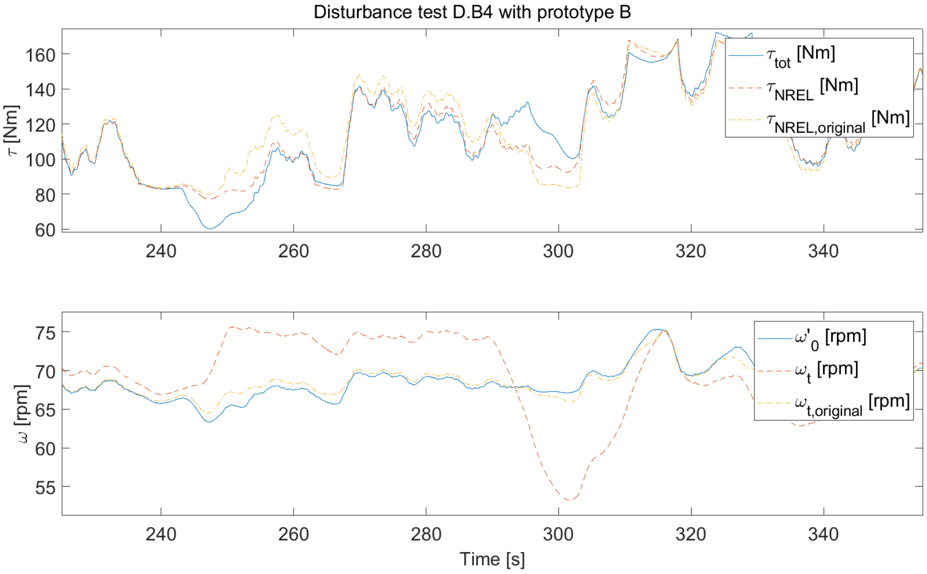

Figure A.62: Disturbance test D.B4, $\tau_{c,HP} = 40$ s, $\tau_{c,NEM} = 20$ s. Simulation with varying wind velocity and *gain* = 6000 W/Hz.

DEPARTMENT OF ELECTRICAL ENGINEERING
CHALMERS UNIVERSITY OF TECHNOLOGY
Gothenburg, Sweden
www.chalmers.se